# Seismic Performance Evaluation of Water Supply Systems
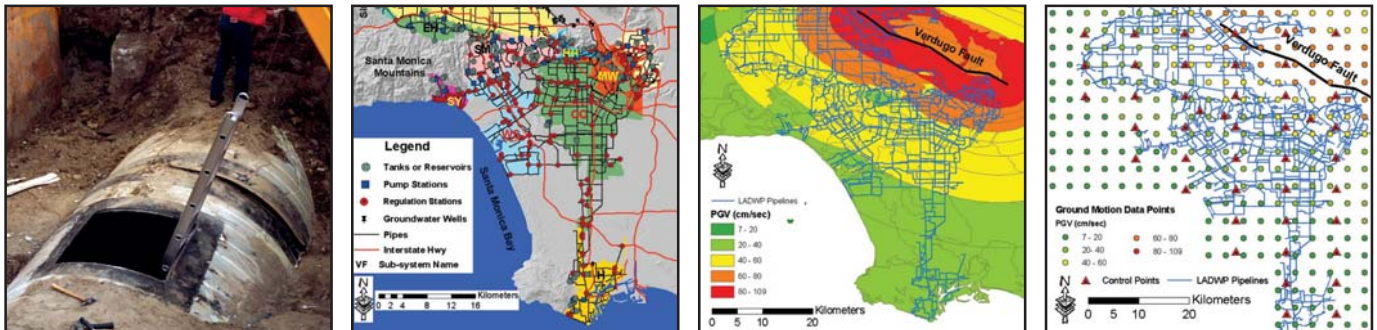
**by**
**Yu Wang and Thomas D. O'Rourke**

**Technical Report MCEER-08-0015**

**May 5, 2008**

# NOTICE

# Seismic Performance Evaluation of Water Supply Systems

by

Yu Wang[1] and Thomas D. O'Rourke[2]

Publication Date: May 5, 2008
Submittal Date: March 28, 2008

Technical Report MCEER-08-0015

Task Number 10.1.2

1   Assistant Professor, Department of Building & Construction, City University of Hong Kong, Kowloon, Hong Kong; former Ph.D. Candidate, School of Civil and Environmental Engineering, Cornell University
2   Thomas R. Briggs Professor of Engineering, School of Civil and Environmental Engineering, Cornell University

MCEER
University at Buffalo, The State University of New York
Red Jacket Quadrangle, Buffalo, NY 14261
Phone: (716) 645-3391; Fax (716) 645-3399
E-mail: *mceer@buffalo.edu*;  WWW Site: *http://mceer.buffalo.edu*

# Preface

The Multidisciplinary Center for Earthquake Engineering Research (MCEER) is a national center of excellence in advanced technology applications that is dedicated to the reduction of earthquake losses nationwide. Headquartered at the University at Buffalo, State University of New York, the Center was originally established by the National Science Foundation in 1986, as the National Center for Earthquake Engineering Research (NCEER).

Comprising a consortium of researchers from numerous disciplines and institutions throughout the United States, the Center's mission is to reduce earthquake losses through research and the application of advanced technologies that improve engineering, pre-earthquake planning and post-earthquake recovery strategies. Toward this end, the Center coordinates a nationwide program of multidisciplinary team research, education and outreach activities.

MCEER's research is conducted under the sponsorship of two major federal agencies: the National Science Foundation (NSF) and the Federal Highway Administration (FHWA), and the State of New York. Significant support is derived from the Federal Emergency Management Agency (FEMA), other state governments, academic institutions, foreign governments and private industry.

MCEER's NSF-sponsored research objectives are twofold: to increase resilience by developing seismic evaluation and rehabilitation strategies for the post-disaster facilities and systems (hospitals, electrical and water lifelines, and bridges and highways) that society expects to be operational following an earthquake; and to further enhance resilience by developing improved emergency management capabilities to ensure an effective response and recovery following the earthquake (see the figure below).
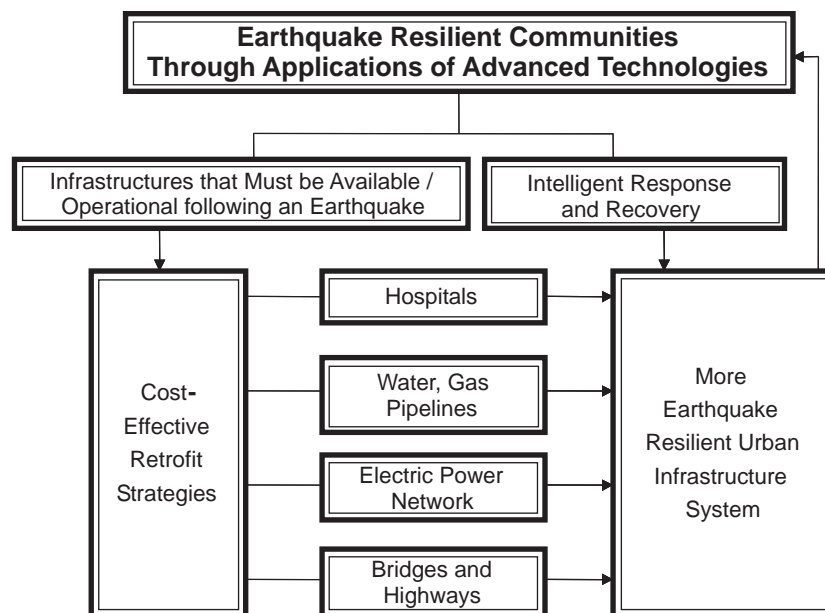
A cross-program activity focuses on the establishment of an effective experimental and analytical network to facilitate the exchange of information between researchers located in various institutions across the country. These are complemented by, and integrated with, other MCEER activities in education, outreach, technology transfer, and industry partnerships.

*This report describes an evaluation process for simulating the seismic performance of large geographically distributed water supply systems and characterizing their performance in terms of reliability and serviceability. The evaluation process makes use of probabilistic seismic hazard analysis tools, theoretical and empirical relationships of pipeline responses, hydraulic analysis of heavily damaged water networks, and multi-scale simulations of complex water systems. The process provides information for decision makers to assess the economic and social impacts of lifeline disruptions due to earthquakes, and works in combination with a computer code, Graphical Iterative Response Analysis for Flow Following Earthquakes (GIRAFFE) developed by the authors to simulate heavily damaged piepline networks and presents the simulation results in GIS format. The framework for decision-making presented in this report describes five basic activities: seismic hazard characterization, system definition, system component response evaluation, global system response evaluation, and consequences assessment. The methodology was applied to evaluate the seismic performance of the water supply operated by the Los Angeles Department of Water and Power (LADWP). The results of the analysis show that the five water districts in the LADWP have significantly different seismic risks and deteriorate to various extents after a 24-hour period following an earthquake. These differences in serviceability and reliability are consistent with the geographical position of the districts in relationship to the seismic faults and their capacity for water storage.*

# ABSTRACT

This report deals with the seismic performance evaluation of water supply systems. An evaluation process is developed for simulating the seismic performance of a large, geographically distributed water supply system and characterizing the performance in terms of system reliability and serviceability. The process makes use of probabilistic seismic hazard analysis, theoretical and empirical relations to estimate pipeline response, hydraulic analysis for heavily damaged water systems, and multi-scale simulations of complex water systems. It provides output that is beneficial for system management and decision-making and necessary for economists and social scientists to assess the economic and community impacts of lifeline disruption by earthquakes.

A general model is presented for the longitudinal force and pullout induced in underground pipelines/conduits by seismic body waves. The model provides a definition for pipelines that are either relatively rigid or flexible in the axial dimension with respect to seismic ground deformation. Both finite element and simplified models are presented that account for the effects of peak ground velocity, wave propagation velocity, predominant period of seismic excitation, shear transfer between soil and conduit, axial stiffness of the conduit, and pullout and compressive capacity of conduit joints. In total, 320 finite element runs were performed to account for different combinations of ground conditions, pipeline properties, and seismic wave characteristics. Dimensionless plots were developed from the simulations that facilitate the computation of relative slip at pipeline joints and connections between tunnels and underground facilities.

The seismic performance was evaluated for the water system operated by the Los Angeles Department of Water and Power (LADWP), and the results show that the system risk curve without storage water loss varies almost linearly in the semi-logarithmetic scale. The results show that the system deteriorates rapidly when storage water losses in tanks are modeled by a 24-hour period of pipeline leakage. The system serviceability index (SSI), which is defined as the ratio of the sum of satisfied water demands after an earthquake to that before an earthquake, decreases significantly. After a 24-hour period of running tanks, the SSI associated with a 475-

year recurrence interval decreases from 0.79 to 0.42. The number of scenario earthquakes that have contributions to the system risk increases as the recurrence interval for the risk decreases. As the recurrence interval decreases, or SSI increases, the contributions increases from scenario earthquakes with relatively large distances from originating faults to the system. The five water districts in LADWP system have significantly different risk curves and deteriorate to various extents after a 24-hour period of running tanks. The difference among the water district serviceability and reliability is consistent with their relative positions and the concentration of most water storage tanks in the system and with the north to the south water flow pattern in the LADWP water supply system.

# ACKNOWLEDGMENTS

**TABLE OF CONTENTS**

**TABLE OF CONTENTS (Cont'd)**

**TABLE OF CONTENTS (Cont'd)**

# LIST OF FIGURES

**LIST OF FIGURES (Cont'd)**

xviii

# LIST OF FIGURES (Cont'd)

# LIST OF TABLES

# LIST OF TABLES (Cont'd)

# CHAPTER 1

# INTRODUCTION

## 1.1. Background

Lifelines are the systems and facilities that provide services vital to the function of an industrialized society and important to emergency response and recovery after disastrous events (Duke and Moran, 1972). These systems and facilities include electric power, natural gas and liquid fuels, telecommunications, transportation (airports, highways, ports, rail and transit), waste disposal, and water (O'Rourke, 1998). Taken individually, or in aggregate, these systems are intricately linked with the economic well-being, security, and social fabric of the communities they serve.

This report focuses on the seismic performance evaluation of water supply systems. The basic function of a water supply system is to deliver water from sources to customers. A water supply system contains a network of pipes, pumps, and valves that move water from sources to customers, tanks and reservoirs that store water to accommodate fluctuations in demand because of varying rates of usage or fire protection needs, and other supporting infrastructures. A survey of the residents in high seismic risk communities (Nigg, 1998) showed that water pipeline systems, major hospitals, and power systems are ranked as the three most important infrastructure elements in the built environment that must remain operational in the

event of a major earthquake. Those surveyed also indicated that they are more willing to invest in the seismic upgrading of these infrastructure elements.

In urban and suburban environments, most lifelines are located underground. As a consequence, ground movements triggered by earthquakes in the form of transient and permanent ground deformation (TGD and PGD, respectively) have direct effects on the integrity of system components as well as the overall system performance. TGD is the dynamic response of the ground, and PGD is the irrecoverable movement that persists after shaking has stopped (O'Rourke et al., 2005). PGD often involves large displacements, such as those associated with surface fault rupture and landslides. TGD can cause soil cracks and fissures triggered by pulses of strong motion that develop localized shear and tensile strains exceeding the strength of surficial soils. The principal causes of TGD and PGD have been summarized and discussed by O'Rourke (1998) and updated by Bird et al. (2004).

To understand and evaluate system performance during earthquakes, this research was conducted in collaboration with the Los Angeles Department of Water and Power (LADWP), which operates one of the largest and most complex water and electric power networks in the United States, serving 3.8 million people in an area of approximately 1,200 km$^2$. The LADWP system is large, complex, and spatially variable. Therefore, models and simulation procedures that can accurately represent LADWP system performance should be applicable to smaller, less complex systems. The LADWP system contains many different facilities, types of pipelines, ground conditions, and geotechnical and seismic hazards. Procedures developed for LADWP, therefore, will have broader application to other systems where similar components and site conditions exist. Because LADWP operates both a water supply and electric

power distribution network, using the LADWP system provides an excellent opportunity to explore the interrelationship and interdependencies between water distribution and electric power. Because the LADWP system is a real system, procedures developed and utilized by LADWP personnel must take account of practical operational issues, which are an essential part of a functioning water supply and an essential feature of effective modeling for any lifeline network.

Research has been performed on the modeling of water and electric power distribution networks in areas vulnerable to earthquakes. This work includes modeling of the Memphis Light, Water, and Gas (MLWG) lifeline systems in Memphis and Shelby County, TN, which are at risk from earthquakes originating in the New Madrid Seismic Zone (Chang et al., 2000a; Shinozuka et al., 1998; Rose et al., 1997; and Chang et al., 1996).

Monte Carlo simulations of system performance were conducted for earthquakes of different magnitudes and distances for both electric power and water systems in the Memphis area. For the MLWG electric power system, the peak ground accelerations, PGAs, were computed for each earthquake scenario, spatially interpolated, and linked with damage states in electric substations. Ratios of power output in the damaged system to that in the undamaged system, and the number of days for restoration power, were evaluated for various parts of Shelby County (Shinozuka and Hwang, 1998). For the water system, procedures similar to those followed for the electric power system were utilized to estimate the ratio of water flow in the damaged system to that in the undamaged system in a hydraulic network model specifically configured for the piping and facilities operated by MLWG (Chang et al., 2002). The regional economic impacts of the MLWG lifeline system disruption caused

by earthquakes were assessed through a methodology that correlates lifeline losses with areas of economic activity, adjusts for business resiliency (remaining percentage output that can still be produced by a specific industry in the event of total losses of lifeline systems), and accounts for direct and indirect economic losses (Chang et al., 2002). Indirect economic losses generated by seismic damage to lifelines were estimated with Input-Output (I-O) analysis and Computable General Equilibrium (CGE) methods (Rose and Benavides, 1998).

For the LADWP electric power system, methodologies have been developed for evaluating the post-earthquake performance of electric power systems (Shinozuka et al., 2003; Shinozuka and Chang, 2004; and Shinozuka et al., 2004). Performance data for LADWP transformers compiled after the 1994 Northridge earthquake were used to develop fragility curves. Modeling of the LADWP power transmission network was performed with the software IPFLOW, available through the Electric Power Research Institute, EPRI. Monte Carlo simulations were performed for a suite of 47 scenario earthquakes, compiled to represent the seismic hazards for the LADWP electric power system, to estimate the ratio of mean power supply in the damaged network to that of the undamaged network for each LADWP service area for a scenario earthquake. Risk curves were derived from the system simulation and 47 scenario earthquakes, for which the annual frequency of exceedance was plotted relative to the percentage of households lacking electricity immediately after an earthquake. The regional economic impact of the LADWP system power losses were estimated, and the results were plotted by the variation of annual frequency of exceedance as a function of the percent of gross regional product (GRP) in the LADWP service area that would be lost, given the electric power outage in each simulation earthquake.

Earthquake effects on water supply systems have been investigated extensively (Ballantyne et al., 1990; Taylor, 1991; Shinozuka et al., 1992; Markov et al., 1994; Tanaka, 1996; and Hwang et al., 1998), and substantial progress has been made in developing modeling procedures that account for soil-structure interaction (O'Rourke and Liu, 1999), PGD and TGD (O'Rourke, 1998), and system reliability (Grigoriu et al., 1989). Work in San Francisco, for example, has focused on characterizing liquefaction hazards, the interaction between PGD generated by liquefaction and pipeline response, water supply system performance, and effects of water supply performance on fire following earthquakes for both the 1906 San Francisco and 1989 Loma Prieta earthquakes (O'Rourke et al., 1992; O'Rourke and Pease, 1992; O'Rourke et al., 2006; and Scawthorn et al., 2006). Of special note are methodologies for estimating the serviceability of a water supply system heavily damaged by an earthquake (Markov et al., 1994). These methodologies account for the limitation of commercially available hydraulic analysis software in predicting unrealistic negative pressures in a heavily damaged system by eliminating portions of the network containing negative pressures in accordance with the commercially available software.

For the LADWP water supply system, a comprehensive geographic information system (GIS) database, containing extensive pipeline damage and strong motion data during the 1994 Northridge earthquake, as well as approximately 10750-km distribution lines and 1000-km trunk lines, was developed (O'Rourke and Toprak, 1997; and Toprak, 1998). Toprak (1998) explored the spatial relationship between cast iron pipeline damage and various seismic parameters, and he found that the damage correlation with peak ground velocity (PGV) is one with the highest statistical significance. Jeon and O'Rourke (2005) and Jeon (2002) focused on the spatial

variability of earthquake strong motion and its relationship with the performance of water distribution pipelines in the LADWP system. Statistically significant correlations were developed among pipeline repair rate, repairs/km, and PGV for cast iron, ductile iron, asbestos cement, and steel pipe. Ordinary kriging was used to develop regressions of pipeline repair rate associated with 90% confidence PGV. Such regressions provide an explicit means of characterizing the uncertainty embodied in the strong-motion data.

## 1.2. Objectives

The overall objective of this research is to develop an evaluation process for simulating the seismic performance of a large, geographically-distributed, water supply system and characterizing the performance in terms of system reliability and serviceability. The process makes use of probabilistic seismic hazard analysis, theoretical and empirical relations to estimate pipeline response, hydraulic analysis for heavily damaged water systems, and multi-scale simulations of complex water systems. It provides output that is beneficial for system management and decision-making and that is necessary for economists and social scientists to assess the economic and community impacts of lifeline disruption by earthquakes. There are five principal objectives of this research that are described briefly under the following subheadings:

### 1.2.1. Framework for Earthquake Effects on Lifelines

A framework for evaluating lifeline system performance under earthquake effects is presented and described. There are five principal steps in the framework,

consisting of seismic hazard characterizations, system property characterizations, system demand / system interaction, system response evaluation, and consequence assessments. Seismic hazards are combined with system characteristics in models that account for the effects of transient ground motion and permanent ground deformation on both above ground and underground facilities. Fragility analyses of system components are used to assess the overall system response, from which the consequences with respect to the broader community of lifeline users are derived. Interaction with other external systems affects the response of the specific system being evaluated. Each of these steps is described, and these interrelationships are discussed. Examples illustrating the application of the framework are presented.

## 1.2.2. Seismic Hazard Characterizations of LADWP System

An important objective of this research is to describe the characterizations of seismic hazards for the LADWP system and to apply the seismic hazard characterizations to evaluate the effects of earthquakes on the Los Angeles water supply system. A process jointly developed by URS Corporation, MCEER, and LADWP is described to characterize the seismic hazards in the LADWP system using a suite of 59 scenario earthquakes and their optimized annual frequencies of occurrence. Strong ground motions, e.g., PGV, for each of the 59 scenario earthquakes are generated in a grid with 572 points in total and an interval of 0.03° longitude or latitude covering the LADWP water supply system. The PGV contour surfaces are interpolated from these 572 points using local polynomial interpolation, and site condition corrections are followed according to the NEHRP-HAZUS procedures. With the aid of GIS software, the spatial distribution of the LADWP system components are

superimposed on the PGV contour surfaces to determine the seismic demand on each component in accordance with their respective locations.

### 1.2.3. Seismic Body Wave Effects on Pipelines

A primary objective of this research is to gain insights into the seismic body wave effects on pipelines. A general model is presented for the longitudinal force and pullout induced in underground lifelines in the form of pipelines/conduits by seismic body waves. The model provides a definition for pipelines that are either relatively rigid or flexible in the axial dimension with respect to seismic ground deformation. Both finite element and simplified models are presented that account for the effects of peak ground velocity, wave propagation velocity, predominant period of seismic excitation, shear transfer between soil and conduit, axial stiffness of the conduit, and pullout and compressive capacity of conduit joints. Modeling results for water trunk line performance during the 1994 Northridge earthquake are shown to compare favorably with observed pipeline behavior during that earthquake. In total, 320 finite element runs were performed to account for different combinations of ground conditions, pipeline properties, and seismic wave characteristics. Dimensionless plots were developed from the simulations that facilitate the computation of relative slip at pipeline joints and connections between tunnels and underground facilities.

### 1.2.4. Prototype for Water Supply System Seismic Performance Evaluation

Another objective of this research is to demonstrate the process of seismic performance evaluation of water supply systems using the LADWP water supply system. Procedures are developed to determine the seismic demands on the system

components, which are compiled into a hydraulic network model. The performance of pipelines affected by transient ground deformation are estimated using regression equations between repair rate and PGV. The Poisson process is utilized to simulate the occurrence of pipe damage, and Monte Carlo simulations are performed to assess system serviceability using a special hydraulic analysis program, GIRAFFE, which is equipped with hydraulic models for pipe break and leak and is capable of eliminating unrealistic negative pressure predicted by commercially available hydraulic analysis software. The evaluation results are organized in the form of system risk curves, plotting the variation of annual exceeding frequency as a function of system serviceability index, SSI, which is the ratio of the sum of satisfied water demands after earthquakes to that before earthquakes.

## 1.2.5. Seismic Performance Evaluation of LADWP Water Supply System

Another objective of this research is to provide a probabilistic seismic performance evaluation of the LADWP water supply system. The system risk curves are developed for both the overall system and the five water districts. Significant impacts on the system performance because of storage water losses in tanks after earthquakes are discussed, and the system deterioration that results from the storage water losses is quantified. The risk levels corresponding to 475-year or 50-year recurrence intervals are deaggregated to identify key scenario earthquakes that significantly contribute to the system risks and their magnitudes and distances to the water system. The evaluation results are organized in a fashion that can be utilized by economists and social scientists as key input information in their economic and community impact assessment. More reliable post-earthquake damage scenarios are provided for the emergency response and recovery activity studies, whose main

objective is to minimize the earthquake losses and to effectively allocate the limited resources.

## 1.3. Scope

This report is divided into eight chapters, the first of which presents objectives and introductory comments. Chapter 2 presents a framework for evaluating earthquake effects on lifeline systems. There are five principal steps in the framework, consisting of seismic hazard characterizations, system property characterizations, system demand / system interaction, system response evaluation, and consequence assessments. Each of these steps is described, and the roles for the various disciplinary professionals are depicted.

Chapters 3 to 7 follow these principal steps and focus on the seismic performance evaluation of the LADWP water supply system. Chapter 3 describes the seismic hazard characterizations of the LADWP water supply system by a suite of 59 scenario earthquakes and presents the procedures utilized to determine the seismic demand on each system component, e.g., peak ground velocity for each water pipeline. Chapter 4 summarizes the system characteristics of the LADWP water supply system, including the physical characteristics, such as system statistics, system structure, and water flow pattern, and the operational characteristics, which are compiled into a hydraulic analysis model provided by LADWP engineers.

Chapter 5 develops simplified and numerical models for the seismic wave interaction with pipelines. Attention is directed to seismic body wave effects on one particular class of pipelines used for trunk and transmission facilities in North

America, referred to collectively in this work as jointed concrete cylinder pipelines (JCCPs). The structural and joint characteristics of JCCPs are described, revealing the vulnerability of JCCPs. Both finite element and simplified models are developed, and the effect of the mortar cracking strain at the JCCP joints is discussed. The models for the JCCP interactions with seismic body waves are expanded to accommodate other type of pipelines or facilities containing locally weak joints.

Chapter 6 describes the system response simulations utilizing GIRAFFE. The structure and capability of GIRAFFE, as well as the verification of GIRAFFE with the observed LADWP water supply system performance during the 1994 Northridge earthquake, are described. Chapter 7 summarizes the process for seismic performance evaluation of the LADWP water supply system and presents the probabilistic evaluation results in the form of system risk curves, plotting the annual exceeding frequency as a function of system water availability to their customers after earthquakes. The final chapter summarizes the research findings and presents conclusions pertaining to this research, as well as some recommendations for future research.

# CHAPTER 2

# FRAMEWORK FOR EARTHQUAKE EFFECTS ON LIFELINES

## 2.1. Introduction

This chapter presents a general framework to evaluate earthquake effects on lifelines, starting with a description of lifelines and lifeline system characteristics. The framework is structured around a basic chain of activities that includes the characterizations of seismic hazards and system properties, analyses of the interaction between seismic demand and lifeline component or facility response, and the assessment of system response and its consequences on the regional economy and community institutions. The framework is applicable to hazards other than earthquakes, including natural disasters and human threats.

## 2.2. Lifelines

Lifelines are the systems and facilities that provide services vital to the function of an industrialized society and important to emergency response and recovery after disastrous events. These systems and facilities include electric power, natural gas and liquid fuels, telecommunications, transportation (airports, highways, ports, rail and transit), waste disposal, and water. Taken individually, or in aggregate,

these systems are intricately linked with the economic well-being, security, and social fabric of the communities they serve.

In general, each lifeline system is a network within which there are sources, major transmission lines, storage, and distribution or collection systems. They are public utilities, each of which has a terminus outside the communities and an extensive matrix of contact or distribution points inside. All lifeline systems share four common characteristics: geographical dispersion, interconnectivity, diversity (O'Rourke, 1998), and interdependencies, which are discussed under the subheadings that follow.

### 2.2.1. Geographical Dispersion

Lifeline systems are usually constructed over a broad geographic area, where the communities they serve are dispersed, thus, are vulnerable to a broad range of natural disaster hazards, such as earthquakes. Consider, for example, the water supply system in the greater Los Angeles region, which is dispersed over an area of more than $1,200$ km$^2$. The geographical dispersion characteristic of lifelines has a profound influence on planning and design as compared with those for a building or local facility. The site of a building or local facility can be chosen and / or remediated on the basis of detailed geotechnical and seismic investigations on a relatively narrow area. However, because of their geographical dispersion, it is not practical to characterize and remediate all sites that lifeline systems cover with the same degree of detail. This characteristic constrains the application of models that require detailed and site-specific input information to evaluate seismic performance. This limitation can be lessened by detailed geotechnical and seismic investigations for critical links of

systems, areas that multiple lifelines are co-located, and known locations of geotechnical hazards to provide site-specific input information for seismic performance modeling.

The geographical dispersion characteristic of lifelines also leads to the application of stochastic simulation procedures to assess lifeline performance. Because the exact locations of failure within the systems are not known with certainty, the lifeline performance can not be evaluated on a deterministic basis, but have to make use of stochastic simulation procedures. Quite often, Monte Carlo techniques are employed in the system performance evaluation to cope with the associated uncertainty.

Although lifeline systems are dispersed over broad geographic areas, many are constrained to follow existing rights-of-way or are routed within river valleys, canyons, and mountain passes, where the saturated alluvial sediments susceptible to liquefaction during earthquakes typically exist. The inability to change location and/or direction within restrictive rights-of-way can create difficulties at fault crossings and landslide areas and lead to potentially troublesome interactions when different lifelines are co-located within narrow corridors.

## 2.2.2. Interconnectivity

Lifelines are usually configured as networks. Consider, for example, water distribution networks in which customers and water treatment plants are interconnected by pipelines, control valves, pumps, tanks, and reservoirs. Transportation networks are also interconnected. A highway system, for example, is

composed of primary roads, bridges, overpasses, interconnections with secondary roads, tunnels, and traffic control and surveillance facilities. Damage to lifelines not only results in the physical impairment and cost of repair at specific locations, but also the losses of connectivity and the potential for more widespread and serious losses of functionality throughout the network. Very often the critical links are bridges and tunnels where damage is not easily fixed, access may be difficult, and alternative pathways are not available. All physically interconnected civil infrastructure systems are characterized by critical links. The identification and quantification of system impact associated with the losses of critical links is an important aspect of any procedure to manage risk and optimize physical network performance.

The performance of a lifeline system will be influenced by the critical paths and the degree of physical and operational redundancy vested in a particular system. Systems with more redundant connectivity are more robust and therefore will perform better when compared with less redundant systems.

### 2.2.3. Diversity

A lifeline system is a collection of many different facilities and components, which contribute to the overall system performance by their unique functionalities. The integration of these parts achieves the designated function of the lifeline system. The seismic performance of lifeline systems depends on the characteristics of each facility and component. Consider, for example, a water supply system. Many water supply systems are composed of pipelines manufactured with steel, cast iron, asbestos cement, and plastic, which have significantly different strengths and ductilities, and perform differently under seismic loads. The joints linking individual sections of pipe

may be fitted with rubber gaskets, rigidly formed with full circumferential welds or riveted cross-sections, or composed of lead or cement-caulked bell-and-spigot couplings. Even if a pipeline system is composed of the same material, there will be a variety of special fittings, valves, joints, tees, and bends that must be considered for a comprehensive analysis.

Additional diversity may result from the fact that most lifeline systems have been built over many years and function with facilities and components produced according to different construction and / or manufacturing techniques, standards, and design procedures. As the knowledge in earthquake engineering and geotechnical hazards advances, it is not unusual to find that existing lifelines are sited in locations that are vulnerable to ground failure or severe transient effects related to the adverse site response characteristics. From this perspective, it is a much different problem to operate an existing system for optimal earthquake response than to site and design new lifeline systems.

The deterioration of an existing lifeline system is another source of variability. Some lifeline systems have components constructed more than 100 years ago, and their degree of deterioration is difficult to quantify. Deterioration, or aging, of system components can be caused by corrosion; deformation associated with settlement, adjacent construction, and past seismic events; repetitive loads leading to fatigue; fracture initiation and propagation; and loss of resilience in polymeric products associated with creep and material degradation. Most often, there is spatial distribution associated with deterioration. Deterioration may vary across different sites within the system and localized deterioration in parts of the systems is not uncommon. System

performance therefore will depend on the degree of local deterioration, the number of deteriorated sites within the network, and the potential for deterioration at critical links.

### 2.2.4. Interdependencies

Lifeline systems have interdependencies, both by virtue of operational interaction and physical proximity. Damage to one lifeline system may, in turn, affect other lifeline systems. For example, the loss of electricity affects water supply systems by rendering pumps and automatic valves inoperable, thereby affecting the flow and pressure in the water system, and impairs transportation systems with malfunctioning traffic lights. As mentioned in the previous section, many lifeline systems are constrained to follow existing rights-of-way and different lifeline systems may co-locate within narrow corridors. Because of this physical proximity, which occurs quite often in the crowded urban environments, the disruption of one lifeline system may affect the performance of another. For example, a break in a water trunk line siting along a main street in an urban area may significantly block the traffic in the vicinity. If other lifeline systems, such as a power system and a telecommunication system, have underground cables running closed to the water trunk line, these systems may be negatively affected as well.

## 2.3. Framework for Earthquake Effects on Lifelines

A framework for evaluating lifeline system performance is shown schematically in Figure 2.1. Seismic hazards are combined with system characteristics in models that account for the effects of transient ground motion and permanent ground deformation on both above ground and underground facilities. Fragility

analyses of system components are used to assess the overall system response, from which the consequences with respect to the broader community of lifeline users are derived. Interaction with other external systems affects the response of the specific system being evaluated. By setting performance goals with respect to consequences, one can determine the desired level of system response. This response is achieved through interaction with the community by altering operational and physical characteristics of the system, as well as mitigating seismic hazards.

There is a basic chain of activities that predominates in this framework. The basic chain starts with the characterizations of seismic hazards and system properties, then proceeds to the analyses of interactions between them, from which system response and the evaluation of community impacts follow. This basic chain is emphasized in Figure 2.1 with bold and enlarged print, and its principal features are discussed under the subheadings that follow.

### 2.3.1. Seismic Hazards

Engineering seismologists can estimate the ground shaking hazards at a particular site quantitatively by either deterministic seismic hazard analysis, DSHA (Reiter, 1990), in which a particular earthquake scenario is assumed, or probabilistic seismic hazard analysis, PSHA (Cornell, 1968; and Reiter, 1990), when uncertainties in earthquake size, location, and time of occurrence are explicitly considered. The seismic hazard analysis, regardless of deterministic or probabilistic, starts with identification and evaluation of earthquake sources by reviewing geologic evidence, tectonic evidence, historical seismicity, and instrumental seismicity (Kramer, 1996). Then, a recurrence relationship, which specifies the average rate at which an
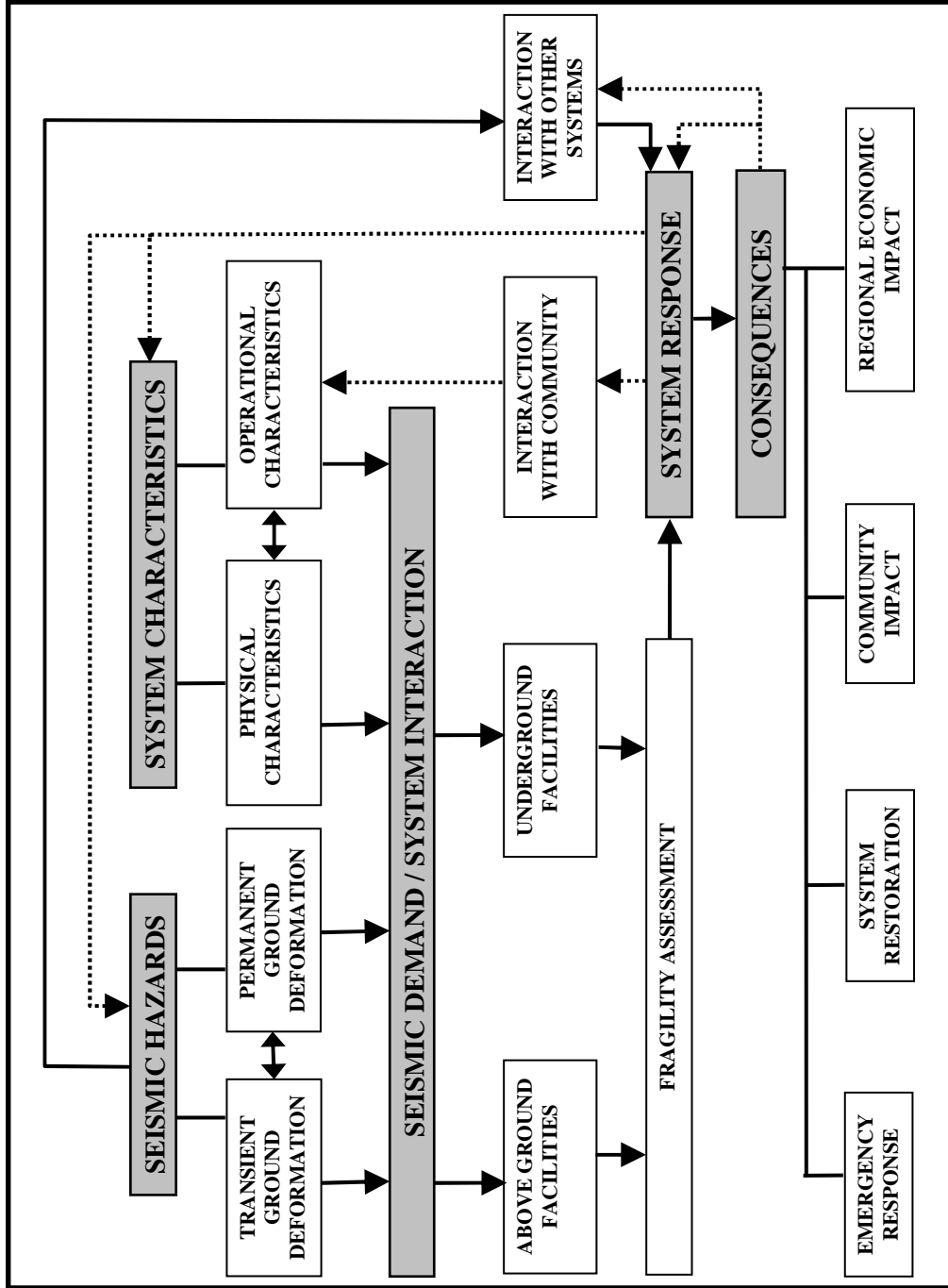
Figure 2.1. Framework for Lifeline System Performance under Earthquake Effects (O'Rourke et al., 2004a)

earthquake of some size will be exceeded, is used to characterize the seismicity of each source zone. The ground motion produced at each site is determined with the aids of some attenuation relationships, which describes the decrease of ground motion with increasing distance. Finally, PSHA combines the uncertainties in earthquake location, earthquake size, and attenuation relationships to obtain the probability that the ground motion level will be exceeded during a particular time period.

The earthquake-induced ground motion deforms the ground and affects lifeline systems by transient and permanent ground deformation (TGD and PGD, respectively). TGD refers to recoverable movement of the ground and soil strain as the seismic wave propagates through. The principal causes and types of TGD were summarized by O'Rourke (1998) and updated by Bird et al. (2004), as reproduced in Table 2.1. The most common cause of TGD is the traveling ground waves by seismic body waves, either compressional or shear waves, propagating from a seismic source. The body waves are characterized by a relatively high apparent wave propagation velocity that results in low ground strains, generally insufficient for serious lifeline damage except for the highly deteriorated lifeline systems and / or near source strong shaking. Surface waves may be amplified as seismic body waves propagate in some specific local geologic settings, such as large sedimentary basins, resulting in TGD capable of considerable lifeline disruption. Significant TGD-induced lifeline damage quite often occurs as the result of adverse ground conditions, such as narrow sediment-filled valleys with respect to relatively rigid valley boundaries, steep ridges and elevated topography accompanied locally by slip in fracture rock, and virtually level ground with liquefiable soils relative to adjacent and underlying competent materials.

Table 2.1.   Principal Causes and Types of Transient Ground Deformation
(After O'Rourke, 1998; and Bird et al., 2004)

| Cause | Description |
|---|---|
| Traveling Ground Waves | Near surface ground deformation caused by body wave propagating from a seismic source. |
| Surface Wave Generation in Large Sedimentary Basins | Surface waves generated by scattering incoming waves in large sedimentary basins typically several km wide, with depths < 1 km. |
| Vibration of Relatively Narrow Soil-filled Valleys | Deformation of sediment-filled valleys with respect to relatively rigid valley boundaries. Valley width and depth are typically several hundreds and several tens of meters, respectively. |
| Ridge Shattering | Ground disturbance along steep ridges and elevated topography that may be accompanied locally by slip in fracture rock. |
| Ground Oscillation | Transient lateral shear strains and horizontal movement of liquefiable soil relative to adjacent and underlying competent materials. |

PGD refers to the irrecoverable movement of the ground that often results from ground failure, but also may be the result of modest levels of volumetric strain and shear distortion. Table 2.2 summarizes the principle causes and types of PGD (O'Rourke, 1998; and Bird, et al., 2004). The main sources of PGD include surface faulting, tectonic uplift and subsidence, liquefaction, landslides, and densification. Surface faulting and tectonic uplift and subsidence are associated with the crustal deformation from which the ground shaking originates. In contrast, local ground conditions are responsible for liquefaction, landslides, and densification. Liquefaction usually occurs in loose saturated granular soils, which transform to a liquefied state or condition of substantially reduced shear strength when subjected to seismic loading. Inertial forces from seismic shaking may trigger mass movement of the ground, i.e., landslides, in the forms of rock falls, relatively shallow slumping and sliding of soils, or relatively deep translation and rotation of soil and rock. The earthquake-induced

Table 2.2. Principal Causes and Types of Permanent Ground Deformation
(O'Rourke, 1998; and Bird et al., 2004)

| Cause | Description |
|---|---|
| Faulting | The principal components of fault movement include: 1) strike, 2) reverse, and 3) normal slip. Reverse and normal faults promote compression and tension, depending on the angle of intersection between lifelines and the fault trace. |
| Tectonic Uplift and Subsidence | Regional changes in dimension associated with crustal deformation. Deformation occurs over a long distance so strains imposed will be small. Subsidence adjacent to water bodies can flood sections of a lifeline and possibly lead to erosion and undermining. |
| Liquefaction | Displacement caused by transformation of saturated, cohesionless soils to liquefied state or condition of substantially reduced shear strength. Liquefaction-induced lifeline deformation can be caused by: 1) lateral spread, 2) flow failure, 3) local subsidence, 4) post-liquefaction consolidation, 5) buoyancy effects, and 6) loss of bearing. |
| Landslide | Mass movement of the ground triggered by inertial forces from seismic shaking. Many displacement patterns are possible. Principal forms of movement include: 1) rock falls, 2) relatively shallow slumping and sliding of soils, and 3) relatively deep translation and rotation of soils and rocks. Landslides include lurching and soil block movement in which ground displacements are triggered by transient loading of gently sloping deposits underlain by weak soil not susceptible to liquefaction. |
| Densification | Decrease in volume caused by seismic vibration of dry or partially saturated cohesionless soils. |

shaking can decrease the volume of dry or partially saturated granular soils, resulting in ground subsidence.

Most PGD are relatively large and capable of severe damage to lifeline systems. For example, the liquefaction is one of the most pervasive causes for lifeline

damage during earthquakes (Hamada and O'Rourke, 1992; and O'Rourke and Hamada, 1992). Numerous investigators (e.g., Hamada et al., 1996; Hamada and Wakamatsu, 1996) have documented and analyzed the effects of large lateral and vertical ground deformation on the damage to lifeline systems.

### 2.3.2. System Characteristics

System characteristics involve both physical and operational attributes. As indicated in Figure 2.2, physical characteristics involve the types and numbers of components that assemble the system, the connectivity among components, the required functionality for each component, and how different components interact with each other to achieve the designated functionality of the system as a whole.

The operational characteristics of the system include its organizational and social aspects. Those who operate the system are the interface between the system and the user communities. Operational characteristics involve the system operating procedures, mapping, monitoring, maintenance, and planning.

As described in the previous section, lifeline systems are usually dispersed over a broad geographical area with tremendous diversity in the systems. The characterization of such systems requires a comprehensive data inventory with reference to spatial coordinates. Geographical information system (GIS), a computer-based system to aid in the collection, maintenance, storage, analysis, output, and distribution of spatial data and information, has unique advantages in characterizing lifeline systems. A GIS is a tool for making and using spatial information, and hence, automatically accommodates the geographical dispersion characteristics of lifeline

```
┌─────────────────────────────────────────────────────────────┐
│  PHYSICAL CHARACTERISTICS   OPERATIONAL CHARACTERISTICS       │
│      • COMPONENTS               • PLANNING                    │
│      • CONNECTIVITY             • MAPPING AND GIS             │
│      • FUNCTIONALITY            • MONITORING                  │
│      • INTERACTION              • MAINTENANCE                 │
│                                 • OPERATING PROCEDURES       │
└─────────────────────────────────────────────────────────────┘
```

Figure 2.2.  Physical and Operational Characteristics of Lifeline Systems

systems. The database embedded in the GIS permits the collection of diverse information regarding the lifeline systems, manipulation of the collected information, exploration of the relationship among system characteristics, and visualization of system performance. GIS is frequently part of the mapping process in lifeline engineering practices. However, it should be recognized that GIS is much more than a mapping process; it is a means of visualizing system performance and of identifying and quantifying multi-dimensional interactions within a two-dimensional surrogate of the real world.

### 2.3.3.  Seismic Demand / System Interaction

The effects of TGD and PGD are evaluated for the components of above ground and underground facilities. The underground facilities performance under seismic loading is assessed primarily by geotechnical engineers, who have developed models for soil-structure interaction, including empirical models based on the observations from the past earthquakes, closed form analytical methods, and numerical simulations, such as finite element and finite difference analyses.

Structural engineers focus typically on the performance of above ground facilities. The principles of structural dynamics (Chopra, 2005) are routinely applied in the engineering analysis and design of above ground structures. Theoretical models, as well as advanced numerical models, have been developed and applied for analyzing the above ground structure responses to ground shaking (Chopra, 2001; and Naeim, 2003).

To account for uncertainty with respect to component or facility response, seismic behavior is frequently characterized by fragility curves that provide the probability of failure as a function of the demand (e.g., peak acceleration or peak velocity) and confidence limit. Fragility curves can be derived from either the observations of past earthquakes or, more typically, Monte Carlo techniques that have special capability in quantifying uncertainty.

### 2.3.4. System Response

After evaluating the interaction between seismic demand and the component response of either above ground or underground facilities, lifeline performance assessment proceeds to system integration, in which performance is evaluated according to the functionality and serviceability of the entire network. Each lifeline system employs its simulation methodologies and / or software consistent with its characteristics. Consider, for example, a water supply system that needs to deliver water with sufficient pressure to customers. Its overall system performance is assessed using hydraulic network analysis, given the estimation of earthquake-induced damage at the component level (such as the damage to the trunk lines, distribution lines, and pump stations). Hydraulic network analysis is based on mass and energy conservation

equations, and is employed to integrate the impacts of component damage into the assessment of the designated system functionality as a whole. More specifically, hydraulic network analysis is performed to determine where the water outage area will be and how the customer demands are satisfied, given the earthquake-induced damage scenario at the component level.

System response is evaluated and used as the basis for changing network characteristics and/or mitigating seismic hazards. In some cases, seismic hazards can be reduced by densification of loose, saturated sand deposits, which are vulnerable to liquefaction, and by dewatering and stabilizing areas subject to landslides. Changes in the system characteristics may involve retrofitting existing facilities or replacing components with more resilient ones. Conventional engineering investigations lead to products that perform at a quantifiably improved level. To understand the ramifications of such improvements, simulations of system response must be performed with the improved component characteristics to show how the overall reliability is increased and broader community impacts are reduced.

### 2.3.5. Consequences

Lifeline systems are interwoven with the fabric of the communities they serve. Therefore, evaluation of earthquake effects on lifeline systems should account for the emergency response and system restoration procedures the communities utilize to reduce the adverse consequences, and quantify lifeline losses in terms of regional economic and social impacts. The economic and social impacts of lifeline system disruption are generally the most important with respect to community well-being.

The evaluation of system performance needs to incorporate larger social and economic effects to provide a realistic assessment of true expenses.

Economists and social scientists have contributed to a growing body of research and applications associated with the economic and social consequences of lifeline damage and loss of functionality. It is well recognized that lifeline disruption has a direct effect on business losses and social consequences. Consider, for example, water supply disruption, which adversely affects fire protection, the loss of which may trigger serious economic and social consequences. One catastrophic example is the 1906 San Francisco earthquake in which most of the city of San Francisco was burned out by the fires following the earthquake because of the water supply disruption and loss of fire fighting capability (Gilbert et al., 1907).

The direct regional economic consequences of lifeline loss often set off a chain reaction of further production cutbacks among successive rounds of customers and suppliers that spread through the entire regional economy, which is depicted vividly as "ripple effect" or "multiplier effect". Some well established analysis methodologies in economics, such as Input-Output (I-O) analysis and computable general equilibrium (CGE) analysis, have been successfully utilized to assess the indirect economic effects of lifeline disruption.

Input-Output analysis was developed by Leontief (1986), who recognized that, when measuring the impact that a particular sector has on regional economy, it is important to look beyond its direct role and to also examine the extent to which it affects other sectors. No economic enterprise stands alone, but rather depends on other businesses as suppliers or customers, which, in turn, rely on suppliers and customers

of their own. Input-Output analysis characterizes the interdependencies among different sectors by a set of tabulated economic statistics pertaining to purchases, inputs, and sales, outputs, among all sectors of the regional economy, and assumes a linear relationship exists between inputs and outputs. Official versions of the Input-Output tables for either the whole nation or many regions of the US, based on an extensive collection of data from nearly all US business establishments, are complied and provided by government agencies (Rose and Benavides, 1998).

A promising alternative to assess economic impacts of earthquakes is computable general equilibrium (CGE) analysis, which is a behavioral model for producer and consumer response to price signals in a multi-market context (Shoven and Whalley, 1992). As opposed to Input-Output analysis, which is generally referred as Vector Autoregressive (VAR) models in economics and relies heavily on statistics of economic data, CGE analysis starts with the construction of economical theoretical models and then finds data that fits the construct. CGE models are nonlinear and readily incorporate behavioral response, such as input substitution and conservation, under explicit constraints (Rose and Liao, 2003).

The typical construction and application of CGE models (Shoven and Whalley, 1992) consist of four steps. First, a theoretical model, which is usually referred as constant elasticity of substitution (CES) production function with multiple tiers and in a nested form, is constructed with some model parameters unspecified. Then a dataset, which is referred as the benchmark dataset, is used to calibrate the unspecified model parameters in such that the mode with the parameters supports the benchmark equilibrium. Once correctly specified, the model will reproduce the initial benchmark dataset as an equilibrium solution using these calibrated parameter values, which is

referred as a replication check. After that, these calibrated parameters can be used to solve for the associated alternative equilibrium in any policy experiment, or counterfactual experiment.

### 2.3.6. Interaction

Interconnectivity among components and interdependencies among different systems are two prominent characteristics of lifeline systems. The damage and disruption to one component may affect other components in the system through interconnectivity. Similarly, the damage and disruption in other systems may, in turn, affect the system being assessed because of physical proximity and / or operational interaction. Hence, a key component of the framework is the interaction of the system under scrutiny with other lifeline systems.

Lifeline systems are critical civil infrastructures that support the well-being of the communities they serve. Therefore, the interaction between lifeline systems and the communities they serve is another important component in the framework. The interaction between them mainly reflects in the operational characteristics of lifeline systems, such as planning, operating procedure, and maintenance.

## 2.4. Summary

Lifelines are the systems and facilities that provide services vital to the function of an industrialized society and important to the emergency response and recovery after disastrous events. These systems and facilities include electric power, natural gas and liquid fuels, telecommunications, transportation, waste disposal, and

water. In general, each lifeline system is a network within which there are sources, major transmission lines, storage, and distribution or collection system. All lifeline systems share four common characteristics: geographical dispersion, interconnectivity, diversity, and interdependencies.

A framework for evaluating lifeline system seismic performance was presented and a basic chain of activities that predominates in the framework was identified. The basic chain starts with the characterizations of seismic hazards and system properties, then proceeds to the analyses of interactions between them, from which system response and the evaluation of community impacts follow. Engineering seismologists may estimate the ground shaking hazards at a particular site quantitatively by either deterministic or probabilistic seismic hazard analysis. The lifeline system properties are usually characterized by the utility companies, who own and operate the systems. Geotechnical engineers and structural engineers focus on the evaluation of component response, which are then integrated to provide an evaluation of system performance in terms of system reliability and serviceability, e.g., water availability after earthquakes for water supply systems. The engineering output of the system response evaluation is then utilized in the social and economic consequence evaluation by social scientists and economists.

# CHAPTER 3

# LADWP SEISMIC HAZARD CHARACTERIZATIONS

## 3.1. Introduction

The seismic performance evaluation of a water supply system often begins with the characterization of seismic hazards affecting the system. This chapter describes the process, which was followed in this work, for characterizing the seismic hazards in the LADWP water supply system and determining the seismic demand on each system component. The seismic hazard characterization for the Los Angeles area was developed by approximating the aggregate seismic hazard in the area that takes into account all currently identified, potential seismic sources in a probabilistic context. This was accomplished by means of 59 scenario earthquakes that were selected to provide probability of exceedance characteristics for strong ground motion similar to those for all currently identified, potential seismic sources in the area (Lee et al., 2005). Strong ground motions are generated for each of the 59 scenario earthquakes in a grid covering the LADWP water supply system. The peak ground velocity (PGV) contour surfaces are interpolated from these grid points using local polynomial interpolation and corrected for site condition corrections using NEHRP-HAZUS procedures. With the aid of GIS software, the spatial distribution of the LADWP system components are superimposed on the PGV contour surfaces to determine the seismic demand on each component in accordance with their respective locations.

## 3.2. Seismic Hazard Characterizations in California

The United States Geological Survey (USGS) developed a probabilistic seismic hazard assessment methodology for all locations in the US, and prepared probabilistic seismic hazard maps in 1996, with revised maps in 2002 (http://earthquake.usgs.gov/hazmaps/). Both USGS and California Geological Survey (CGS) applied this methodology for locations in California, and the resulting 1996 and 2002 maps are available at the same web sites. The maps revised in 2002 are referred in this work as the USGS 2002 dataset. The USGS 2002 dataset represents the consensus within the geo-scientific community regarding earthquake parameters that contribute to the seismic hazards. This section briefly describes the processes that USGS and CGS utilized to assess the probabilistic seismic hazards in California, and the earthquake parameters they used. Most of this section draws on the contributions of Reiter (1990), Frankel et al. (1996), Petersen et al. (1996), Harmsen et al. (1999), Harmsen and Frankel (2001), Frankel et al. (2002), and Cao et al. (2003).

### 3.2.1. Basic Steps of Probabilistic Seismic Hazard Analysis

The USGS 2002 dataset incorporates seismic and geologic information to consider the probability of all possible damaging scenario earthquakes, calculates the potential range of ground motions for each scenario earthquake, and arrives at a level of ground shaking that has a given probability, using the formulation first developed by Cornell (1968). Figure 3.1 shows the basic steps of probabilistic seismic hazard analysis, as described in the following subheadings:
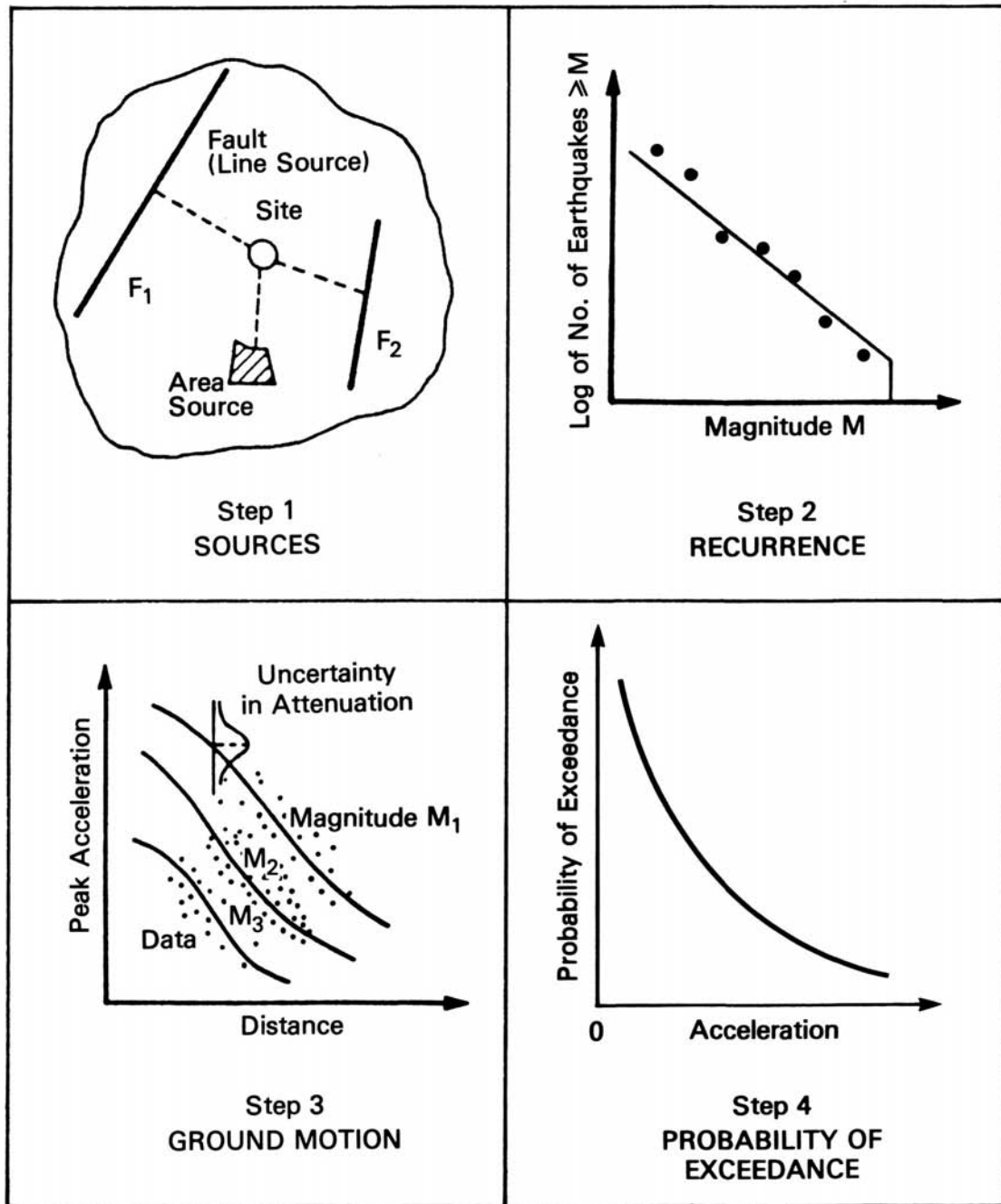
Figure 3.1.   Basic Steps of Probabilistic Seismic Hazard Analysis (after Reiter, 1990)

### 3.2.1.1. Earthquake Sources

The earthquake sources are delineated in accordance with geologic evidence, tectonic evidence, historical seismicity, and instrumental seismicity. Sources may range from clearly understood and defined faults to less well understood and less well defined geologic structures to hypothetical seismotectonic provinces, extending over many thousands of square kilometers, whose specific relationships to the earthquake generating process are not known. The configuration of individual sources could be points, lines, areas or volumes, depending on the type of source chosen and the ability to define it in geologic space. In Figure 3.1, the site at which the seismic hazard is to be estimated is shown with connecting lines illustrating the closest distances of these various sources to the site.

### 3.2.1.2. Seismicity Recurrence Characteristics for Each Source

After the earthquake sources are defined, each of them is characterized by an earthquake probability distribution or recurrence relationship, which indicates the chance of an earthquake of a given size occurring anywhere inside the source during a specified period of time, usually one year. A maximum or upper bound earthquake is chosen for each source which represents the maximum event to be considered. Recurrence relationships for individual sources have classically been represented by a linear regression line on the recorded data in a semi-logarithmic scale, as shown in Figure 3.1.

*3.2.1.3. Ground Motion*

The ground motion, such as peak ground velocity or spectral acceleration, due to each potential earthquake is estimated by means of an earthquake ground motion attenuation relationship which provides estimates of ground motion for an earthquake with a given magnitude at different distances by means of a curve fitted to observed data. A family of attenuation relationships, each of which relates a ground motion parameter to distance for an earthquake with a given size, is required to cover the range of earthquake sizes for all potential earthquakes.

*3.2.1.4. Probabilistic Seismic Hazard Curves*

As Reiter (1990) pointed out, the effects of all the earthquakes with different sizes, occurring at different locations in different earthquake sources at different probabilities of occurrence are integrated into one probabilistic seismic hazard curve that shows the probability of exceeding different levels of ground motion (e.g., peak ground acceleration) at the site during a specified period of time. The integration can be written as

$$E(z) = \sum_{i=1}^{N} \alpha_i \int_{m_0}^{m_u} \int_{r=0}^{r=\infty} f_i(m) f_i(r) P(Z > z \mid m,r) dr dm \qquad (3.1)$$

where E(z) is the expected probability of exceedance of ground motion level, z, during a specified time period, t, N is the number of earthquake sources affecting the site, $\alpha_i$ is the mean rate of occurrence of earthquakes between lower and upper bound magnitudes, $m_0$ and $m_u$, being considered in the ith earthquake source, $f_i(m)$ is the

probability density distribution of magnitude, recurrence relationship, within the ith earthquake source, $f_r(m)$ is the probability density distribution of epicentral distance between the various locations within earthquake source i and the site for which the hazard is being estimated, and $P(Z>z \mid m, r)$ is the probability that a given earthquake of magnitude m and epicentral distance, r, will exceed ground motion level, z.

### 3.2.1.5. Treatment of Uncertainties

The probabilistic seismic hazard analysis contains two types of uncertainties, aleatory uncertainties, which account for the intrinsic randomness of data or observations and epistemic uncertainties, which account for the model uncertainties. The probabilistic seismic hazard analysis assumes that the distribution of the aleatory uncertainties can be defined and incorporated into the hazard curves, contributing to the overall estimate of probability of exceedance. Consider, for example, the aleatory uncertainties of attenuation relationships, as shown in Figure 3.1 Step 3. The aleatory uncertainties of attenuation relationships can be divided into inter-event uncertainties due to "source effect", which is attributed to different earthquake source characteristics, such as style of faulting and depth of faults, and intra-event uncertainties due to "path effect", which describes the variation of ground motion resulting from different paths through which seismic waves propagate from the same earthquake source. The probability distribution of both inter- and intra-event uncertainties can be derived from the data or observations and incorporated in the estimation of ground motion in the Step 3 of Figure 3.1, playing a part in the calculations of $P(Z>z \mid m, r)$ term in Eqn 3.1 and resulting in contributions to the final probabilistic seismic hazard curves.

Epistemic uncertainties account for the model uncertainties that are with respect to the physical nature the models intend to simulate. In reality, there is only one true state of nature, as opposed to a certain number of competing models developed by different groups of researchers. Consider, for example, four competing attenuation relationships for southern California, which are proposed by Boore et al. (1997), Sadigh et al. (1997), Abrahamson and Silva (1997), and Campbell and Bozorgnia (2003), respectively. Similarly, multiple input values may exist for the various input parameters specified in Eqn 3.1 and shown graphically in Figure 3.1, and the incorporation of them can become quite cumbersome when multiple input values reflecting model uncertainties are taken into account. Thousands of scenario earthquakes may exist, corresponding to thousands of possible seismic source zonations, recurrence parameters, and ground motion attenuation combinations.

A method for combining these inputs is a logic tree, which is a decision flow path consisting of nodes and branches. Figure 3.2 shows an example of a logic tree. Each branch represents a discrete choice of input parameters and is assigned a likelihood of being correct. Logic tree is a convenient way of displaying input parameters, the options available, and the likelihood associated with each individual choice and scenario of choices. The analysis can be easily disassembled and hazard calculations can be carried out at a particular node point showing the effect that each element, such as style of faulting, has on the final hazards.

### 3.2.2. California Earthquake Sources

California is a high seismic hazard area, where a number of large earthquakes have occurred during historic time. California has had an average of about one $M \geq 6$

Figure 3.2 — Logic Tree Example

| Sense of Slip | Dip (deg) | Maximum Depth (km) | Total Length (km) | Rupture Length (km) | Maximum Displacement (m) | Average Displacement (m) | Maximum Historical | Magnitude Technique | Recurrence Method | Slip Rate (mm/yr) | Magnitude Distribution |
|---|---|---|---|---|---|---|---|---|---|---|---|
| Strike Slip (0.65) | 90 (0.6); 70 (0.4) | 9 (0.1); 12 (0.8); 15 (0.1) | 410 (1.0) | 20 (0.25); 45 (0.4); 70 (0.25); 110 (0.1) | No Data (1.0) | 1 (0.4); 2 (0.5); 3 (0.1) | <6 (1.0) | Rupture Length (0.25); Rupture Area (0.25); Total Length (0.25); Moment (0.25) | Moment Rate (1.0) | 0.5 h (0.1); 1 h (0.4); 3 h (0.4); 6 h (0.1) | Exponential (0.4); Characteristic (0.6) |
| Oblique (0.3) | 90 (0.3); 60 (0.6); 45 (0.1) | 9 (0.1); 12 (0.7); 15 (0.2) | 110 (0.5); 250 (0.4); 410 (0.1) | 20 (0.5); 45 (0.3); 70 (0.1); 110 (0.1) | No Data (1.0) | No Data (1.0) | <6 (1.0) | Rupture Length (0.5); Rupture Area (0.5) | Moment Rate (1.0) | 0.4 v 0.2 h (0.25); 0.4 v 0.4 h (0.5); 0.4 v 0.8 h (0.25) | Exponential (0.4); Characteristic (0.6) |
| Thrust (0.05) | 60 (0.4); 30 (0.5); 15 (0.1) | 9 (0.1); 12 (0.6); 15 (0.3) | 110 (0.5); 160 (0.3); 250 (0.2) | 20 (0.5); 45 (0.3); 70 (0.2) | No Data (1.0) | No Data (1.0) | <6 (1.0) | Rupture Length (0.4); Rupture Area (0.6) | Moment Rate (1.0) | 0.4 v (1.0) | Exponential (0.4); Characteristic (0.6) |

Notes:
Values in parentheses are probabilities
h = horizontal component of slip rate,
v = vertical component of slip rate

Figure 3.2.   Logic Tree Example (Yeats et al., 1997)

event every 2 to 3 years, and losses from individual earthquake have resulted in several billions of dollars of damage (e.g., 1906 San Francisco, 1933 Long Beach, 1971 San Fernando, 1989 Loma Prieta, and 1994 Northridge earthquakes).

The USGS and CGS evaluated fault length, geometry, and slip rates for about 180 faults statewide with reported displacements during late Pleistocene and Holocene times. Several major fault systems accommodate high slip rates and significantly contribute to the hazards in California including: the San Andreas Fault, the Cascadia subduction zone, the Eastern California Shear Zone, and compressional faults associated with the Western Transverse Ranges, as shown in Figure 3.3. Blind thrusts have recently been identified beneath the Los Angeles and San Fernando basins, the
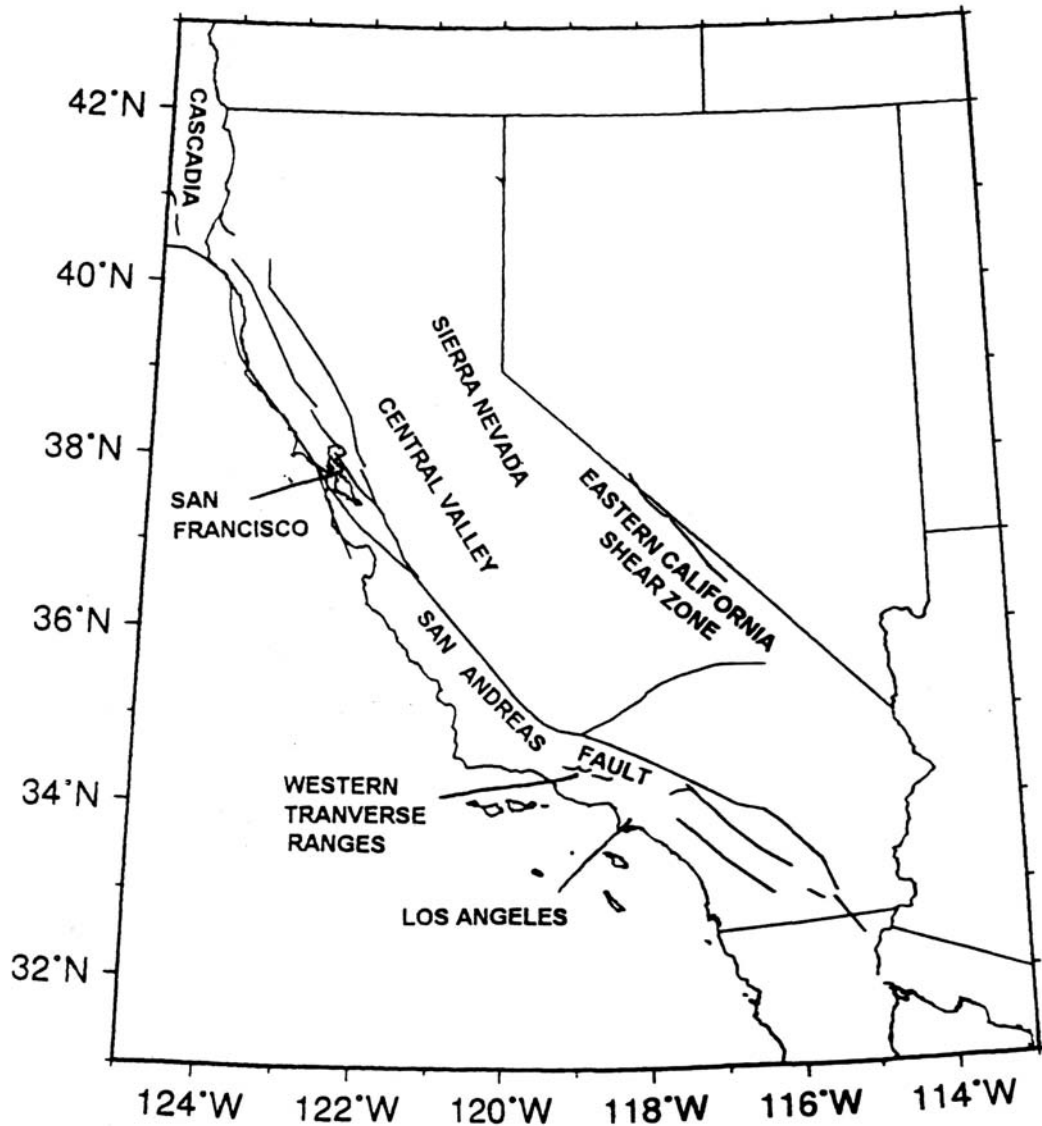
Figure 3.3. Major Fault Systems in California (Peterson et al., 1996)

Western Transverse Ranges, Santa Barbara Channel, and along the western flank of the Central Valley. In addition, several offshore faults have been identified and significantly contribute to the seismic hazards in coastal areas. Many late Quaternary faults are near a complex triple junction intersection of the Mendocino fracture zone, the San Andreas Fault, and the Cascadia subduction zone. Other significant faults are

found in the eastern portion of California along a broad zone of a portion of the state (Eastern California Shear Zone in Figure 3.3). Additional faults with Quaternary offsets are scattered over almost every strike-slip and normal faults distributed across the Mojave Desert, the Owens Valley, eastern Nevada, and across the northeastern region of California.

For each fault, the associated length, slip rate, quality of slip rate, maximum moment magnitude, characteristic earthquake rate and recurrence interval for the maximum magnitude, down dip width of the seismogenic zone, the top and bottom of the rupture surface, as well as the rake, dip, and dip azimuth of the rupture surface, and the endpoints of the fault or fault segment are determined and utilized as input parameters in the probabilistic seismic hazard analysis.

Earthquakes also occur in areas where they cannot be clearly assigned to a particular fault. Earthquake recurrence in these zones is based on models that consider the historic occurrence of earthquakes in the area and calculate magnitude-frequency distributions for each zone. A Gaussian smoothing process is applied to the historical background seismicity to distribute the earthquake potential through a grid of points that covers the zone.

### 3.2.3. California Seismicity Recurrence Characteristics

The annual number of earthquakes of various sizes, which is assigned to each fault, is based on the slip rate information and is defined using a combination of two recurrence distributions: (1) the characteristic earthquake model that implies that a typical size of earthquake ruptures repeatedly along a particular segment of the fault

(Schwartz and Coppersmith, 1984), and (2) the exponential model that implies that earthquakes on a given fault follow the Gutenberg-Richter relationship: $n(m) = 10^{a-bm}$ where n is the incremental number of earthquakes, a is the incremental number of earthquakes of m > 0, b is the slope of the distribution, and m is moment magnitude. These two recurrence distributions are both considered to be reasonable models either for specific faults or for larger areas of California. A combination of the two distributions is also thought to characterize the behavior of many fault systems (Petersen et al., 1996). This composite model allows for a greater number of large earthquakes than predicted by the exponential distribution, and also for earthquakes of sizes different than the characteristic event.

All the faults are categorized into two classes, i.e., A and B, each of which utilizes different recurrence distributions. The class A faults generally have slip rates greater than 5 mm/yr and well constrained paleoseismic data (i.e., the San Andreas, San Jacinto, Elsinore, Imperial, Hayward, and Rodgers Creek faults). The characteristic earthquake model is applied to the Class A faults. The class B faults include all of the other faults lacking paleoseismic data necessary to constrain the recurrence intervals of large events. Both the characteristics model and the Gutenberg-Richter model with a b-value = 0.8 are applied to Class B faults with a likelihood of 2/3 and 1/3, respectively, to account for the epistemic uncertainties.

### 3.2.4. Attenuation Relationships for California

The fault sources and area sources in California are divided into two types of regions: extensional and non-extensional tectonic regions. The extensional region is mostly located in eastern California and the non-extensional region is in western and

southern California. For the fault and area sources in the extensional tectonic region, five equally weighted attenuation relations are used. They are Abrahamson and Silva (1997), Boore et al. (1997), Sadigh et al. (1997), Campbell and Bozorgnia (2003), and Spudich et al. (1999). For the non-extensional tectonic region, only the first four equally weighted relations are used. The attenuation relations used for the Cascadia subduction zone are Youngs et al. (1997) and Sadigh et al. (1997) with equal weight. For the deep earthquakes (depth > 35 km) in northern California, the attenuation relations used are Youngs et al. (1997), and Atkinson and Boore (2003) with equal weight.

Because this work focuses on the seismic performance evaluation of the LADWP water supply system in the greater Los Angeles area, which lies in the non-extensional tectonic region, more details on the four attenuation relationships used in this region are provided in the following subheadings:

*3.2.4.1. Abrahamson and Silva (1997) Attenuation Relationship*

Abrahamson and Silva (1997) developed an attenuation relationship with a general function form of

$$\ln Sa(g) = f_1(M, r_{rup}) + Ff_3(M) + HWf_4(M, r_{rup}) + Sf_5(\overline{pga_{rock}}) \qquad (3.2)$$

where Sa(g) is the spectral acceleration in g, M is moment magnitude, $r_{rup}$ is the closest distance to the rupture plane in km, F is the fault type (1 for reverse, 0.5 for reverse/oblique, and 0 otherwise), HW is the dummy variable for hanging wall sites (1

for sites over the hanging wall, 0 otherwise), and S is a dummy variable for the site class (0 for rock or shallow soil, 1 for deep soil).

The function $f_1(M, r_{rup})$ is the basic functional form of the attenuation for strike-slip event recorded at rock sites, and is expressed as

for $M \leq c_1$

$$f_1(M, r_{rup}) = a_1 + a_2(M - c_1) + a_{12}(8.5 - M)^n + [a_3 + a_{13}(M - c_1)]\ln R \qquad (3.3)$$

for $M > c_1$

$$f_1(M, r_{rup}) = a_1 + a_4(M - c_1) + a_{12}(8.5 - M)^n + [a_3 + a_{13}(M - c_1)]\ln R \qquad (3.4)$$

where

$$R = \sqrt{r_{rup}^2 + c_4^2} \qquad (3.5)$$

The function $f_3(M)$ is the style-of-faulting factor with a functional form

$$f_3(M) = \begin{cases} a_5 & \text{for } M \leq 5.8 \\ a_5 + \dfrac{(a_6 - a_5)}{c_1 - 5.8} & \text{for } 5.8 < M < c_1 \\ a_6 & \text{for } M \geq c_1 \end{cases} \qquad (3.6)$$

The function $f_4(M, r_{rup})$ accounts for the hanging wall effect and is expressed as

$$f_4(M, r_{rup}) = f_{HW}(M) f_{HW}(r_{rup}) \tag{3.7}$$

where

$$f_{HW}(M) = \begin{cases} 0 & \text{for } M \leq 5.5 \\ M - 5.5 & \text{for } 5.5 < M < 6.5 \\ 1 & \text{for } M \geq 6.5 \end{cases} \tag{3.8}$$

and

$$f_{HW}(r_{rup}) = \begin{cases} 0 & \text{for } r_{rup} \leq 4 \\ a_9 \dfrac{r_{rup} - 4}{4} & \text{for } 4 < r_{rup} < 8 \\ a_9 & \text{for } 8 < r_{rup} < 18 \\ a_9 \left(1 - \dfrac{r_{rup} - 18}{7}\right) & \text{for } 18 < r_{rup} < 24 \\ 0 & \text{for } r_{rup} > 25 \end{cases} \tag{3.9}$$

The non-linear soil response is modeled by

$$f_5(\overline{pga_{rock}}) = a_{10} + a_{11} \ln(\overline{pga_{rock}} + c_5) \tag{3.10}$$

where $\overline{pga_{rock}}$ is the expected peak acceleration in rock in g (as predicted by the median attenuation relation with $S = 0$).

The total standard error (i.e., aleatory uncertainty), $\sigma_{total}$, is given by

46

$$\sigma_{total}(M) = \begin{cases} b_5 & \text{for } M \le 5.0 \\ b_5 - b_6(M-5) & \text{for } 5.0 < M < 7.0 \\ b_5 - 2b_6 & \text{for } M \ge 7.0 \end{cases} \quad (3.11)$$

The coefficients in Eqns 3.3 to 3.11 (i.e., $a_1$, $a_2$, $a_3$, $a_4$, $a_5$, $a_6$, $a_9$, $a_{10}$, $a_{11}$, $a_{12}$, $a_{13}$, $c_1$, $c_4$, $c_5$, $n$, $b_5$, and $b_6$) are determined by regression analysis and given by Abrahamson and Silva (1997). Consider, for example, the coefficients for spectral acceleration at period, T=1 sec, are: $a_1$=0.828, $a_2$=0.512, $a_3$=-0.8383, $a_4$=-0.144, $a_5$=0.490, $a_6$=0.013, $a_9$=0.281, $a_{10}$=0.423, $a_{11}$=0.00, $a_{12}$=-0.1020, $a_{13}$=0.17, $c_1$=6.4, $c_4$=3.70, $c_5$=0.03, n=2, $b_5$=0.83, and $b_6$=0.118.

### 3.2.4.2. Boore et al. (1997) Attenuation Relationship

Boore et al. (1997) proposed an attenuation relationship expressed as

$$\ln Y = b_1 + b_2(M-6) + b_3(M-6)^2 + b_5 \ln r + b_v \frac{V_S}{V_A} \quad (3.12)$$

where

$$r = \sqrt{r_{jb}^2 + h^2} \quad (3.13)$$

and

$$b_1 = \begin{cases} b_{1SS} & \text{for strike - slip earthquakes} \\ b_{1RS} & \text{for reverse - slip earthquakes} \\ b_{1ALL} & \text{if mechanism is not specified} \end{cases} \quad (3.14)$$

In Eqns 3.12 to 3.14, Y is the ground motion parameters (peak ground acceleration or spectral acceleration in g), M is the moment magnitude, $r_{jb}$ is the distance in km, and $V_S$ is the average shear-wave velocity up to 30 m in units of m/sec. Coefficients to be determined are $b_{1SS}$, $b_{1RS}$, $b_{1ALL}$, $b_2$, $b_3$, $b_5$, h, $b_V$, and $V_A$, which are all determined by regression analysis.

The overall variance, $\sigma_{\ln Y}$, of the regression is given by

$$\sigma_{\ln Y}^2 = \sigma_r^2 + \sigma_e^2 \qquad (3.15)$$

where $\sigma_e^2$ represents the earthquake-to-earthquake component of the variability and $\sigma_r^2$ represents all other components of variability.

The coefficients for spectral accelerations at various periods T are given by Boore et al. (1997). For example, the coefficients for the spectral acceleration at a period of T= 1 sec, are: $b_{1SS}$ = -1.133, $b_{1RS}$ = -1.009, $b_{1ALL}$ = -1.080, $b_2$ = 1.036, $b_3$ = -0.032, $b_5$ = -0.798, h = 2.90, $b_V$= -0.698, $V_A$ =1406, $\sigma_r$ = 0.575, and $\sigma_e$ = 0.214.

### 3.2.4.3. Sadigh et al. (1997) Attenuation Relationship

Sadigh et al. (1997) suggested an attenuation relationship for strike-slip faulting in rock sites expressed as

$$\begin{aligned} \ln(Y) = &\, C_1 + C_2 M + C_3 (8.5M)^{2.5} \\ &+ C_4 \ln(r_{rup} + \exp(C_5 + C_6 M)) + C_7 \ln(r_{rup} + 2) \end{aligned} \qquad (3.16)$$

where Y is the ground motion parameters (peak ground acceleration or spectral acceleration in g), M is moment magnitude, $r_{rup}$ is the closest distance to the rupture plane in km, $C_1$, $C_2$, $C_3$, $C_4$, $C_5$, $C_6$, and $C_7$ are coefficients determined by regression analysis. The total standard error, $\sigma_{lnY}$, is also determined by regression analysis. The ground motions for reverse/thrust faulting are 1.2 times greater than those for strike-slip faulting obtaining from Eqn 3.16.

The coefficients for spectral accelerations at various periods T are given by Sadigh et al. (1997). When M ≤ 6.5, the coefficients for the spectral acceleration at period, T= 1 sec, are: $C_1$ = -1.705, $C_2$ = 1.0, $C_3$ = -0.055, $C_4$ = -1.800, $C_5$ = 1.29649, $C_6$ = 0.250, and $C_7$ = 0. When M > 6.5, the coefficients for the spectral acceleration at period, T= 1 sec, are: $C_1$ = -2.355, $C_2$ = 1.1, $C_3$ = -0.055, $C_4$ = -1.800, $C_5$ = -0.48451, $C_6$ = 0.524, and $C_7$ = 0. The standard error for spectral acceleration at T = 1 sec is given by

$$\sigma_{\ln Y} = \begin{cases} 1.53 - 0.14M & \text{for M} < 7.21 \\ 0.52 & \text{for M} \geq 7.21 \end{cases} \tag{3.17}$$

### 3.2.4.4. Campbell and Bozorgnia (2003) Attenuation Relationship

Campbell and Bozorgnia (2003) developed another attenuation relationship in the form of

$$\begin{aligned} \ln(Y) = c_1 &+ f_1(M_w) + c_4 \ln \sqrt{f_2(M_w, r_{seis}, S)} \\ &+ f_3(F) + f_4(S) + f_5(HW, F, M_w, r_{seis}) + \varepsilon \end{aligned} \tag{3.18}$$

Where the magnitude scaling characteristics are given by

$$f_1(M_w) = c_2 M_w + c_3(8.5 - M_w)^2 \qquad (3.19)$$

the distance scaling characteristics are given by

$$f_2(M_w, r_{seis}, S) = r_{seis}^2 + g(S)^2 (\exp[c_8 M_w + c_9(8.5 - M_w)^2])^2 \qquad (3.20)$$

in which the near-source effect of local site conditions is given by

$$g(S) = c_5 + c_6(S_{VFS} + S_{SR}) + c_7 S_{FR} \qquad (3.21)$$

the effect of faulting mechanism is given by

$$f_3(F) = c_{10} F_{RV} + c_{11} F_{TH} \qquad (3.22)$$

the far-source effect of local site conditions is given by

$$f_4(S) = c_{12} S_{VFS} + c_{13} S_{SR} + c_{14} S_{FR} \qquad (3.23)$$

and the effect of the hanging wall (HW) is given by

$$f_5(HW, F, M_w, r_{seis}) = HWf_3(F) f_{HW}(M_w) f_{HW}(r_{seis}) \qquad (3.24)$$

where

$$HW = \begin{cases} 0 & \text{for } r_{jb} \geq 5 \text{ km or } \delta > 70° \\ (S_{VFS} + S_{SR} + S_{FR})(5 - r_{jb})/5 & \text{for } r_{jb} < 5 \text{ km and } \delta \leq 70° \end{cases} \tag{3.25}$$

$$f_{HW}(M_w) = \begin{cases} 0 & \text{for } M_w < 5.5 \\ M_w - 5.5 & \text{for } 5.5 \leq M_w \leq 6.5 \\ 1 & \text{for } M_w > 6.5 \end{cases} \tag{3.26}$$

and

$$f_{HW}(r_{seis}) = \begin{cases} c_{15}(r_{seis}/8) & \text{for } r_{seis} < 8 \text{ km} \\ c_{15} & \text{for } r_{seis} \geq 8 \text{ km} \end{cases} \tag{3.27}$$

In Eqns 3.18 to 3.27, Y is the ground motion parameters (i.e., peak ground velocity or spectral acceleration in the units of g), $M_w$ is moment magnitude, $r_{seis}$ is the closest distance to seismogenic rupture in a unit of km, $r_{jb}$ is the closest distance to the surface projection of fault rupture in units of km, $\delta$ is fault dip in degrees, $S_{VFS} = 1$ for very firm soil, $S_{SR} = 1$ for soft rock, $S_{FR} = 1$ for firm rock, and $S_{VFS} = S_{SR} = S_{FR} = 0$ for firm soil, $F_{RV} = 1$ for reverse faulting, $F_{TH} = 1$ for thrust faulting, and $F_{RV} = F_{TH} = 0$ for strike-slip and normal faulting, and $\varepsilon$ is a random error term with zero mean and standard deviation equal to $\sigma_{\ln Y}$.

The standard error, $\sigma_{\ln Y}$, is defined as a function of magnitude,

$$\sigma_{\ln Y} = \begin{cases} c_{16} - 0.07 M_w & \text{for } M_w < 7.4 \\ c_{16} - 0.518 & \text{for } M_w \geq 7.4 \end{cases} \tag{3.28}$$

Coefficients $c_1$, $c_2$, $c_3$, $c_4$, $c_5$, $c_6$, $c_7$, $c_8$, $c_9$, $c_{10}$, $c_{11}$, $c_{12}$, $c_{13}$, $c_{14}$, $c_{15}$, and $c_{16}$ are determined by regression analysis and given by Campbell and Bozorgnia (2003). For

example, the coefficients for spectral acceleration at T = 1 sec are: $c_1$ = -3.867, $c_2$ = 0.812, $c_3$ = -0.101, $c_4$ = -0.964, $c_5$ = 0.019, $c_6$ = 0, $c_7$ = 0, $c_8$ = 0.842, $c_9$ = -0.105, $c_{10}$ = 0.329, $c_{11}$ = 0.338, $c_{12}$ = -0.073, $c_{13}$ = -0.072, $c_{14}$ = -0.858, $c_{15}$ = 0.281, and $c_{16}$ = 1.021.

### 3.2.5. California Seismic Hazards

USGS and CGS integrated the effects of all earthquakes with different sizes, occurring at different locations in different earthquake sources at different probabilities of occurrence, and the consideration of uncertainties, using Eqn 3.1 and logic trees, to provide the probabilistic seismic hazard assessment results (i.e., USGS 2002 dataset), which are available at the USGS website (http://eqhazmaps.usgs.gov/). Figure 3.4 shows an example of a seismic hazard curve for a rock site in Los Angeles with geographical coordinates (34°, -118.4°), in which the annual probability of exceedance is plotted as a function of spectral acceleration at T = 1 sec in units of g. Obviously, the annual probability of exceedance decreases as the spectral acceleration increases. The seismic hazard curves at different sites may be combined and interpolated to generate the spatial distribution of seismic hazards in California. Figure 3.5 shows the spatial distribution of spectral acceleration at T = 1 sec with a 475-yr recurrence interval (10% probability of exceedance in 50 years) in California and Nevada. The state boundaries are indicated by blue lines and the areas with high seismic hazards are signified by red. The spatial distribution of the high seismic hazard areas are consistent with that of the major fault systems (i.e., the San Andreas Fault, the Cascadia subduction zone, the Eastern California Shear Zone, and compressional faults associated with the Western Transverse Ranges), as shown in Figure 3.3.
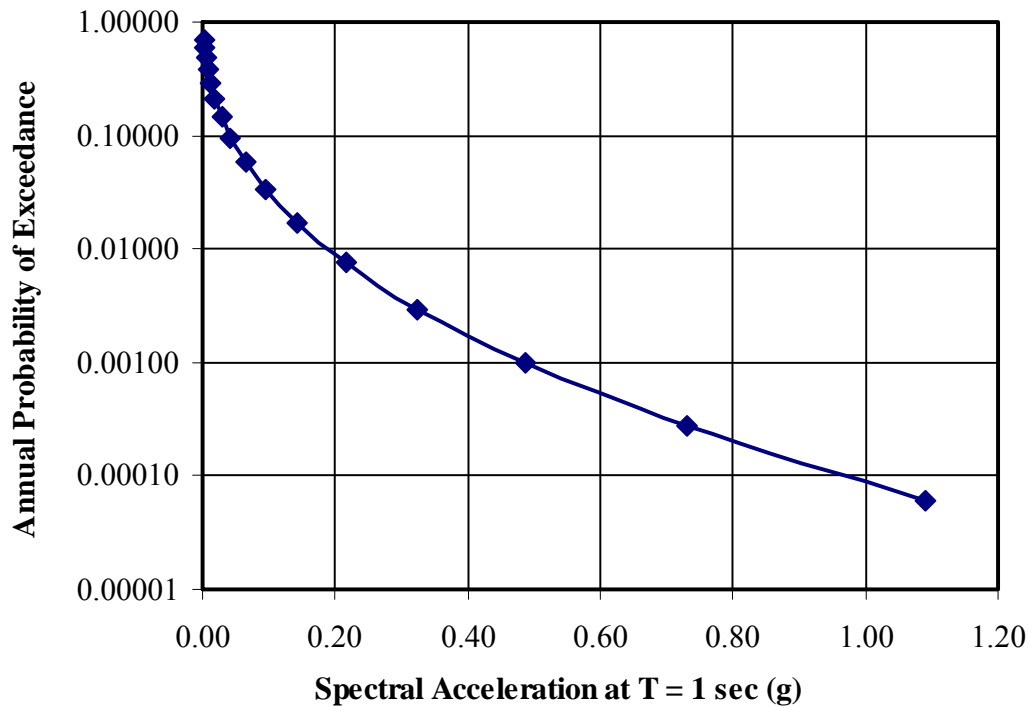
Figure 3.4.   Example of Seismic Hazard Curve from USGS 2002 Dataset [for A Site

in Los Angeles with Geographical Coordinates (-118.4°, 34°)]

## 3.3.  LADWP Seismic Hazard Characterizations

Although the USGS 2002 dataset represents the consensus within the geo-scientific community regarding earthquake parameters that contribute to the seismic hazards, difficulty exists in applying the dataset directly to the seismic performance evaluation of lifeline systems, such as a water supply system. This section starts with explanations of the difficulties involved in this process, followed by the development of a suite of 59 scenario earthquakes by URS Corporation, MCEER, and LADWP to approximate the seismic hazards in the Los Angeles area as represented by the USGS 2002 dataset. For more details on the development of the 59 scenario earthquakes, please refer to Lee et al. (2005).
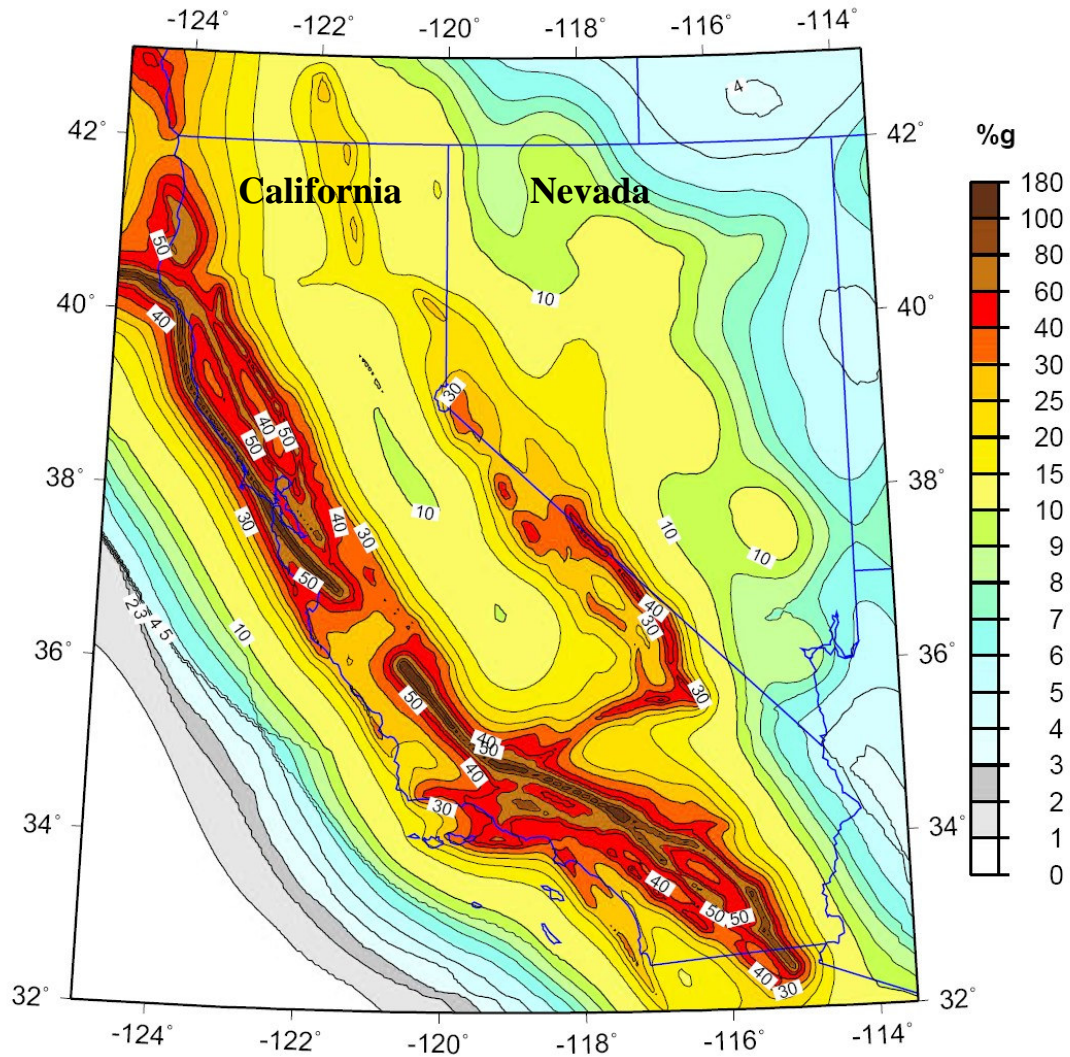
Figure 3.5.  475-yr Recurrence Spectral Acceleration at T = 1 sec for Rock Sites in
California and Nevada (USGS, 2005)

### 3.3.1.  Limitation of Applying USGS 2002 Dataset to Lifeline Systems

The probabilistic seismic hazard information generated in accordance with the
procedures described in Section 3.2 is commonly used for site-specific seismic
performance evaluation, in which only earthquake ground motion in one site is

required and spatial correlation among earthquake ground motions across many sites is never a concern. In contrast, the seismic performance evaluation of lifeline systems, which are dispersed over a broad geographic area, requires seismic hazard information at various sites across the system. For example, the seismic hazard information over an area of approximately 1,200 km$^2$ is required in the seismic performance evaluation of the LADWP water supply system. The earthquake ground motions with the same annual probability of exceedance differ, but correlate at various sites over the LADWP service area. The USGS 2002 dataset is for the aggregated hazard at a particular site associated with potentially thousands of earthquakes. If it were used simultaneously at a number of different sites distributed throughout a functioning system, it would overweight the earthquake effects on system performance by neglecting the spatial correlation that exists among different sites affected by the same earthquake.

One potential approach to account for the spatial correlation is to simulate lifeline system performance for a comprehensive set of scenario earthquakes, each of which is associated with an annual frequency of occurrence. Each scenario earthquake represents one branch of the logic trees described in Section 3.2.1.5, and denotes a discrete choice of input parameters and models. However, since detailed models of a large lifeline system are often quite complex, it may not be practical to simulate the system response for an exhaustive set of scenario earthquakes (which may contain thousands of scenario earthquakes for high seismic hazard areas, such as California). This raises a challenge on how to account for the large number of scenario earthquakes omitted and their contribution to the probabilistic hazard analysis results.

Chang et al. (2000b) proposed an approach in which a select number of scenario earthquakes are chosen based on their combined contribution to the aggregate

hazard, and the contribution of omitted earthquakes is accounted for by optimizing the annual frequencies of the earthquakes. Using this approach, a new set of event annual frequencies is sought such that the relevant ground shaking hazards computed from the selected set at the principal sites of interest matches the target probabilistic hazards, such as those associated with the USGS 2002 dataset. This procedure assumes that, when the seismic hazards of the USGS 2002 data set and select number of scenario earthquakes match, the lifeline system seismic performance matches as well.

### 3.3.2. Development of 59 Scenario Earthquakes

An approach was developed by Lee et al. (2005), which is similar to the one proposed by Chang et al. (2000b) to characterize the seismic hazards in the LADWP water supply system by choosing a suite of 59 scenario earthquakes so that their optimized annual frequencies of occurrence match the USGS 2002 probabilistic seismic hazards in the LADWP service area. Some information relevant to the development the 59 scenario earthquakes are described in the following subheadings:

*3.3.2.1. Control Points*

The 59 scenario earthquakes match the USGS 2002 dataset on a group of control points spatially distributed over the LADWP system. Figure 3.6 shows 56 control points specified by researchers at Cornell University. The 56 control points include 53 grid points (green dots in Figure 3.6) spatially distributed over the LADWP water supply system and 3 additional points (i.e., 54, 55, and 56) representing the locations of 3 key facilities, i.e., Lower Stone Canyon Reservoir, Lower Franklin Reservoir, and Silver Lake Reservoir (yellow triangles in Figure 3.6). Figure 3.6 also
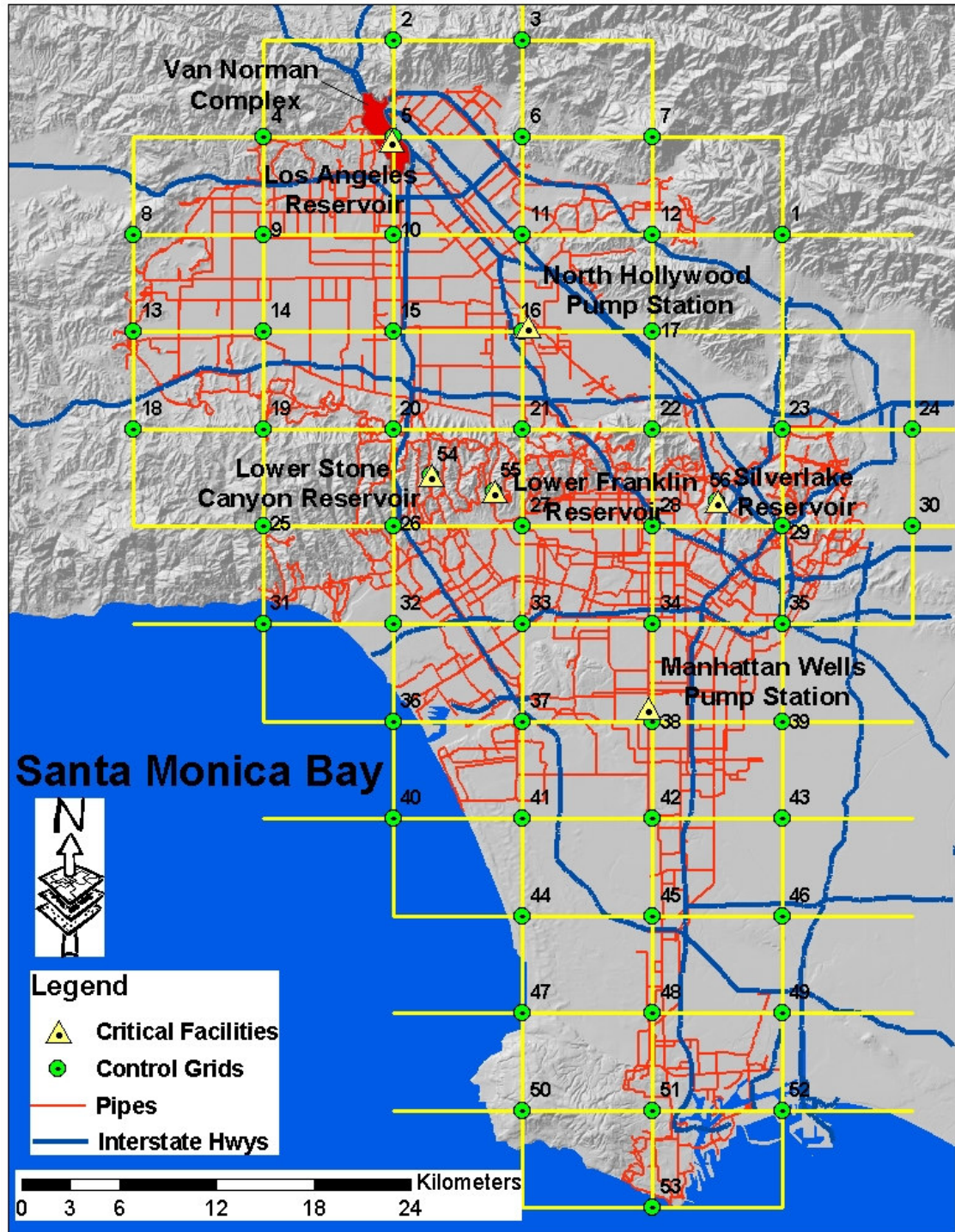
Figure 3.6. Spatial Distribution of 56 Control Points for Seismic Hazard Matching

between USGS 2002 Dataset and 59 Scenario Earthquakes

shows another 3 key facilities, i.e., LA Reservoir, North Hollywood Pump Station, and Manhattan Well Pump Station, which are located close to grid points 5, 16, and 38, respectively, and hence, require no additional control points. The probabilistic seismic hazards at the 56 control points are calculated from both the 59 scenario earthquakes and USGS 2002 dataset, and the annual frequencies of occurrence for the 59 scenario earthquakes are adjusted until both datasets give consistent seismic hazard characterizations at the 56 control points.

### 3.3.2.2. Ground Motion Parameters

The seismic performance of a water supply system is mostly influenced by the performance of the pipeline system, which is closely related to one particular ground motion parameter, peak ground velocity (Toprak, 1998). Models on the seismic wave interaction with pipelines are discussed in Chapter 5. In this work, the regression equations between the pipeline repair rate and peak ground velocity (Jeon, 2002) are utilized to simulate the seismic performance of the pipeline system, as described in Chapter 7. Therefore, the seismic hazards in the LADWP water supply system are characterized using peak ground velocity, and the 59 scenario earthquakes and USGS 2002 datasets are compared according to peak ground velocity.

As described in Section 3.2.4, the attenuation relationships used in the USGS 2002 dataset depict the variation of peak ground acceleration or spectral acceleration at various predominant periods, T, as a function of distance and other seismic parameters. The peak ground velocity is often inferred from the spectral acceleration, $S_{A1}$, at T = 1 sec using the equation adopted in HAZUS (FEMA, 1999),

$$V_p = \frac{386.4 \times S_{A1}}{2\pi \times 1.65} \qquad\qquad (3.29)$$

where $V_p$ is the peak ground velocity in units of inch/sec, and $S_{A1}$ is in units of g. The seismic hazards in the LADWP water supply system are characterized by calculating the $S_{A1}$ at equivalent rock sites, i.e., NEHRP B or BC site category (FEMA, 2003), at the 56 control points shown in Figure 3.6, and comparing them with the $S_{A1}$ from the USGS 2002 dataset at the same control points.

### 3.3.2.3. *Selection of Scenario Earthquakes*

The USGS 2002 dataset considers numerous uncertainties in the seismic input parameters, such as the geometric parameters of the seismic sources, and characteristics or Gutenberg-Richter reoccurrence models, resulting in thousands of scenario earthquakes (i.e., logic tree branches in Figure 3.2) for California. To reduce the number of earthquakes to be considered for hazard characterization, earthquakes that generate ground motion without engineering significance in the LADWP water supply system performance are eliminated. According to Jeon (2002), a peak ground velocity less than 10 cm/sec, corresponding to a $S_{A1} < 0.1$ g by Eqn 3.29, has negligible effect on the pipeline performance. Accordingly, the scenario earthquakes are eliminated if they do not produce $S_{A1} \geq 0.1$ g at any of the 56 control points spatially distributed over the LADWP water supply system. In addition, expert judgment is exercised to reduce uncertainties in some other input parameters, such as limiting magnitude uncertainty and background area seismic sources (Lee et al., 2005).

The elimination process leads to a suite of 59 scenario earthquakes, as shown in Table 3.1. Among the 59 scenario earthquakes, 55 (i.e., Scenario ID 12 to 454) of them are associated with specific fault segments, as indicated in the second column of Table 3.1. The other 4 scenarios (i.e., Scenario ID 559 to 562) are related to background area sources. The corresponding moment magnitude for each scenario earthquake is indicated in the third column of Table 3.1. Figure 3.7 shows the spatial distribution of the faults from which the 59 scenario earthquakes originate. Most faults are located with a distance less than 100 km from the LADWP water supply system.

### 3.3.2.4. Optimized Annual Frequencies of Occurrence

The seismic hazard associated with the 59 scenario earthquakes is adjusted to match that of the USGS 2002 dataset over the LADWP water supply system by a multivariate, nonlinear optimization process. The 59 annual occurrence frequencies for the 59 scenario earthquakes are the optimized variables. The target function is selected by minimizing an error function for the sum of the differences between the hazard curves (i.e., the variation of annual exceedance frequency as a function of $S_{A1}$ at equivalent rock sites) from the 59 scenario earthquakes and USGS 2002 dataset at each of the 56 control points. The error function is measured at all 56 points with equal weights, except the 6 control points (i.e., 5, 16, 38, 54, 55, and 56) representing the locations of key facilities, in which the weights are increased by 6 times.

Following the USGS 2002 probabilistic seismic hazard analysis procedures, four attenuation relationships (i.e., Abrahamson and Silva, 1997; Boore et al., 1997; Sadigh et al., 1997; and Campbell and Bozorgnia, 2003) with equal weights, as described in Section 3.2.4, are utilized to calculated the $S_{A1}$ and annual exceedance

Table 3.1.  Characteristics of 59 Scenario Earthquakes

| Scenario ID | Scenario Name | Magnitude Mw | Annual Occurrence Frequency |
|---|---|---|---|
| 12 | el15 | 6.8 | 3.60E-03 |
| 18 | SAF - Mojave | 7.3 | 4.13E-03 |
| 19 | SAF - Carrizo | 7.4 | 2.28E-03 |
| 21 | SAF-All southern segments | 8.1 | 3.00E-03 |
| 22 | SAF - 1857 | 7.8 | 9.61E-03 |
| 23 | SAF - Southern 2 segments | 7.7 | 3.37E-03 |
| 118 | Holser | 6.5 | 1.66E-04 |
| 119 | Hollywood | 6.4 | 6.64E-06 |
| 120 | Raymond | 6.5 | 7.41E-04 |
| 122 | Clamshell-Sawpit | 6.5 | 1.06E-03 |
| 141 | Newport-Inglewood offshore | 7.1 | 2.56E-03 |
| 145 | Coronado Bank | 7.6 | 1.75E-03 |
| 159 | Newport-Inglewood | 7.1 | 8.10E-04 |
| 160 | Newport-Inglewood | 6.6 | 2.37E-03 |
| 161 | Newport-Inglewood | 6.6 | 5.58E-04 |
| 162 | Newport-Inglewood | 6.6 | 1.50E-04 |
| 166 | Sierra Madre | 7.2 | 7.45E-04 |
| 167 | Sierra Madre | 6.7 | 4.40E-03 |
| 168 | Sierra Madre | 6.7 | 2.21E-04 |
| 169 | San Gabriel | 7.2 | 1.53E-03 |
| 170 | San Gabriel | 6.7 | 9.97E-05 |
| 171 | San Gabriel | 6.7 | 1.27E-03 |
| 173 | Malibu Coast | 6.7 | 2.70E-06 |
| 174 | Santa Monica | 6.6 | 5.23E-04 |
| 175 | Verdugo | 6.9 | 9.65E-04 |
| 176 | Verdugo | 6.4 | 1.57E-05 |
| 177 | Verdugo | 6.4 | 2.84E-06 |
| 189 | Oak Ridge-onshore | 7 | 4.13E-03 |
| 191 | Oak Ridge-onshore | 6.5 | 3.86E-03 |
| 195 | San Cayetano | 7 | 6.86E-03 |
| 196 | San Cayetano | 6.5 | 6.03E-03 |
| 198 | Santa Susana | 6.7 | 3.01E-03 |
| 202 | Simi-Santa Rosa | 7 | 6.35E-04 |
| 203 | Simi-Santa Rosa | 6.5 | 2.87E-04 |
| 219 | Anacapa-Dume | 7.5 | 9.36E-04 |

Table 3.1. (Continued)

| Scenario ID | Scenario Name | Magnitude Mw | Annual Occurrence Frequency |
|---|---|---|---|
| 220 | Anacapa-Dume | 7 | 5.70E-04 |
| 221 | Anacapa-Dume | 7 | 9.43E-04 |
| 222 | Anacapa-Dume | 6.5 | 1.29E-06 |
| 370 | Northridge | 7 | 1.43E-03 |
| 371 | Northridge | 6.5 | 2.88E-04 |
| 372 | Northridge | 6.5 | 2.37E-05 |
| 378 | Channel Island Thrust | 7.5 | 5.12E-04 |
| 388 | Upper Elysian Park | 6.4 | 6.13E-05 |
| 397 | Puente Hills blind thrust | 7.1 | 8.63E-04 |
| 398 | Puente Hills blind thrust | 6.6 | 1.04E-05 |
| 399 | Puente Hills blind thrust | 6.6 | 8.21E-05 |
| 440 | Cucamonga | 6.9 | 6.18E-03 |
| 443 | Sierra Madre-San Fernando | 6.7 | 9.41E-04 |
| 444 | Palos Verdes | 7.3 | 1.05E-03 |
| 446 | Palos Verdes | 6.8 | 8.20E-04 |
| 447 | Palos Verdes | 6.8 | 6.24E-04 |
| 451 | Palos Verdes | 6.3 | 3.27E-03 |
| 452 | Palos Verdes | 6.3 | 1.44E-03 |
| 453 | Palos Verdes | 6.3 | 2.07E-03 |
| 454 | Palos Verdes | 6.3 | 2.17E-03 |
| 559 | Background Source | 7 | 1.05E-03 |
| 560 | Background Source | 7 | 7.75E-04 |
| 561 | Background Source | 7 | 1.29E-03 |
| 562 | Background Source | 7 | 7.63E-04 |

frequency relationships at the 56 control points for the 59 scenario earthquakes. As discussed under Section 3.2.1.5, the attenuation relationships contain both aleatory uncertainties and epistemic uncertainties, which are accounted by the application of four equal-weighted attenuation models. The probability distribution of aleatory uncertainties can be defined from the regression analysis and is given by Eqns 3.11, 3.15, 3.17, and 3.28 for the four attenuation models, respectively. When calculating
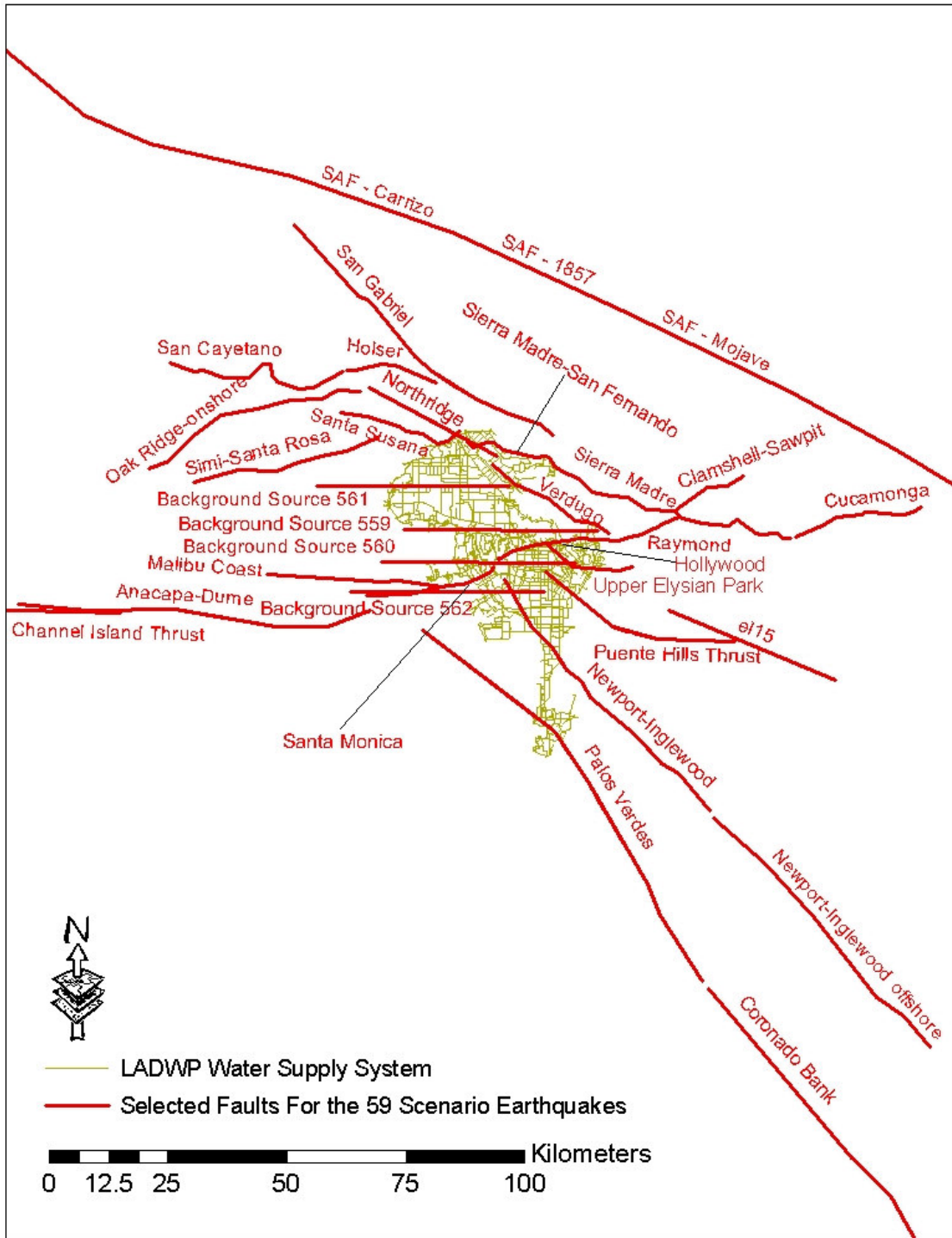
Figure 3.7.   Spatial Distribution of the Faults for 59 Scenario Earthquakes

the $S_{A1}$ and annual exceedance frequency relationships, two relationships are developed: one with the incorporation of the aleatory uncertainties in attenuation models and the other without the consideration of attenuation aleatory uncertainties. Both relationships are utilized with equal weights in the optimization process and compared with the $S_{A1}$ and annual exceedance frequency relationship from the USGS 2002 dataset, respectively.

The multivariate nonlinear optimization is then solved to obtain a set of optimized annual occurrence frequencies for the 59 scenario earthquakes. Table 3.1 includes the optimized annual occurrence frequencies in the fourth column. Please note that the optimized annual occurrence frequencies are not the real occurrence frequencies of the scenario earthquakes they are associated with, but the "equivalent" occurrence frequencies of the earthquakes that are similar to the scenario earthquakes. In aggregate, the 59 scenario earthquakes and corresponding optimized annual occurrence frequencies are a proxy representing the probabilistic seismic hazards in the LADWP water supply system, as defined by the USGS 2002 dataset.

*3.3.2.5. Comparison of Seismic Hazards between USGS 2002 Dataset and 59 Scenario Earthquakes*

The 59 scenario earthquakes and associated optimized annual occurrence frequencies are capable of reproducing the seismic hazard curves (i.e., annual exceedance frequency and $S_{A1}$ in rock sites relationships) at the 56 control points spatially distributed over the LADWP water supply system. Figure 3.8 shows the comparison of the seismic hazard curves from both the 59 scenario earthquakes and USGS 2002 datasets at control points 5 and 29, which are located at Van Norman
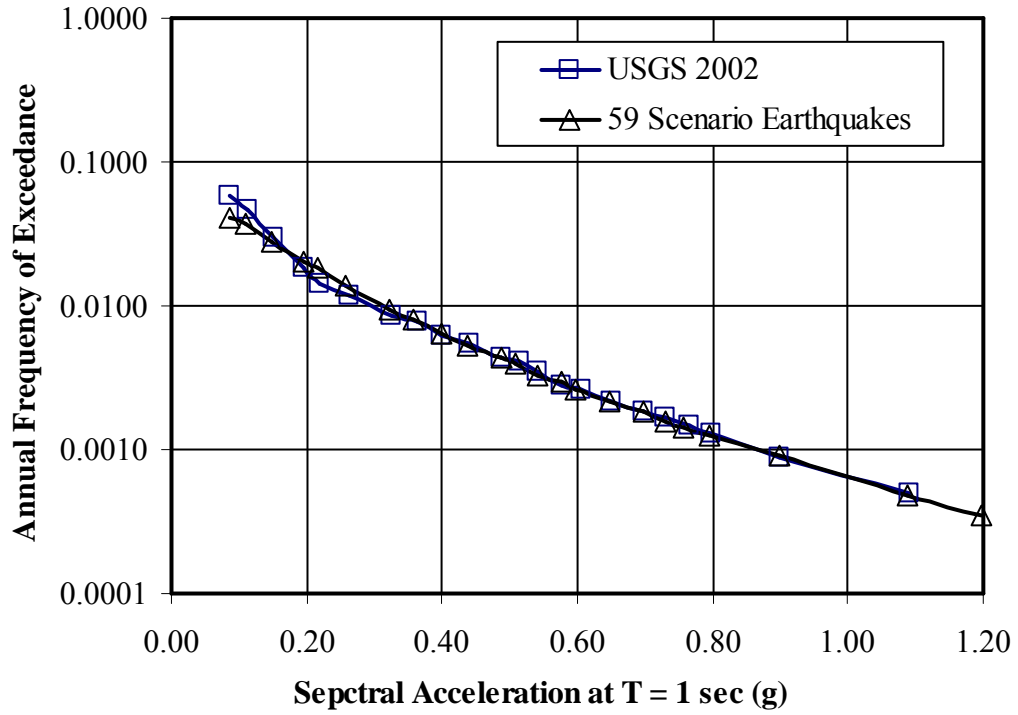
(a) Control Point 5
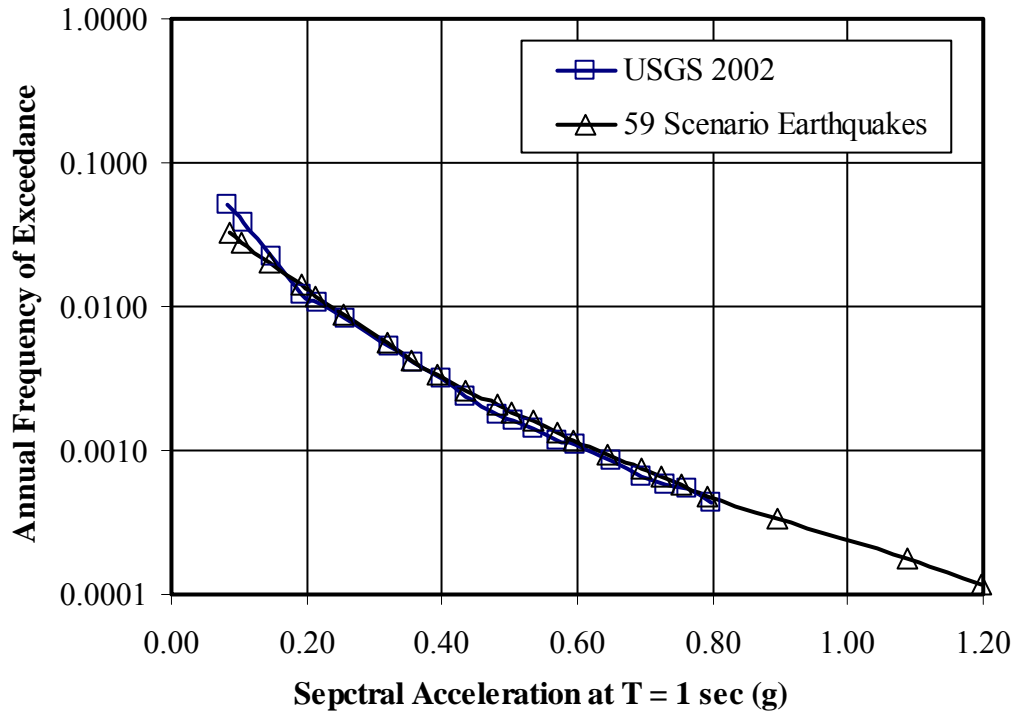


(b) Control Point 29

Figure 3.8.   Comparison between 59 Scenario Earthquakes and USGS 2002 Dataset

Complex in the northern San Fernando valley and the central city (Figure 3.6), respectively. The seismic hazard curves from the 59 scenario earthquakes and USGS 2002 datasets are shown by open triangles and open rectangles, respectively. It is evident in the Figure 3.8 that the seismic hazard curves are consistent with each other and the 59 scenario earthquakes match the USGS 2002 dataset reasonably well. For more details on the comparison between the 59 scenario earthquakes and USGS 2002 datasets, please refer to Lee et al. (2005).

### 3.3.3. Strong Ground Motion Data

For each of the 59 scenario earthquakes, several strong ground motion parameters at equivalent rock sites, i.e., peak ground acceleration (PGA), peak ground velocity (PGV), and spectral acceleration with 5% damping at $T = 0.2$ sec ($S_{A0.2}$), and $T = 1.0$ sec ($S_{A1}$), respectively, are generated at 572 points in a grid with uniform separation of points and interval of 0.03° longitude and latitude covering the LADWP water supply system. The grid is shown in Figure 3.9. The LADWP trunk line system and 56 control points utilized during the matching process are superimposed in Figure 3.9.

The PGAs, $S_{A0.2}$, and $S_{A1}$ are generated from the four attenuation relationships mentioned above, while the PGVs are inferred from $S_{A1}$ using Eqn 3.29. For each strong ground motion parameter at the 572 grid points, strong motion data are generated corresponding to both the mean and mean $\pm\,\sigma$, where $\sigma$ is the total standard error from the four attenuation models utilized. The standard error, $\sigma_{inter-event}$, associated with inter-event variability accounting for the "source" effects only (refer to Section 3.2.1.5) is estimated as 0.31 for PGA, PGV, and $S_{A1}$, and 0.35 for $S_{A0.2}$
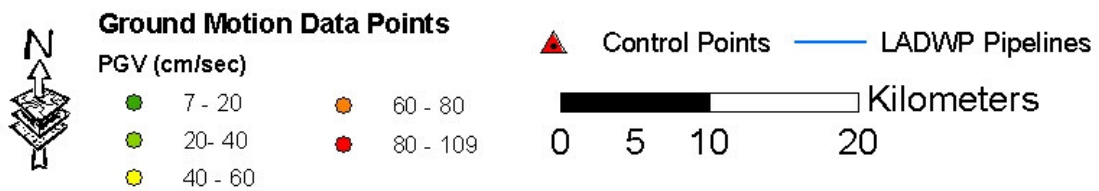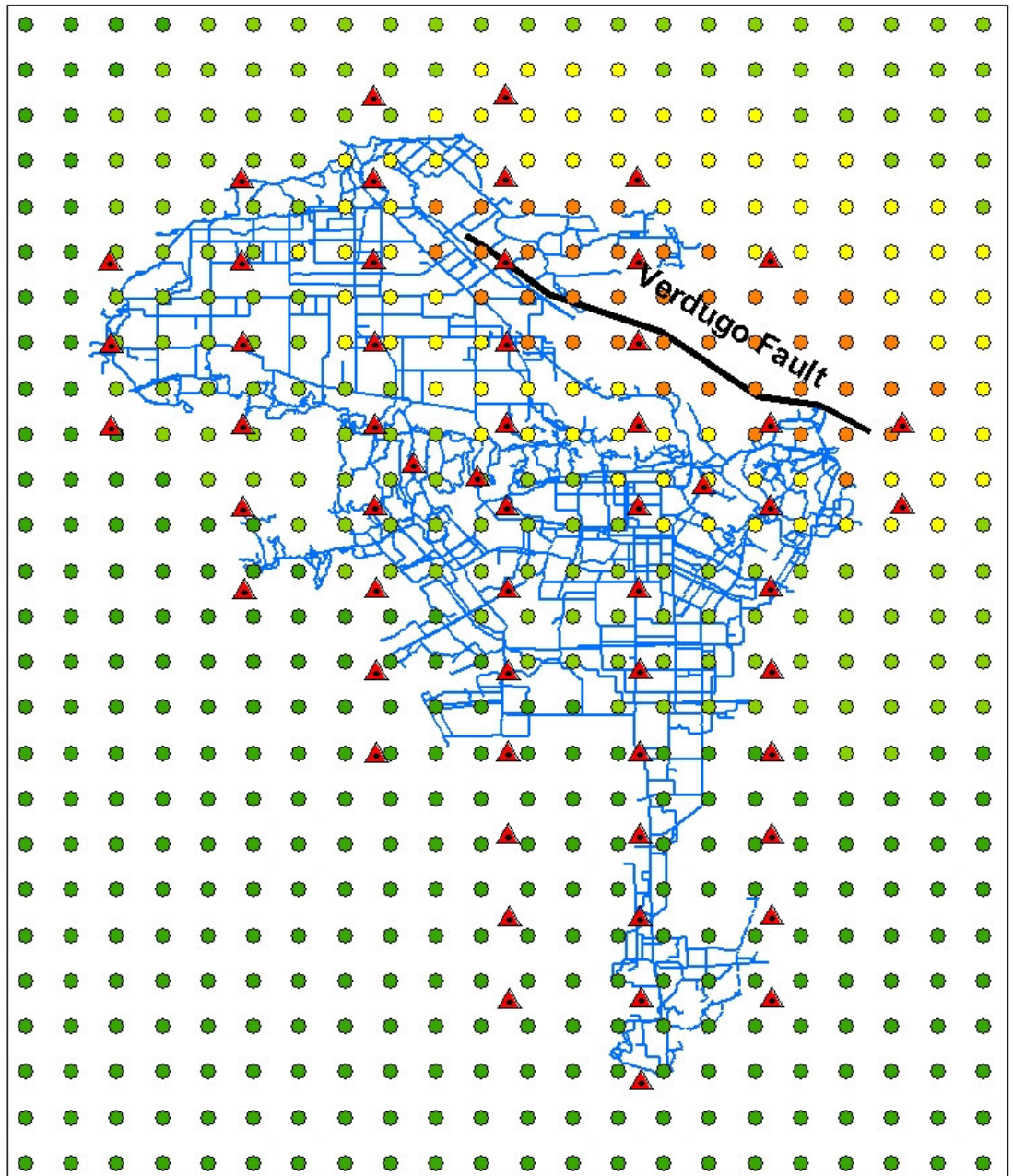
Figure 3.9.   Spatial Distribution of Strong Motion Data Grid

(Color-coded by Mean + $\sigma_{\text{inter-event}}$ PGV at Rock Sites from Scenario 175 Verdugo

Earthquake)

(Lee et al., 2005). Since the $\sigma_{\text{inter-event}}$ is the standard deviation of the natural log of the strong ground motion, the strong motion data corresponding to mean $\pm$ $\sigma_{\text{inter-event}}$, can be calculated from the mean strong motion data by:

$$mean \pm \sigma_{\text{int }er-event} = mean \times \exp(\pm\sigma_{\text{int }er-event}) \qquad (3.30)$$

In Figure 3.9, the 572 data grid points are color-coded by the mean + $\sigma_{\text{inter-event}}$ PGVs generated from Scenario 175 Verdugo Earthquake (Table 3.1). The high PGVs are indicated in orange and occur at the upper right quarter of the figure, where the Verdugo fault is located. The PGVs decrease as the distance to the Verdugo fault increases, as showed by the gradual conversion from orange to yellow, and then to green in Figure 3.9.

## 3.4. Seismic Demands on LADWP System Components

For each of the 59 scenario earthquakes, strong ground motion data at 572 points are generated, and the seismic demands on the system components in the LADWP water supply system are determined accordingly. Ground motion contour surfaces are developed from the data at the 572 points using local polynomial interpolation in a GIS software, and further corrected for the site conditions. Then, the seismic demands on the system components are determined according to their locations. As mentioned before, this work mostly focuses on the pipeline performance, which is closely related to the PGVs they are subjected to. Therefore, the PGV is utilized as the primary seismic demand parameter, based on which the contour surfaces are developed. This section employs Scenario 175 Verdugo earthquake (Table 3.1 and Figure 3.9) as an example to illustrate the procedures on determining

the PGVs on both link-type components (i.e., trunk lines) and node-type components (i.e., demand nodes representing local distribution systems). Similar procedures are applied to other 58 scenario earthquakes, as well as other ground motion parameters, if necessary.

### 3.4.1. Data Interpolation

The PGV contour surfaces are developed from the PGV values at the 572 points using the local polynomial interpolation in the Geostatistical Analyst module of a GIS software, ArcGIS (ESRI, 2001). Local polynomial interpolation fits many polynomials to the 572 data, each within specified overlapping neighborhoods. The polynomial parameters (i.e., the order of polynomial function and coefficients in the polynomial functions) and the number of specified overlapping neighborhoods are determined by an optimization process minimizing the root-mean-square prediction error, RMSPE. The RMSPE is the statistic that is calculated from cross-validation, in which, each measured point is removed and compared to the predicted value for that location. It is a summary statistic quantifying the error of the prediction surface. The final contour surface is developed by iteratively cross-validating the output surfaces that are calculated using different polynomial parameters and the number of specified overlapping neighborhoods until the minimum RMSPE is obtained.

Figure 3.10 shows an example of the contour surfaces developed from the mean + $\sigma_{inter-event}$ PGV at equivalent rock sites from the Scenario 175 Verdugo earthquake, as shown in Figure 3.9. Similar to Figure 3.9, high PGV values occur in the upper right quarter of Figure 3.10, where the Verdugo fault is located, and the PGVs decrease as the distance to the Verdugo fault increases. Local polynomial
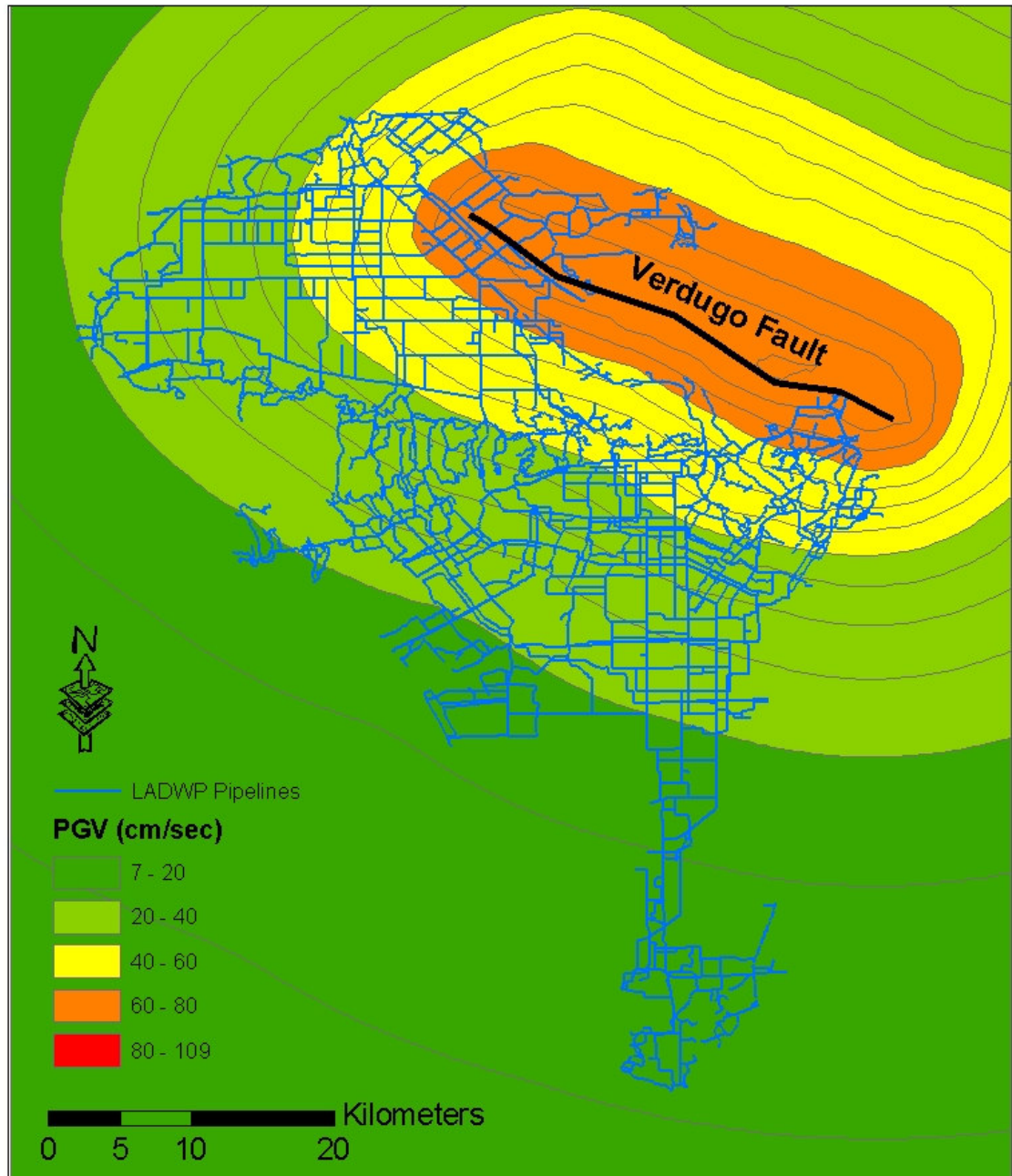
Figure 3.10.   Contour Surface Corresponding to Mean + $\sigma_{\text{inter-event}}$ PGV at Rock Sites
from Scenario 175 Verdugo Earthquake

interpolation is able to develop the contour surfaces that are capable of representing the PGVs at 572 points reasonably well.

### 3.4.2. Correction for Site Conditions

The strong ground motion data are generated for the rock site conditions, i.e., NEHRP B or BC category site conditions (FEMA, 2003). However, the site conditions in the LADWP water system service areas do not necessarily fall into the NEHRP B or BC site categories. Table 3.2 summarizes the site classification according to the 2003 NEHRP provisions (FEMA, 2003). The site conditions are divided into 6 categories, from A to F, representing the site conditions from hard rock to soft soils, to soils requiring site specific evaluation. Intermediate categories, such as BC, CD, and DE, can also be assigned to accommodate the site conditions that fall close to the category boundary.

Wills et al. (2000) developed a site-condition map for California based on geologic units and the average shear wave velocity in the upper 30-m subsurface layer. Figure 3.11 shows the site-condition map in the greater Los Angeles area, where most site categories are not B or BC, but C, CD, D, and DE. The LADWP pipeline system is superimposed in Figure 3.11 and most of the pipelines are located in either a category C or CD site.

The 2003 NEHRP provision (FEMA, 2003) does not provide the site condition correction coefficients for PGV directly, but supplies the coefficients for $S_{A1}$, as reproduced in Table 3.3. The $S_{A1}$ for category site conditions (other than B and B/C) can be calculated by

Table 3.2. NEHRP Site Classification (after FEMA, 2003)

| Site Class | Description | Shear Wave Velocity (m/s) | |
|---|---|---|---|
| | | **Minimum** | **Maximum** |
| A | **HARD ROCK** | 1500 | |
| B | **ROCK** | 760 | 1500 |
| C | **VERY DENSE SOIL AND SOFT ROCK** Undrained shear strength $s_u > 100$ kPa or SPT-N > 50 | 360 | 760 |
| D | **STIFF SOIL** Undrained shear strength 50 kPa $\leq s_u \leq 100$ kPa or $15 \leq$ SPT-N $\leq 50$ | 180 | 360 |
| E | **SOFT SOIL** Undrained shear strength $s_u < 50$ kPa or SPT-N < 15, or any profile with more than 3 m of soft clay defined as soil with plasticity index PI > 20, water content w $\geq 40\%$ | | 180 |
| F | **SOIL REQUIRING SITE SPECIFIC EVALUATIONS** 1. Soils vulnerable to potential failure or collapse under seismic loading such as liquefiable soils, quick and highly sensitive clays, collapsible weakly cemented soils. 2. Peats and/or highly organic clays with thickness $\geq 3$ m. 3. Very high plasticity clays with thickness $\geq 8$ m and plasticity index PI > 75. 4. Very thick soft/medium stiff clays with thickness $\geq 36$ m. | | |

$$S_{A1i} = F_{SA1i} S_{A1B} \tag{3.31}$$

where $S_{A1i}$ is the $S_{A1}$ for site condition i (i.e., site conditions corresponding to A, C, D, or E), $S_{A1B}$ is the $S_{A1}$ for site category B, and $F_{SA1i}$ is the site condition correction factor for various site categories i and is given in Table 3.3. HAZUS (FEMA, 1999) extends the methodology to the PGV by
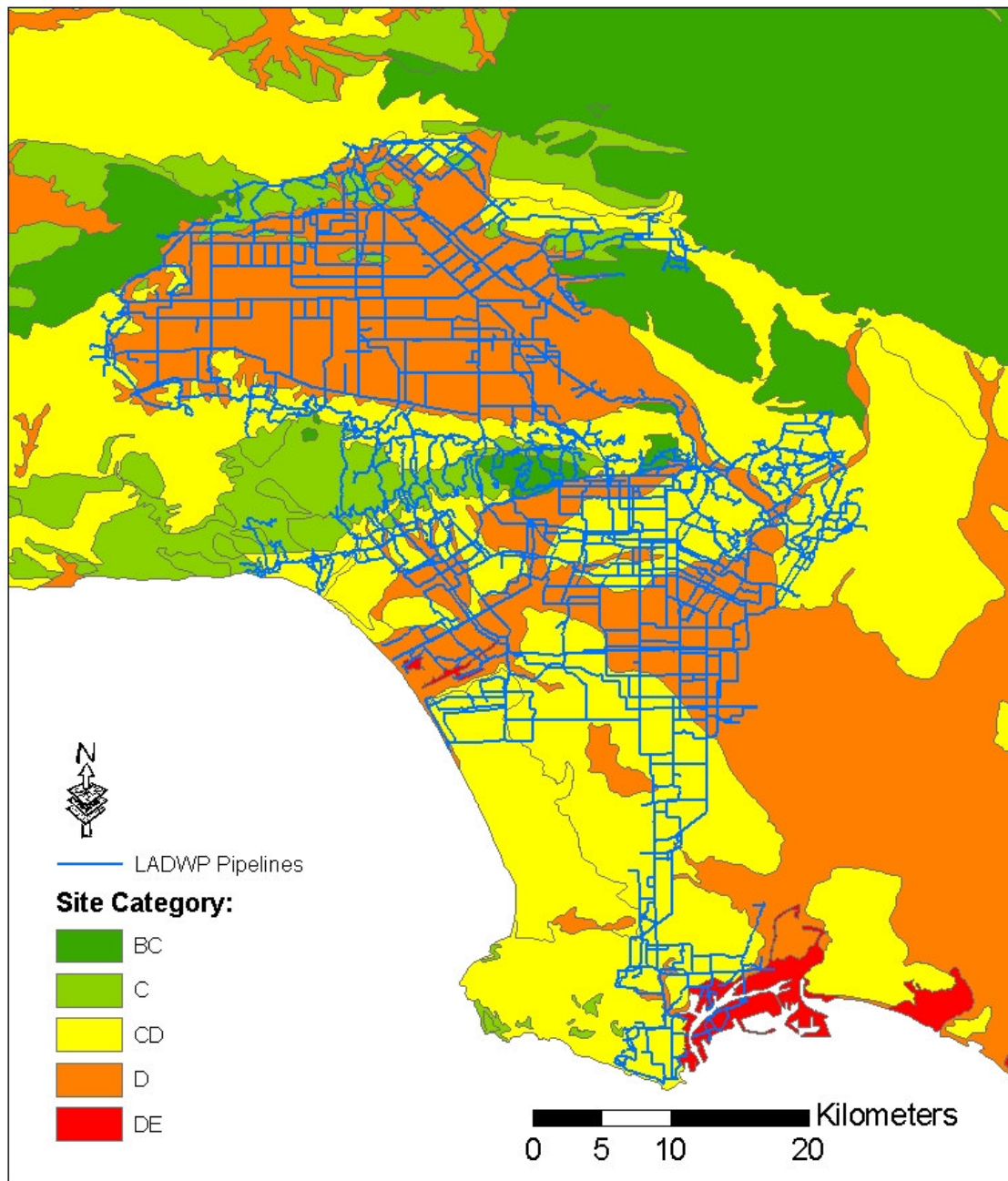
Figure 3.11.   Map of NEHRP Site Classification in Los Angeles Superimposed by

LADWP Pipeline System (after Wills et al., 2000)

Table 3.3.   Site Condition Correction Factor $F_{SA1}$ for $S_{A1}$ (FEMA, 2003)

| Site Class | $S_{A1} \leq 0.1$ g | $S_{A1} = 0.2$ g | $S_{A1} = 0.3$ g | $S_{A1} = 0.4$ g | $S_{A1} \geq 0.5$ g |
|:---:|:---:|:---:|:---:|:---:|:---:|
| A | 0.8 | 0.8 | 0.8 | 0.8 | 0.8 |
| B | 1.0 | 1.0 | 1.0 | 1.0 | 1.0 |
| C | 1.7 | 1.6 | 1.5 | 1.4 | 1.3 |
| D | 2.4 | 2.0 | 1.8 | 1.6 | 1.5 |
| E | 3.5 | 3.2 | 2.8 | 2.4 | 2.4 |
| F | ---[a] | ---[a] | ---[a] | ---[a] | ---[a] |

Note: a: Site-specific geotechnical investigation and dynamic site response analyses should be performed.
   b: Use straight line interpolation for intermediate values of $S_{A1}$.

$$V_{pi} = F_{SA1i}V_{pB} \tag{3.32}$$

where $V_{pi}$ is the PGV for category site condition i (i.e., site conditions corresponding to A, C, D, or E), and $V_{pB}$ is the PGV for site category B.

Since the PGVs in the ground motion data are inferred from the $S_{A1}$ using Eqn 3.29, the $S_{A1}$ values in Table 3.3, according to which the $F_{SA1}$ is divided into 5 subcategories, can be converted to corresponding PGV values by Eqn 3.29 as well. Table 3.4 shows the site correction factor, $F_{PGV}$, for PGV with respect to PGV. Similar to Eqn 3.32, the PGV on other category site conditions rather than B category can be calculated by

$$V_{pi} = F_{PGVi}V_{pB} \tag{3.33}$$

74

Table 3.4.   Site Condition Correction Factor $F_{PGV}$ for PGV

| Site Class | PGV ≤ 9 cm/sec | PGV = 19 cm/sec | PGV = 28 cm/sec | PGV = 38 cm/sec | PGV ≥ 47 cm/sec |
|---|---|---|---|---|---|
| A | 0.8 | 0.8 | 0.8 | 0.8 | 0.8 |
| B | 1.0 | 1.0 | 1.0 | 1.0 | 1.0 |
| C | 1.7 | 1.6 | 1.5 | 1.4 | 1.3 |
| D | 2.4 | 2.0 | 1.8 | 1.6 | 1.5 |
| E | 3.5 | 3.2 | 2.8 | 2.4 | 2.4 |
| F | ---[a] | ---[a] | ---[a] | ---[a] | ---[a] |

Note: a: Site-specific geotechnical investigation and dynamic site response analyses should be performed.

   b: Use straight line interpolation for intermediate values of PGV.

where $F_{PGVi}$ is the site condition correction factor for PGV for various site categories i. Please note that the $F_{SA1i}$ in Table 3.3 and $F_{PGVi}$ in Table 3.4 are identical under the same conditions.

Corrections for site conditions to the PGV data are performed using GIS software, ArcGIS (ESRI, 1999). The PGV contour surface data layer (e.g., Figure 3.10 for Scenario 175 Verdugo earthquake) is intersected with the site condition data layer (i.e., Figure 3.11) to combine both sets of information into the same data layer, after which the corrected PGV values are calculated using Eqn 3.33 and Table 3.4, and the corrected PGV contour surfaces can be generated. The $F_{PGVi}$ for the intermediate site category, i.e., CD and DE, are taken as the average of the $F_{PGVi}$ for the two bounded categories, i.e., C and D, and D and E, respectively. Figure 3.12 shows the corrected PGV contour surfaces for the Scenario 175 Verdugo earthquake. Comparison of Figures 3.10 and 3.12 reveals the site amplification effects. High PGV values on the southwest side of the Verdugo fault in Figure 3.12 result from the CD or D category
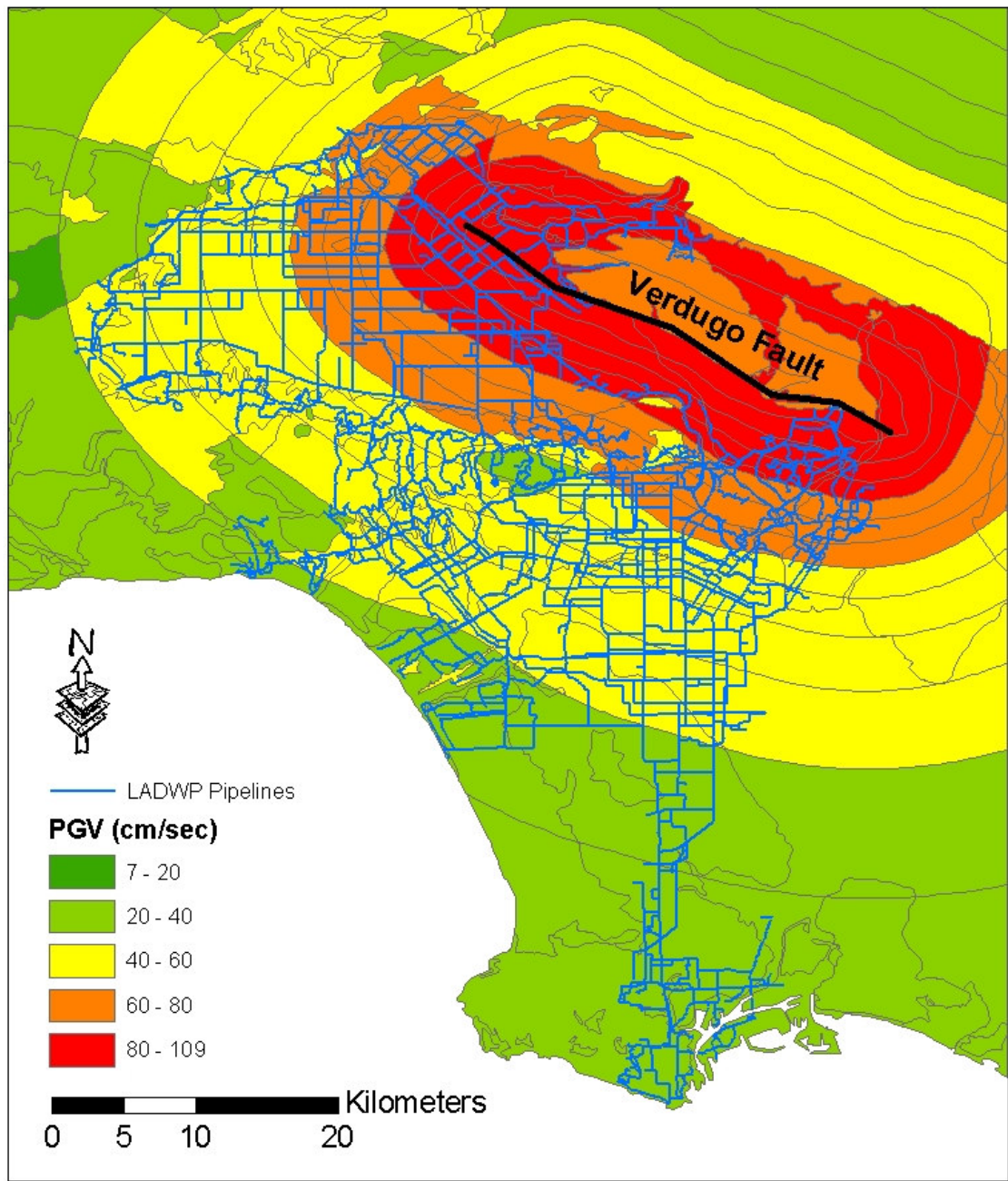
Figure 3.12.   PGV Contour Surface after Site Condition Corrections

(Mean + $\sigma_{\text{inter-event}}$ PGV from Scenario 175 Verdugo Earthquake)

76

site conditions in those locations, as opposed to the northeast side of the Verdugo fault, where no significant amplification effect is observed as a result of BC category site conditions in those locations.

### 3.4.3. Seismic Demands on Link-type Components

The components in water supply systems can be divided into two broad categories: link-type components, such as pipelines, and node-type components, such as demand nodes and tanks. The procedures to determine the seismic demands on the link-type components are described in this section and those for the node-type components are given in the next section.

The seismic performance of the pipeline system is of primary concern in this work. The LADWP pipeline system is superimposed on the corrected PGV contour surfaces, as shown in Figure 3.12. To determine the PGV that each pipeline is subjected to, the LADWP pipeline data layer is combined with the corrected PGV contour surfaces in the ArcGIS. The "Intersect" function in ArcGIS not only combines the information from both input data layers into an output layer, but also divides the pipelines according to the PGV contour interval they fall into. Consider, for example, a pipeline that is so long that extends over three PGV contour intervals, saying 40-45, 45-50, and 50-55 cm/sec intervals. The ArcGIS "Intersect" function automatically divides the long pipeline into three new short pipelines and assigns a PGV interval of 40-45, 45-50, or 50-55 cm/sec to each of them according to their locations, respectively. Although PGV values in Figures 3.10 and 3.12 are color-coded with an interval of 20 cm/sec, a relatively small PGV interval of 5 cm/sec is utilized when developing the contour surfaces (i.e., four PGV intervals in each color interval in

Figure 3.10), intending to determine the PGV values to each system component with relatively high accuracy. The mean of the PGV interval (e.g., 22.5 cm/sec for 40-45 cm/sec interval) is taken as the seismic demands for the system components located within the PGV interval. The lengths of the divided pipelines are then calculated in ArcGIS and utilized as input parameter to estimate the seismic performance of pipelines, as described in Chapter 7.

### 3.4.4. Seismic Demands on Node-type Components

The procedures for determining seismic demands on node-type components, such as demand nodes and tanks, are relatively straightforward. Figure 3.13 shows the spatial distribution of the demand nodes in the LADWP water supply system superimposing on the corrected PGV contour surfaces generated from the Scenario 175 Verdugo earthquake. The PGVs, which the demand nodes are subjected to, are determined by an ArcGIS function, "Spatial Joint", which combines the information in the two input data layers (i.e., the demand node layer and PGV contour surface layer) into an output data layer according to their spatial positions. Again, the seismic demands, i.e., PGV, assigned to the demand nodes are the mean of the PGV contour interval in which the demand nodes are located.

## 3.5. Summary

This chapter describes the process for characterizing the seismic hazards in the LADWP water supply system and determining the seismic demand on each system component. The seismic hazard characterization for the Los Angeles area was developed by approximating the aggregate seismic hazard, i.e., USGS 2002 Dataset, in
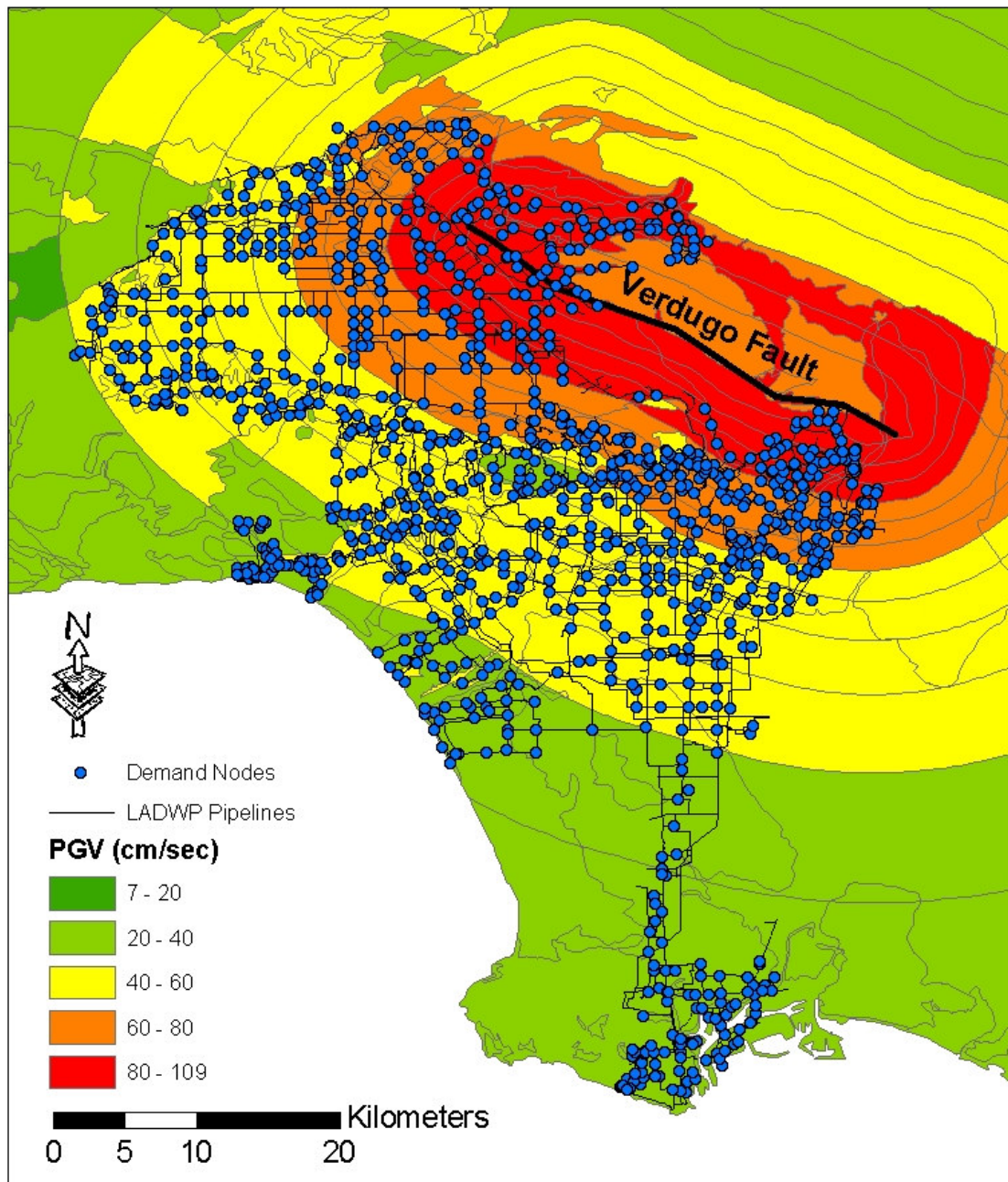
Figure 3.13. Map of LADWP Demand Nodes Superimposed by Corrected PGV Contour Surfaces (Mean + $\sigma_{\text{inter-event}}$ PGV from Scenario 175 Verdugo Earthquake)

the area that takes into account all currently identified, potential seismic sources in a probabilistic context. The approximation was accomplished by means of 59 scenario earthquakes that were selected to provide probability of exceedance characteristics for strong ground motion similar to those for all currently identified, potential seismic sources in the area (Lee et al., 2005). Scenario earthquakes that generate ground motion without engineering significance in the LADWP water supply system were screened from the original USGS 2002 dataset. In addition, expert judgments were exercised to screen out other scenario earthquakes in the original USGS 2002 dataset.

The seismic hazard associated with the 59 scenario earthquakes was adjusted to match that of the USGS 2002 dataset over the LADWP water supply system by a multivariate, nonlinear optimization process. The 59 annual occurrence frequencies for the 59 scenario earthquakes are the optimized variables. The target function was selected by minimizing an error function for the sum of the differences between the hazard curves, i.e., the variation of annual exceedance frequency as a function of $S_{A1}$ at equivalent rock sites, from the 59 scenario earthquakes and USGS 2002 dataset at each of the 56 control points spatially distributed over the LADWP water supply system.

Strong ground motions, e.g., PGV, for each of the 59 scenario earthquakes were generated at 572 points in a grid covering the LADWP water supply system. The PGV contour surfaces were interpolated from these 572 points, and site condition corrections were applied according to the NEHRP-HAZUS procedures. With the aid of GIS software, the spatial distribution of the LADWP system components were superimposed on the PGV contour surfaces to determine the seismic demand on each component in accordance with its respective location.

# CHAPTER 4

# SYSTEM CHARACTERISTICS OF LADWP WATER SUPPLY SYSTEM

## 4.1. Introduction

The water supply system in Los Angeles, operated primarily by the Los Angeles Department of Water and Power (LADWP), is utilized as a test bed in this research. The system characteristics necessary for the evaluation of water supply system seismic performance are described in this chapter. The chapter starts with the system physical characteristics, such as system statistics, system structure, and water flow pattern, followed by the system operational characteristics, which are compiled into a hydraulic network model provided by LADWP engineers. The system characteristics described in this chapter are mostly provided by LADWP in the form of hydraulic network model (LADWP, 2002a), water flow diagrams (LADWP, 2002b), water maps (LADWP, 2002c), and Digital Ortho Photographs of the greater Los Angeles area.

## 4.2. Physical Characteristics

LADWP acts as a water "retailer" in the greater Los Angeles area, supplying water directly to individual customers. The LADWP water supply system provides water to about 660,000 customers, representing 3.8 million people in a service area of

approximately 1,200 km$^2$. The total water consumption of the LADWP system in a typical summer and winter day is about 2.5×10$^6$ and 1.2×10$^6$ m$^3$, respectively. Two-thirds and one-third of the water consumption is accounted for by residential, and commercial and governmental uses, respectively. Only a very small portion of water is consumed by industries (Toprak, 1998).

### 4.2.1. System Structure

The LADWP water service areas are divided into five water districts, namely West Valley, East Valley, Western, Central, and Harbor water districts. Figure 4.1 shows a spatial distribution of these water districts. The whole system can be divided into thirteen subsystems, geographically, each of which consists of various types of system components, such as water tanks, pumps, regulation stations, pipes, and customer demands, and can be treated individually. Each of the thirteen subsystems can be further divided to multiple pressure zones, resulting in a total of 106 pressure zones within the LADWP system. More descriptions on the subsystems and pressure zones are provided in the following subheadings:

*4.2.1.1. Subsystems*

Figure 4.2 shows a spatial distribution of the thirteen subsystems, which, from the north to the south, are: Foothills (FH), Granada Hills (GH), Sunland/Tujunga (ST), Valley Floor (VF), Encino Hills (EH), Santa Monica Mountains (SM), Hollywood Hills (HH), Highland Park (HP), Mountain Washington (MW), Santa Ynez (SY), Central City (CC), Westside (WS), and Harbor (H) subsystems. Among the thirteen subsystems, the Valley Floor and Central City are the two largest and serve the highly
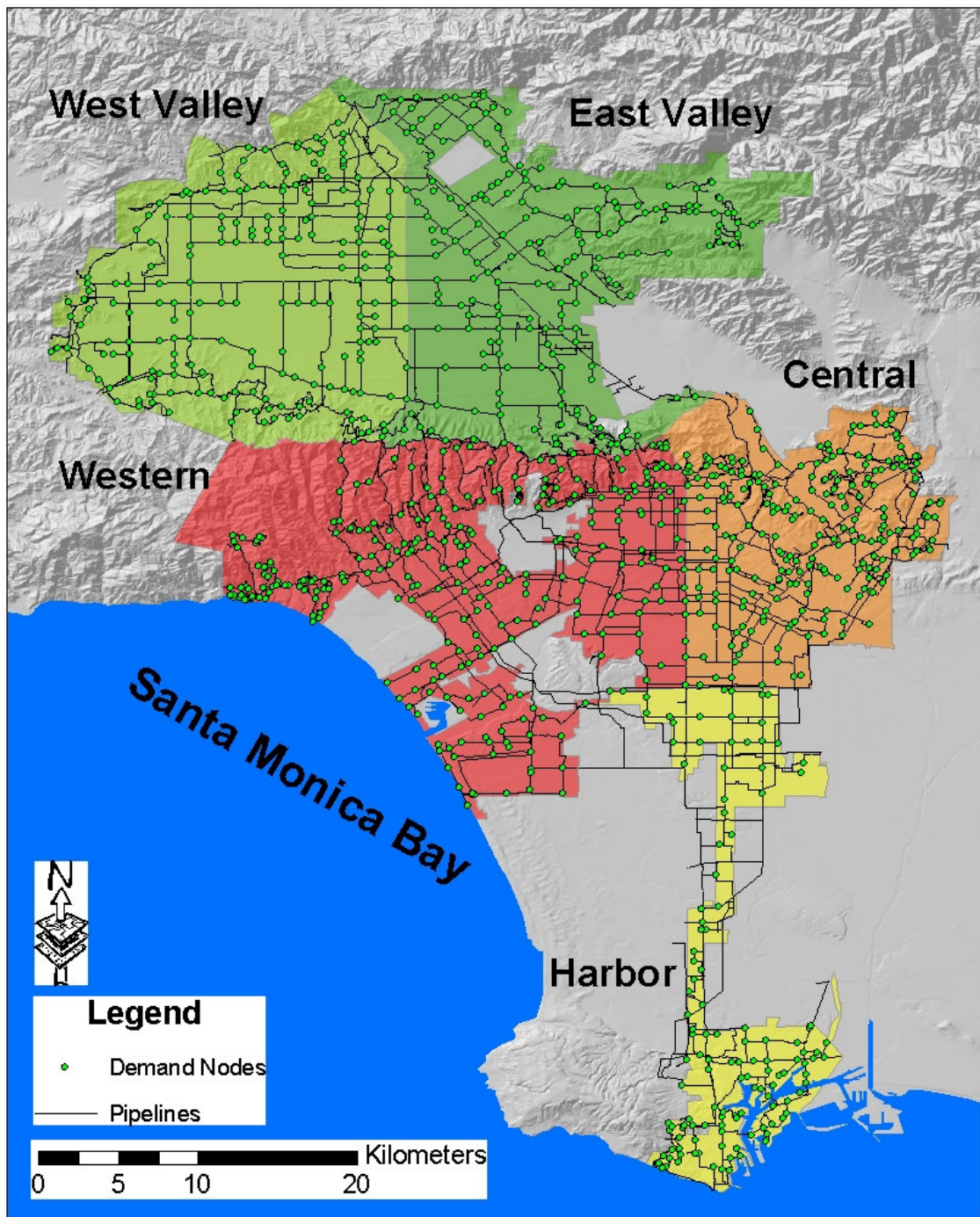
Figure 4.1.   Map of LADWP Water Districts
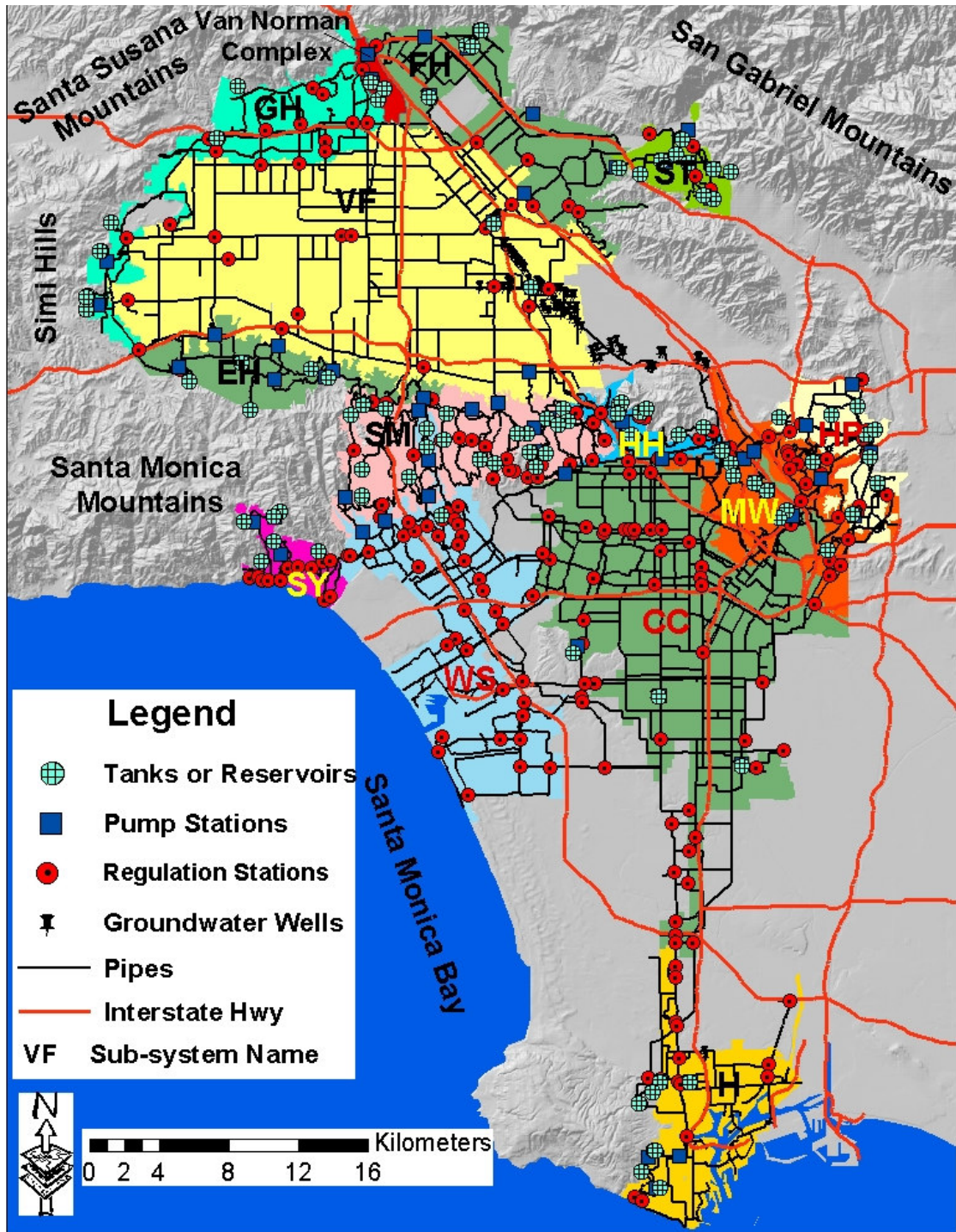
Figure 4.2.  Overview of LADWP Water Supply System

Table 4.1.   Daily Water Consumption of Each Subsystem in LADWP System

| Subsystem | Summer Day ($m^3$/Day) | Summer Day Percentage (%) | Winter Day ($m^3$/Day) | Winter Day Percentage (%) |
|---|---|---|---|---|
| VF | 699531 | 28 | 327834 | 28 |
| CC | 661461 | 26 | 299777 | 25 |
| WS | 282184 | 11 | 131361 | 11 |
| GH | 172806 | 7 | 74060 | 6 |
| H | 134172 | 5 | 86845 | 7 |
| FH | 125283 | 5 | 56113 | 5 |
| MW | 124723 | 5 | 55466 | 5 |
| EH | 122292 | 5 | 55064 | 5 |
| HP | 58861 | 2 | 26130 | 2 |
| HH | 42920 | 2 | 20498 | 2 |
| SY | 36836 | 1 | 17847 | 2 |
| SM | 35458 | 1 | 15787 | 1 |
| ST | 32117 | 1 | 13765 | 1 |
| Sum | 2528647 | 100 | 1180545 | 100 |

populated San Fernando Valley and Los Angeles Central City areas, respectively. The other eleven subsystems are positioned around these two large subsystems, mostly in the mountainous areas with higher elevations with the exception of the Harbor subsystem, which is located in the low elevation Harbor area.

Table 4.1 shows the daily water consumption of each subsystem and the percentage with respect to the water consumption of the whole system in a typical summer or winter day. The water consumption in each subsystem, as well as the water consumption in the whole system, in a typical summer day is about twice that in a typical winter day. However, regardless of winter or summer day, the water consumption percentage of each subsystem with respect to the whole system water consumption remains more or less constant. Corresponding to their largest service areas, the Valley Floor and Central City are the two largest water consumers,

contributing 28% or 26% (in summer or 25% in winter) to total water consumption, respectively. The Valley Floor and Central City together account for more than 50% of total water consumption.

In addition to the thirteen subsystems, there is a special area in the LADWP system known as Van Norman Complex, located in the northern San Fernando Valley, as shown in Figure 4.2. Van Norman Complex does not belong to any of the thirteen subsystems, but serves as the heart of the system, treating roughly 85% of the water circulated in the system. More details on the Van Norman Complex are given under the subheading: 4.2.2.3. Van Norman Complex.

### 4.2.1.2. Pressure Zones

LADWP supplies water to its customers with pressures up to 1380 kPa (200 psi). Although some variations could be tolerated, extremely high pressures will cause damage to the system, such as pipe leakages and breaks. On the other hand, extremely low pressures will lead to water outage and fire fighting inadequacy. To meet the pressure requirements in a service area of 1200 km$^2$ and with significant elevation difference [i.e., 0 to 735 m (1 to 2411 ft)], the thirteen subsystems in the LADWP system is further divided into 106 pressure zones, which are numbered after the highest hydraulic grades, the sum of pressure and elevation heads, in the zones in units of feet. Figure 4.3 shows a spatial distribution of the 106 pressure zones. In general, the hydraulic grades decrease from the north to the south, with the exception of the Santa Monica Mountains area. The hydraulic grades in the Granada Hills and Foothills subsystems, north of San Fernando Valley, are typically higher than 427 m (1400 ft). The hydraulic grades in the Valley Floor subsystem are between 244 m (800 ft) and
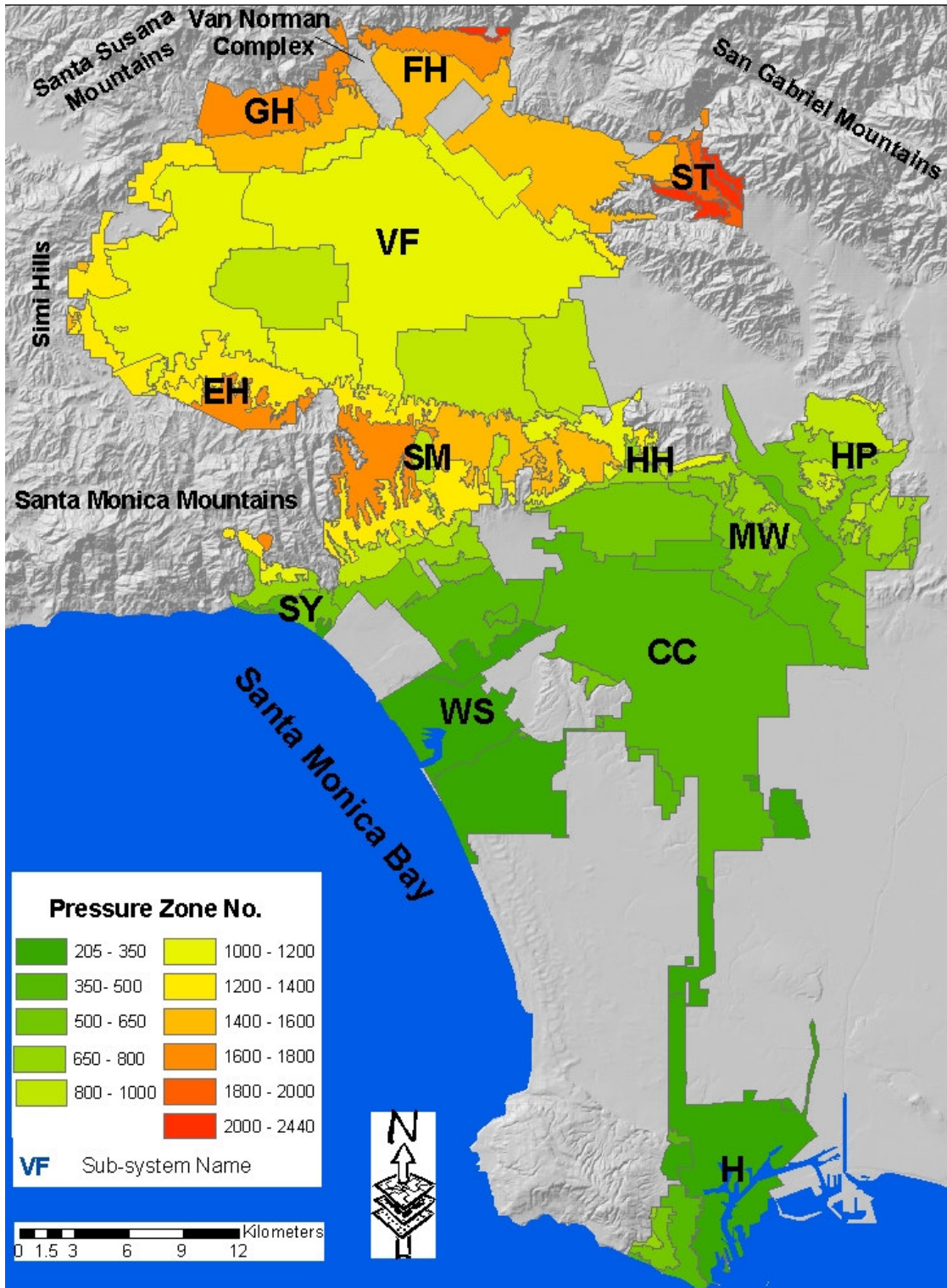
Figure 4.3. Spatial Distribution of Pressure Zones in LADWP System

427 m (1400 ft). The hydraulic grades in the Los Angeles Central City and Harbor areas are generally lower than 244 m (800 ft).

The LADWP system has two broad categories of pressure zones: gravity or pumped. The water in a gravity pressure zone is driven by gravitational force resulting from elevation difference, as opposed to those in a pumped pressure zone, where water is driven by external energy provided by pump stations. Since gravity pressure zones do not consume electric energy to deliver water, it is more desirable for water system planners to deploy a water system with as many gravity zones as possible. There is no exception for the LADWP system, in which 75 to 77% of pressure zones, with respect to water consumption, are gravity zones, and water is primarily driven by gravitational force. Seven of the total thirteen subsystems are completely gravity pressure zones, including the three largest water consumption subsystems (Valley Floor, Central City, and Westside subsystems) and other four subsystems (Harbor, Highland Park, Hollywood Hills, and Santa Ynez subsystems). The other six subsystems (Foothills, Granada Hills, Sunland/Tujunga, Encino Hills, Santa Monica Mountains, and Mountain Washington subsystems) located in the mountainous areas, where the elevations are high and the variation in elevation are also significant, are dominated by pumped pressure zones.

In pumped pressure zones, water is provided to customers after a pump station, where different operational strategies may be utilized. The pump station may convey water to a tank for subsequent gravity feed and provide water to a closed service zone directly, or be used in conjunction with a hydro-pneumatic tank. Most frequently, a pump feeds a pressure zone with a tank floating in the zone. A storage tank is considered to be "floating in the pressure zone" if the hydraulic grade of the tank is the

highest hydraulic grade in the pressure zone. The floating tank is normally constructed at a high elevation and served by a pump station. The operation of the pump is dynamically controlled by the water level of the tank. When the water level of the tank is higher than a pre-specified upper limit, the pump station is shut off and the tank supplies water to the customers by gravity. When the water level in the tank is lower than a pre-specified lower limit, the pump station becomes operative and water is pumped from an external source to the tank. For certain small service zones, where there may not be sufficient customers, or enough consumption to justify installing a tank, a pump may feed water to customers directly. A pump station may be used in conjunction with hydro-pneumatic tanks, which are pressure tanks that can be used to store water at the correct hydraulic grade using a pressure head instead of elevation head. Because hydro-pneumatic tanks are expensive, they are only used for small service zones.

### 4.2.2. Water Flow Pattern

The critical components that comprise the LADWP water supply system are described in this section. These components are treated according to the general water flow pattern in the system, i.e., water source, aqueduct systems that transfer water from water source to Los Angeles, water treatment and distribution hub, Van Norman Complex, and major trunk lines.

*4.2.2.1. Water Sources*

LADWP has three sources to meet its water demands: the local groundwater basins, the Los Angeles Aqueducts, and purchases from Metropolitan Water District

(MWD) that acts as a regional water "wholesaler" providing water to water supply agencies, such as LADWP. Figure 4.4 shows the water sources of Los Angeles.

The local groundwater, most of which is provided by groundwater wells in the eastern San Fernando Valley, contributes about 15% of the total LADWP water supply (Toprak, 1998). The Los Angeles Aqueducts, owned by LADWP, include the First Los Angeles Aqueduct (FLAA) and Second Los Angeles Aqueduct (SLAA), both of which transport water from the Sierra Nevada Mountains in the northern California to Los Angeles. Water from the FLAA and SLAA accounts for roughly 50% of the LADWP water supply. MWD has two water sources: water from the northern California through the California Aqueduct (also known as the State Water Project - West Branch), and water from the Colorado River through the Colorado Aqueduct (also known as the State Water Project - East Branch). The purchased water from the MWD is normally supplied via the California Aqueduct, which connects to the LADWP system through the Foothill feeder. On average, the MWD provides LADWP with approximately 35% of water supply to make up the deficit between demand and supply from the FLAA, SLAA, and local groundwater basins. Water from northern California, including FLAA, SLAA and MWD water source, is the major water source (about 85%) for the LADWP system.

*4.2.2.2. Aqueduct Systems*

Figure 4.5 shows an expanded view of Figure 4.4 in the vicinity of the connection between aqueduct system and LADWP distribution system. The FLAA and SLAA are connected with the Los Angeles Aqueduct Filtration Plant (LAAFP), and the California Aqueduct is connected with the Jensen Filtration Plant through the
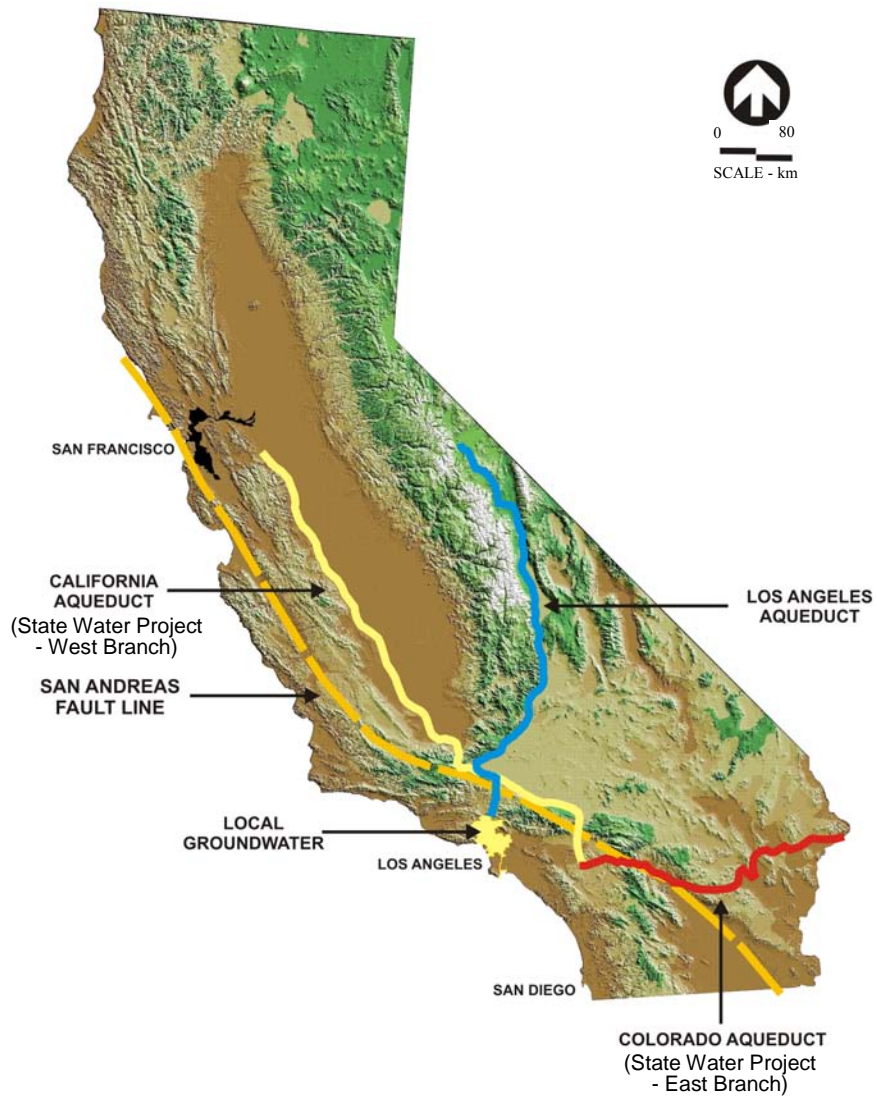
Figure 4.4.   LADWP System Water Sources

Foothill Feeder. Both filtration plants are located in the Van Norman Complex, a water treatment and distribution hub of the LADWP system.

The FLAA and SLAA originate from Owens Valley in the Sierra Nevada Mountains in northern California and terminate at the southern slope of Terminal Hill, connecting with the LADWP distribution system in Van Norman Complex. The
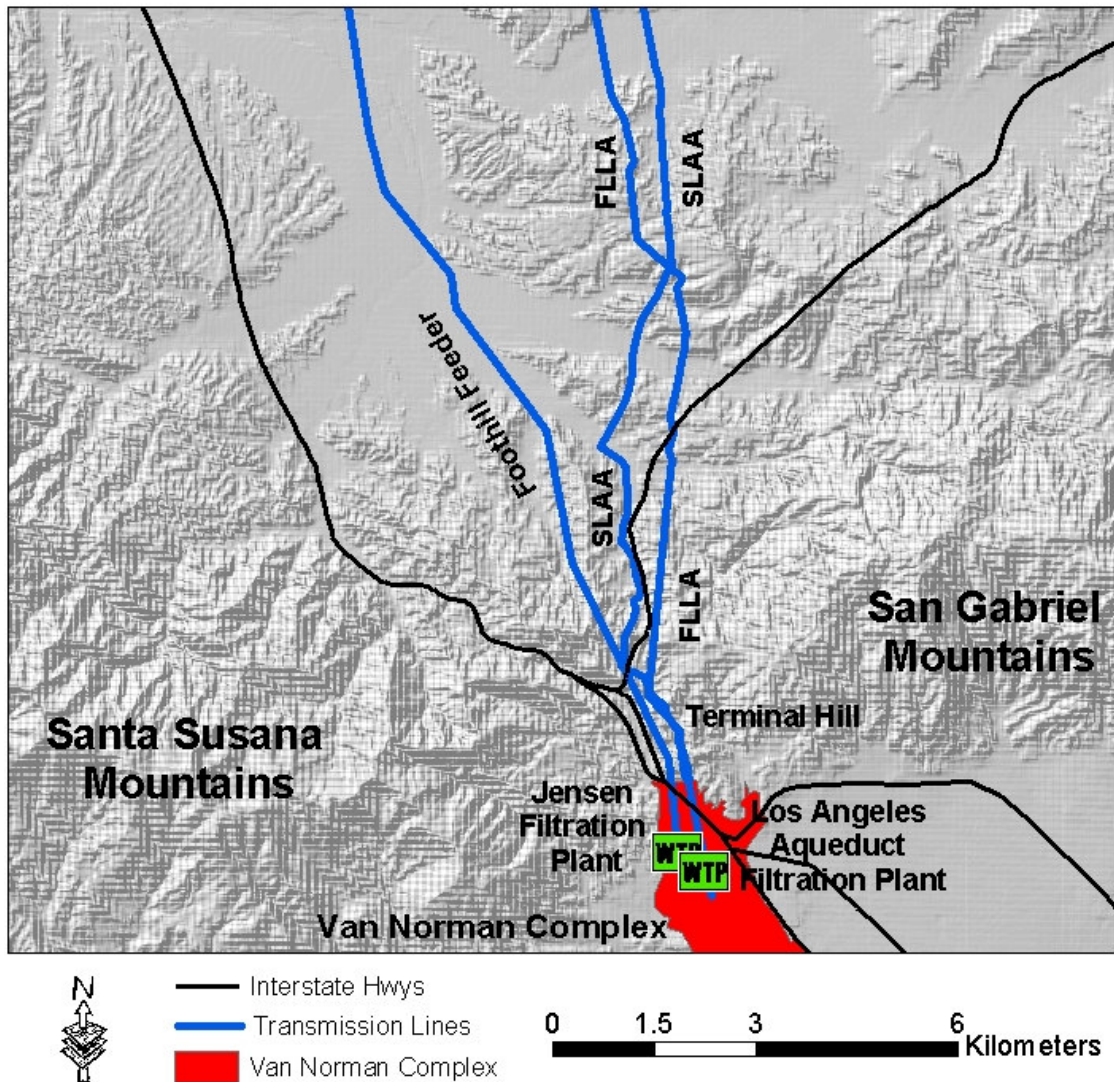
Figure 4.5.   Aqueduct System and LADWP System Connection

FLAA passes beneath Terminal Hill in a tunnel and the SLAA traverses the steep ridge of Terminal Hill.  To take advantage of the natural gradient from the Owens Valley (elevation of approximately 1200 meters above sea level) to Los Angeles (elevation near sea level), both aqueducts normally discharge water to the south side of Terminal Hill into above-ground penstocks, which convey water from the FLAA to the San Fernando Power Plant and water from the SLAA to the Foothill Power Plant,

to generate hydroelectricity for the operation of the Van Norman Complex and local residency usage. Water that does not flow to the power plant penstocks is automatically diverted to cascade structures on the southern slope of Terminal Hill to dissipate energy. Thereafter, water flows into the Van Norman Complex for treatment.

*4.2.2.3. Van Norman Complex*

As shown in Figures 4.2 and 4.5, Van Norman Complex is located in the northern San Fernando Valley, between the Granada Hills and Foothills subsystems. Van Norman Complex serves as the "heart" of the LADWP water supply system, receiving, treating, storing, and distributing water throughout the LADWP system. It controls about 80% of the water supply for the City of Los Angeles and 100% of the water supply for the northern San Fernando Valley. Figure 4.6 shows a Digital Ortho Photograph of Van Norman Complex. Van Norman Complex contains several critical water facilities, including the Jensen Filtration Plant, Los Angeles Aqueduct Filtration Plant (LAAFP), Van Norman Pump Stations No. 1 and 2, Los Angeles Reservoir, Van Norman Bypass Reservoir, and the origins of eight major trunk lines, i.e. Granada, Rinaldi, Susana, Foothill, Olden Street, Hayvenhurst, Haskell, and LA City Trunk Lines.

The water from the FLAA and SLAA and purchased raw water from MWD are treated in the LAAFP. As mentioned in the previous section, part of the water from the FLAA and SLAA is transported to the San Fernando Power Plant and Foothill Power Plant for generating hydroelectricity, respectively. The locations of the power plants in the Van Norman Complex are shown in Figure 4.7 (LADWP, 1997). After the San Fernando Power Plant, water from the FLAA flows through the Tailrace and
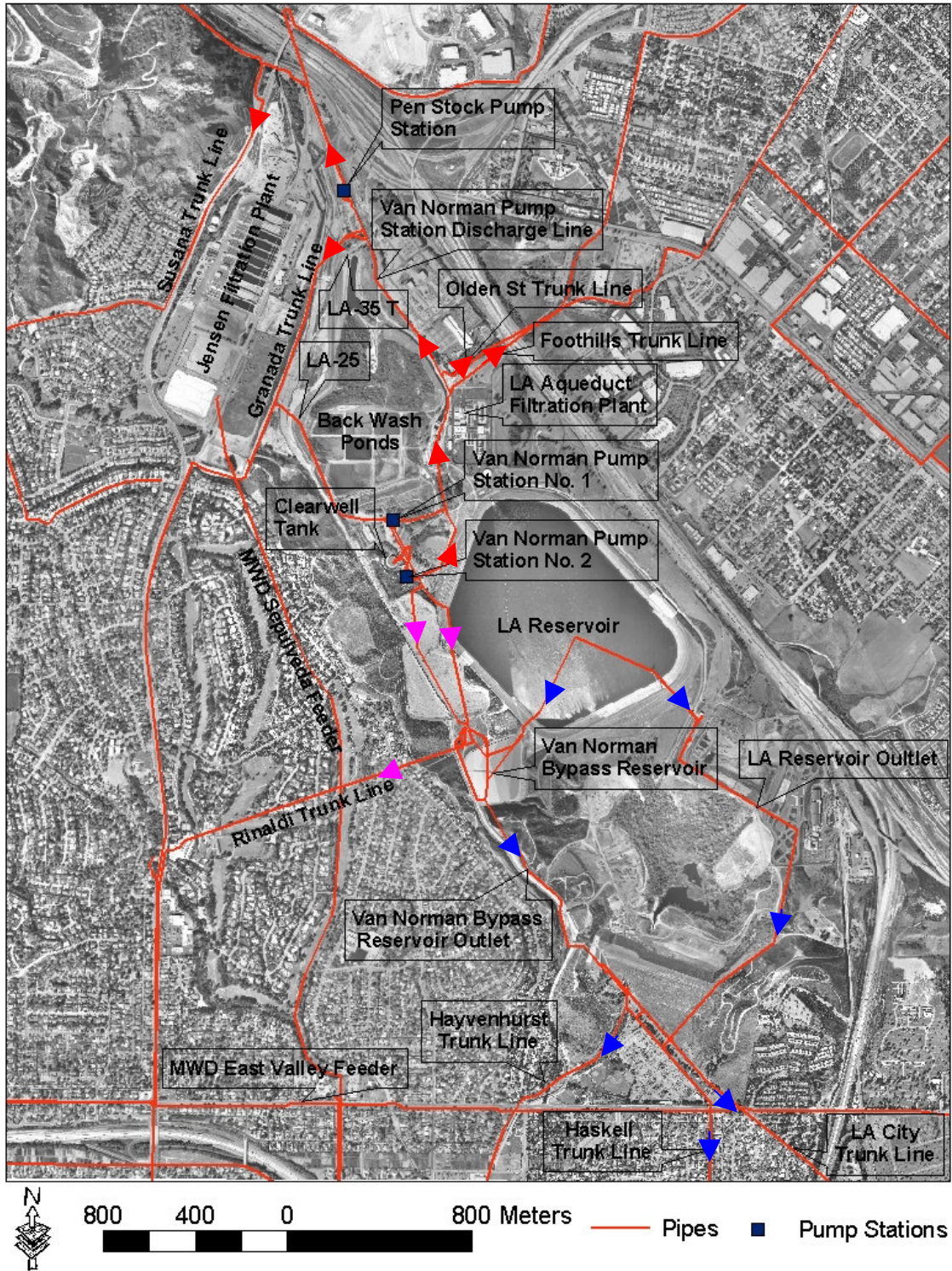
Figure 4.6.   Overview of Van Norman Complex
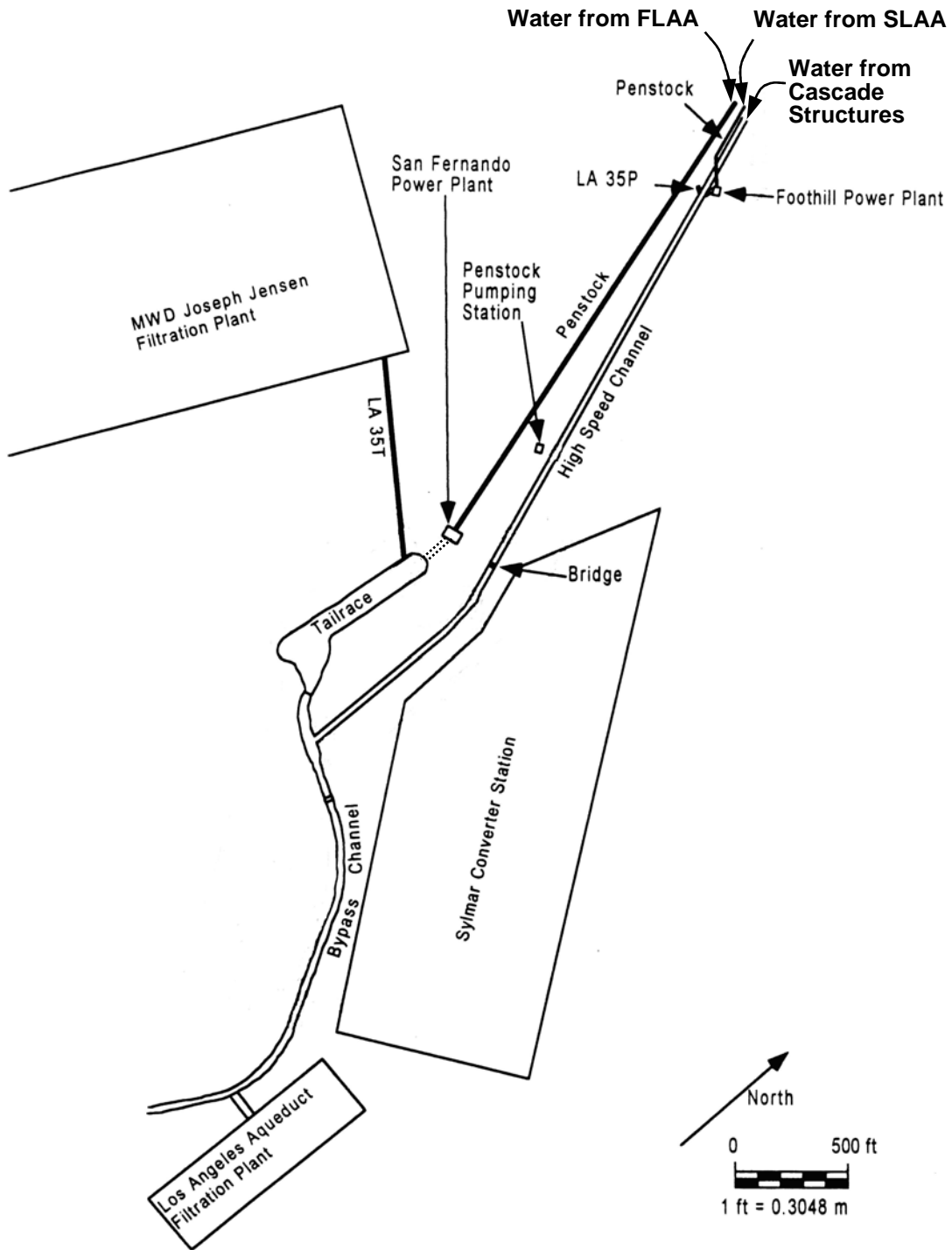
Figure 4.7. Plan View of Water Facilities in Van Norman Complex
(After LADWP, 1997)

95

Bypass Channel to the LAAFP for treatment. After the Foothill Power Plant, water from the SLAA flows through the High Speed Channel and Bypass Channel to the LAAFP for treatment. The other part of water from the FLAA and SLAA, which dissipates energy through the cascade structures, flows through the High Speed Channel and Bypass Channel to the LAAFP for treatment.

The Foothill Feeder, consisting of the Newhall and Balboa Tunnels, transports water from the California Aqueduct to the Jensen Filtration Plant. A plan view of the Jensen Filtration Plant in Van Norman Complex is shown in Figure 4.8 (Toprak, 1998). The Jensen Filtration Plant and Balboa Tunnel are connected by the Balboa Influent Conduit, which begins at the south portal of the Balboa Inlet Tunnel. Raw water purchased from MWD is transported through the Balboa Influent Conduit, the LA-35T, Tailrace, and the Bypass Channel to the LAAFP for treatment, as shown in Figures 4.7 and 4.8.

After treatment, potable water from the LAAFP is divided into three parts, one flowing into the Clearwell Tank, one being conveyed to the Rinaldi Trunk Line directly, and the remaining water filling the Los Angeles Reservoir and Van Norman Bypass Reservoir.

The water flowing into the Clearwell Tank, as shown by red arrows in Figure 4.6, is then pumped by Van Norman Pump Station No. 2 to the Van Norman Pump Station Discharge Line, which extends to the north of Van Norman Complex and supplies the Foothill, Olden Street, and Granada Trunk Lines sequentially. On the north of the connection between the Granada Trunk Line and the Van Norman Pump Station Discharge Line, water is further pumped by the Pen Stock Pump Station to the
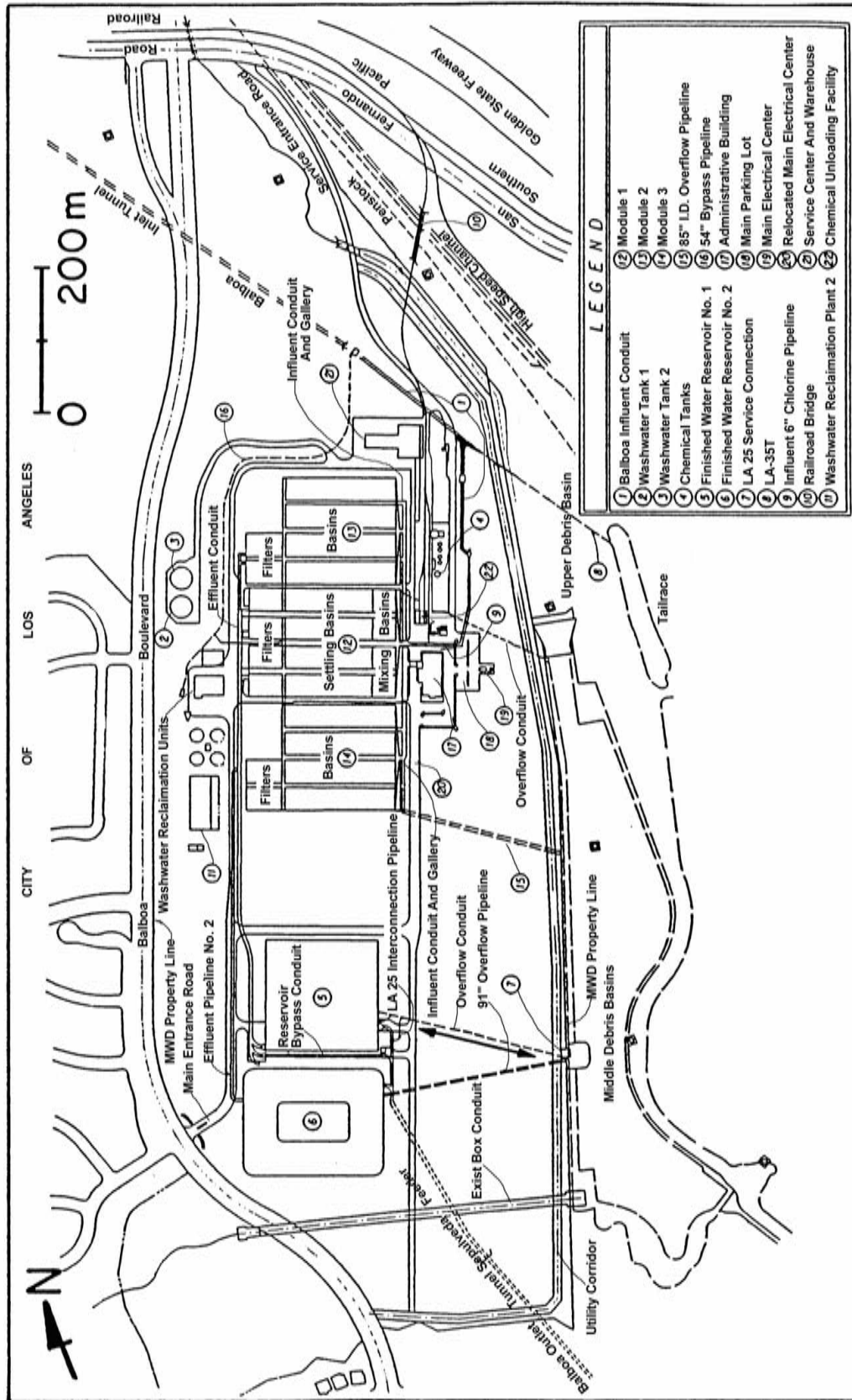
Figure 4.8.  MWD Transmission and Trunk Lines around Jensen Filtration Plant (After Toprak, 1998)

Susana Trunk Line. The water storing in the Los Angeles Reservoir and Van Norman Bypass Reservoirs, as indicated by with blue arrows in Figure 4.6, is transported through the Los Angeles Reservoir Outlet and Van Norman Bypass Reservoir Outlets, supplying the Hayvenhurst, Haskell, and LA City Trunk Lines. The water being conveyed to the Rinaldi Trunk Line, as shown by pink arrows in Figure 4.6, supplies the northern and western San Fernando Valley directly.

Van Norman Complex also contains two critical MWD owned trunk lines, Sepulveda Feeder and LA-25 Trunk Line, both of which can provide potable water to the LADWP system through MWD connections under emergency conditions. The Sepulveda Feeder originates at the Jensen Filtration Plant and extends through Van Norman Complex to the Valley Floor, Encino Hills, Santa Monica Mountains, Westside, and Harbor subsystems. It is one of the major water sources for the Harbor subsystem in daily operation.  In emergency situations, it can provide water to other service areas of the LADWP system through MWD/LADWP connections, which is described under subheading, 4.2.2.5 MWD Feeders and MWD/LADWP Connections. The LA-25 is capable of carrying water from the Jensen Filtration Plant and providing water to the eight major LADWP trunk lines mentioned above through the Van Norman Complex Pump Station No.1.  To the north, it can supply water to the Granada, Foothill, Olden Street and Susana Trunk Lines through the Van Norman Pump Station Discharge Line. To the south, it can provide water to the Rinaldi, Hayvenhurst, Haskell, and LA City Trunk Lines. Therefore, if necessary, potable water from the Jensen Filtration Plant, operated by MWD, can be distributed to virtually every part of the LADWP system.

*4.2.2.4. Major LADWP Trunk Lines*

After treatment in Van Norman Complex, potable water is distributed into eight major trunk lines, the Susana, Granada, Foothill, Olden Street, Rinaldi, Hayvenhurst, Haskell, and LA City Trunk Lines, which transport water to different parts of the LADWP system. Figure 4.9 shows the major LADWP trunk lines, reservoirs and tanks, which serve as the main water source of each subsystem.

The Susana and Granada Trunk Lines both originate from the Clearwell tank in Van Norman Complex and mainly supply the northern and southern part of Granada Hills subsystem, respectively. The Granada Trunk Line also supplies water to part of the Valley Floor subsystem along the western rim of the San Fernando Valley.

The Foothill and Olden Street Trunk Lines also originate from the Clearwell tank in Van Norman Complex, but mainly supply the Foothills subsystem and eastern part of the Valley Floor subsystem. In addition, the Foothill Trunk Line fills the Green Verdugo Reservoir, which serves as the only water source of the Sunland/Tujunga subsystem.

The Rinaldi Trunk Line transports water from the LAAFP to the De Soto Reservoir, supplying water to the northern and western parts of the Valley Floor subsystem through the De Soto Trunk Line. The De Soto Trunk Line also provides water to the Encino Hills subsystem.

The Hayvenhurst Trunk Line transports water from the Los Angeles Reservoir and Van Norman Bypass Reservoir to the Valley Floor subsystem and the Encino
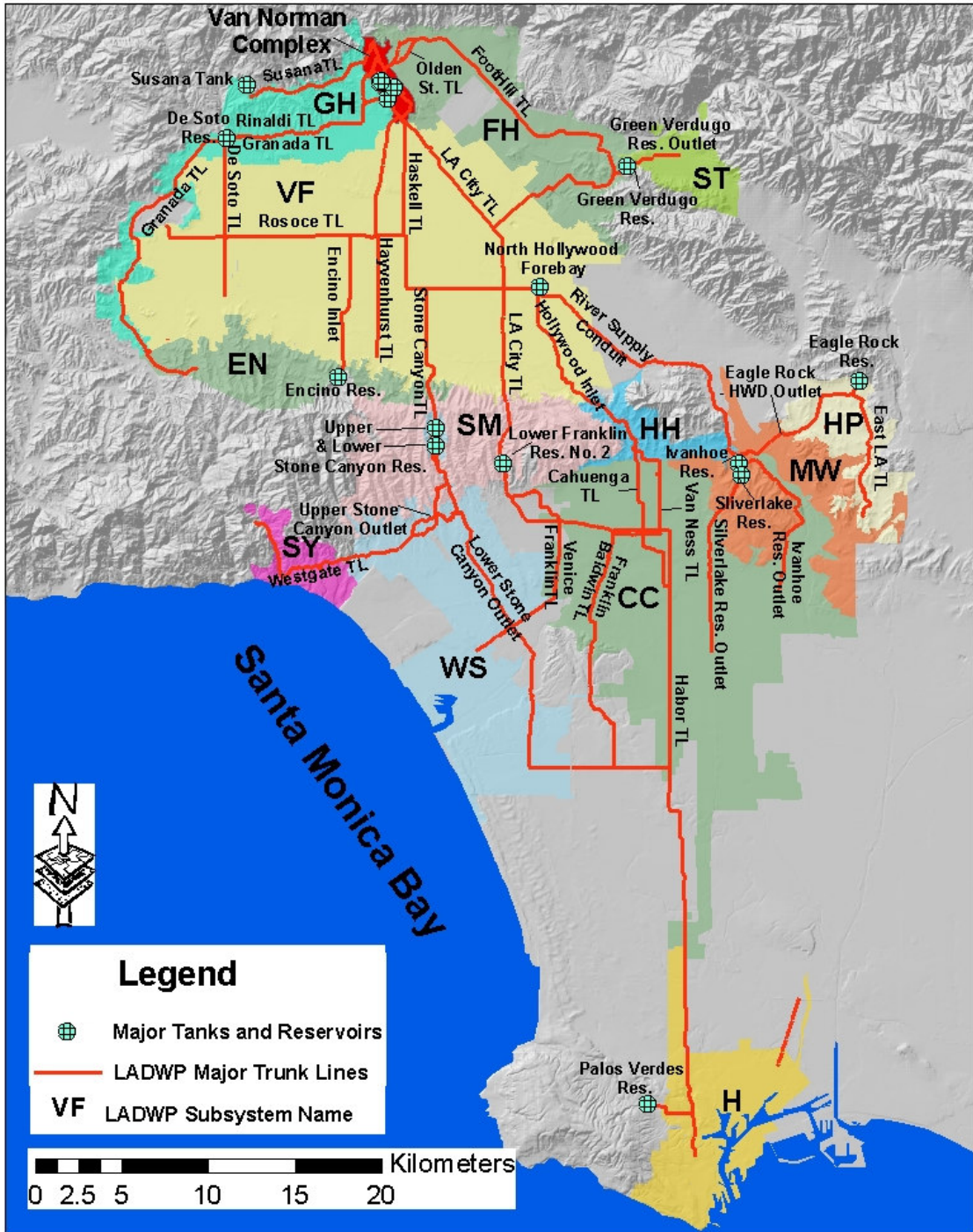
Figure 4.9.   Major Trunk Lines, Reservoirs, and Tanks in LADWP System

Reservoir, which serves as the major source of the Encino Hills subsystem.

The Haskell Trunk Line, with the water from the Los Angeles Reservoir and Van Norman Bypass Reservoir, supplies the Valley Floor subsystem and provides a part of water to the Upper and Lower Stone Canyon Reservoirs through the Stone Canyon Trunk Line. The Upper and Lower Stone Canyon Reservoirs supply the Westside subsystem, through the Upper and Lower Stone Canyon Reservoir Outlets, and the Santa Ynez subsystem, through the Westgate Trunk Line.

The LA City Trunk Line transports water from the Los Angeles Reservoir and Van Norman Bypass Reservoir to the Valley Floor subsystem and the Lower Franklin Reservoir No. 2, which supplies the Central City Subsystem through the Venice - Franklin and Franklin - Baldwin Trunk Lines.

Hollywood Inlet and River Supply Conduit collect water from the Haskell and LA City Trunk Lines, as well as the water pumped from local ground water wells in the eastern San Fernando Valley and the water collected in the North Hollywood Forebay. The Hollywood Inlet provides water to the Hollywood Hills and Central City subsystems, and the River Supply Conduit mainly supplies the Eagle Rock Reservoir, Ivanhoe Reservoir, and Silverlake Reservoir. Then, the Eagle Rock Reservoir distributed water to the Highland Park and Mount Washington subsystems through the Eagle Rock-HWD Conduit and East LA Trunk Line. The Ivanhoe Reservoir supplies water to the Mount Washington and Central City subsystems through the Ivanhoe Reservoir Outlet. The Silverlake Reservoir supplies water to the Mount Washington and Central City Subsystems through the Silverlake Reservoir Outlet.

It is noted that, according to LADWP (2002a), the Harbor subsystem is not supplied by LADWP trunk lines (such as the Harbor Trunk Line), but by the MWD feeders, which are discussed in the next Section 4.2.2.5 MWD Feeders and MWD/LADWP Connections.

### 4.2.2.5.  MWD Feeders and MWD/LADWP Connections

In addition to the major LADWP trunk lines mentioned above, the LADWP system also contains more than ten MWD feeders, spatially distributed among the system. Figure 4.10 shows the spatial distribution of the MWD feeders. The major MWD feeders include the East Valley, West Valley No. 1 and 2, Sepulveda, Santa Monica, and Palos Verdes Feeders. These feeders can supply water to the LADWP system through MWD/LADWP connections, as shown in Figure 4.10. In total, 30 connections in the LADWP system are identified in accordance with the LADWP hydraulic model (2002a). In normal situations, these connections do not supply water to the LADWP system, except for connections 21 and 16, both of which supply water to the Harbor subsystem during daily operation.

The East Valley Feeder receives water from the Colorado Aqueduct and extends along the east and north rim of the San Fernando Valley.  In emergencies, it can supply water to the San Fernando Valley through connection LA-32.  In addition, the East Valley Feeder connects with the Rinaldi Trunk Line and Sepulveda Feeder at connections LA-34A and LA-34B, respectively.

West Valley Feeder No. 1 and the Rinaldi Trunk Line are essentially the same pipeline, whose western portion, west of the De Soto Reservoir, is called the West
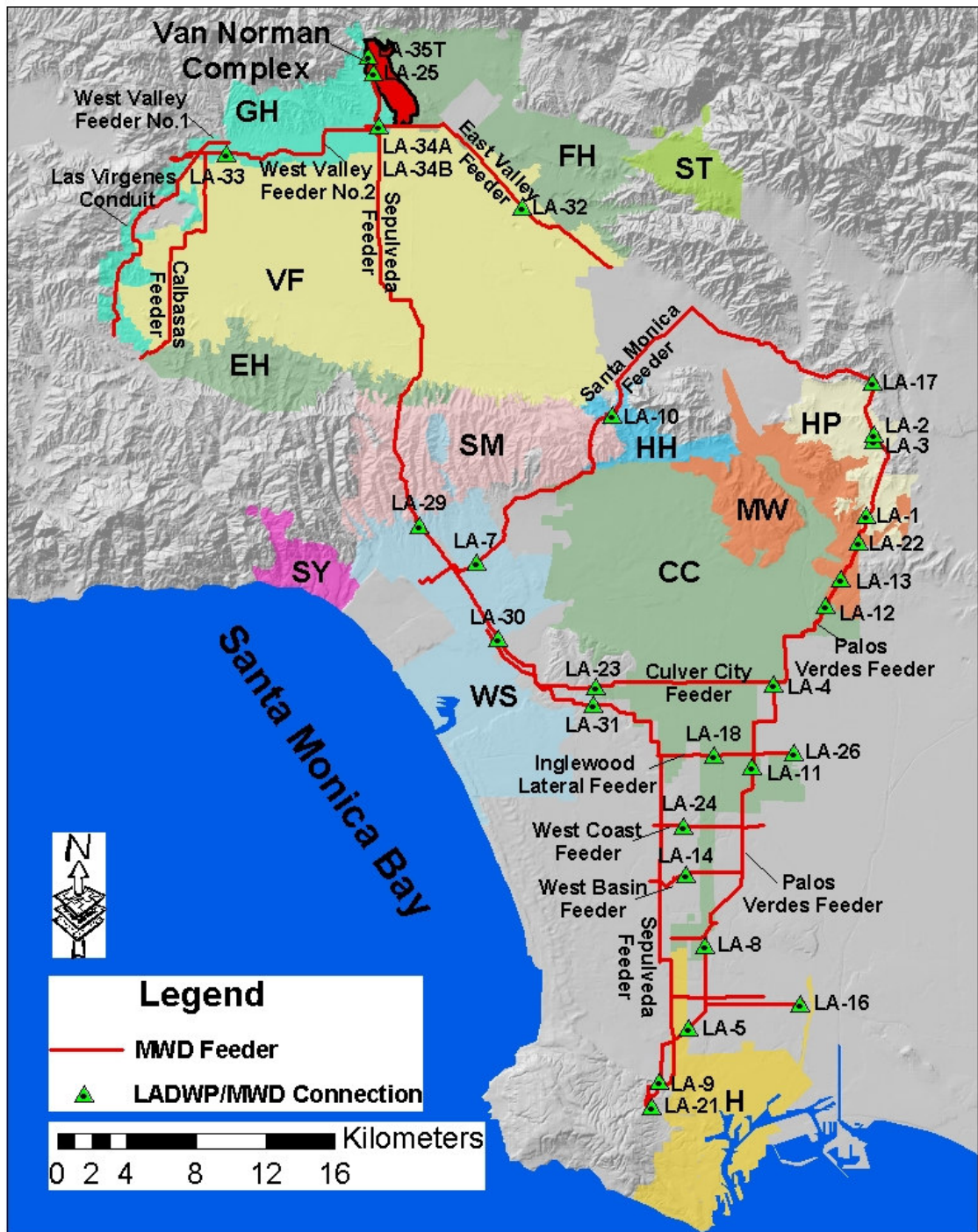
Figure 4.10.  Major MWD Feeders and LADWP/MWD Connections

Valley Feeder No.1, as opposed to its eastern portion known as the Rinaldi Trunk Line. The Rinaldi Trunk Line is owned by MWD, but rented to LADWP. Because the Rinaldi Trunk Line supplies water to the LADWP system during daily operation, it is treated as a major LADWP trunk line in Section 4.2.2.4 Major LADWP Trunk Lines. In emergencies, the West Valley Feeder No. 1 can transport water from the MWD water source located in the western part of the San Fernando Valley to the LADWP system. Similarly, West Valley Feeder No. 2 is also capable of transporting MWD water from the west to the LADWP system through the LA-33 connection.

The MWD Sepulveda Feeder originates at the Jensen Filtration Plant and extends through the Valley Floor, Encino Hills, Santa Monica Mountains, Westside, and Harbor subsystems. It is one of the major water sources for the Harbor subsystem during daily operation by supplying water to the Palos Verdes Reservoir, and connecting with the LADWP system via connection LA-21. In emergency situations it can provide water to other LADWP service areas through the LA-29, 30, and 31 connections.

The Santa Monica Feeder transports water from the east of the San Fernando Valley to the LADWP system, extending through the Hollywood Hills, Santa Monica, and Westside subsystems. In emergencies, it can supply water to the LADWP customers through the LA-10 and 7 connections.

The Palos Verdes Feeder follows the eastern rim of the Central City subsystem and can supply water to the LADWP system through the LA-17, 2, 3, 1, 22, 13, 12, 4, 11, 8, 5, and 9 connections.

## 4.3. Operational Characteristics

The LADWP system operational characteristics, such as the system operating procedure, monitoring, maintenance, and planning, are consolidated into a hydraulic network model (LADWP, 2002a) by LADWP engineers, using a commercial software, H2ONET (MWH Soft, Inc., 1999). H2ONET is an interactive, multi-application software program for the modeling of water distribution piping systems. It combines a point and click interface for network construction, drawing, and database management, highly advanced and computationally efficient hydraulic and water quality simulation modules based on EPANET (EPA, 2005), and a graphical interface running within the AutoCAD (Autodesk, 2005) for the Windows environment. H2ONET not only is capable of construction and maintenance of the comprehensive water supply system data inventory with reference to spatial coordinates, but also offers flexible data exchange with other software, such as EPANET and GIS, enabling integration with other relevant information and data.

The LADWP H2ONET hydraulic network model used in this research is developed under the supervision of LADWP engineers for system planning and management purposes. It contains all kinds of physical components in the system, such as tanks, reservoirs, pump stations, regulation stations, pipe, and user demands, as well as operational aspects of the system, such as behavior and control parameters for pump stations and regulation stations. It also contains twelve simulation scenarios, enabling hydraulic simulations of the entire LADWP system or parts of the system individually. More descriptions on the H2ONET hydraulic network model are provided in the following subheadings:

### 4.3.1. Physical Components of H2ONET Hydraulic Network Model

The H2ONET hydraulic network model contains 9,287 nodes and 10,665 links, representing about 2,186 km of pipelines, 230 regulation stations, 110 tanks and reservoirs, 151 local groundwater wells, and 73 pump stations. To control the water flows in different pipes or to provide redundancy to increase the performance reliability of the regulation stations, a regulation station usually contains multiple control valves, resulting in 591 valves in the 230 regulation stations, including 493 pressure reducing valves, 50 throttle control valves, 35 flow control valves, 8 user defined valves, and 5 pressure sustaining valves. Similarly, 73 pump stations contain 284 pumps, in addition to 151 pumps in 151 local groundwater wells.

Figures 4.11 and 4.12 show the statistics regarding pipe diameters and pipe materials, respectively. As shown in Figure 4.11, 90% of the pipelines, with respect to pipe length, in the H2ONET hydraulic network model have diameters larger than or equal to 305 mm (12 inch) and roughly half of pipelines have diameters larger than or equal to 610 mm (24 inch). Most of the pipelines with diameters smaller than 305 mm (12 inch) are in the mountainous areas where the water demand is small. Since the H2ONET hydraulic network model was originally used by LADWP engineers for system planning and management purposes, only pipelines with relatively large diameters or significant serviceability are included in the model. Most local distribution pipelines with relatively small diameters are included implicitly in the H2ONET hydraulic model by aggregating them to demand nodes. Figure 4.12 shows that 75% of the pipelines in the model are composed either of steel with slipped joints or cast iron.
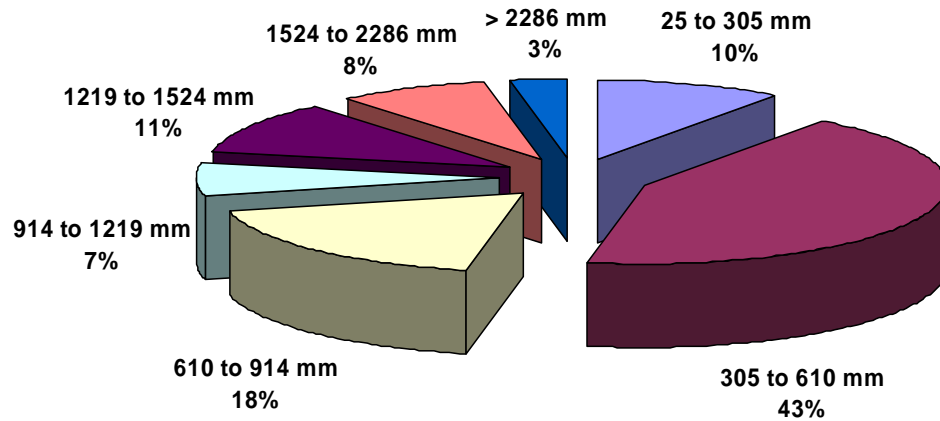
Figure 4.11.  Statistics on Pipe Diameter in LADWP H2ONET Hydraulic Model
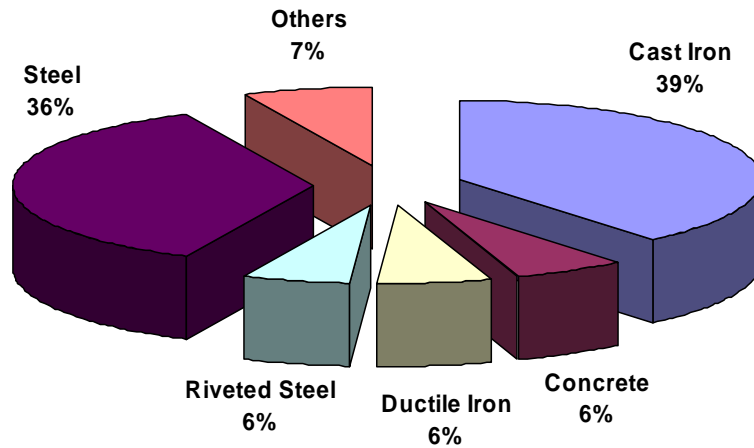


Figure 4.12.  Statistics on Pipe Material in LADWP H2ONET Hydraulic Model

### 4.3.2.  Operational Aspects of H2ONET Hydraulic Network Model

The H2ONET hydraulic network model also contains a comprehensive data inventory describing operational aspects of the LADWP system and other relevant information required for hydraulic analysis. The operational aspects include the pre-defined setting parameters for each regulation valve, such as pressure setting for

pressure reducing valves, pump characteristic curves for each pump representing the relationship between the variations of hydraulic heads as a function of the flow rate through the pump, pump net positive suction head curves used in the design and evaluation of pumping systems for cavitations avoidance, and controls on links (pipes, valves, or pumps) indicating a change in the operational status of the links.

Controls on links (pipes, valves, or pumps) include initial status, operational and logic controls. The most common types of controls include pipes and pumps going on/off line, and changes in pump speed and valve setting. Initial status controls specify the operational status of the link at the outset of simulation. Operational controls allow for pipe, pump, and valve settings to be changed at specific times (time switch), pressures (pressure switch), link flow rates (flow switch), or tank water levels (grade switch). With logic controls, control rules can be defined using decision logic to permit more flexibility and robustness in the ways that operation of water distribution networks can be simulated. They can be combined using standard If, Elseif, and Else logic statements, and logical connectors such as Not, And, and Or. The logic controls in the daily operation of the LADWP system are mostly applied to pumps. General control rules for pumps are as follows: a pump will be turned on if the downstream nodal pressure or the water level of the tank it serves is lower than a specific level; the pump will be turned off if the downstream nodal pressure and tank water level are higher than specific levels, or the net positive suction head on the upstream side of the pump is lower than the required level. The pump net positive suction head curve is based on pump performance tests and is normally available from pump manufacturers.

Other relevant information required for hydraulic analysis includes:

- Geocoordinates and elevation of every node, as well as nodal demands, typically given by demand patterns used to characterize the variation of demands with time.

- Length, diameter, and friction loss coefficient of each pipe.

- Bottom elevation and location of each reservoir and local groundwater well.

- Bottom elevation, location, shape characteristics, and minimum and maximum level of each tank.

### 4.3.3. Simulation Scenarios of H2ONET Hydraulic Network Model

H2ONET allows for users to develop multiple specific simulation scenarios for one water distribution system model, or to simulate the entire system or parts of the system individually. When modeling parts of the system, some virtual components are added to represent the other parts of the system, based on the flow input-output relationships. For example, if the parts of the system simulated receive water from other parts of the system, which are not included in the model, then a virtual tank is added to represent them as an external water source.

To model different operational scenarios with different demands, the LADWP H2ONET hydraulic network model contains twelve scenarios as follows:

- PLANNING_MODEL_NO_CV, All thirteen Subsystems without closed valves

- SUMMER, All thirteen Subsystems without closed valves

- S_12 SUBMODELS, Entire planning model except Harbor

- SUMMER-12, Entire planning model except for Harbor

- S_HARBOR, Subsystem Harbor only

- SUMMER_HARBOR, Subsystem Harbor only

- S_VALLYSIX, Subsystems VF, GH, FH, ST, SM, and EH

- SUMMER_VALLYSIX, Subsystems VF, GH, FH, ST, SM, and EH

- S_CITYSIX, Subsystems CC, HH, HW, HP, WS, and SY

- SUMMER_CITY, Subsystems CC, HH, HW, HP, WS, and SY

- S_RESERVOIRS, Subsystems VF, SM, HH, WS, and CC

- SUMMER_RESERVOIRS, Subsystems VF, SM, HH, WS, and CC

The twelve scenarios can be used to simulate the entire LADWP system or parts of the system individually for summer and winter, respectively. The PLANNING_MODEL_NO_CV scenario is a planning model for the entire system including all of the thirteen subsystems. The other five scenarios are used to model the system without the Harbor subsystem (S_12 SUBMODELS), only the Harbor subsystem (S_HARBOR), six subsystems, VF, GH, FH, ST, SM, and EH, around the San Fernando Valley (S_VALLYSIX), six subsystems, CC, HH, HW, HP, WS and SY, around the Central City (S_CITYSIX), five subsystems, VF, SM, HH, WS, and CC, which are supplied by water from the Los Angeles and Van Norman Bypass Reservoirs (S_RESERVOIRS). Two different demand sets, winter or summer demands, respectively, are simulated for the whole LADWP system or each subsystem set, resulting in twelve simulation scenarios in total. It is noted that the LADPW hydraulic network model also contains the third set of demand data, historical high demand, 70% or 30% of which are considered as typical summer or winter demands,

respectively, except for the larger users, whose summer and winter demands are considered the same as the historical high demand.

## 4.4. Summary

This chapter describes the characteristics of the LADWP water supply system. The LADWP system provides water to about 3.8 million people in a service area of approximately 1,200 km$^2$. The total water consumption of the LADWP system in a typical summer and winter day is about 2.5×10$^6$ and 1.2×10$^6$ m$^3$, respectively. About 85% of the water is transferred from northern California and treated in the Van Norman Complex before distribution, primarily by gravity flow from north to south throughout the LADWP service area. The system is divided into five water districts, thirteen subsystems, and 106 pressure zones. The system characteristics are embodied in a H2ONET hydraulic network model. The H2ONET hydraulic network model was developed under the supervision of LADWP engineers. It contains 9,287 nodes and 10,665 links, representing about 2,186 km of pipelines, 1,052 demand nodes, 591 control valves, 110 tanks and reservoirs, 151 local groundwater wells, and 284 pumps. The H2ONET hydraulic network model contains both typical winter and summer demand sets. It is capable of simulating the entire LADWP system, as well as various portions of the system.

# CHAPTER 5

# SEISMIC BODY WAVE EFFECTS ON PIPELINES

## 5.1. Introduction

The earthquake performance of a water supply system is often closely related to the performance of water trunk and transmission lines, whose seismic wave interactions are examined in this chapter. The chapter starts with characterizing the seismic body waves, followed by analytical and finite element (FE) modeling of seismic wave-pipeline interactions. Attention is then directed to a particular class of pipelines, used for trunk and transmission facilities in North America, referred to collectively in this work as jointed concrete cylinder pipelines (JCCPs). The performance of JCCPs during previous earthquakes and typical JCCP joint characteristics are reviewed. Both simplified and FE models are developed to characterize seismic body wave effects on pipelines with or without existing cracked joints. The effect of the mortar cracking strain at the joints is discussed. Models for JCCP interaction with seismic body waves are expanded to accommodate other pipelines containing locally weak joints, such as cast iron pipelines, by appropriate modification of the joint characteristics. This chapter focuses on seismic body wave effects on pipelines, and a parallel study on seismic surface wave effects on pipelines is reported by Shi (2006).

## 5.2. Seismic Body Wave Characteristics

Two types of seismic waves occur during earthquakes: body waves which propagate within a body of earth, and surface waves whose motion is restricted to near the ground surface. The body waves are generated by seismic faulting, while for the simplest case surface waves are generated by the reflection and refraction of body waves at the ground surface. There are two types of body waves: P-waves (compressional wave) and S-waves (shear waves). P-waves, whose ground motion is in the same direction as the wave propagation, generate alternating compressional and tensile strain. In contrast, the ground motion of S-waves is perpendicular to the direction of wave propagation. Surface waves include Rayleigh waves and Love waves. Most of the seismic surface wave motion is located near the ground surface, and as the depth below this surface increases, wave displacements decrease.

Since pipelines are typically buried within the shallow depth, i.e., 1 to 3 m, below the ground surface, both body and surface waves may influence the performance of pipelines during earthquakes. A systematic study on the seismic body wave effects on pipelines is presented in this chapter. For counterpart study of the seismic surface wave effects on pipelines, please refer to Shi (2006).

### 5.2.1. Typical Strong Motion Ground Velocity Record

Figure 5.1 shows the ground velocity record at Rinaldi receiving substation during the 1994 Northridge earthquake (Trifunac et al., 1998). P-waves firstly arrived the site at about Time = 1.5 sec, quickly followed by S-waves at about Time = 2.0 sec, which generated the largest velocity pulse in the record. Please note that no surface
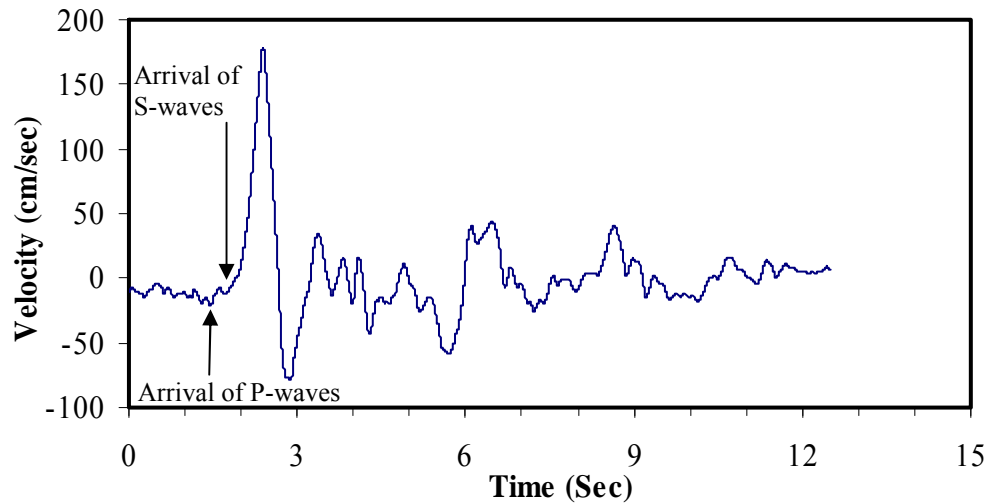
Figure 5.1. Ground Velocity Record at Rinaldi Station during 1994 Northridge

Earthquake

waves can be discerned from the record. Generally speaking, if surface waves are present because of certain local geological setting, such as large sedimentary basins, they occur a certain time after the arrival of direct body waves when the ground motion generated from body waves is diminishing. Therefore, strong velocity pulses at the beginning of a record are general distinct and recognizable with respect to surface wave effects.

Figure 5.1 also indicates that S-waves carry much more energy and generate much larger ground motion than P-waves. Therefore, it is reasonable to consider only the S-waves and neglect the P-waves in seismic body wave interaction with pipelines, as recommended by O'Rourke and Liu (1999).

### 5.2.2. Near Source Strong Ground Motion Characteristics

To characterize further the near source seismic body waves, 18 near source strong ground motion records were collected from Consortium of Organizations for Strong-Motion Observation Systems (COSMOS) Virtual data center (COSMOS, 2004), as summarized in Table 5.1. The collected strong ground motion records include eight records from the 1994 Northridge earthquake, four records from the 1995 Kobe earthquake, five records from the 1989 Loma Prieta earthquake, and one from the 1992 Landers earthquake. All the recording stations are rested on soils, subjected to free field motion, and located within 12 km to the faults generating the earthquakes. COSMOS performed baseline correction, which accounts for the error caused by the level of motion at the time of record triggering, for all records. The records with seismic surface wave presence were screened out to allow the concentration on the characteristics of the seismic body waves.

Two horizontal components of the strong ground motion records, which are perpendicular to each other, are combined to determine the maximum vector peak ground velocity, $V_p$, and the corresponding direction. As shown in Figure 5.1, the typical records are characterized by the first arrival of P-waves, followed by a single pulse with an amplitude of $V_p$ generated by the S-waves, and then diminish gradually. In the context of seismic body wave interaction with pipeline, where the maximum pipeline strain depends only on the $V_p$ and apparent wave propagation velocity, C (please refer to Section 5.3 for details), the waveform of the strong ground motion records can be simplified as a sinusoidal pulse with the same $V_p$ and C. The direction of particle motion for the S-waves can be defined by the direction of $V_p$, whose perpendicular direction also defines the wave propagation direction. Wald et al. (1996)

Table 5.1.  Near Source Strong Ground Motion Characteristics

| Earthquake | Station | Latitude (°) | Longitude (°) | Closest Distance To Fault (km) | Max. PGV (cm/sec) | Max. Vector Azimuth | Original Pulse Period $T_0$ (sec) | Sine Pulse Period T (sec) | $T/T_0$ |
|---|---|---|---|---|---|---|---|---|---|
| Northridge | Arleta - San Valley | 34.236 | -118.439 | 9.5 | 41 | S82W | 0.96 | 0.84 | 0.87 |
| | Jensen Filtration Plant Admin. Bldg | 34.312 | -118.496 | 8.6 | 106 | S20W | 1.92 | 1.55 | 0.81 |
| | Newhall - LA County Fire Station | 34.387 | -118.530 | 10.9 | 119 | S38W | 0.92 | 0.75 | 0.82 |
| | Pacoima -Kagel Canyon | 34.288 | -118.375 | 10.6 | 56 | S26W | 0.76 | 0.66 | 0.87 |
| | Rinaldi Receiving Station | 34.281 | -118.479 | 8.6 | 179 | S31W | 1.52 | 1.09 | 0.72 |
| | Sun Valley 13248 Roscoe Blvd | 34.221 | -118.421 | 10.5 | 43 | S78W | 1.00 | 0.86 | 0.86 |
| | Sylmar Converter Station (Valve Group1-6) | 34.311 | -118.490 | 8.7 | 130 | S13W | 1.86 | 1.65 | 0.89 |
| | Sylmar Converter Station (Valve Group 7) | 34.311 | -118.490 | 8.7 | 122 | S58W | 1.65 | 1.46 | 0.89 |
| Kobe | Nishi - Osaka | 34.664 | 134.964 | 11.1 | 39 | S71W | 0.60 | 0.54 | 0.90 |
| | OSAJ | 34.678 | 135.520 | 8.5 | 20 | N32W | 2.04 | 1.87 | 0.92 |
| | Takarazuka | 34.809 | 135.344 | 1.2 | 90 | N18E | 0.92 | 0.83 | 0.90 |
| | Takatori | 34.649 | 135.612 | 0.3 | 170 | N43W | 1.56 | 1.45 | 0.93 |

Table 5.1. (Continued)

| Earthquake | Station | Latitude (°) | Longitude (°) | Closest Distance To Fault (km) | Max. PGV (cm/sec) | Max. Vector Azimuth | Original Pulse Period $T_0$ (sec) | Sine Pulse Period T (sec) | $T/T_0$ |
|---|---|---|---|---|---|---|---|---|---|
| | Corralitos | 37.046 | -121.803 | 2.8 | 56 | S10E | 0.56 | 0.50 | 0.89 |
| | Gilroy # 1 | 36.973 | -121.572 | 2.8 | 39 | N39E | 0.72 | 0.64 | 0.89 |
| Loma Prieta | Gilroy # 2 | 36.982 | 121.556 | 4.5 | 46 | N47E | 1.52 | 1.35 | 0.89 |
| | Gilroy # 3 | 36.987 | -121.536 | 6.3 | 49 | N46E | 1.44 | 1.18 | 0.82 |
| | Gilroy # 4 | 37.005 | -121.522 | 7.9 | 40 | N65E | 1.28 | 1.13 | 0.88 |
| Landers | Joshua Tree | 34.131 | -116.314 | 10 | 46 | S29W | 1.04 | 1.02 | 0.98 |
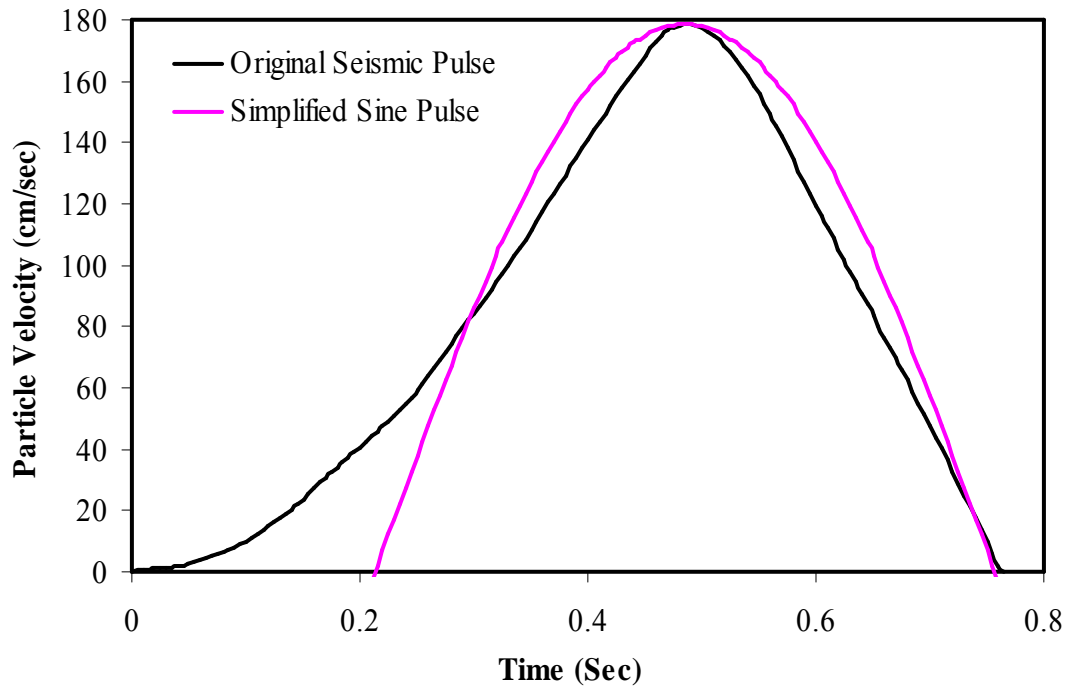
Figure 5.2. Original and Simplified Sinusoidal Pulses for Strong Ground Motion
Record at Rinaldi Station during 1994 Northridge Earthquake

studied the strong ground motion records from previous California earthquakes and crustal conditions and estimated the C equal to 2.5 km/sec for west coast earthquakes.

Figure 5.2 shows the original waveform for strong ground motion at Rinaldi station during the 1994 Northridge Earthquake (Figure 5.1) and the corresponding simplified sinusoidal pulse. The sinusoidal pulse is simplified in such that both $V_p$s occur at the same time and the areas under both pulses are the same. Table 5.1 summarizes the periods for both original and simplified sinusoidal pulses, $T_0$ and T, and the ratio between them. The simplified sinusoidal pulse represents the characteristics of the original strong ground motion record reasonably well, indicating by the same $V_p$ value at the same time and a high value of period ratio, 0.72-0.98.

### 5.2.3. Resolution of Particle and Wave Velocities Relative to Pipeline

Figure 5.3 shows a pipeline subjected to shear wave propagation with an angle of incidence, $\gamma_i$, with respect to the normal of the pipelines. The S-wave propagation velocity, C, and particle velocity, V, can be resolved into apparent S-wave propagation velocity, $C_a$, and particle velocity, $V_a$, directed along the longitudinal axis of the pipeline, respectively. The $C_a$ and $V_a$ can be expressed as:

$$C_a = C/\sin\gamma_i \qquad\qquad (5.1)$$

$$V_a = V\cos\gamma_i \qquad\qquad (5.2)$$

The $C_a$ and $V_a$ induce ground strain parallel to the pipeline, which can be derived as the ratio of $V_a$ over $C_a$ and results in the axial strain along the pipeline. The detailed description of the seismic wave-pipeline interaction is discussed in the next Section: Seismic Wave Interactions with Pipelines.

The magnitudes of $V_a$ and $C_a$ depend on the incidence angle $\gamma_i$. Particle motion in S-waves occurs at the right angle to the direction of wave propagation. If a seismic S-wave intersects the longitudinal axis of a pipeline at $\gamma_i = 0°$, all particle motion is imposed along the longitudinal axis of the pipeline at the same magnitude in the same direction simultaneously. This leads to a $C_a$ that is infinite and the strain along the pipeline that is zero. As $\gamma_i$ changes from a $0°$ angle of incidence to an acute angle that becomes increasingly larger, $C_a$ decreases until it equals C, the wave propagation velocity in the free field, while $V_a$ also decreases from V to 0. This occurs when both the seismic wave propagation and pipeline are in the same direction, resulting in zero
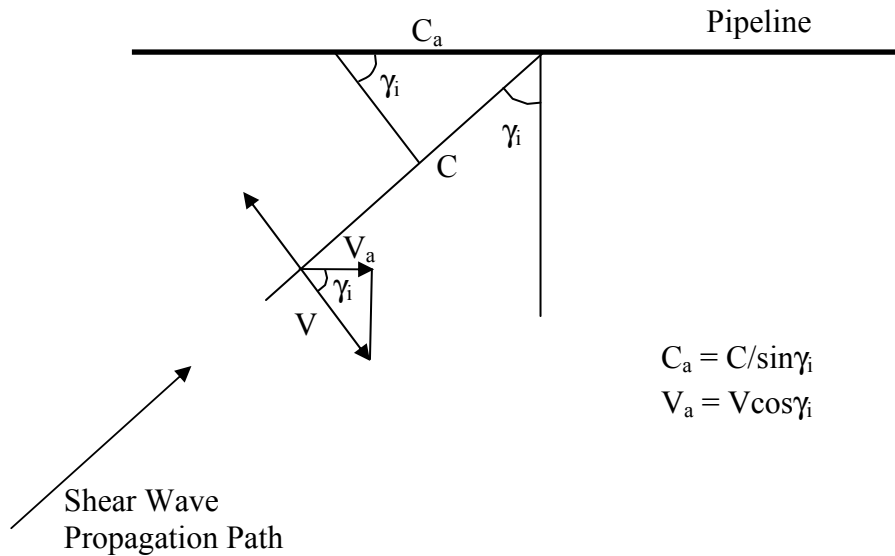
Figure 5.3.   Pipeline Subjected to Shear Wave Propagation

axial strain along the pipeline.

## 5.3.  Seismic Wave Interactions with Pipelines

Simplified procedures for assessing seismic wave interaction with pipelines were first developed by Newmark (1967), and have since been used and/or extended by a number of researchers. The study presented in this chapter follows some basic assumptions proposed by Newmark (1967). The first assumption is that the seismic ground motions (i.e., acceleration, velocity and displacement time histories) at two points along the propagation path differ only by a time lag. That is, the excitation is modeled as a traveling wave. The second assumption is that pipeline inertia terms are small and may be neglected. Experimental evidence (Kubo, 1974) as well as analytical studies (Sakurai and Takahashi, 1969; and Shinozuka and Koibe, 1979) indicates that

121

this is a reasonable engineering approximation. The assumptions lead to the expression of ground strain parallel to pipe axis, $\varepsilon_g$, as following:

$$\varepsilon_g = V_a/C_a \tag{5.3}$$

where $V_a$ and $C_a$ are the ground velocity and the apparent wave propagation velocity along the axial direction of the pipeline and defined by Eqns 5.1 and 5.2, respectively. Combining Eqns 5.1, 5.2, and 5.3 leads to

$$\varepsilon_g = \frac{V \sin \gamma_i \cos \gamma_i}{C} \tag{5.4}$$

which can be rewritten as

$$\varepsilon_g = \frac{V \sin 2\gamma_i}{2C} \tag{5.5}$$

Eqn 5.5 implies that $\varepsilon_g$ varies as the $\gamma_i$ changes. When the pipeline is oriented with an incidence angle, $\gamma_i = 45°$, maximum ground strain, $\varepsilon_{gmax} = V/2C$, occurs along the axial direction of the pipeline. Minimum ground strain, $\varepsilon_{gmin} = 0$, occurs when $\gamma_i = 0°$ or $90°$.

When the direction of $C_a$ is in the same direction as the polarity, or direction of $V_a$, the longitudinal strain imposed on the pipe is compressive. When the direction of $C_a$ is in the opposite direction as the polarity, or direction of $V_a$, the longitudinal strain imposed on the pipe is tensile. Pipelines may have different resistance against compressive or tensile loads because of their structure and joint characteristics.

Consider, for example, JCCPs which are more vulnerable under tension than under compression as a result of low pullout capacity at the joints (see Section 5.4.2).

### 5.3.1. Analytical Model

An analytical model for the pipeline interactions with seismic waves, which are simplified as sinusoidal waves, is presented in the section. Section 5.2 shows that the seismic body wave can be simplified as a single S-wave pulse. Similarly, Shi (2006) studied the seismic surface wave characteristics and found that the seismic surface waves can be characterized by several cycles of sinusoidal waves with constant amplitude and period. Therefore, the model described in this section is applicable for both seismic body and surface waves.

Figure 5.4 shows an incremental section of a continuous buried pipeline, dx, subjected to a seismic wave, simplified as a sinusoidal wave with maximum amplitude of ground strain $\varepsilon_{gmax} = V_{ap}/C_a$, where $V_{ap}$ and $C_a$ are the peak ground velocity and apparent wave propagation velocity along the axial direction of the pipeline, respectively. The shear transfer between pipe and soil is f, and the pipe axial stiffness is equal to the product of the pipe material modulus, E, and cross-sectional area, A. The rate of pipe strain, $\varepsilon_p$, accumulation is given by

$$\frac{d\varepsilon_p}{dx} = \frac{f}{EA} \tag{5.6}$$

If the ratio of $V_{ap}/C_a$ to the rise distance, $\lambda/4$, is defined as R
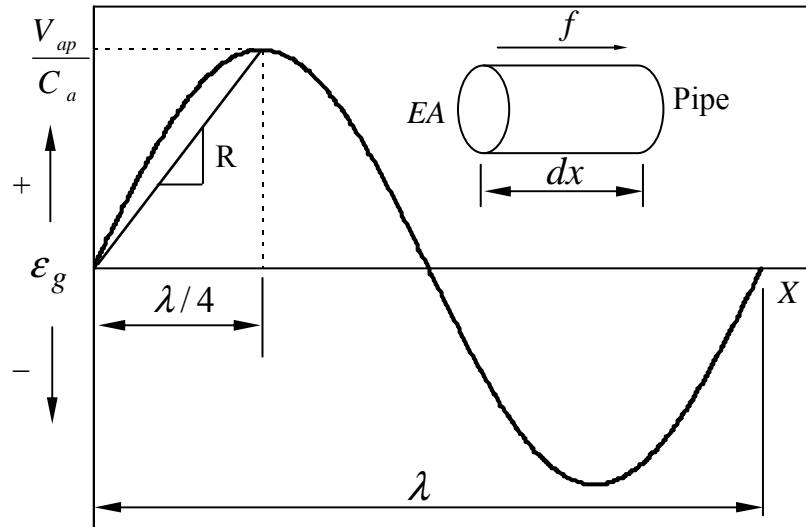
Figure 5.4.  Sinusoidal Wave Interaction with Pipe Element

$$R = \frac{4V_{ap}}{\lambda C_a} \tag{5.7}$$

where $\lambda$ is the wave length along the axial direction of the pipeline, expressed as

$$\lambda = TC_a \tag{5.8}$$

where T is predominant period of the seismic waves. R characterizes the seismic body waves and can be rapidly discerned from strong motion records.

When the pipeline is axially flexible with respect to ground strain accumulation, no relative displacement occurs between the surrounding soils and the pipeline, and the pipeline deforms coincidentally with the ground surrounding the pipeline, resulting in $\varepsilon_p = \varepsilon_g$ everywhere the pipeline is continuous. The ratio between maximum pipe strain, $\varepsilon_{pmax}$, and $\varepsilon_{gmax}$, is equal to 1:

$$\frac{\varepsilon_{p\max}}{\varepsilon_{g\max}} = 1 \qquad\qquad (5.9)$$

On the other hand, when the pipeline is relatively rigid with respect to axial ground strain accumulation, relative displacement occurs between soil and pipeline. The strain in the continuous pipeline will accumulate linearly at a slope of f/EA. The soil-pipeline interaction for the relatively rigid pipeline subjected to seismic waves is shown in Figure 5.5. Please note that the pipeline is a linear structure, which may be considered symmetric at each location along the pipeline. Also, the seismic sinusoidal wave is symmetric at each amplitude and anti-symmetric at each location of $\varepsilon_g = 0$. Therefore, as a result of the symmetric structure subjected to symmetric loading or anti-symmetric loading, the pipeline strain will attain its maximum value, $\varepsilon_{pmax}$, at each seismic wave amplitude and will be zero at each location of $\varepsilon_g = 0$. The $\varepsilon_{pmax}$ can be calculated as:

$$\varepsilon_{p\max} = \frac{f}{EA}\frac{\lambda}{4} \qquad\qquad (5.10)$$

This leads to a ratio between $\varepsilon_{pmax}$ and $\varepsilon_{gmax}$ expressed as:

$$\frac{\varepsilon_{p\max}}{\varepsilon_{g\max}} = \frac{\dfrac{f}{EA}\dfrac{\lambda}{4}}{\dfrac{V_{ap}}{C_a}} = \frac{f}{EA}\frac{\lambda C_a}{4V_{ap}} = \frac{f}{EAR} \qquad\qquad (5.11)$$

Combining Eqns 5.9 and 5.11 not only unites the relationship between $\varepsilon_{pmax}/\varepsilon_{gmax}$ and f/EAR for both flexible and rigid pipeline, but also establishes the criterion on
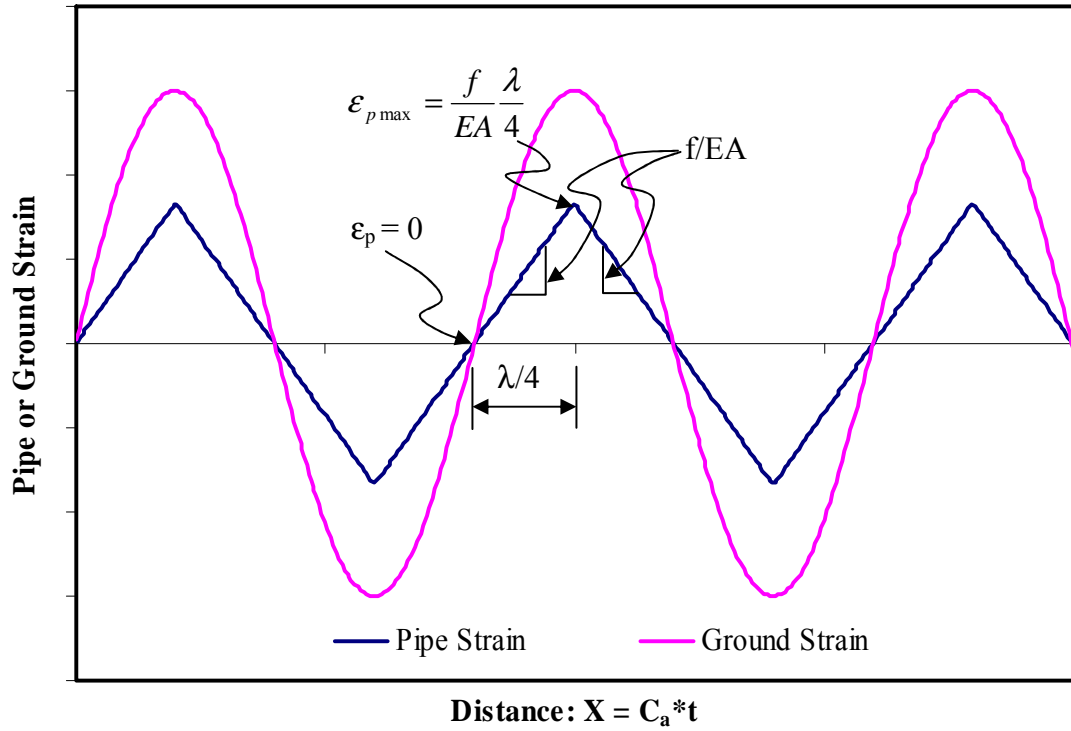
Figure 5.5. Seismic Wave-pipeline Interaction for Rigid Pipeline

determining the pipeline is either flexible or rigid. When f/EAR ≥ 1, the pipeline is axially flexible with respect to ground deformation induced by seismic waves and

$$\frac{\varepsilon_{p\,max}}{\varepsilon_{g\,max}} = 1 \qquad (5.12)$$

When f/EAR < 1, the pipeline is relatively rigid and the pipe strain is less than ground strain. The ratio of maximum strains can be expressed as

$$\frac{\varepsilon_{p\,max}}{\varepsilon_{g\,max}} = \frac{f}{EAR} \qquad (5.13)$$

126

## 5.3.2.  Finite Element Model

A set of finite element (FE) simulations were performed, using the program BSTRUCT (Chang, 2006; and Goh and O'Rourke, 2000), to verify both the seismic wave-pipeline interaction model and $\varepsilon_{pmax}/\varepsilon_{gmax}$ and f/EAR relationship described above.

### 5.3.2.1.  FE Analysis Setup

Figure 5.6 shows a schematic of the FE model. The pipeline was modeled with beam column elements that were connected to the ground by spring-slider elements capable of representing shear transfer as an elasto-plastic process. Strong motion time history, which is simplified as a sinusoidal wave, was converted to displacement versus distance records by assuming that $X = C_a t$, in which X is distance, t is time from the strong motion recording, and $C_a$ is calculated from Eqn 5.1 with C equals to 2.5 km/sec. The seismic displacement versus distance record was superimposed on the spring-slider elements, which then conveyed ground movement to pipeline by means of the elasto-plastic properties utilized to characterize the spring-sliders. As recommended by the ASCE Committee on Gas and Liquid Fuel Lifelines (CGLFL, 1984), Figure 5.7 shows that the relation between f and relative pipe-soil displacement was modeled as a bilinear relationship with linear rise to f at a relative displacement of 3 mm and constant f thereafter. In total, 12 FE simulations with f/EAR varying from 0.01 to 11 were performed to verify the seismic wave-pipeline interaction model. The variation of f/EAR is achieved by changing either f, EA, or R intentionally.
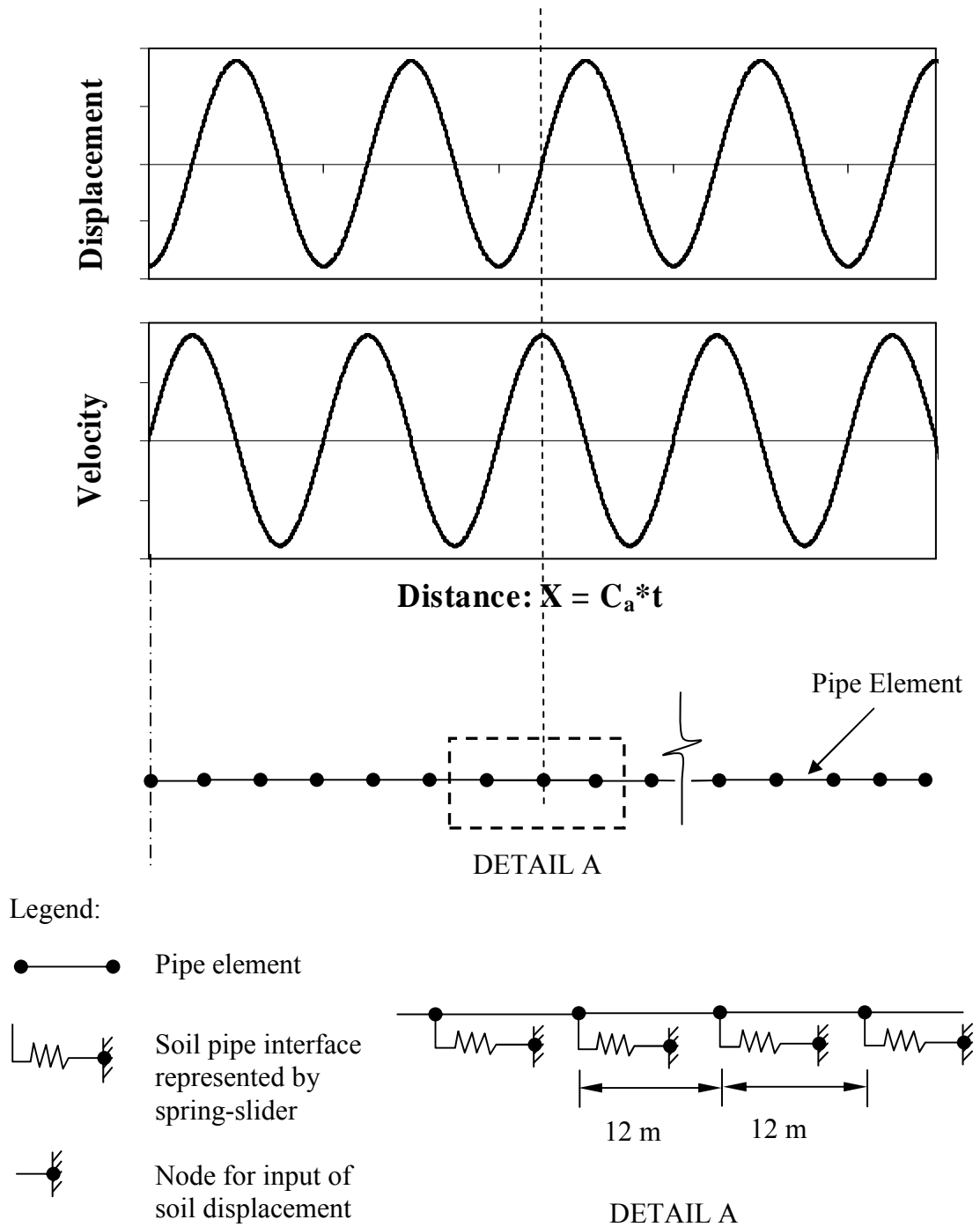
Figure 5.6.   Finite Element Model for Seismic Wave and Pipeline Interaction
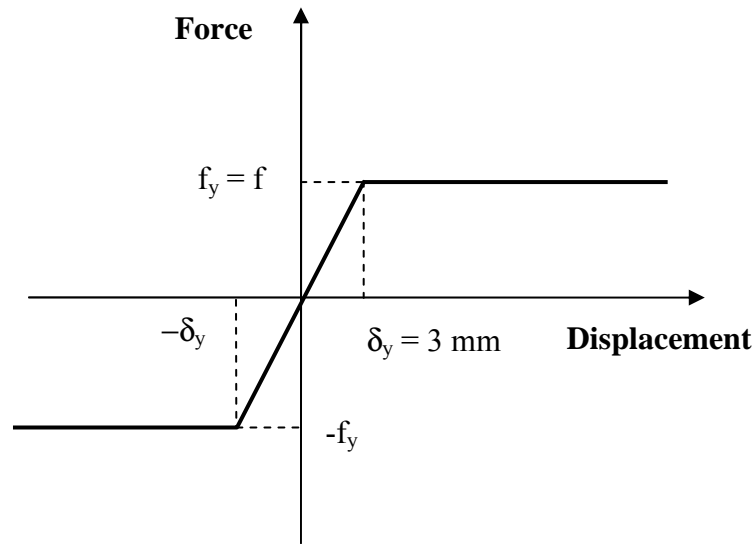
Figure 5.7.  Shear Transfer and Soil-pipe Relative Displacement Relationship

*5.3.2.2. Flexible Pipe Behavior*

In total 12 FE simulations, flexible pipe behavior is expected in 5 FE simulations, which have f/EAR $\geq$ 1. Figure 5.8 shows the typical results of the 5 simulations. The pipe strain, $\varepsilon_p$, and ground strain, $\varepsilon_g$, are shown by open triangles and rectangles, respectively. It is evident that the pipeline moves together with the ground and $\varepsilon_p = \varepsilon_g$ everywhere along the pipeline. No relative displacement occurs between the surrounding soils and the pipeline, and the pipeline deforms coincidentally with the ground surrounding the pipeline. The FE results confirm that the analytical model for the flexible pipe behavior is appropriate.

*5.3.2.3. Rigid Pipe Behavior*

Figure 5.9 shows a FE simulation result with a f/EAR = 0.559. Relative displacement occurs between the pipeline and the surrounding soils, and $\varepsilon_p$ does not

**Distance: X = C$_a$*t**
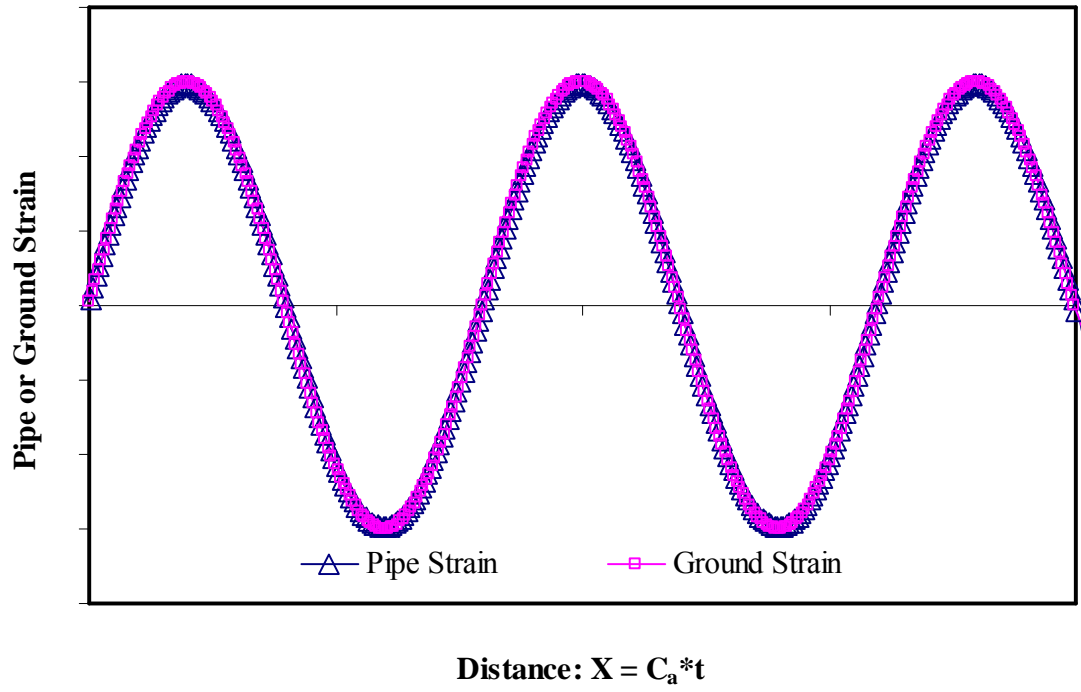
Figure 5.8.   FE Results for Flexible Pipes



$$\varepsilon_{p\max} = \frac{f}{EA}\frac{\lambda}{4}$$

f/EA

$\varepsilon_p = 0$

$\lambda/4$

**Distance: X = C$_a$*t**
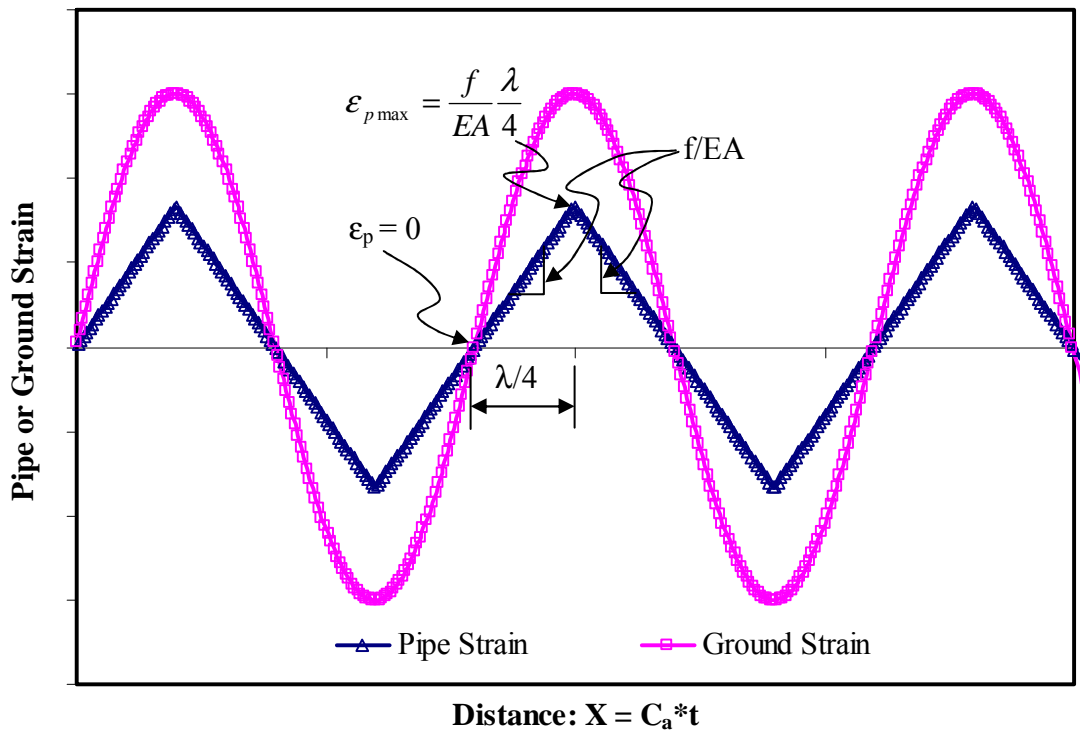
Figure 5.9.   FE Results for Rigid Pipes
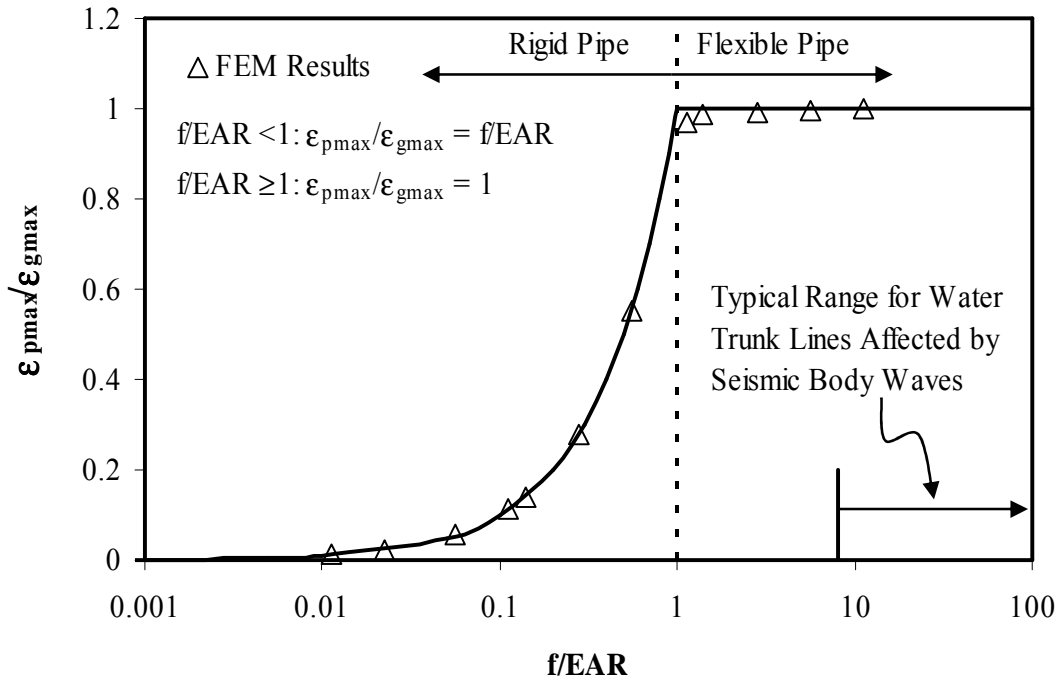
Figure 5.10.    $\varepsilon_{pmax}/\varepsilon_{gmax}$ and f/EAR Relationship

equal to the $\varepsilon_g$ of surrounding soils. The $\varepsilon_p$ varies linearly at a slope of f/EA with the maximum occurred at amplitudes of the $\varepsilon_g$ and $\varepsilon_p = 0$ occurred at $\varepsilon_g = 0$. The $\varepsilon_{pmax}/\varepsilon_{gmax}$ ratio from the FE result is about 0.553, which is remarkably consistent with f/EAR, i.e., 0.559. The FE simulation results indicate that the analytical model is able to depict the rigid pipe behavior reasonable well.

### 5.3.2.4. $\varepsilon_{pmax}/\varepsilon_{gmax}$ and f/EAR Relationship

Figure 5.10 plots the data pairs of $\varepsilon_{pmax}/\varepsilon_{gmax}$ and f/EAR from the twelve FE simulations by triangles. The FE results show that $\varepsilon_{pmax}/\varepsilon_{gmax}$ increases as the f/EAR increases from 0 to 1, and remains constant, i.e., 1, after f/EAR is greater than 1. The proposed $\varepsilon_{pmax}/\varepsilon_{gmax}$ and f/EAR relationship in accordance with the analytical model is

also plotted in Figure 5.10. It is evident that the FE results are consistent with the proposed relationship.

### 5.3.3. Calculating Shear Transfer f

O'Rourke (1998) summarized the approaches of calculating shear transfer between soils and pipelines, which is generally adopted in soil-pipeline interaction modeling. For a pipeline buried in cohesionless soil, the maximum shear transfer per unit distance, f, is

$$f = 0.5(1 + K_0)\gamma z_p \pi D \tan \delta \tag{5.14}$$

in which $z_p$ is the depth to pipe centerline, $\gamma$ is soil unit weight, $K_0$ is the coefficient of at-rest horizontal soil stress (generally $0.5 \le K_0 \le 1.0$ for pipe in backfilled trenches), $\delta$ is the angle of interface frictional resistance, and D is the outside pipe diameter. The angle of interface friction for sands between pipe and soil generally varies between 25° and 45°

If the pipeline is buried in cohesive soil, the maximum f is

$$f = \alpha s_u \pi D \tag{5.15}$$

in which $s_u$ is the undrained shear strength of the surrounding soil and $\alpha$ is an adhesion factor that accounts for the degree of bonding between the pipe and soil. Figure 5.11 shows the relationship between $\alpha$ and $s_u$ developed by Chen and Kulhawy (1994), Kulhawy and Chen (2003), and ASCE Committee on Gas and Liquid Fuel Lifelines

132
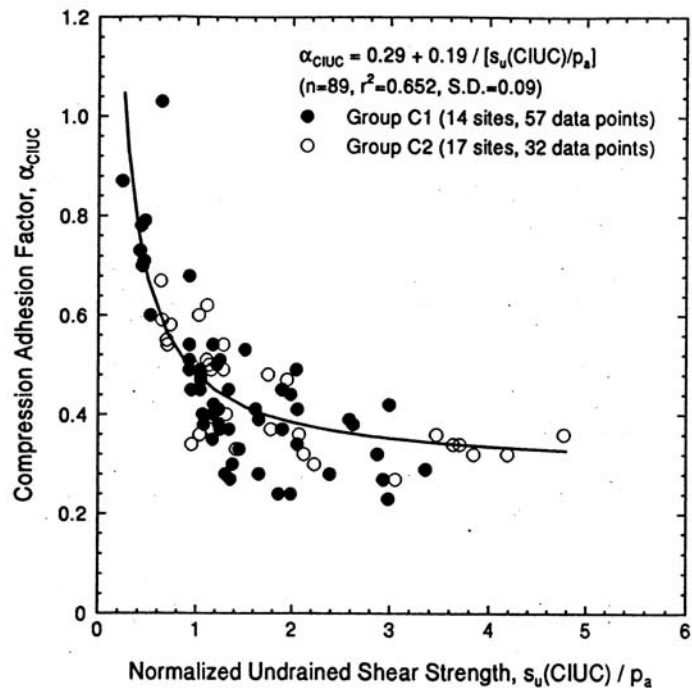
(a) Chen and Kulhawy (1994) and Kulhawy and Chen (2003)
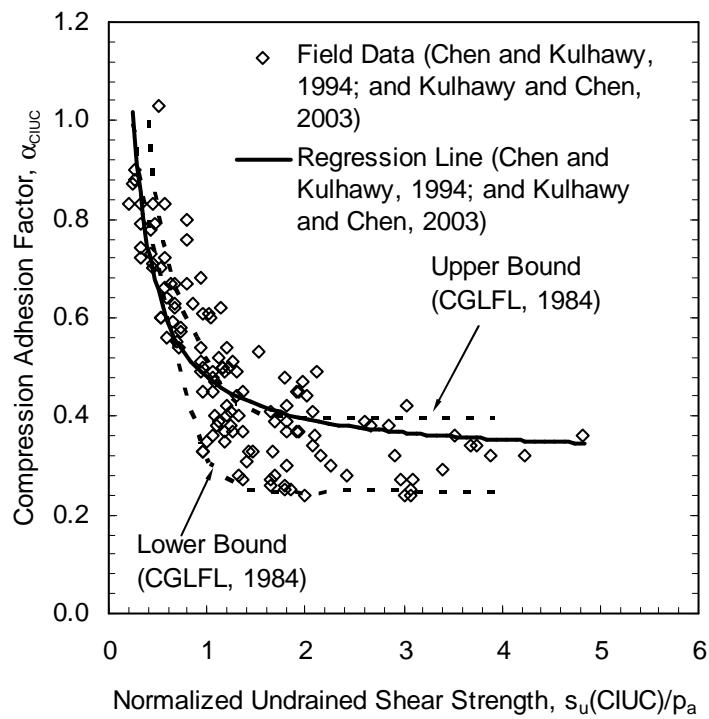


(b) CGLFL (1984)

Figure 5.11.  Relationship between $\alpha$ and $s_u(CIUC)/p_a$

133

(CGLFL, 1984). Following the format of Chen and Kulhawy (1994) and Kulhawy and Chen (2003), $s_u$ determined from isotropically consolidated undrained triaxial compression, CIUC, tests is normalized with respect to atmospheric pressure, $p_a = 101.3$ kN/m$^2$. For shallow buried pipelines in recompacted, overconsolidated clay, a reasonable range for $s_u(CIUC)/p_a$ would be 0.5 to 1.0, for which the adhesion between pipe and soil, $\alpha s_u$, varies between 25 and 60 kN/m$^2$.

It is worthwhile to point out that Goh et al. (2005) reanalyzed the database from Chen and Kulhawy (1994) using a Bayesian neural network approach and found that there is a clear trend of decreasing $\alpha$ value with increasing mean effective overburden stress, $\sigma'_{vm}$, and increasing undrained strength ratio, $s_u/\sigma'_{vm}$. Because pipelines are typically buried at a shallow depth, i.e., 1 to 3 m, below the ground surface, the $s_u/\sigma'_{vm}$ ratio might be relatively large, resulting in relatively small $\alpha$ value.

Please also note that the effects of the constructions can be accounted for by properly modifying Eqns 5.14 and 5.15, although the detailed discussion regarding the effects of constructions on the pipe performance is beyond the scope of this study. The $K_0$ value in Eqn 5.14 or $\alpha$ value in Eqn 5.15 can be modified to consider the effects of constructions. A suite of modification factors for $K_0$, originally developed by Kulhawy et al. (1983) for pile foundations, might be applicable for the calculation of shear transfer between the pipe and the surrounding soil.

### 5.3.4. Typical Range of f/EAR for Water Trunk Lines

The typical range of f/EAR for water trunk lines when affected by seismic body waves can be estimated by considering the typical ranges for all the input

parameters necessary for calculating f/EAR, which include $\alpha s_u$ (25 to 60 kN/m$^2$) for cohesive soils, $K_0$ (0.5 to 1.0), $\gamma$ (or $\gamma'$, 6 to 20  kN/m$^3$), $z_p$ (1 to 3 m), and $\delta$ (25° to 45°) for cohesionless soils, pipe diameter D (610 to 2540 mm), pipe wall thickness (4 to 254 mm), E (200 $\times$ 10$^6$ kPa for steel and 26 $\times$ 10$^6$ kPa for concrete), $V_p$ (up to 200 cm/sec), C (2500 m/sec), and T (1 to 2 sec). When the pipe is oriented with a 55° incidence angle with respect to the shear wave propagation direction, the maximum R occurs. Combining 55° incidence angle with ranges for other input parameters results in a minimum f/EAR of about 8, as indicated in Figure 5.10. It is evident that the typical range is much greater than 1 and that the water trunk lines tend to behave as flexible pipes when affected by seismic body waves. Rigid pipe behavior only occurs under extremely adverse conditions, such surrounding by liquefied soils, where the f approaches 0, resulting in f/EAR less than 1.

Rigid pipe behavior tends to occur when the water trunk lines are affected by the seismic surface waves, which are characterized by moderate $V_p$ with low C, resulting in a much larger $\varepsilon_p$, larger R, and smaller f/EAR (Shi, 2006). For more details on the seismic surface wave interaction with pipelines, please refer to Shi (2006).

### 5.3.5. Model Applications

With known ground conditions, pipeline properties, and seismic wave characteristics, f/EAR can be calculated and the pipe behavior under seismic wave loading can be predicted in accordance with the model described in the previous sections. Consider, for example, a steel pipe with 1524-mm diameter and 10-mm wall thickness subjected to a near source velocity pulse with $V_p$ = 200 cm/sec, C = 2500

m/sec, and T = 1sec. The pipeline is oriented with a 45° incidence angle with respect to the S-wave propagation direction and buried at a depth of 1.69 m to the center of pipeline in soils with $\gamma = 18.5$ kN/m$^3$ and $\delta = 25°$. The f and f/EAR are calculated as 54.3 kN/m and 13, respectively. Because f/EAR is larger than 1, the steel pipe behaves as a flexible pipe. $\varepsilon_p = \varepsilon_g$ everywhere along the pipe and the variation of $\varepsilon_p$ also follows a sinusoidal function of distance. The maximum pipe strain equals to the maximum ground strain, which is $V_{ap}/C_a = 0.0004$. If the surrounding soils liquefy and the shear transfer f between the liquefied soils and the pipe is reduced to 2 kN/m, f/EAR reduces to 0.45 and the pipe behaves as a rigid pipe. The $\varepsilon_p$ varies linearly with the maximum occurred at amplitudes of the $\varepsilon_g$ and $\varepsilon_p = 0$ occurred at $\varepsilon_g = 0$, as shown in Figures 5.5 and 5.9. The $\varepsilon_{pmax}/\varepsilon_{gmax}$ ratio is about 0.45 and $\varepsilon_{pmax} = 0.00018$.

## 5.4. Seismic Body Wave Interaction with JCCPs

The seismic body wave interaction with a particular class of pipelines used for trunk and transmission facilities in North America, referred to collectively in this work as jointed concrete cylinder pipelines (JCCPs), is further studied in this section. In this work the term JCCPs is used to represent pipelines composed of reinforced concrete and steel cylinders that are coupled with mortared, rubber-gasket bell-and-spigot joints. Pipe lengths are generally 6 to 12 m. Governing standards for the current design of such pipelines include AWWA C301 (AWWA, 1999) and C303 (AWWA, 2003).

### 5.4.1. Performance of JCCPs during Previous Earthquakes

The performance of JCCPs during previous earthquakes has varied significantly, depending on their structural and joint characteristics and on the location

and nature of the transient ground deformation (TGD) and permanent ground deformation (PGD) they were subjected to. Ayala and O'Rourke (1989) reported significant repairs in JCCPs after the 1979 Guerrero and 1985 Michoacan earthquakes. Repairs were concentrated at the joints of the trunk and transmission pipelines, and were especially severe for the 1985 Michoacan earthquake. For example, there were 60 repairs in Federal District JCCP transmission lines, which conveyed water to Mexico City, resulting in a relatively high repair rate of 1.7 repair/km. Ayala and O'Rourke (1989) reported that most of the water system damage did not coincide with locations of PGD, but was due to the effects of seismic wave propagation.

Damage to JCCP trunk lines after the 1994 Northridge earthquake was also high. Lund and Cooper (1995) reported that significant damage was sustained by 1370-mm- and 838-mm-diameter JCCP trunk lines in the Santa Clarita Valley at welded compound bends and as pullout of rubber gasket joints on long horizontal reaches. They further reported that there were fifteen to twenty major pulled joints on a 1980-mm-diameter JCCP trunk line in Simi Valley. In all cases, there is strong evidence that significant damage was caused by TGD.

In contrast, damage to JCCP trunk lines after the 1989 Loma Prieta earthquake was low (Eidinger, 1998). The significantly different performance of JCCPs when subjected to seismic wave propagation invites a systematic study on the seismic wave interaction with JCCPs, which includes studies on the typical JCCP joint characteristics, on developing both simplified and FE models to characterize the seismic body wave effects on the JCCPs with or without existing cracked joints, and on the effect of the mortar cracking strain at the joints.

## 5.4.2. JCCP Characteristics

### 5.4.2.1. JCCP Joint Details

Figure 5.12 shows representative cross-sections of pipeline joints collected from design and as-built drawings of trunk lines investigated as part of this study. There is a variety of JCCPs in service. The concrete cylinder pipe (CCP) in Figure 5.12a relies primarily on a relatively thick steel cylinder with supplemental reinforcement and protection provided by exterior and interior concrete layers. In contrast, the reinforced concrete cylinder pipe (RCCP), bar wrapped concrete cylinder pipe (BWCCP), and prestressed concrete cylinder pipe (PCCP), shown in Figures 5.12b, 5.12c, and 5.12d, respectively, utilize either circumferential steel coil or helically wrapped steel bar or prestressed circumferential steel reinforcement in addition to a relatively thin steel cylinder for structural support of internal pipe pressure. Among the varieties of JCCPs, the RCCPs and PCCPs prevail in current practices.

### 5.4.2.2. Axial Pullout Capacity Immediately after Construction

All designs and methods of construction rely on a rubber-gasket bell-and-spigot connection. The rubber gasket is often 18 to 22 mm wide when compressed to form a water-tight seal. Cement mortar is poured in the field to further seal the joint. The pullout capacity of the joint in terms of axial slip to cause leakage depends on how much movement can occur before the rubber gasket loses its compressive seal. The design and as-built drawings examined in the previous section (Figure 5.12) show that the forward end of the gasket is ideally positioned between 20 to 60 mm from a
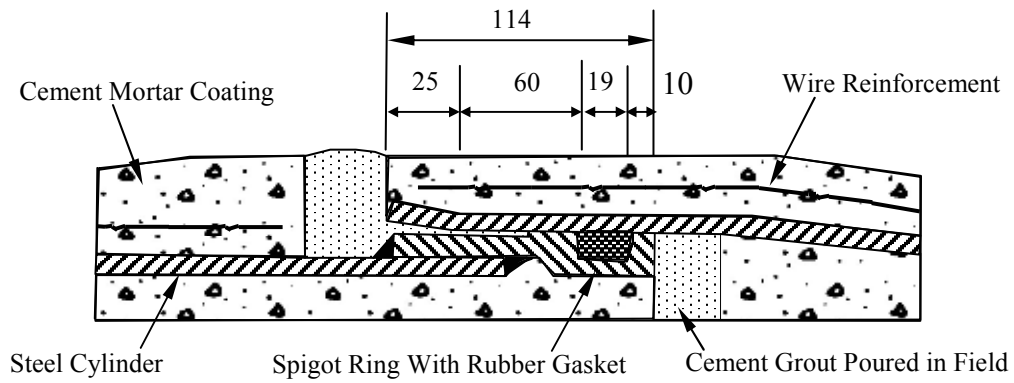
(a) Concrete Cylinder Pipe (CCP)
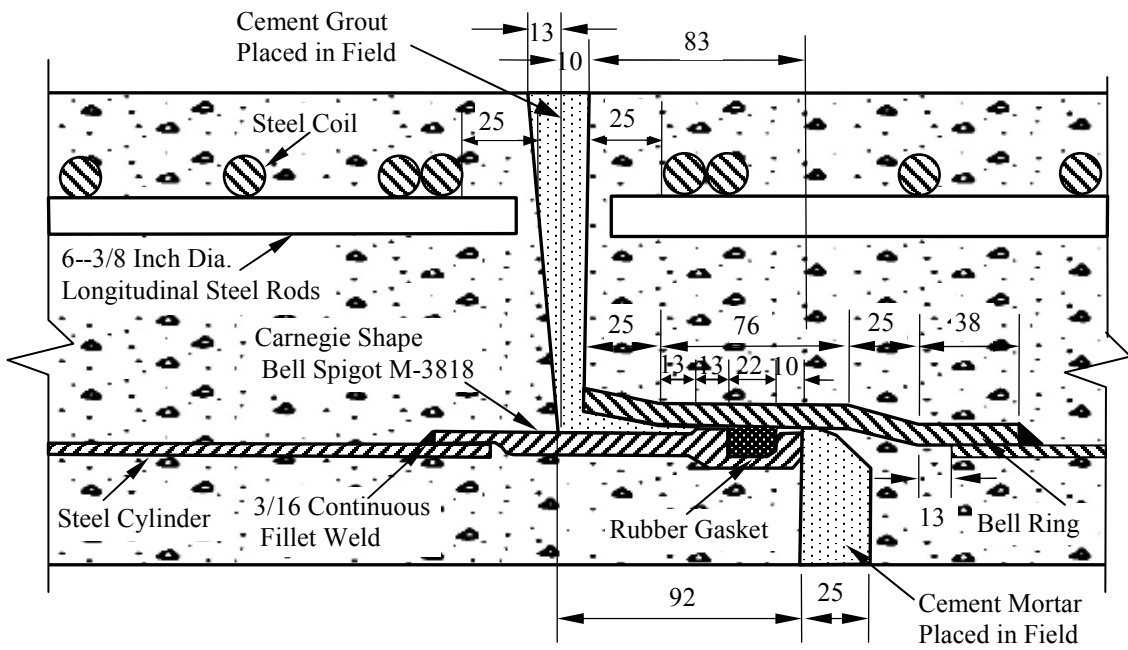


(b) Reinforced Concrete Cylinder Pipe (RCCP)

Figure 5.12.　Cross sections of Representative Joints on JCCPs (Unit: mm)

139

Figure 5.12.    (Continued)
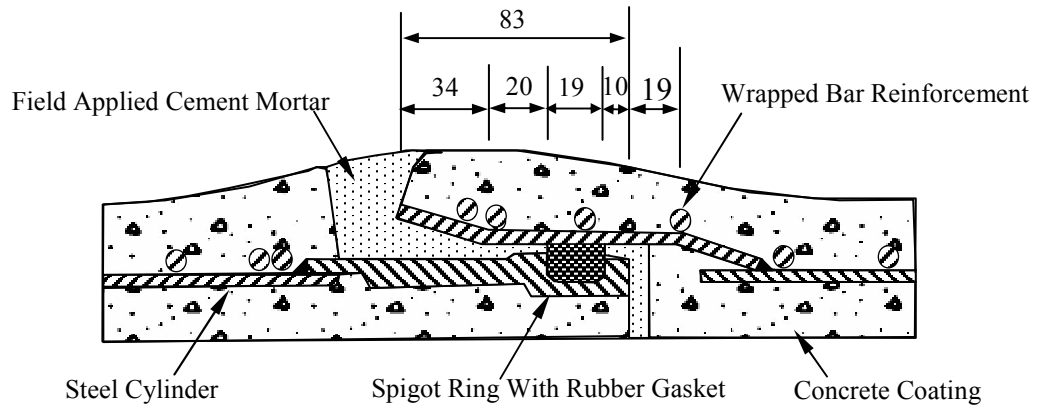


(c) Bar Wrapped Concrete Cylinder Pipe (BWCCP)
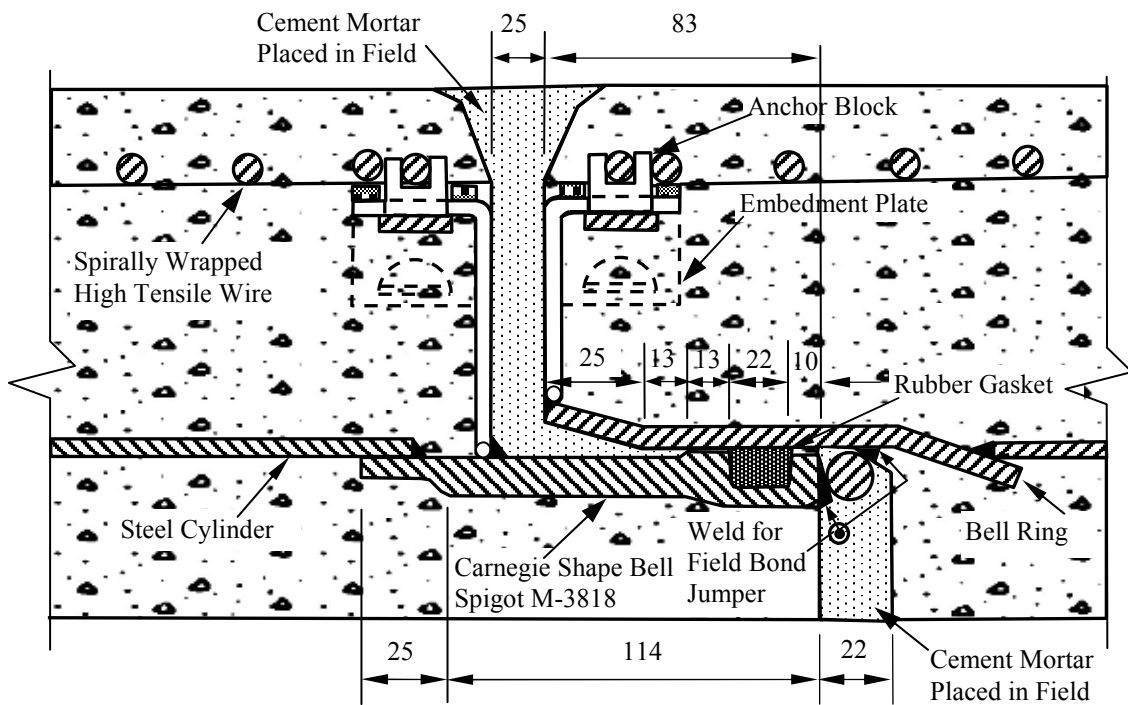


(d) Prestressed concrete cylinder pipe (PCCP)

location where the bell is angled outward away from the spigot. For RCCPs and PCCPs, the prevailing form of JCCPs, the forward end of the gasket is ideally positioned about 26 mm, and hence, approximately 26 mm of outward movement is required before the gasket starts to decompress, assuming that the gasket is positioned as shown on design and as-built drawings.

In this work, there are several different states identified with respect to joint position in RCCPs and PCCPs. Outward spigot movement of 26 mm will result in initial loss of gasket compression, and outward spigot movement of 37 mm and 48 mm will lead to significant loss of gasket compression and substantial loss of gasket compression, respectively. Significant loss of gasket compression may be associated with leakage at minor to severe levels, whereas substantial loss of gasket compression is likely to be associated with severe leakage and potentially full pullout of the joint. Figure 5.13 illustrates the various pullout states and a close-up view of the region around the gasket which the slip distances of 26, 37, and 48 mm are shown, corresponding to initial, significant, and substantial loss of gasket compression, respectively.

It is important to account for variation in the initial gasket position. As illustrated in Figure 5.13, the maximum inward position (MIP) of the spigot is about 13 mm. This MIP establishes the deepest penetration that is possible during construction. Please note that some JCCPs (e.g., Figure 5.12d) are equipped with field bond jumpers to promote electrical conductivity along the pipeline for cathodic protection. Although the bond jumpers are connected by weak tack welds that do not provide significant resistance against pullout, they might result in a MIP value as low as 6 mm.

Maximum Outward Position, MOP
Maximum Inward Position, MIP

(a) Joint detail

(b) Joint pullout capacity
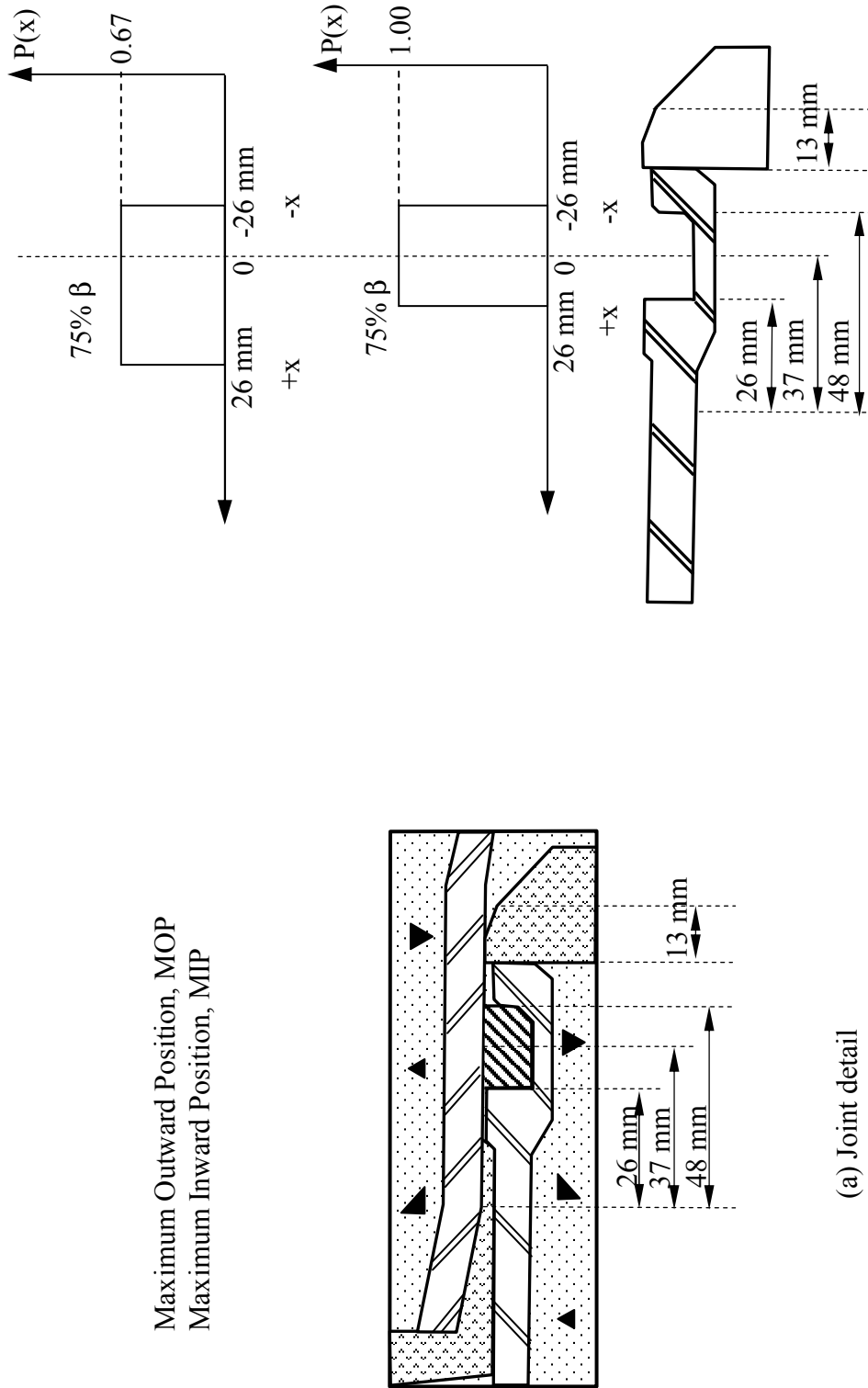
Figure 5.13. Close-up Views of Joints and Probability Density Functions for Gasket Positions

It is assumed that construction control would have resulted in initial positioning of the gasket to avoid initial loss of compression. Hence, the maximum outward position (MOP) can be selected at any location short of initial compression loss. In the model this position is treated as a parameter that can be varied.

The actual initial position of the gasket is modeled probabilistically by treating the position of the gasket as a random variable that ranges between the MIP and MOP and has the highest probability of occurring at the gasket position shown in the as-built drawings. The MIP is fixed at 13 mm.

Because the actual probability density function is not known, a beta function was selected to characterize the uncertainty with respect to joint position. Beta functions can be tailored to all joint conditions and allow for testing the sensitivity of the results to the assumed shape of the probability density function. The beta function was defined for 75%, 85%, and 95% of all candidate positions falling inside 75% of the distance from the MIP to the MOP. The beta functions for these conditions are referred to as 75%β, 85%β and 95%β. A 75%β refers to a uniform probability distribution function, whereas 85%β and 95%β correspond to distributions that are increasingly skewed towards the position of the gasket shown on the as-built drawings.

Figure 5.13 shows the beta function, 75%β, corresponding to MOP = 13 mm and 26 mm. When MOP = 13 mm, it is identical to the MIP. As a result, the probability density function is symmetrical. When MOP = 26 mm, the probability density function is asymmetrical.

A cumulative probability function, F(X), can be obtained for each beta distribution. The probability of exceedance, 1 − F(X), is plotted to evaluate the chances that the gasket position will be located beyond the as-built target location. The probabilities of exceedance are plotted for MOP = 26 mm and 75%β, 85%β and 95%β in Figure 5.14. The a and b coefficients for the beta distributions are shown in the legend.

The model for joint pullout capacity is based on the as-built dimensions of the JCCP joints. Various serviceability states are defined relative to the position of the gasket shown on the as-built drawings. The initial position of the gasket is characterized probabilistically by means of beta functions that vary from a maximum outward to a maximum inward position. The maximum values of the beta functions correspond to the as-built position of the gasket. The model accounts for the actual joint dimensions, uncertainty in the initial gasket position, and variations in the value selected for the maximum outward position of the gasket.

When the initial position of the gasket during construction is modeled by a 75%β distribution, i.e., a uniform distribution, the 90% exceedance value is the distance of the gasket inside the joint that is exceeded by nine out of ten JCCP joints, and corresponds to 3-4 mm of axial slip before initial loss of compression. Subsequent operational loads and pipeline movement, as described in next section, will subtract from this slip capacity. As a minimum, therefore, about one of every ten joints cannot reliably accommodate more than 3-4 mm of axial slip. Given this level of tolerance, JCCP joints are sensitive to seismic wave interaction, which has the potential to induce leakage and even complete disengagement of adjoining pipe sections under severe seismic motions.
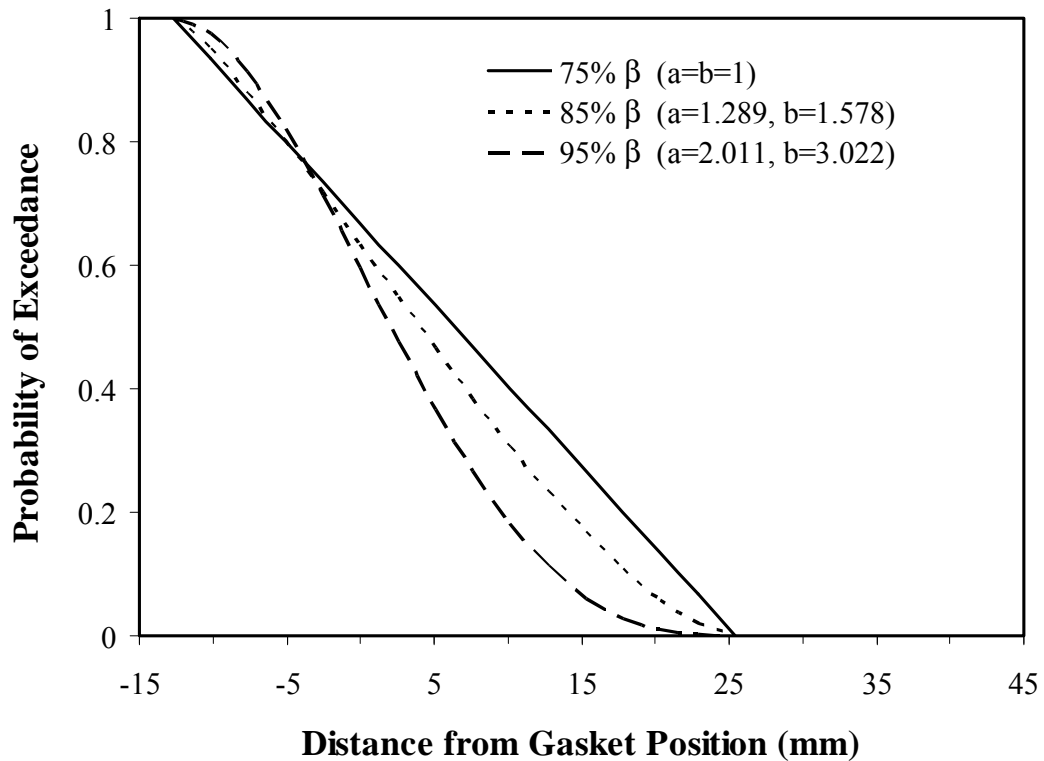
Figure 5.14.   Probabilities of Exceedance for Initial Gasket Position

with MOP = 26 mm

### 5.4.2.3.  Joint Movement after Construction and Existing Cracked Joints

Subsequent to the initial positioning of the gasket during construction, additional pullout at the joint can occur because of mortar shrinkage during curing, thrust near bends, pipe adjustment to bedding, subsidence, influence of adjacent construction, and many other factors. To provide an estimate of these types of movement, the inspection records in the JCCPs of Bay Division Pipelines (BDPLs), the major water trunk lines for the San Francisco Bay area, were examined as part of this study. The observed separations at cracked joints are summarized in Table 5.2.

Table 5.2. Summary of Observed Joint Separation in BDPLs

| BDPL Location | Length Inspcected (m) | No. of Gasket Joints | Observed Joint Separation (mm) | | | | |
|---|---|---|---|---|---|---|---|
| | | | 2 | 3 | 6 | 13 | 19 |
| BDPL2_R1 | 2147 | 514 | 0 | 3 | 1 | 0 | 0 |
| BDPL2_R2 | 3598 | 862 | 25 | 0 | 3 | 0 | 0 |
| BDPL2_R5 | 2426 | 581 | 0 | 0 | 0 | 1 | 1 |
| BDPL3_R1 | 11022 | 1760 | 0 | 0 | 12 | 0 | 0 |
| BDPL4_R1 | 13792 | 1982 | 0 | 6 | 2 | 1 | 0 |
| Totals | 32984 | 5699 | 25 | 9 | 18 | 2 | 1 |
| % Total Joints | 55/5699 = 0.98% | | 0.44 | 0.16 | 0.32 | 0.04 | 0.02 |

Table 5.2 lists various inspection reaches of the JCCPs for which documentation in the inspection records can be found. Five inspection reaches along 3 different JCCPs, i.e., BDPL2, 3, and 4, with a total length of about 33 km and 5699 gasket joints are included in Table 5.2. The observed joint separations are listed by aggregating the number of observations at the maximum observed separation. For example, when the separations at several joints were reported as being less than or equal to a particular dimension, the number of observed separations are listed under the maximum recorded dimension. Although this method of reporting the available data is conservative, it is warranted because the inspection records are infrequent and are performed under conditions where access is limited and only approximate estimates of separation are acquired.

Table 5.2 shows that about 1% of the joints, 55 joints over 5699 joints in about 33 km JCCPs, are cracked and separated with a maximum separation up to 19 mm. Comparing with the as-designed capacity of 20 mm to 60 mm with a typical value of 26 mm, only small additional joint displacement is required to cause pullout at these existing cracked joints when subjected to seismic body waves.

146
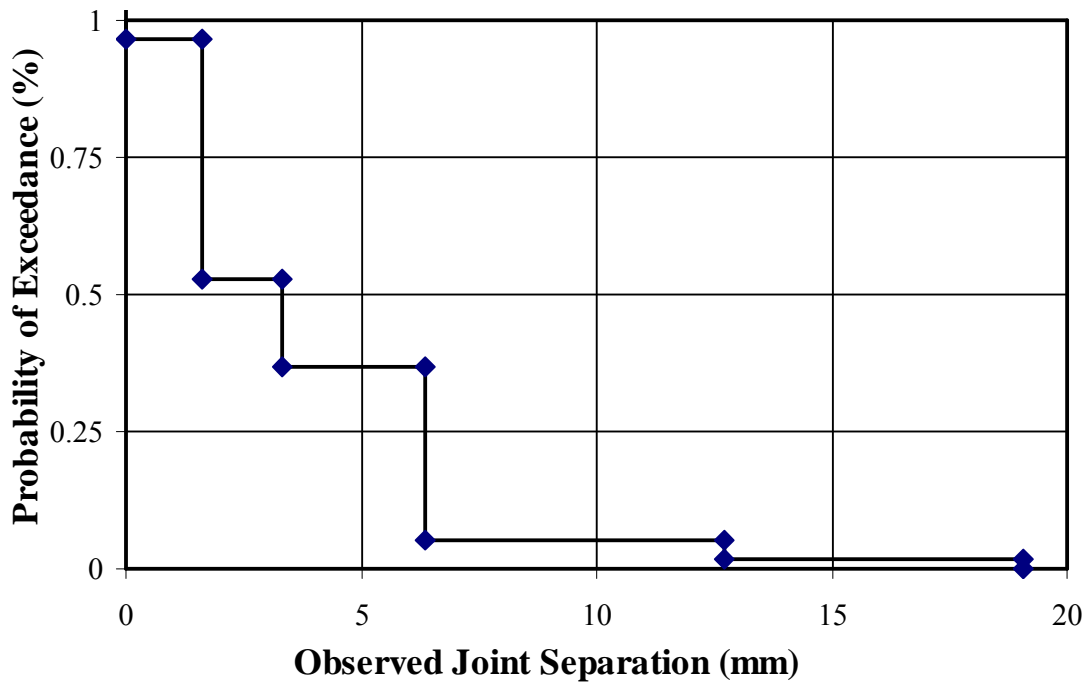
Figure 5.15.    Subsequent Field Displacement Exceedance Probability

The data in Table 5.2 are plotted in terms of probability of exceedance with respect to observed separation during inspection, as shown in Figure 5.15. These data can be used in conjunction with the probability of exceedance plots for the initial gasket position discussed in Section 5.4.2.2 (see Figure 5.13). Because the initial gasket position and subsequent outward slip are independent random variables, the probability of encountering the gasket at a distance y from the as-built location is given by

$$P(Y > y) = \sum_{j=1}^{6} P(X_i > y - x_{sj})P(X_s = x_{sj}) \qquad (5.16)$$

in which $X_i$ is the initial gasket position, $X_s$ is the subsequent slip after construction, and $x_{sj}$ is a discrete subsequent slip value for $X_s$, taken as 0, 2, 3, 6, 13, and 19 mm for j equals 1 to 6, respectively.

When the probability of initial position is combined with the probability of subsequent slip, the probability of exceedance is computed as illustrated in Figures 5.16 and 5.17. Figure 5.16 is obtained by combining the 75%β probability of exceedance in Figure 5.14 with Figure 5.15 in accordance with Eqn. 5.16. Because the field inspection records show that subsequent slip occurs in a very low percentage of the joints, the effect of slip after construction is rather small and relegated to the tail portion of the plot, as shown in Figure 5.17.

*5.4.2.4. Axial Tensile Resistance*

The axial tensile resistance of the joint depends on the tensile strength of the poured mortar connection, which is relatively low, and pullout resistance of the gasket, which is much lower compared with the tensile strength of mortar and can be ignored practically. In other words, the pullout capacity of the joints relies on the tensile behavior of the cement mortar at the joints. Figure 5.18 shows a typical stress strain relationship for mortar under tension. The mortars experience a brittle failure immediately after the peak, before which the tensile stress increases almost linearly as the tensile strain increases. The cracking strain, $\varepsilon_T$, varies typically between $0.5 \times 10^{-4}$ and $1.5 \times 10^{-4}$ (Avram et al., 1981; and Carino, 1974). For modeling purposes, the stress strain relationship can be simplified as linearly elastic behavior before the peak and no tensile strength after the peak, as shown by the dash lines in Figure 5.18. Please note that the $\varepsilon_T$ is relatively low and the axial tensile strain generated by the seismic body waves (i.e., $\varepsilon_p = V_a/C_a$, which can be up to $4 \times 10^{-4}$) is sufficient to crack the mortars as the seismic body waves propagate.
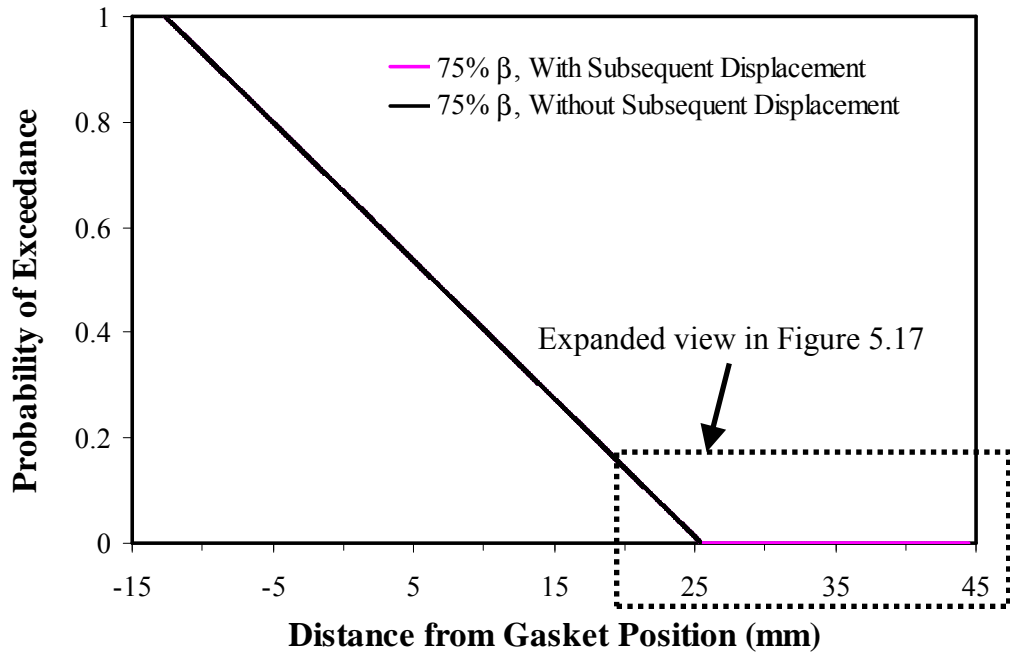
Figure 5.16.   Probability of Exceedance for Combined Initial Position and

Subsequent Slip
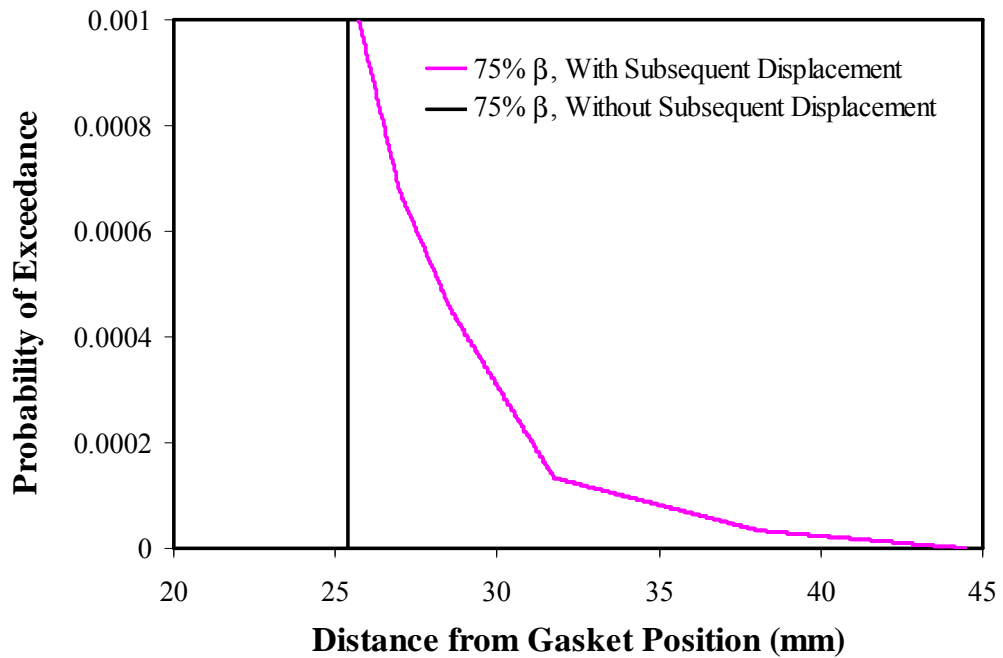


Figure 5.17.   Expanded View of Probability of Exceedance for the Tail Portion of

Figure 5.16
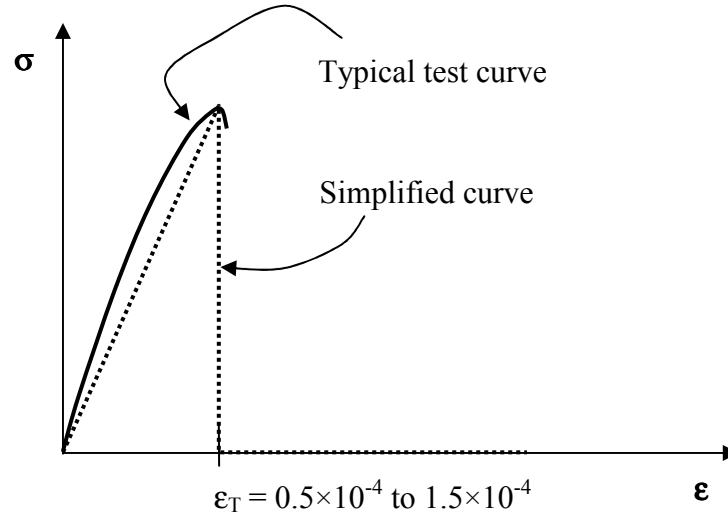
Figure 5.18. Typical Stress Strain Relationship for Mortars under Tension

### 5.4.3. Simplified Model for JCCPs with Existing Cracked Joints

When seismic body waves propagate along the axial direction of the pipes, ground strain, $\varepsilon_g$, is generated along axial direction of the pipes, as defined by Eqn 5.3. As described in the Section 5.3, when affected by seismic body waves, water trunk lines, including JCCPs, behave as flexible pipes and $\varepsilon_p = \varepsilon_g$ everywhere the pipe is continuous. Therefore, $\varepsilon_p = \varepsilon_g$ everywhere along the JCCPs except in the vicinity of the cracked joints, if there is any. If the maximum pipe strain, $\varepsilon_{pmax}$, is smaller than the tensile cracking strain of mortar, $\varepsilon_T$, no additional cracked joint occurs, and relatively joint displacement only occurs at the existing cracked joints. On the other hand, when $\varepsilon_{pmax} \geq \varepsilon_T$, the mortar at joints may be cracked and the pipe transfers from a continuous pipe to a segmented pipe as the seismic body waves propagate along the pipe. Simplified and FE models for the seismic body wave interaction with JCCPs containing existing cracked joints for the case of $\varepsilon_{pmax} < \varepsilon_T$ are presented in this

section and Section 5.4.4, respectively; while a simplified model for the case of $\varepsilon_{pmax} \geq$ $\varepsilon_T$ is described in Section 5.4.5.

Figure 5.19 illustrates seismic displacement and ground strain interaction with a JCCP with an existing cracked joint. As discussed previously, joints in the field are occasionally cracked and separated because of mortar shrinkage during curing, thrust near bends, pipe adjustment to bedding, subsidence, influence of adjacent construction, and many other factors. Such joints, being cracked and separated, have such low axial pullout resistance that for modeling purposes can be taken as negligible. Please note that in Figure 5.19 the ground strain at vertical axis, $\varepsilon_g$, is expressed as $V_a/C_a$, while the distance along the pipeline at horizontal axis, X, is expressed as the product of wave propagation time, t, and $C_a$. Joint displacement during wave interaction is a consequence of variable pullout resistance among the joints in the pipelines.

It is assumed that the joints on either side of the cracked joint have full mortar connectivity to mobilize tensile capacity across the joint. Because the pipeline is fully flexible, $\varepsilon_p = \varepsilon_g$ everywhere the pipeline is continuous. At the cracked joint, the pipeline cannot sustain strain, so $\varepsilon_p = 0$. As the wave passes across the cracked joint, strain in the continuous pipeline on each side of the joint will accumulate linearly at a slope of f/EA until $\varepsilon_p = \varepsilon_g$, after which pipe and ground strain are indistinguishable. The shaded area in Figure 5.19 represents the integration of the differential strain between the pipeline and ground from the cracked joint to the positions in the pipe where no relative displacement occurs between the pipe and the soils. The integration equals to the sum of the relative displacement at both ends of the cracked joint with respect to the soil at the cracked joint, or the relative joint displacement at the cracked
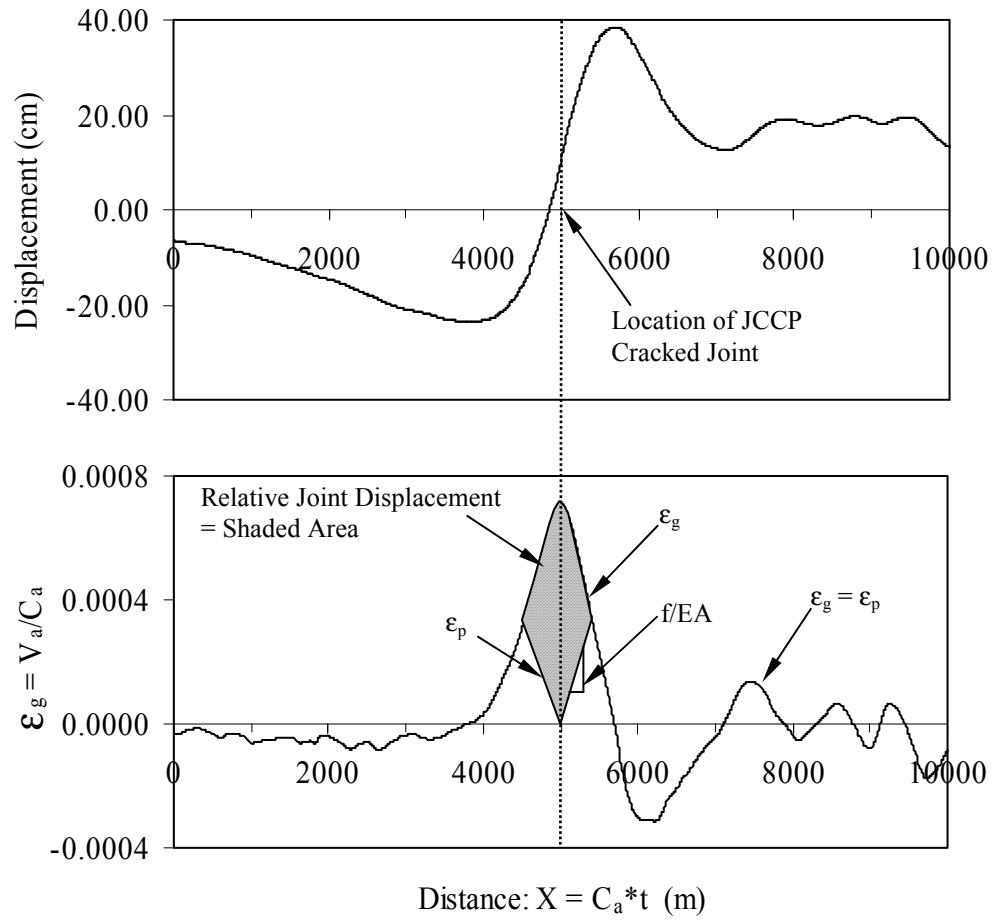
Figure 5.19. Seismic Displacement and Velocity Interaction with JCCPs with

Existing Cracked Joint

joint, which in this case occurs as axial slip.

As illustrated in Figure 5.20, the area between the $\varepsilon_p$ and $\varepsilon_g$ versus distance plots can be approximated as the area of two right triangles to provide a simplified expression for relative joint displacement, $\delta_j$, as

$$\delta_j = \left[\frac{V_{ap}}{C_a}\right]^2 \frac{EA}{f} \tag{5.17}$$

$V_a/C_a$

$V_{ap}/C_a$

Relative Joint Displacement
$\approx$ Shaded Area

$$\approx \frac{V_{ap}}{C_a}\left(\frac{EA}{f}\frac{V_{ap}}{C_a}\right)$$

$$=\left(\frac{V_{ap}}{C_a}\right)^2\frac{EA}{f}$$

f/EA

X
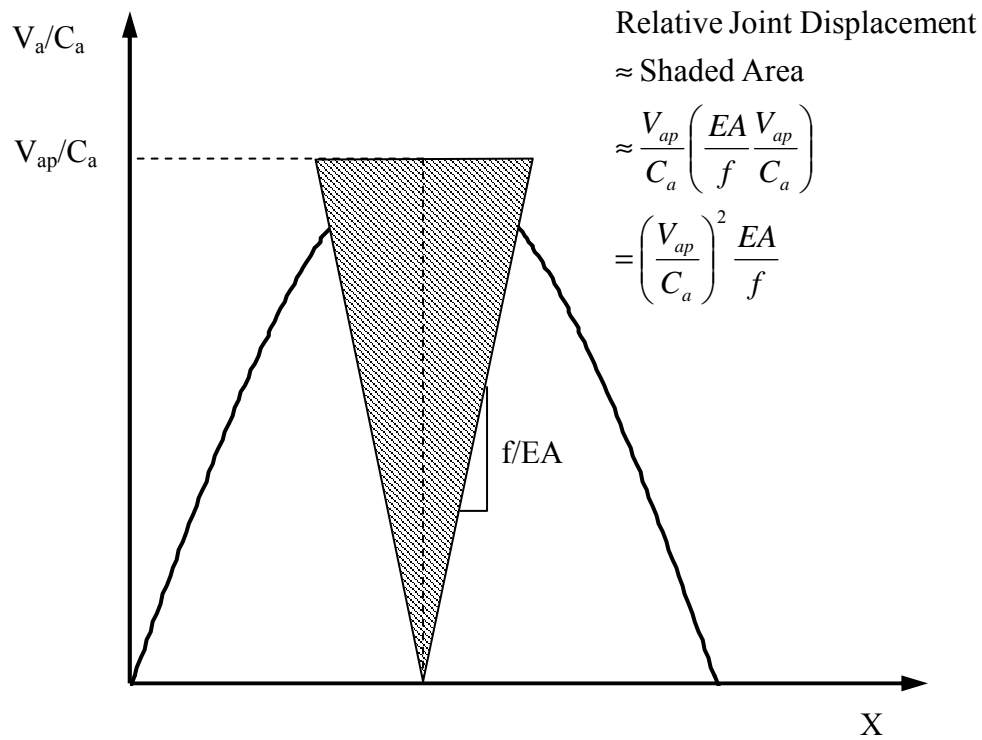
Figure 5.20.   Simplified Model for Seismic Wave Interaction with JCCPs

Eqn 5.17 indicates that the relative joint displacement at cracked joints increases proportionally to $V_p^2$, which is consistent with the regressions developed by O'Rourke et al. (2001) and O'Rourke et al. (2004b) according to water pipeline performance records during the 1994 Northridge earthquake. The regression analyses show the repair rate for the water pipelines increases approximately proportionally to $V_p^a$, where parameter a ranges from 1.82 to 2.42 for the pipelines composed of different materials.

It should be pointed out that relative joint displacement obtained is a conservative estimation corresponding to the worst case scenario. It is assumed that the joints on either side of the cracked joint remain integrity to mobilize tensile capacity across the joint. However, the existing cracked joints in the fields are

distributed stochastically, and therefore, it is possible for multiple cracked joints to occur within a distance that is necessary for pipe strain accumulation to reach $\varepsilon_p = \varepsilon_g$. As the number of cracked joints increases, relative joint displacement decreases (please refer to Section 5.4.6).

### 5.4.4. Finite Element Model for JCCPs with Existing Cracked Joints

FE model for seismic body wave interaction with JCCPs containing existing cracked joints is developed, using the program BSTRUCT (Chang, 2006; and Goh and O'Rourke, 2000). The FE model is similar to that described in Section 5.3.2.

#### 5.4.4.1. FE Analysis Setup

Figure 5.21 shows a schematic of the FE model, similar to Figure 5.6. The pipeline was modeled with beam column elements that were connected to the ground by spring-slider elements capable of representing shear transfer as an elasto-plastic process. The existing cracked joint on the JCCP was also modeled with a spring-slider element representing a brittle failure mode of mortar (Figure 5.18). Time histories of strong motion recorded for the 1994 Northridge earthquake were converted to displacement versus distance records by assuming that $X = C_a t$, in which X is distance, t is time from the strong motion recording, and $C_a$ is calculated from Eqn 5.1 with C equal to 2.5 km/sec. The bilinear relationship between f and relative pipe-soil displacement shown in Figure 5.7 is utilized to characterize the spring-slider elements. Figure 5.22 shows the pullout force and joint displacement relationship adopted for the existing cracked joint. The pullout force at the existing cracked joint, $P_u$, is generally taken as low as 1 kN, while the corresponding displacement is taken as low as 0.01
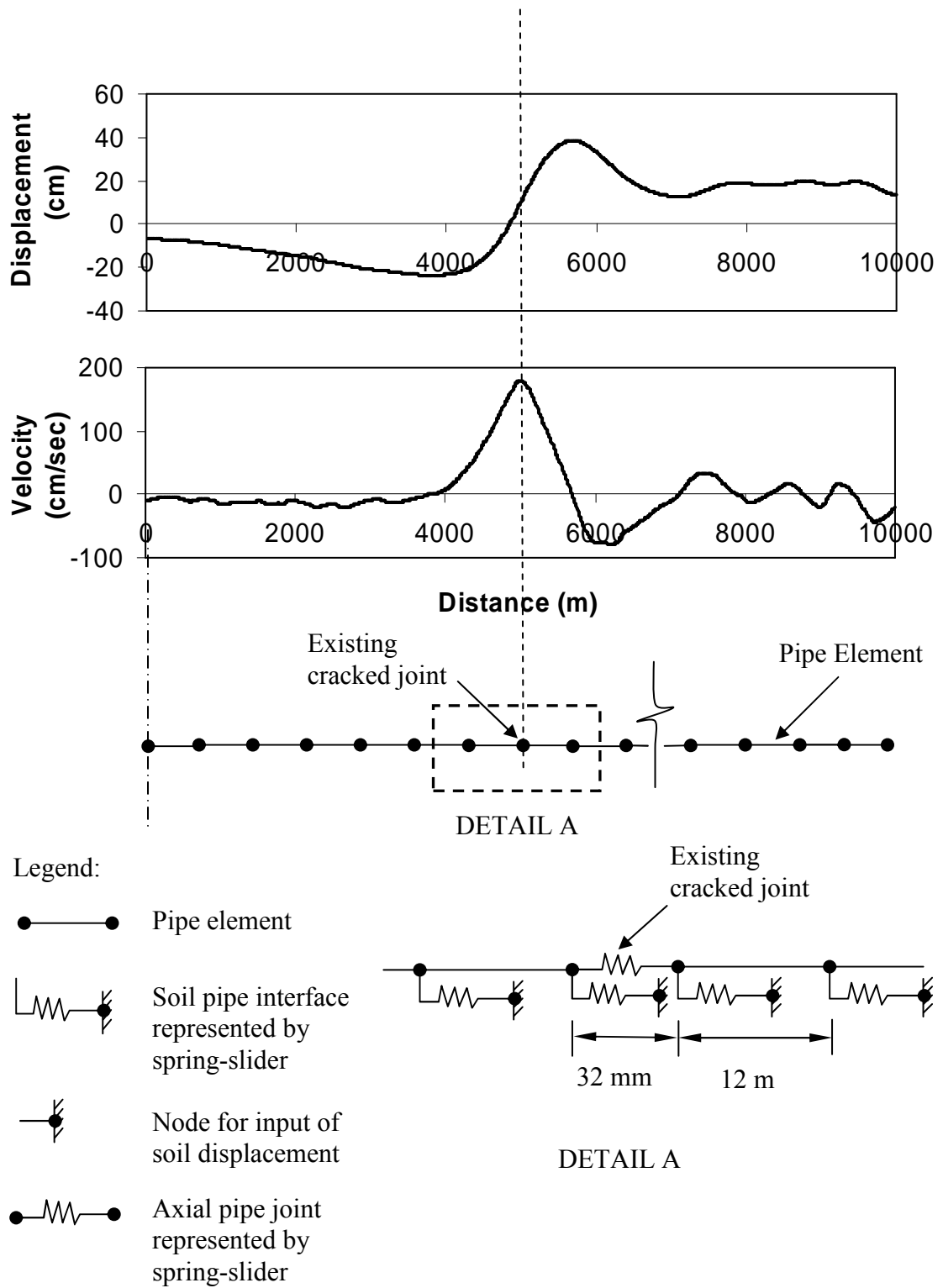
Figure 5.21.   Finite Element Model for JCCPs with Existing Cracked Joints

155
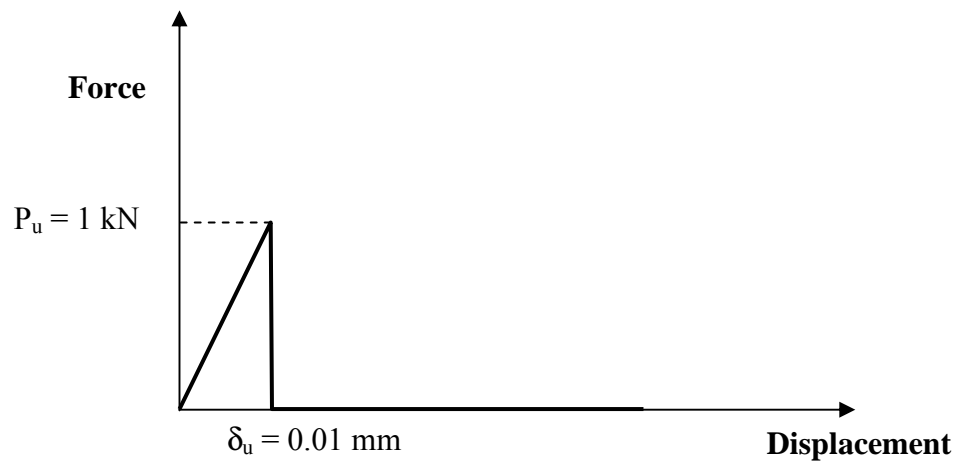
Figure 5.22.   Pullout Force and Joint Displacement Relationship for Existing Cracked

Joints

mm. As illustrated in Figure 5.21, when the maximum slope of the displacement

versus distance record (corresponding to $V_{ap}$ in the velocity record) was superimposed

on the cracked pipeline joint, the maximum axial slip of the joint occurred.

*5.4.4.2.  FE Analysis Example*

The FE analysis was used to evaluate seismic body wave interaction with a

1370-mm-diameter PCCP trunk line in Santa Clarita Valley during the 1994

Northridge earthquake, where there is documented evidence of multiple joint pullouts.

Figure 5.23 shows the shear waves intersect a section of pipeline oriented at N25W,

where the joint pullouts were documented, with an incidence angle of 63° and $V_p$ =

119 cm/sec. The strong motion recording at Newhall Station, approximately 4.0 km

from this section of pipeline, was resolved in the direction of the pipeline and used in

the analysis. Since the direction of $C_a$ is in the opposite direction as the polarity, or
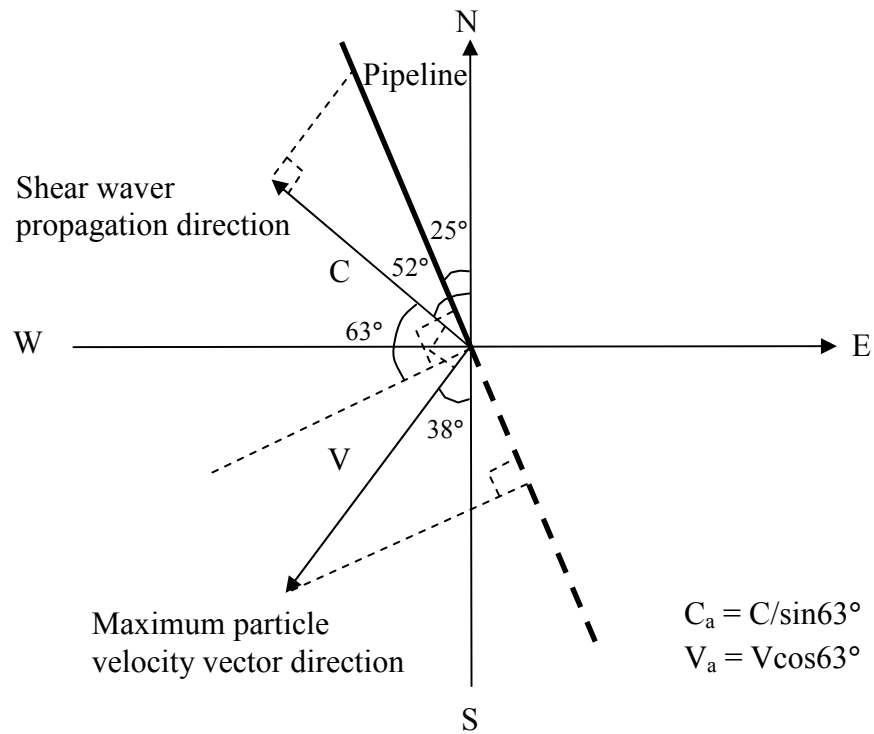
Figure 5.23.   Shear Wave Record at Newhall Station Intersect a Section of Pipeline

Oriented at N25W

direction of $V_a$, the longitudinal strain imposed on the pipe is tensile, resulting in the potential pull-out at the existing cracked joint.

The pipeline was assumed to be buried at a depth of 1m to the top of pipe in sand with unit weight, $\gamma = 18.9$ kN/m$^2$, and angle of shearing resistance $\phi' = 35°$. It was further assumed that the interface friction angle, $\delta$, between soil and pipe is $\delta = \phi'$. The finite element model was composed of 200 pipe elements and 203 spring-slider elements over a distance of 11 km for an element length of 56 m. The length of the element is consistent with the time intervals, i.e., 0.02 sec, of the strong motion time history used in the analysis

The FE results are presented in Figure 5.24. Figure 5.24a shows the maximum relative joint displacement, which represents pullout for the field condition of wave propagation at this site. The maximum analytical pullout is 9.1 mm, which is distributed somewhat asymmetrically either side of the cracked joint to reflect the slightly asymmetric shape of the ground strain pulse. Figure 5.24b shows the pipe and ground strains on the same plot. It can be seen that, away from the cracked joint, $\varepsilon_g = \varepsilon_p$, as the characteristic of a flexible pipeline. The area between the $\varepsilon_g$ and $\varepsilon_p$ plots in the vicinity of the cracked joint represents the relative joint displacement.

When accounting for a typical as-designed capacity of 25 mm with a 90% exceedance capacity of 3-4 mm (please refer to Section 5.4.2.2), and subsequent operational loads and pipeline movement (please refer to Section 5.4.2.3), the predicted displacement is consistent with pullout of sufficient magnitude to cause leakage and occasional disengagement of the pipeline, as observed in the field.

### 5.4.4.3. Parametric Studies

The FE model was used to simulate seismic wave interaction for various ground conditions, pipeline properties, and seismic body wave characteristics. Table 5.3 summarizes the parameters adopted in the FE analysis. The ground conditions studied included clay with undrained strength from 1 to 200 kPa, saturated or dry sands with various friction angles from 25° to 45°. Four pipelines with various diameter and wall thickness were modeled and the axial deformation stiffness, EA, of the three of them was varied intentionally to study the effect of EA. The parameters characterizing the seismic body waves included $V_{ap}$ (177 cm/sec or 150 cm/sec), $C_a$ (1000 to 3000 m/sec), and T (1 sec or 1.5 sec). Similar FE analyses for the effects of
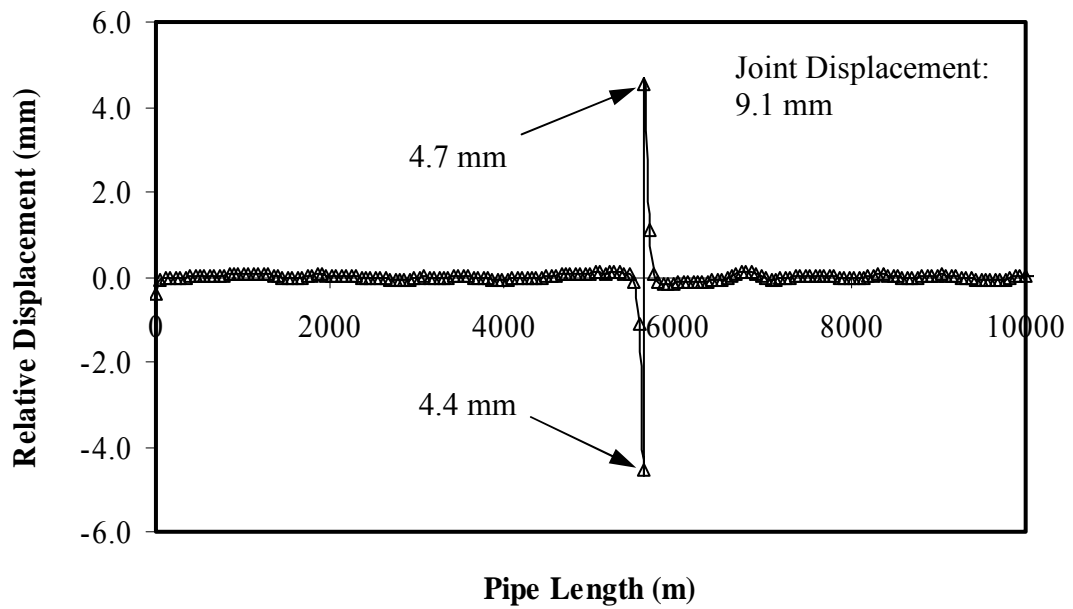
(a) Ground-pipeline Relative Displacement
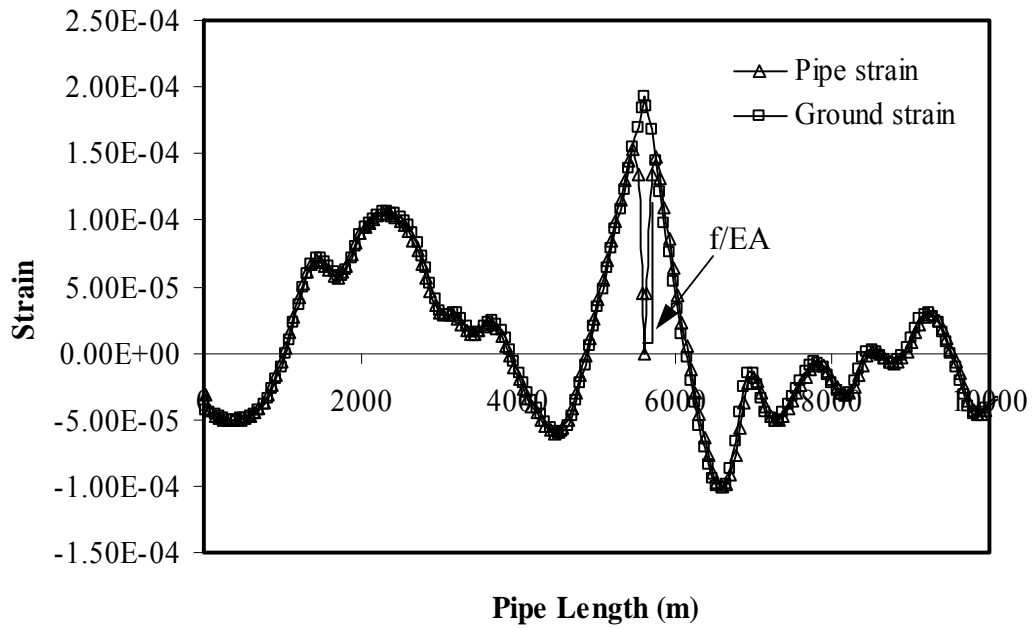


(b) Ground and Pipe Strains

Figure 5.24. FE Results for PCCP in Santa Clarita Valley Subjected to 1994
Northridge Earthquake

159

Table 5.3.  Summary of FE Modeling Parameters Characterizing Seismic Wave Interaction with JCCPs with Existing Cracked Joints

| | |
|---|---|
| **Ground Conditions** | Clay With Undrained Strength $S_u$: 1~200 kPa<br><br>Dry Sand With Friction Angle f: 25°~43°<br><br>Saturated Sand With Effective Friction Angle $\phi'$: 35° |
| **Pipeline Properties** | 1370-mm Diameter and 146-mm wall thickness Pipe With Axial Deformation Stiffness EA: $1.87 \times 10^7$ kN<br><br>1829-mm Diameter and 178-mm wall thickness Pipe With Axial Deformation Stiffness EA: $1.97 \times 10^6 \sim 6.29 \times 10^9$ kN<br><br>1981-mm Diameter and 146-mm wall thickness Pipe With Axial Deformation Stiffness EA: $3.25 \times 10^5 \sim 3.25 \times 10^9$ kN<br><br>2438-mm Diameter and 216-mm wall thickness Pipe With Axial Deformation Stiffness EA: $3.12 \times 10^6 \sim 4.99 \times 10^{10}$ kN |
| **Seismic Body Wave Characteristics (Sinusoidal Wave)** | Peak Particle Velocity Along Pipe Axial Direction $V_{ap}$: 150 cm/sec or 177 cm/sec<br><br>Wave Propagation Velocity Along Pipe Axial Direction $C_a$: 1000 ~ 3000 m/sec<br><br>Predominant Period T: 1 sec or 1.5 sec |
| **Seismic Surface Wave Characteristics (Sinusoidal Wave)\*** | Peak Particle Velocity $V_p$: 10 ~ 60 cm/sec<br><br>Phase Velocity C: 50 ~ 2500 m/sec<br><br>Predominant Period T: 1 ~ 20 sec |

\*: Please refer to Shi (2006) for details

seismic surface waves on JCCPs were performed by Shi (2006). The parameters used by Shi (2006), which include $V_p$ from 10 to 60 cm/sec, C from 50 to 2500 m/sec, and T from 1 to 20 sec, were also summarized in Table 5.3. In total, 320 FE runs were performed to account for different combinations of ground conditions, pipeline properties, and seismic body wave and surface wave characteristics.

### 5.4.4.4. Universal $\delta_j/\delta_0$ and f/EAR Relationship

The finite element results are summarized in Figure 5.25 with two dimensionless parameters, $\delta_j/\delta_0$ and f/EAR. $\delta_0$ is defined as the area under the seismic sinusoidal ground strain pulse and can be calculated by

$$\delta_0 = \int_0^{\lambda/2} \frac{V_{ap}}{C_a} \sin(\frac{2\pi x}{\lambda}) dx \tag{5.18}$$

When combined with Eqn 5.8, $\delta_0$ can be expressed as

$$\delta_0 = \frac{V_{ap}T}{\pi} \tag{5.19}$$

The dimensionless parameter, $\delta_j/\delta_0$, is the relative joint displacement normalized with respect to a displacement index of the seismic wave characteristics. The dimensionless parameter, f/EAR, represents a combination of key ground conditions, pipeline properties, and seismic wave characteristics, and determines whether the pipelines behave as flexible or rigid pipes, as described in Section 5.3.
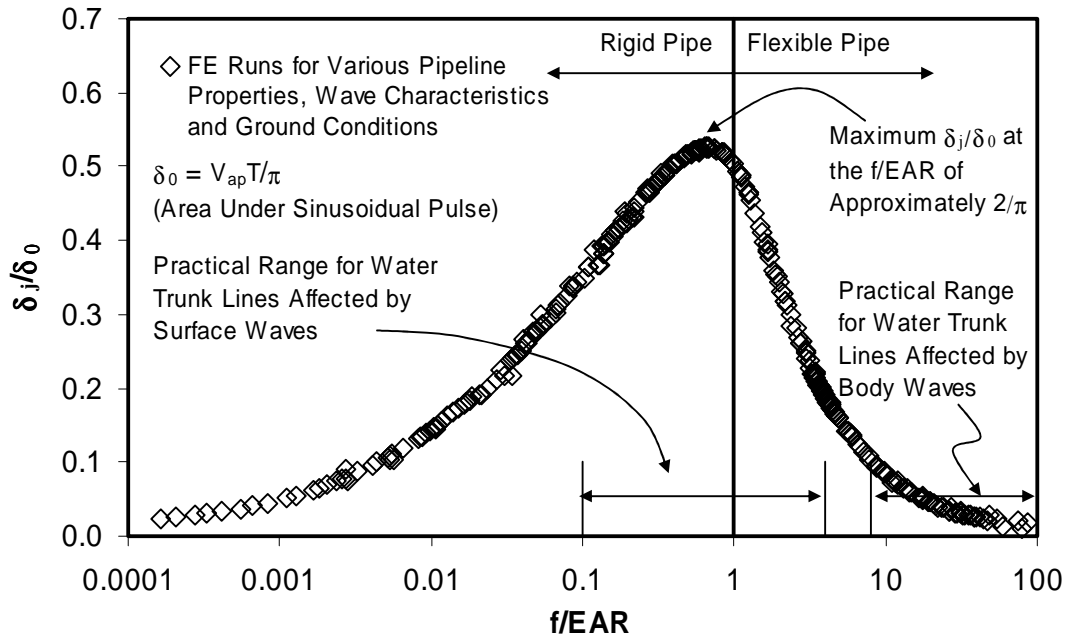
Figure 5.25.   Universal Relationship between $\delta/\delta_0$ and f/EAR

Figure 5.25 shows the relationship between $\delta_j/\delta_0$ and f/EAR based on the results from 320 FE simulations. When f/EAR is greater than 100 or less than 0.001, $\delta_j/\delta_0$ approaches 0. The $\delta_j/\delta_0$ increases to a maximum at f/EAR of approximately $2/\pi$, after which it decreases to zero at f/EAR of 100. Practical ranges of f/EAR for water trunk lines affected by seismic body waves, as well as those by seismic surface waves (Shi, 2006), are shown in Figure 5.25. Water trunk lines tend to behave as relatively flexible pipelines when affected by body waves, and act as relatively rigid pipelines when affected by surface waves.

With known ground conditions, pipeline properties, and seismic wave characteristics, f/EAR and $\delta_0$ can be calculated and joint displacement $\delta_j$ can be estimated directly using Figure 5.25. Consider, for example, a JCCP with 1575-mm diameter and 157-mm wall thickness subjected to a near source velocity pulse with $V_p$

= 150 cm/sec, C = 2500 m/sec, and T = 1sec. The pipeline is oriented with an incidence angle $\gamma_i$ = 45° with respective to seismic wave propagation direction and is buried at a depth of 1.86 m to the center of pipeline in soil with unit weight $\gamma$ = 18.8 kN/m$^3$ and friction angle $\phi'$ = 35°, which is assumed equal to the pipe-soil interface friction angle, $\delta$. The EA, R, f, and $\delta_0$ are calculated as $2.7 \times 10^7$ kN, $3.4 \times 10^{-7}$ m$^{-1}$, 103.9 kN/m, and 333 mm, respectively, resulting in f/EAR = 11.3. Using Figure 5.25, $\delta_j/\delta_0$ is estimated as 0.072, and the relative joint displacement, $\delta_j$, is about 24 mm.

## 5.4.5. Simplified Model for JCCPs without Existing Cracked Joints

Sections 5.4.3 and 5.4.4 describe the simplified and FE models for JCCPs with existing cracked joints when $\varepsilon_{pmax} < \varepsilon_T$ and relative joint displacement only occurs in the vicinity of the cracked joints. When $\varepsilon_{pmax} < \varepsilon_T$ occurs in a JCCP without existing cracked joints, the JCCP is a continuous pipe and deforms coincidently with the ground, and hence, no relative joint displacement occurs. The section proposes a simplified model for JCCPs without existing cracked joints but with a $\varepsilon_{pmax} \geq \varepsilon_T$. The continuous JCCPs without existing cracked joints may crack at joints as a result that $\varepsilon_{pmax}$ induced by seismic body waves exceeds the $\varepsilon_T$ at the joints. The cracking of joints transforms the pipeline from a continuous structure to a segmented one. Therefore, geometric nonlinearity has to be accounted for in the modeling.

### 5.4.5.1. Seismic Body Wave Propagation along JCCPs

Figure 5.26 illustrates seismic ground strain by body wave interaction with a continuous JCCP without existing cracked joints. Each part of Figure 5.26 shows the ground strain, $\varepsilon_g$, expressed as $V_a/C_a$, plotted on the vertical axis. The horizontal axis

(a) Seismic wave interaction with pipeline (Overview)

(b) Seismic wave interaction with pipeline ($t = t_1$)

(c) Seismic wave interaction with pipeline ($t = t_2$)

(d) Seismic wave interaction with pipeline ($t = t_3$)

(e) Seismic wave interaction with pipeline ($t = t_4$)
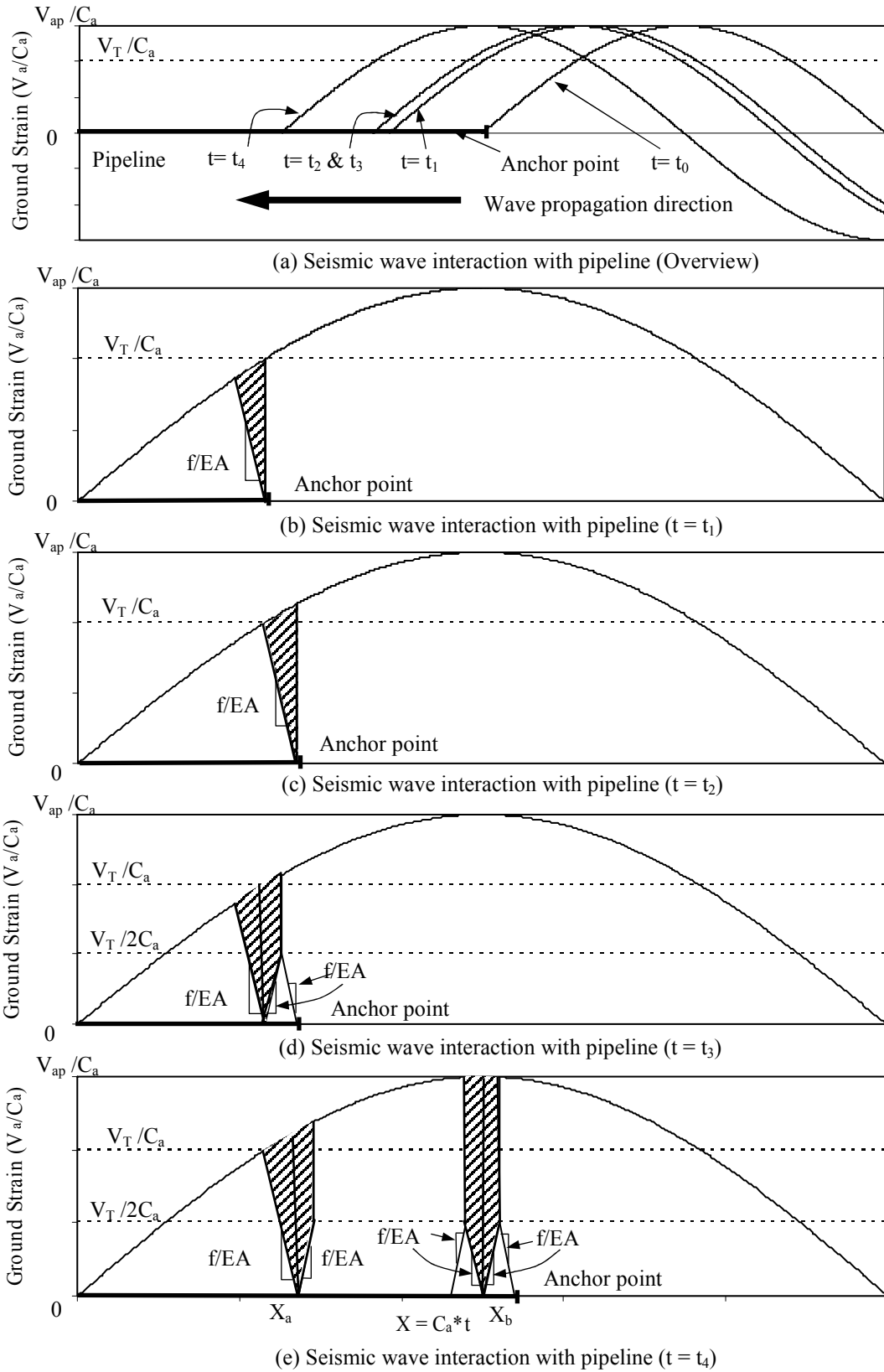
Figure 5.26. Seismic Wave Interaction with JCCPs Without Existing Cracked Joints

is the distance, X, along the longitudinal axis of the JCCP. The distance is expressed as the product of the wave propagation velocity, $C_a$, and the wave propagation time, t. The velocity pulse shown in Figure 5.26 corresponds to half of a sinusoidal wave, and develops tensile strains in the ground. It is assumed that no joint is cracked before the seismic wave interaction and the JCCP joints have full mortar connectivity so that the tensile capacity of each joint is mobilized.

Figure 5.26a shows the progression of a seismic wave at various times, $t_0$ through $t_4$, as it approaches and moves into the ground surrounding a JCCP that terminates at an anchor point. Because the pipeline is flexible, $\varepsilon_g = \varepsilon_p$ everywhere on the pipeline until $t_1$, when the first joint next to the anchor point reaches its tensile strain capacity, $\varepsilon_T = V_T/C_a$, and cracks (Figure 5.26b). The threshold velocity, $V_T$, is the velocity that generates ground strain equal to the tensile strain capacity of the pipeline joint. A joint, which is cracked and separated, has very low axial pullout resistance that for modeling purpose can be taken as negligible. At the cracked joint, the pipeline cannot sustain strain, so $\varepsilon_p = 0$. As the wave passes across the cracked joint, the strain in the continuous pipeline on the downstream side of that joint will accumulate linearly at a slope of f/EA until $\varepsilon_p = \varepsilon_g$, after which pipe and ground strain are indistinguishable and no relative displacement occurs between the pipe and soils. On the upstream side, the pipeline is anchored so that the pipe and ground move together.

The shaded area in Figure 5.26b represents the integration of the differential strain between the pipeline and ground from the cracked joint to the position in the pipe where no relative displacement occurs between the pipe and the soil, which equals the relative joint displacement and occurs as axial slip. In a similar fashion, the

165

shaded areas in the subsequent figures represent relative joint displacement or axial slip. As the seismic wave propagates, another joint downstream of the first cracked joint is also subjected to its tensile strain limit at $t_2$ (Figure 5.26c). The distance between these two joints, L, can be determined by:

$$L = \frac{V_T EA}{C_a f} \tag{5.20}$$

The joint cracks when its tensile strain capacity is exceeded (Figure 5.26d) at $t_3$, which occurs immediately after $t_2$. Since the pipeline strain at the newly cracked joint is zero, the strain in the continuous pipeline on the downstream side of that joint will accumulate linearly from $\varepsilon_p = 0$ to $\varepsilon_p = \varepsilon_g$ at a slope of f/EA. On the upstream side of the cracked joint, the pipeline segment between the two cracked joints must have zero strain at each cracked end. To satisfy equilibrium, the strain will accumulate linearly from both ends at the same slope of f/EA, but in opposite directions, until $\varepsilon_p = \varepsilon_T/2$ at the midpoint of L, where shear transfer between the pipe and soils reverses to its opposite direction and no relative displacement occurs between the pipe and soil. The relative joint displacement in the newly cracked joint at $t_3$ is the sum of the relative displacement at both ends of the cracked joint with respect to the soils at the location of the cracked joint, as indicated by the shaded area in Figure 5.26d. With continued wave propagation, the next joint will crack at a distance, L, downstream of the previously cracked joint (Figure 5.26e). This process repeats itself as the wave moves forward along the pipeline. The cracking of joints transforms the pipeline from a continuous structure to a segmented one.

## 5.4.5.2. *Relative Joint Displacement*

The two most critical cases for relative joint displacement are illustrated in Figure 5.26e. The relative joint displacement attains its first local maximum at $X_a$ just before another joint downstream of $X_a$ cracks. The joint displacement, $\delta_a$, can be calculated from the shaded area on the left of Figure 5.26e. The shaded area on the right of Figure 5.26e at $X_b$ illustrates the second possible maximum joint displacement, $\delta_b$. This movement occurs when the peak ground velocity, $V_p$, passes across the upstream end of the cracked pipeline. The maximum relative joint displacement is the larger of the two possible joint displacements.

Figure 5.27 illustrates a simplified procedure for calculating the shaded areas in Figure 5.26e. The relative joint displacement for the first potentially maximum case, $\delta_a$, can be decomposed into four area components

$$\delta_a = A_1' + A_2' + A_3' + A_4' \tag{5.21}$$

in which the subscripts of A' correspond to the triangles or rectangle at $X_a$, the areas A'$_1$, A'$_2$, A'$_3$, and A'$_4$, are calculated as

$$A'_1 = \frac{1}{2}\left(\frac{V_T}{C_a}\right)^2 \frac{EA}{f} \tag{5.22}$$

$$A'_2 = \frac{9}{2}\left(\frac{V_T}{C_a}\right)^2 \frac{EA}{f} \frac{EAV_{ap}}{fC_a^2 T} \tag{5.23}$$

167
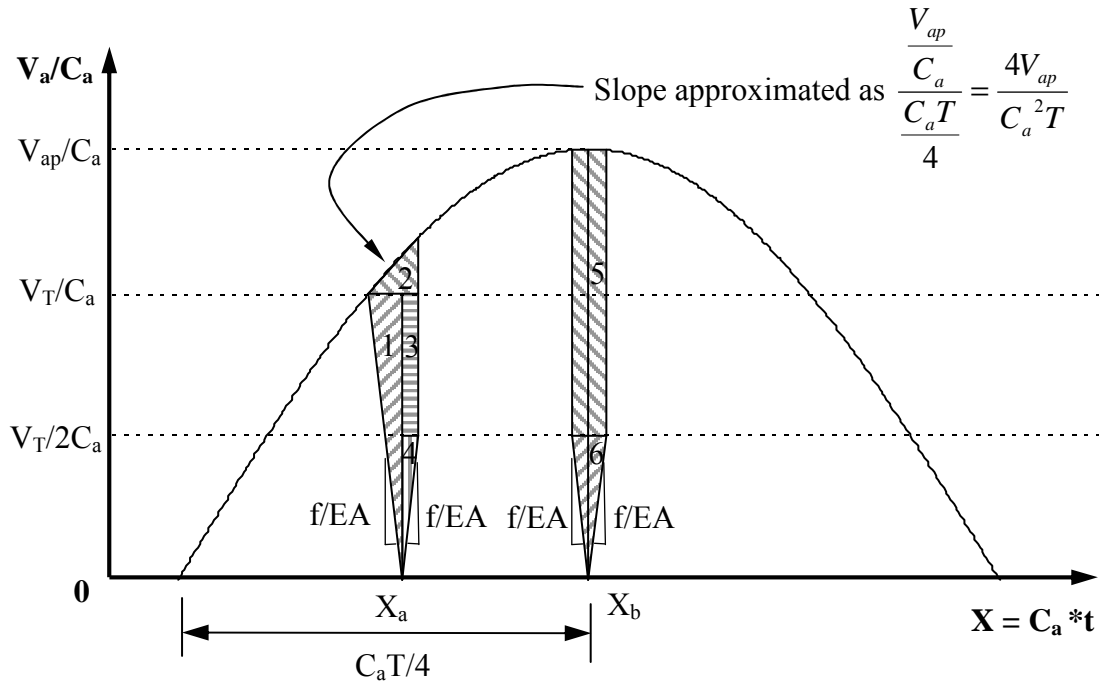
Figure 5.27. Simplified Model for Seismic Wave Interaction with JCCPs Without

Existing Cracked Joints

$$A'_3 = \frac{1}{4}\left(\frac{V_T}{C_a}\right)^2 \frac{EA}{f} \tag{5.24}$$

$$A'_4 = \frac{1}{8}\left(\frac{V_T}{C_a}\right)^2 \frac{EA}{f} \tag{5.25}$$

Combining Eqns. 5.22 through (5.25) results in

$$\delta_a = A'_1 + A'_2 + A'_3 + A'_4 = \left(\frac{V_T}{C_a}\right)^2 \frac{EA}{f}\left[\frac{9EAV_{ap}}{2fC_a^2T} + \frac{7}{8}\right] \tag{5.26}$$

Please note that A'$_2$ is simplified as a triangle with a slope $4V_{ap}/C_a^2T$. The error associated with this simplification for the calculated joint displacement is very small, generally less than 2%.

The value of $V_T/C_a$ is equivalent to the tensile cracking capacity of the JCCP joints, $\varepsilon_T$. Combining $\varepsilon_T = V_T/C_a$ and Eqn 5.26, results in

$$\delta_a = \varepsilon_T^{\,2} \frac{EA}{f} \left[ \frac{9EAV_{ap}}{2fC_a^2T} + \frac{7}{8} \right] \tag{5.27}$$

Similarly, the relative joint displacement for the alternative maximum case, $\delta_b$, can be decomposed into two area components

$$\delta_b = A'_5 + A'_6 \tag{5.28}$$

where A'$_5$, and A'$_6$ are calculated as

$$A'_5 = \left( \frac{V_T}{C_a} \right)^2 \frac{EA}{f} \left[ \frac{V_{ap}}{V_T} - \frac{1}{2} \right] \tag{5.29}$$

$$A'_6 = \frac{1}{4} \left( \frac{V_T}{C_a} \right)^2 \frac{EA}{f} \tag{5.30}$$

Combining Eqns 5.28 through 5.30 results in

$$\delta_b = A'_5 + A'_6 = \left( \frac{V_T}{C_a} \right)^2 \frac{EA}{f} \left[ \frac{V_{ap}}{V_T} - \frac{1}{4} \right] \tag{5.31}$$

Again, combining $\varepsilon_T = V_T/C_a$ and Eqn 5.31, results in

$$\delta_b = \varepsilon_T{}^2 \frac{EA}{f}\left[\frac{V_{ap}}{C_a\varepsilon_T} - \frac{1}{4}\right] \tag{5.32}$$

The relative magnitude of $\delta_a$ with respect to $\delta_b$ is determined by the ratio $V_{ap}/V_T$ and $C_aT$. For each section of pipeline affected by a different $V_{ap}$, the largest relative joint displacement is chosen from either Eqn 5.27 or 5.32.

When $V_{ap}/C_a < \varepsilon_T$, which implies that no joint will be cracked by the seismic body waves and relative joint displacement only occurs at existing cracked joints, the joint displacement, $\delta_b$, contains only component A'$_6$ with the $V_T$ replaced by $V_{ap}$, and can be simplified as Eqn 5.33, which is the same as Eqn 5.17 that gives the joint displacement at existing cracked joints.

$$\delta_b = \left(\frac{V_{ap}}{C_a}\right)^2 \frac{EA}{f} \tag{5.33}$$

### 5.4.6. Effect of Mortar Cracking Strain

The seismic wave pipeline interaction models depend on the relative magnitude of the cracking strain and maximum pipe strain induced by seismic waves. When $\varepsilon_{pmax} \geq \varepsilon_T$, the mortar at joints may be cracked and the pipe transfers from a continuous pipe to a segmented pipe. In contrast, when $\varepsilon_{pmax} < \varepsilon_T$, no joint will be cracked by the seismic body waves and relative joint displacement only occurs at existing cracked joints.

For relatively flexible pipes, the $\varepsilon_{pmax}$ is the same as $\varepsilon_{gmax}$, which can be expressed as the ratio of $V_{ap}/C_a$. Therefore, when $V_{ap} \geq \varepsilon_T \times C_a$, resulting $\varepsilon_{pmax} \geq \varepsilon_T$, the mortar at joints may be cracked by the seismic body waves. The whole sequence of transformation from continuous pipe to segmented pipe, as described in the Section 5.4.5, occurs and the pipe transfers from a continuous pipe to a segmented pipe as the seismic body waves propagate across the pipeline. The joint displacement occurs along the pipe with an interval of L given by Eqn 5.20. The maximum relative joint displacement is the larger of the two possible joint displacements calculated from Eqn 5.27 or 5.32. In contrast, when $V_{ap} < \varepsilon_T \times C_a$, and hence, $\varepsilon_{pmax} < \varepsilon_T$, no joint will be cracked by the seismic body waves and relative joint displacement only occurs at existing cracked joints. The pipeline is considered as continuous pipeline with existing cracked joint and the analytical approach and finite element results described in Sections 5.4.3 and 5.4.4 are applicable.

The magnitude of mortar cracking strain not only determines the appropriate model to apply but also affects the magnitude and occurrence frequency of the relative joint displacement. Figure 5.28 shows an illustration of the effect of mortar cracking strain on the magnitude of joint displacement. Figures 5.28a and 5.28b show the similar pipelines subjected to the same seismic body wave except that the $\varepsilon_T$ in Figure 5.28a is larger than that in Figure 5.28b. It is obvious that actual strain accumulation length in Figure 5.28a is greater than that in Figure 5.28b and the shaded areas at both $X_a$ and $X_b$ in Figure 5.28a are larger than those in Figure 5.28b. Therefore, as $\varepsilon_T$ decreases, the strain accumulation length decreases, resulting in an increased number of cracked joints for a given pipe length, and a decrease of relative joint displacement at each cracked joint. In other word, lower $\varepsilon_T$ causes smaller relative joint
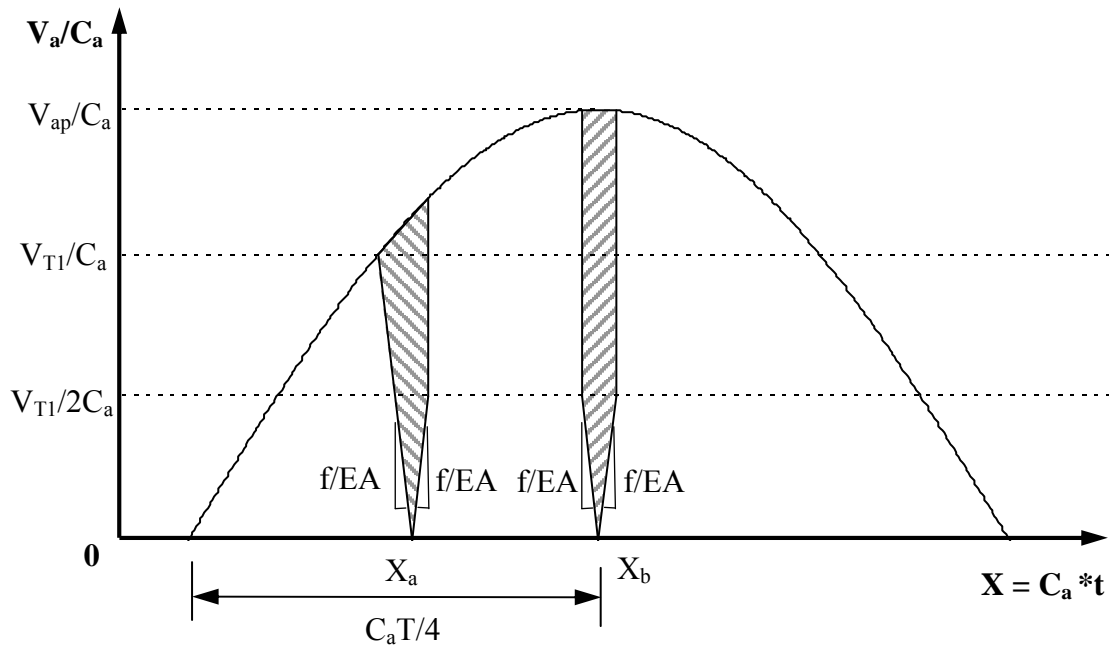
(a) $V_T = V_{T1}$ ($V_{T1} > V_{T2}$)
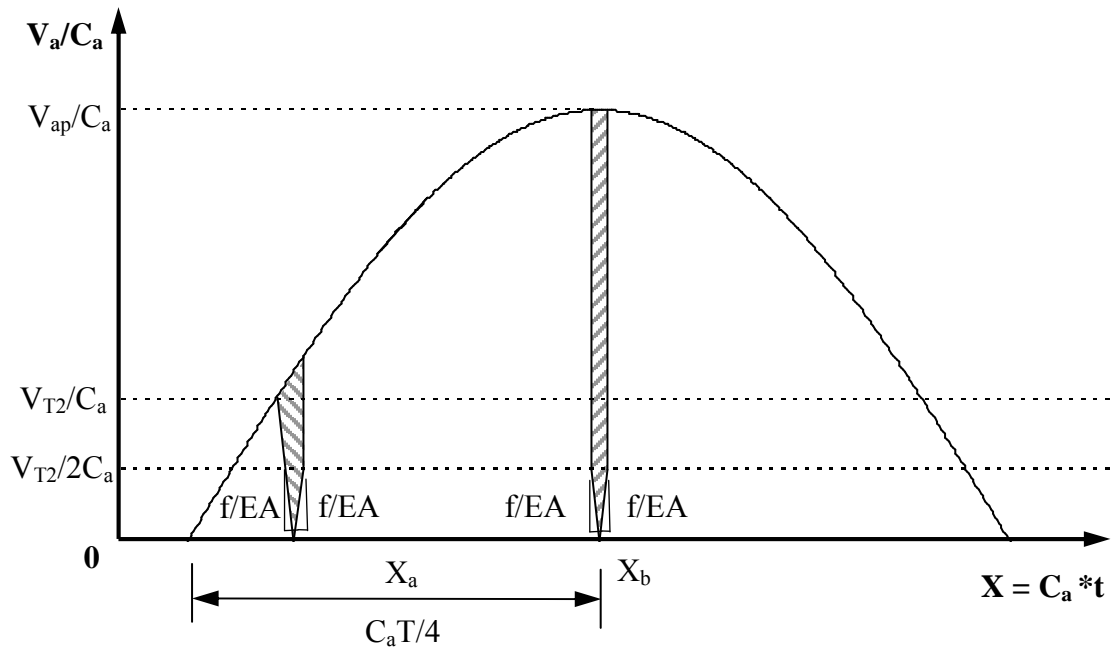


(b) $V_T = V_{T2}$ ($V_{T1} > V_{T2}$)

Figure 5.28. Effects of $V_T$ on Magnitude of Relative Joint Displacement

172

displacement with higher occurrence frequency. The joint displacement distributes more evenly along the pipeline with a smaller interval. In contrast, higher $\varepsilon_T$ results in larger relative joint displacements concentrated at fewer locations of cracked joints.

The effect of mortar cracking strain on the magnitude and occurrence frequency of joint displacement suggests an innovative design and construction principle for JCCPs. The JCCPs may be designed and constructed such that all the joints have zero or very low axial pullout resistance, i.e., $\varepsilon_T = 0$. This condition allows very small displacements to occur at each joint, with no appreciable strain accumulation along pipe segments or displacement concentrations at existing cracked joints. The absence of mortar cracking strain or low strain capacity may be accomplished by cracking each joint intentionally or reducing the adhesion between mortar and pipe segments by inserting some low adhesion materials, such as Teflon or high density polyethylene (HDPE) at the mortar and pipe segment interface.

## 5.5. Seismic Body Wave Interaction with Pipelines Containing Locally Weak Joints

The seismic wave - JCCP interaction model described in Section 5.4 can be modified to assess the seismic wave effects on pipelines composed of other materials and with different structure and joint characteristics. This section describes a modification to account for the locally weak joints in pipelines composed of other materials, such as cast iron.

### 5.5.1. Locally Weak Joint Characteristics

JCCPs rely on the cement mortar poured in the field to seal the rubber-gasket bell-and-spigot joints and to resist the axial pullout. Therefore, the joint behavior is dictated to the behavior of the cement mortar, which demonstrates a brittle failure mode under tension (see Figure 5.18), as opposed to the ductile failure mode in the joints of pipelines composed of other materials, such as cast iron.

O'Rourke et al. (1996) performed pullout tests to investigate the repetitive resistance and ultimate pullout capacity of cast iron pipelines with lead-caulked bell and spigot joints. Figure 5.29 shows the axial force and displacement relationship for a 305-mm diameter pipe. The equivalent monotonic envelop for the axial force and displacement relationship can be characterized by a rapid increase of axial force as axial displacement increases from 0 to about 2.5 mm (0.1 inch) and a more or less constant axial force thereafter. Prior (1935) conducted pullout tests on cast iron pipelines with lead caulked joints. Figure 5.30 shows the axial force vs. displacement data on 450- and 600-mm diamater pipelines from Prior (1935) and the equivalent monotonic envelop for the axial force and displacement relationship from O'Rourke et al. (1996). The axial force is expressed in terms of kN per circumferential distance to accomdate the data for different pipe diameter. The axial force increases rapidly up to a maximum of 0.15 kN/mm as the axial displacement increases from 0 to about 2.5 mm, and remains more or less constant thereafter. The force-displacement behavior can be characterized by a bilinear elasto-plastic model with a pullout force, $P_u$, of 0.15 kN per circumferetial distance in units of mm and pullout displacement, $\delta_u$, of 2.5 mm, as shown in Figure 5.30. Because the actual force-displacement relationship shows some strain hardening behavior (O'Rourke et al., 1996), a bilinear characterization
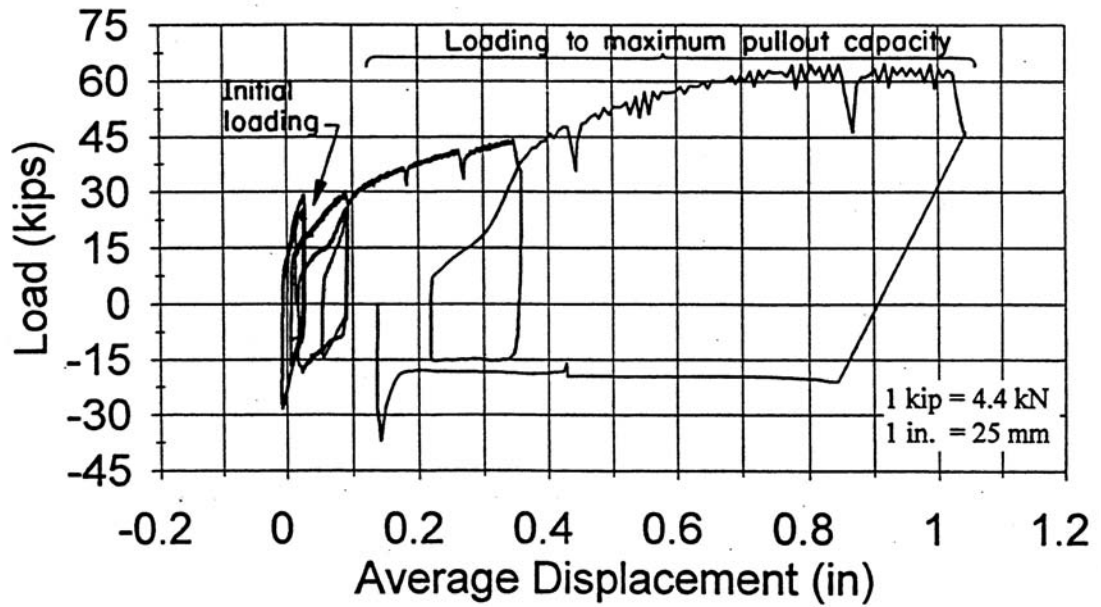
Figure 5.29.   Cast Iron Joint Pullout Test Results (O'Rourke et al., 1996)
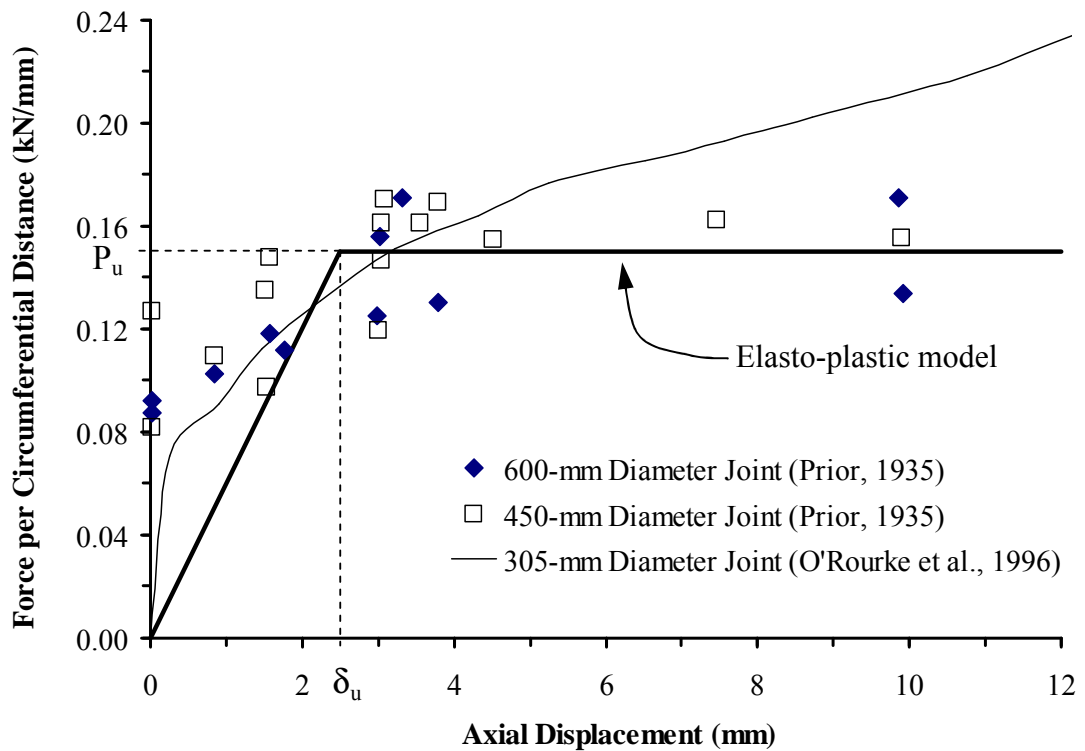


Figure 5.30.   Axial Force and Displacement Relationship for Cast Iron Pipeline with

Lead Caulked Joints

175

can be adjusted to provide a small conservative bias in the representation of maximum pullout capacity.

### 5.5.2. Simplified Model

Figure 5.31 shows a simplified model of seismic body wave interaction with a pipeline with a locally weak joint. The joints on either side of the weak joint are assumed to mobilize full tensile capacity across the joints, and the pipelines on either side of the weak joint behave as continuous pipelines. Because the pipeline is fully flexible, $\varepsilon_p = \varepsilon_g$ everywhere the pipeline is continuous. At the weak joint, the maximum axial force the pipeline can sustain corresponds to the pullout strain $\varepsilon_u = P_u/EA$. After $P_u$ occurs at the weak joint, the weak joint yields and deforms similarly to a free end. As the seismic wave passes across the weak joint, strain in the pipeline on each side of the joint will accumulate linearly at a slope of $f/EA$ from $\varepsilon_p = \varepsilon_u = P_u/EA$ to $\varepsilon_p = \varepsilon_g$, after which pipe and ground strain are indistinguishable. The shaded area in Figure 5.31 represents the integration of the differential strain between the pipeline and ground, which equals to the relative joint displacement because of the plastic deformation of the weak joint. As the elastic deformation of the weak joint becomes an increasingly smaller fraction of the plastic deformation, the relative joint displacement because of plastic deformation will converge on the total relative joint displacement.

### 5.5.3. Finite Element Model

Similar to JCCPs, the seismic body wave interaction with pipelines containing locally weak joints was modeled by a set of finite element analyses. The FE model
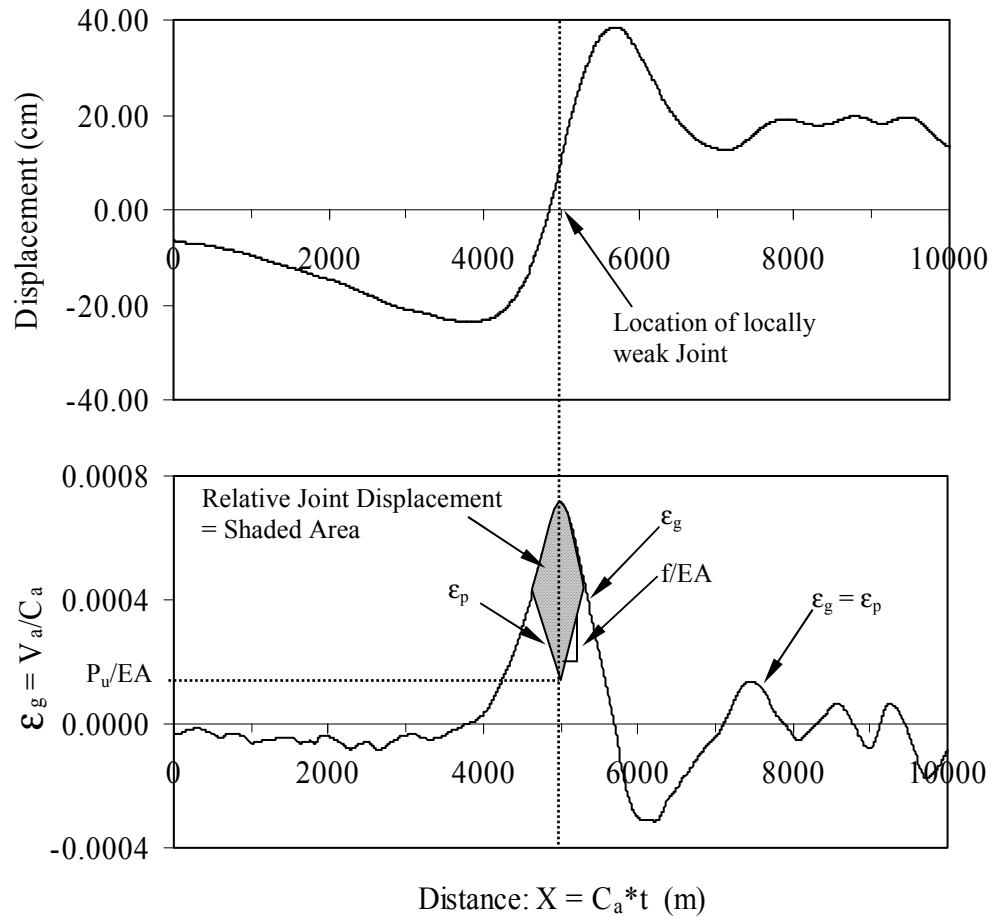
Figure 5.31.   Seismic Displacement and Velocity Interaction with Pipeline Containing

Locally Weak Joints

was similar to those described in Section 5.4.4.1, except for the adoption of elasto-plastic force-displacement behavior (Figure 5.30) for the locally weak joints. In total, 55 FE simulations with $\varepsilon_u/\varepsilon_{pmax}$ [i.e., $(P_u/EA)/(V_{ap}/C_a)$] varying from 0 to 1 were performed and the results are summarized in Figure 5.32, plotting the relative joint displacement correction factor, $\delta_d/\delta_j$, as a function of strain ratio, $\varepsilon_u/\varepsilon_{pmax}$ [i.e., $(P_u/EA)/(V_{ap}/C_a)$], where $\delta_d$ is the relative joint displacment in a locally weak joint and $\delta_j$ is the relative joint displacement for pipelines with an existing cracked joint, i.e., $P_u$ = 0. The value of $\delta_j$ can be estimated directly from Figure 5.25.

177
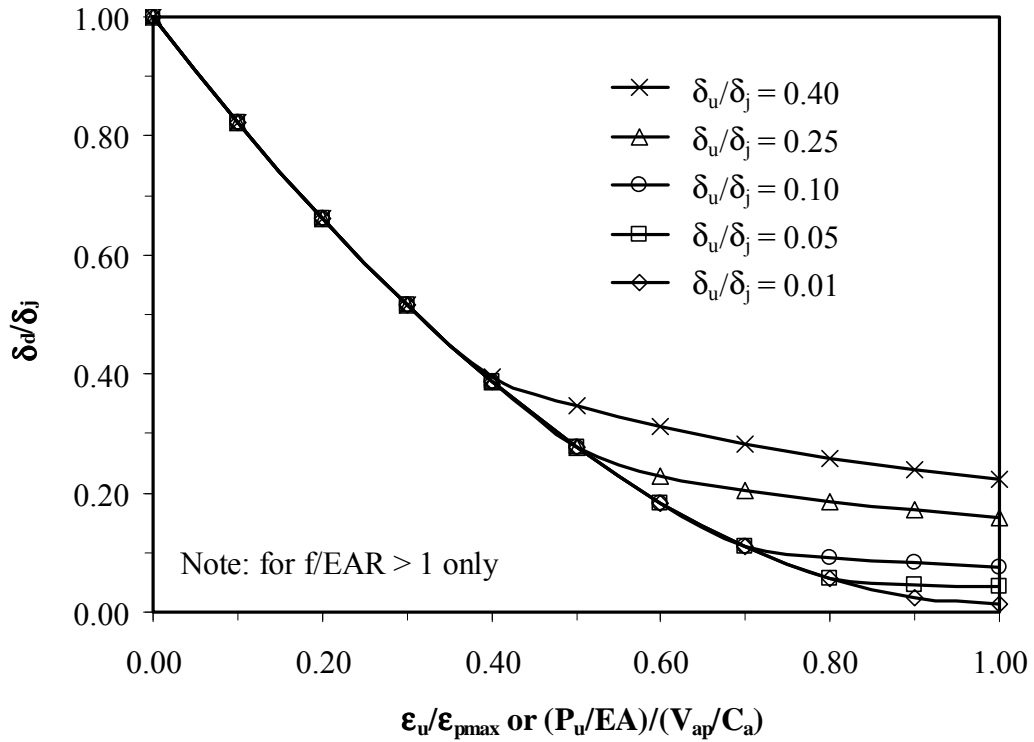
Figure 5.32.   Joint Displacement Correction Factor As a Function of Strain Ratio

Figure 5.32 shows that, in general, $\delta_d/\delta_j$ decreases as $\varepsilon_u/\varepsilon_{pmax}$ increases. When $\varepsilon_u$ is much smaller than the maximun pipe strain, $\varepsilon_{pmax}$, generated by an earthquake, i.e., $(P_u/EA)/(V_{ap}/C_a)$ approaches 0, the weak joint yields at a relatively small strain and the resulting joint displacement, $\delta_d$, is approximately equal to that of a cracked joint, $\delta_j$. In contrast, when $\varepsilon_u$ at the weak joint is larger than the $\varepsilon_{pmax}$, i.e., $(P_u/EA)/(V_{ap}/C_a)$ is greater than 1. The joint does not yield, and the joint displacement is limited to elastic deformation. The ratio, $\delta_d/\delta_j$, depends on the deformation characteristics, i.e., $\delta_u$, of weak joints before yielding.

Figure 5.32 shows $\delta_d/\delta_j$ and $\varepsilon_u/\varepsilon_{pmax}$ relationships associated with 5 different $\delta_u$, i.e., $\delta_u/\delta_j$ = 0.40, 0.25, 0.10, 0.05, and 0.01. When $\delta_u/\delta_j$ is smaller than $\delta_d/\delta_j$, i.e., $\delta_u < \delta_d$, all 5 relationships converge to a single line. On the other hand, when $\delta_u/\delta_j$ is

178

larger than $\delta_d/\delta_j$, i.e., $\delta_u > \delta_d$, the joint does not yield, and only elastic deformation occurs. It is, therefore, conservative to use the maximum elastic deformation, $\delta_u$, as $\delta_d$.

The line that all $\delta_d/\delta_j$ and $\varepsilon_u/\varepsilon_{pmax}$ relationships converge to in Figure 5.32 can be used to estimate $\delta_d$. The $\delta_d/\delta_j$ can be determined in accordance with the strain ratio $\varepsilon_u/\varepsilon_{pmax}$, and checked with $\delta_u/\delta_j$. If $\delta_u/\delta_j$ is larger than $\delta_d/\delta_j$, $\delta_u/\delta_j$ should be taken as $\delta_d/\delta_j$.

With known properties of a locally weak joint, as well as known ground conditions, pipeline properties, and seismic wave characteristics, the displacement at a locally weak joint, $\delta_d$, can be estimated directly with Figures 5.25 and 5.32. Consider, for example, a pipeline similar to that described in Section 5.4.4.4 with a locally weak joint with $P_u$ = 1620 kN and $\delta_u$ = 2.5 mm. The displacement at the cracked joint, $\delta_j$, is estimated as 24 mm as described in Section 5.4.4.4. The strain ratio, $\varepsilon_u/\varepsilon_{pmax}$, i.e., $(P_u/EA)/(V_{ap}/C_a)$, is calculated as 0.2. Using Figure 5.31, $\delta_d/\delta_j$ is estimated as 0.66. Because $\delta_u/\delta_j$ is about 0.1, $\delta_u/\delta_j$ is smaller than $\delta_d/\delta_j$, and the relative displacement at the locally weak joint, $\delta_d$, is about 16 mm.

It should be pointed out that Figure 5.32 is only applicable for flexible pipes, i.e., $f/EAR \geq 1$, such as water pipelines affected by seismic body waves. A family of $\delta_d/\delta_j$ vs. $\varepsilon_u/\varepsilon_{pmax}$ relationships for rigid pipes, i.e., $f/EAR < 1$, was been developed by Shi (2006), based on the interaction of seismic surface waves with pipelines.

## 5.6. Model Applications to Other Linear Structures

Although the models described in this chapter are intended for the analysis of seismic wave interaction with pipelines, they are applicable to seismic wave interaction with other linear structures, as long as the two basic assumptions proposed by Newmark (1967) are deemed acceptable. As discussed in Section 5.3, Newmark (1967) proposed two basic assumptions for assessing seismic wave interaction with pipelines: 1) the seismic ground motions, i.e., acceleration, velocity and displacement time histories, at two points along the propagation path differ only by a time lag; 2) pipeline inertia terms are small and may be neglected.

The models can be applied to other linear structures, such as deformation at flexible connections between subaqueous tunnels and shore facilities when subjected to near source strong motion. For example, recent work to retrofit the Bay Area Rapid Transit System has focused on the potential slip of seismic joints connecting the Transbay Tube with ventilation structures on either side of San Francisco Bay (Wu et al., 2003). Concerns about relative joint displacement during seismic wave interaction, similar to those for pipelines, have a strong influence on the retrofitting requirements for this transporation lifeline.

## 5.7. Summary

The earthquake performance of a water supply system is often closely related to the performance of water trunk and transmission lines, whose seismic wave interactions were studied in this chapter. Examinations of near-source strong ground motion records during previous earthquakes indicate that seismic waves can be

approximated by sinusoidal waves, and it is reasonable to simplify the seismic body waves as a single sinusoidal pulse in seismic wave-pipeline interactions.

Depending on the seismic wave characteristics, R, ground conditions, f, and pipeline properties, EA, pipelines behave either flexibly or rigidly in the axial dimension. When f/EAR > 1, the pipeline is axially flexible with respect to ground strain accumulation. No relative displacement occurs between the pipeline and the surrounding soil, and the pipeline deforms coincidentally with the ground surrounding the pipeline, resulting in $\varepsilon_p = \varepsilon_g$ everywhere the pipeline is continuous. The ratio between maximum pipe strain, $\varepsilon_{pmax}$, and maximum ground strain, $\varepsilon_{gmax}$, is equal to 1. When f/EAR < 1, the pipeline is relatively rigid with respect to axial ground strain accumulation, and relative displacement occurs between soil and pipeline. The strain in the continuous pipeline will accumulate linearly at a slope of f/EA. The $\varepsilon_{pmax}$ occurs at the locations corresponding to the amplitude of the sinusoidal seismic wave, and the ratio between $\varepsilon_{pmax}$ and $\varepsilon_{gmax}$ is equal to f/EAR.

The typical range of f/EAR values for water trunk lines, when affected by seismic body waves, is much greater than 1, and the water trunk lines tend to behave as flexible pipes when affected by seismic body waves. Rigid pipe behavior only occurs under extremely adverse conditions, such as where surrounded by liquefied soils, where the f approaches 0, resulting in f/EAR less than 1.

Attention is drawn to the seismic body wave interaction with jointed concrete cylinder pipelines (JCCPs), the performance of which has varied significantly during previous earthquakes. Close examinations of the design and as-built drawings of the JCCPs reveal that the pullout capacity of the JCCP joints depends on the tensile

behavior of the cement mortar at the joints. Moreover, it is not uncommon to observe cracks in the cement mortar and separation at the joints before earthquakes because of shrinkage of mortar cement during curing and subsequent operational loads and movements in the field.

A simplified model for seismic body wave interactions with JCCPs containing existing cracked joints was developed to estimate relative joint displacements. The relative joint displacement at a cracked joint equals the integration of the differential strain between the pipeline and ground from the cracked joint to the positions in the pipe where no relative displacement occurs between the pipe and the soil.

Extensive parametric studies with various ground conditions, seismic body wave parameters, and pipe properties were performed using finite element models. In total, 320 finite element runs were performed, and the results were summarized by a universal relationship between two dimensionless parameters, $\delta_j/\delta_0$ and f/EAR. With known ground conditions, pipeline properties, and seismic wave characteristics, f/EAR and $\delta_0$ can be calculated, and the joint displacement, $\delta_j$, can be estimated directly using the universal relationship.

The continuous JCCPs without existing cracked joints may crack at joints as a result of seismic body wave propagation when $\varepsilon_{pmax}$ exceeds the cracking strain, $\varepsilon_T$, at the mortar joints. The cracking of joints transforms the pipeline from a continuous structure to a segmented one. Therefore, geometric nonlinearity has to be incorporated in the modeling. The relative joint displacement varies as the seismic body waves pass through the pipelines. The two most critical cases for relative joint displacement were found to be immediately before the joint cracks and when the $\varepsilon_{pmax}$ occurs at the

cracked joint. The equations for calculating the corresponding relative joint displacement were derived.

The JCCP response to seismic body waves depends on the relative magnitude of the mortar cracking strain and maximum pipe strain induced by seismic waves. When $\varepsilon_{pmax} \geq \varepsilon_T$, the mortar at the joints may be cracked and the pipe changes from a continuous pipe to a segmented pipe. In contrast, when $\varepsilon_{pmax} < \varepsilon_T$, no joint will be cracked by the seismic body waves and the relative joint displacement only occurs at existing cracked joints. The mortar cracking strain also has significant effect on the magnitude and occurrence frequency of relatively joint displacement. Low $\varepsilon_T$ causes small relative joint displacement to occur frequently with a small interval along the pipeline. In contrast, high $\varepsilon_T$ results in large relative joint displacement concentrated at fewer locations of cracked joints.

Understanding the interaction of seismic waves and JCCPs leads to some design and construction concepts that may improve earthquake performance. The JCCPs may be designed and constructed such that all the joints have zero or very low axial pullout resistance, i.e., $\varepsilon_T = 0$. The zero or low axial pullout resistance allows very small displacements to occur at each joint, with no appreciable strain accumulation along pipe segments or displacement concentrations at existing cracked joints. The absence of mortar cracking strain or low strain capacity may be accomplished by cracking each joint intentionally or reducing the adhesion between mortar and pipe segments by inserting some low adhesion materials, such as Teflon or high density polyethylene (HDPE) at the mortar and pipe segment interface.

183

The model for seismic body wave interaction with JCCPs was extended for the locally weak joints in pipelines composed of other materials, such as cast iron. A relative joint displacement correction factor, $\delta_d/\delta_j$, was introduced and the relationship between $\delta_d/\delta_j$ and strain ratio, $\varepsilon_u/\varepsilon_{pmax}$ [i.e., $(P_u/EA)/(V_{ap}/C_a)$], was provided. The relative joint displacment at the locally weak joint is a product of the relative joint displacement at the existing cracked joint and the correction factor.

The models for seismic wave interaction with pipelines also have application to other linear structures, such as displacement at flexible connections between subaqueous tunnels and shore facilities when subjected to near-source strong motions.

# CHAPTER 6

# SYSTEM RESPONSE EVALUATION WITH GIRAFFE

## 6.1. Introduction

Water supply systems provide water to their customers, and hence, the seismic performance of water supply systems, given the earthquake-induced damage scenario at component levels, should be evaluated with respect to the flow and pressure available for fire protection and water consumption for domestic and industrial use. The evaluation of flow and pressure at various locations requires hydraulic analysis. This chapter provides a brief description of a special hydraulic analysis computer program, Graphical Iterative Response Analysis of Flow Following Earthquakes (GIRAFFE), developed at Cornell University for hydraulic network analysis of damaged water supply systems. It starts by describing the limitations of commercial hydraulic network analysis software for simulating damaged water supply systems. It then describes a special algorithm for the treatment of negative node pressures in damaged water supply systems to provide a more accurate assessment of the performance. A discussion is provided for the structure and capability of GIRAFFE, which incorporates the special algorithm for simulating damaged systems. Finally, the LADWP water supply system performance during the 1994 Northridge earthquake is modeled with GIRAFFE and simulation results are compared with measurement of flow after the earthquake. Only the most prominent features of GIRAFFE are

described in this chapter. For more details on the development, capability, and validation of GIRAFFE, please refer to Shi (2006).

## 6.2. Hydraulic Analysis For Damaged Water Supply Systems

Hydraulic network analysis is governed by two sets of well-known equations, the equations of continuity and energy conservation. The equations of continuity are simple implications of the law of conservation of mass, which requires that in every junction of water systems, there must be a balance between the sum of the flows coming in and going out. Consider the equation of continuity at node i of water systems:

$$\sum_{k=1}^{n_i} Q_{ik} - \overline{Q_i} = 0 \tag{6.1}$$

where $Q_{ik}$ is the flow in pipe k at node i, which connects to $n_i$ pipes in total, and $\overline{Q_i}$ is the demand or supply at node i.

The energy equation for a pipe k connecting nodes i and j can be expressed as

$$H_i - H_j = h_{fk} + h_{mk} \tag{6.2}$$

where $H_i$ and $H_j$ are the hydraulic heads, i.e., the sum of pressure heads and elevation heads, at nodes i and j, respectively, $h_{fk}$ is the friction head loss in pipe k, and $f_{mk}$ is the minor loss in pipe k, associated with the additional turbulence that occurs at bends, fittings, junctions, contractions, expansions, meters, and valves.

### 6.2.1. Limitation of Hydraulic Analysis for Damaged Water Supply Systems

A fundamental but implicit assumption imbedded in the equations of continuity is that flows are continuous everywhere in the systems and all customer demands must be satisfied. Although this assumption holds true for undamaged water supply systems, quite often it is violated when the systems sustain damage and water outage occurs, indicating occurrence of unsatisfied customer demands and discontinuous flows in the systems. It is quite likely that, after some pipe breakage and/or leakage occur in the systems, water flows out from the systems through the pipe breaks and/or leaks, and parts of the water systems have no water flows, leaving some customer demands unsatisfied. However, if the commercial hydraulic analysis software is utilized to simulate the damaged water supply systems, it will provide a prediction of all customer demands satisfied with unrealistic negative node pressures in the systems, as a result of the violation of the continuous flow assumption. When the commercial hydraulic analysis software solves two sets of energy equations and continuity equations, to provide the simulation results, the software reduces the hydraulic heads at the nodes, where the customer demands are not satisfied in reality, to satisfy the demands mathematically, resulting in negative pressures at the nodes. Because water systems are not airtight, particularly for damaged water systems, air can be admitted when the pressure falls below the atmospheric pressure, no negative pressure can actually occur in the systems. The hydraulic analysis for the damaged water supply systems may provide misleading results if the violation of the continuous flow assumption is not accounted for.

### 6.2.2. Negative Pressure Analysis

Markov et al. (1994) developed an iterative approach on the treatment of negative node pressures to account for the violation of continuous flow assumption, and applied this method to assess the seismic serviceability of the auxiliary water supply system in the city of San Francisco. Similar approach was also described by Tanaka (1996) and Hwang et al. (1998). A brief review on the negative pressure analysis approach by Markov et al. (1994) is provided as follows.

Consider, for example, a node i, as shown in Figure 6.1, in water systems with pressure $P_i < 0$, where zero stands for the atmospheric pressure. If air is allowed into the systems, node i will have a pressure equal to the atmospheric pressure, i.e., $P_i = 0$, and no flow will occurs in node i and pipe k connecting nodes i and j. Markov et al. (1994) proposed an iterative approach to eliminate the nodes with negative pressures, such as node i in Figure 6.1, in the damaged water supply systems systematically. The elimination of negative pressure nodes from the damaged water systems starts with the identification of nodes with negative pressure. The negative pressure nodes and the pipes converging to these nodes are eliminated sequentially, starting with the node with the lowest negative pressure. Flows and pressures are recalculated for the adjusted systems after elimination of each single negative pressure node. If the negative pressure nodes isolate a portion of the systems, that portion of the systems is simply taken out from the systems.

Markov et al. (1994) validated the negative pressure analysis algorithm by simulating both small-scale artificial water systems and a full-scale water supply system, i.e., San Francisco Auxiliary Water Supply System. It was shown that the
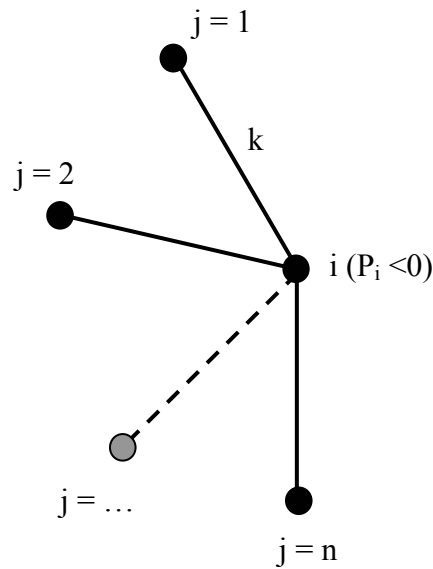
Figure 6.1.  Negative Pressure Analysis

negative pressure analysis algorithm was able to eliminate nodes with negative pressures and simulate the flow pattern in the small-scale water systems properly. The negative pressure analysis algorithm was then utilized in the assessment of seismic serviceability of the San Francisco Auxiliary Water Supply System and was capable of reproducing the flow and pressure distributions in the System during the experimental tests performed by San Francisco Fire Department as well as the 1989 Loma Prieta earthquake.

## 6.3.  GIRAFFE

A special hydraulic analysis program, Graphical Iterative Response Analysis of Flow Following Earthquakes (GIRAFFE), equipped with the negative pressure analysis algorithm (Markov et al., 1994), is developed at Cornell University (Shi, 2006), dedicating for the hydraulic analysis of the damaged water supply systems.

This Section provides a brief description of GIRAFFE, starting with the overall structure of GIRAFFE, followed by system damage simulation, treatment of local distribution system damage, and Monte Carlo simulations. Only the most prominent features of GIRAFFE are described here, and more details on the development, capability, and verification of GIRAFFE are given by Shi (2006).

### 6.3.1. Structure of GIRAFFE

GIRAFFE, equipped with the negative pressure analysis algorithm (Markov et al., 1994), is built on an open source hydraulic analysis program, EPANET (EPA, 2005). EPANET was developed by the U.S. Environmental Protection Agency, and is available in its website (http://www.epa.gov/ORD/NRMRL/wswrd/epanet.html). Figure 6.2 shows the flowchart of GIRAFFE, which contains three major components: preprocessor, analysis module, and postprocessor. Water systems can be defined and edited through the EPANET Windows interface (Rossman, 2000) or imported directly from other hydraulic network analysis software, such as H2ONET (MWH Soft, Inc., 1999). GIRAFFE then imposes the system damage scenarios, either deterministically or probabilistically, and proceeds to hydraulic network analysis, using the EPANET hydraulic engine, which firstly checks the connectivity of the damaged systems. If parts of the systems are isolated from water sources as a result of the imposed system damage scenario, these parts of the systems have no flow and are eliminated from the systems sequentially. If no connectivity error occurs in the systems, hydraulic analysis is conducted and the simulation results regarding the flow and pressure in the systems are generated. GIRAFFE then assesses the simulation results and eliminates the negative pressure nodes (i.e., $P_i < P_{limit} = 0$) accordingly until no negative pressure occurs in the system. Finally, GIRAFFE compiles the simulation results in a tabulated
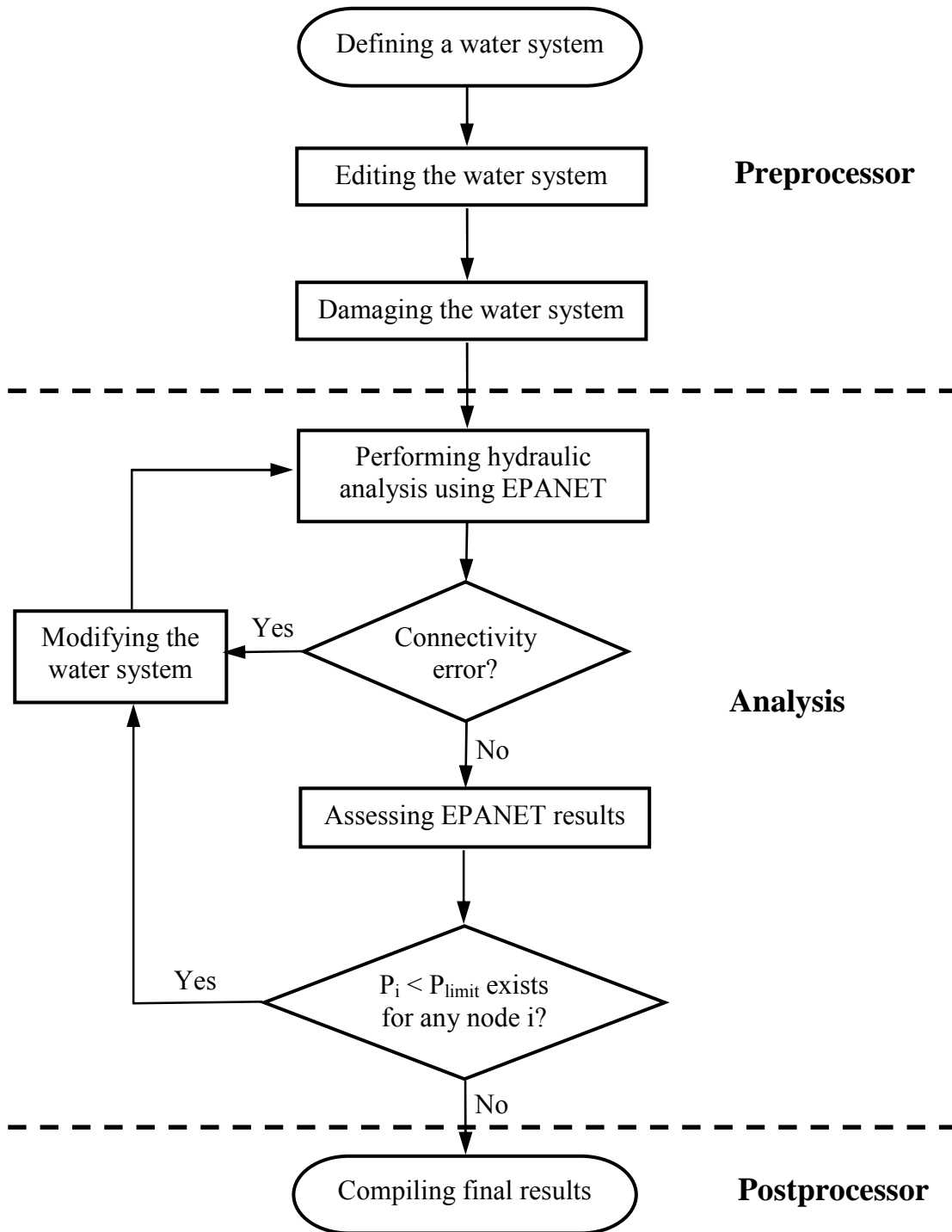
Figure 6.2.   GIRAFFE Flow Chart

format which can be directly linked to Geographic Information System (GIS) software, and enables visualization and manipulation in a GIS platform. The simulation results include flow and/or pressure at each system component (i.e., junction, pipe, control valve, pump, tank, and reservoir) and system serviceability index (SSI), which is defined as:

$$SSI = \frac{\sum_{i=1}^{n_i} \overline{Q_i}}{\sum_{i=1}^{n_{i0}} \overline{Q_i}} \qquad (6.3)$$

where $\overline{Q_i}$ is the customer demand at node i, $n_{i0}$ and $n_i$ are number of satisfied customer demands before and after imposing damage scenario, respectively.

## 6.3.2. System Damage Simulations

GIRAFFE offers two options for system damage simulations: deterministic and probabilistic. The deterministic option enables users to specify damage to any specific component, including pipe, pump, control valve, tank, and reservoir, anywhere in the systems. The damaged pumps, control valves, tanks, and reservoirs are turned off and disconnected from the systems. The damaged pipes can be further categorized into pipe break and pipe leak, which are simulated accordingly using the approaches described in Sections 6.3.2.2 and 6.3.2.3, respectively. The probabilistic option utilizes a Poisson process to simulate the occurrence of pipe damage and divides the pipe damage into pipe break and pipe leak stochastically. More descriptions on this regard are provided in the following sections:

*6.3.2.1. Probabilistic Pipe Damage Occurrence Simulations*

If the randomly distributed pipe damage in the systems is assumed to follow a Poisson process with a mean pipe damage rate, $\lambda$, which is a function of seismic demands, such as peak ground velocity, along the pipes, the distance from the pipe origin to the first pipe damage or the distance between two consecutive pipe damages can be simulated by an exponential random variable, $L_k$, expressed as:

$$L_k = -\frac{1}{\lambda}\ln[rand(0,1)] \tag{6.4}$$

where rand(0,1) is the uniform random variable between [0,1] available in many computer language packages, such as C++ and Matlab. Consider, for example, a pipe with length L and mean damage rate $\lambda$, as shown in Figure 6.3. A series of exponential random numbers, $L_1$, $L_2$, …$L_n$, are generated using Eqn 6.4 and compared with the pipe length L until $\sum_{k=1}^{n}L_k > L$. Pipe damage occurs at location with a distance $\sum_{k=1}^{n}L_k$ from the pipe origin when $\sum_{k=1}^{n}L_k < L$. In the pipe shown in Figure 6.3, two damages in total occur in the pipe, the first one at point A with a distance $L_1$ from the pipe origin, and the second one at point B with a distance from $L_1 + L_2$ from the pipe origin.

The pipe damage is further categorized into pipe break and pipe leak in accordance with the characteristics of pipe damage during previous earthquakes. Shi (2006) evaluated the characteristics of pipe damage during previous earthquakes reported in literature and found that about 80% of the pipe damages in cast iron, ductile iron, rivet steel, or concrete pipes are leak, and only about 20% of the pipe damages may be characterized as pipe break, a complete loss of water conveyance
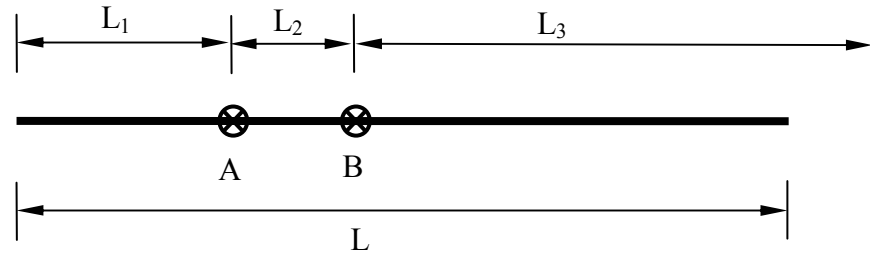
Pipe with length L and mean damage rate $\lambda$

$$L_k = -\frac{1}{\lambda}\ln[rand(0,1)], \ k = 1, 2, 3, \ldots, n \text{ until } \sum_{k=1}^{n} L_k > L$$

Figure 6.3.   Probabilistic Pipe Damage Occurrence Simulations

capability. The majorities of the reported damage in steel pipes are described as extensive deformation on the pipes. However, only about 20% of the reported steel pipe damages are associated with water leakage and it is quite unlikely that pipe break may occur in the steel pipes.

An uniform random number, $P_1$, between [0,1] is utilized to classify each pipe damage as pipe leak, pipe break, or no hydraulic damage in accordance with the material types of the pipes in which the damage occurs. If the damage occurs in cast iron, ductile iron, rivet steel, or concrete pipes, and $P_1 > 0.2$, the damage is classified as a pipe leak. The damage in cast iron, ductile iron, rivet steel, or concrete pipes, with $P_1 \leq 0.2$, is considered as a pipe break. Similarly, for steel pipes, damage with $P_1 \leq 0.2$ is classified as pipe leak, while damage with $P_1 > 0.2$ is labeled as no hydraulic damage, in which no water conveyance capability is compromised and no damage is simulated in hydraulic analysis, although extensive pipe deformations may occur. No break in steel pipes is considered possible in this research.

*6.3.2.2. Hydraulic Simulations of Pipe Break*

After the occurrences of pipe breaks and/or leaks are determined, the hydraulic models for pipe break and leak are implemented, as described in this and the next sections, respectively.

Figure 6.4 shows a schematic diagram for the hydraulic simulation of pipe break. Consider, for example, a break A occurred in a pipe with a length of L connecting nodes i and j and located at a distance $L_1$ from the upstream node of the pipe, i.e., node i. At point A, the pipe is divided into two pipes with lengths $L_1$ and L-$L_1$ connecting nodes i and j to two new reservoirs 1 and 2, respectively. The pressure heads, P, at the reservoirs 1 and 2 are fixed at atmospheric pressure, i.e., 0, to simulate the fact that the pipe is open to atmosphere at the location of break. Therefore, the hydraulic heads, H (i.e., elevation head, E, plus pressure head, P) at reservoirs 1 and 2 are equal to their respective elevation heads, which can be interpolated from the elevations at nodes i and j as follows:

$$H_{reservoir1} = H_{reservoir2} = E_{nodei} + \frac{L_1 \times (E_{nodej} - E_{nodei})}{L} \tag{6.5}$$

In order to prevent water from back-flowing from the reservoirs to the water system, two check valves, which only allow for one-way flow from the system to the reservoirs, are added in the divided pipes, as shown in Figure 6.4.
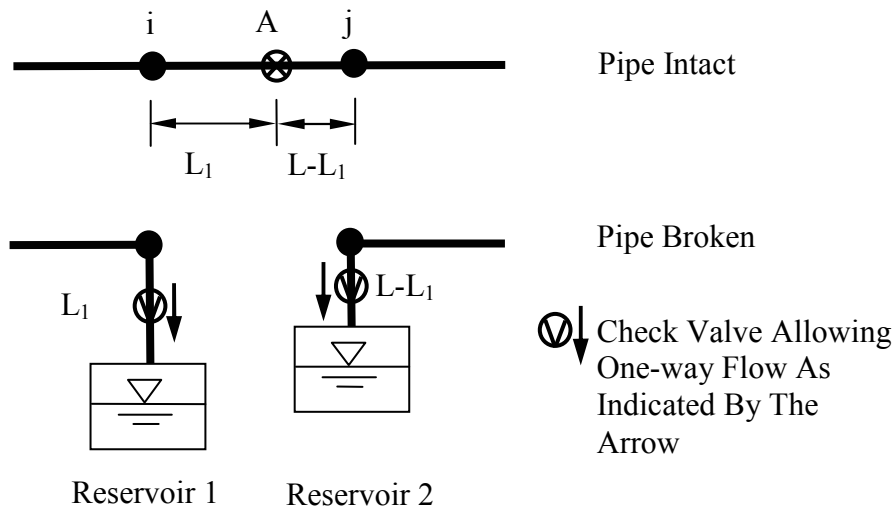
Figure 6.4.   Schematic Diagram of Pipe Break Hydraulic Simulation

### 6.3.2.3.  Hydraulic Simulations of Pipe Leak

In the context of hydraulic simulations, pipe leakage induced by earthquakes can be considered as an analogy of sprinklers, which are governed by the following hydraulic equation:

$$Q = C_D P^{0.5} \tag{6.6}$$

where $Q$ is the flow rate through the sprinklers, $C_D$ is the sprinkler discharge coefficient, and $P$ is the sprinkler operating pressure. Shi (2006) found that the equivalent sprinkler discharge coefficient for a pipe leak with an open area of $A_1$ in the pipe wall can be expressed as:

$$C_D = \left( \frac{2g}{\gamma_w} \right)^{0.5} A_1 \tag{6.7}$$
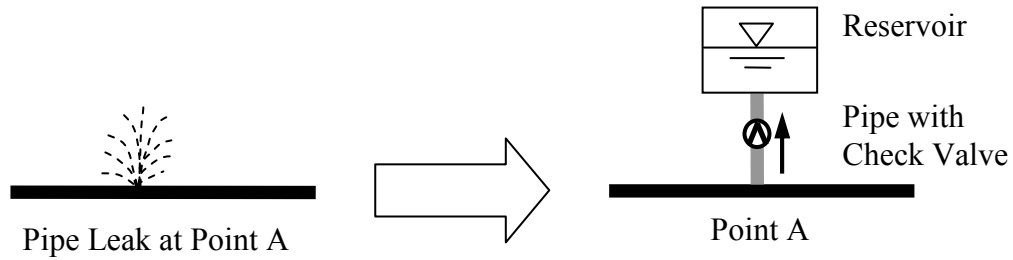
Figure 6.5. Schematic Diagram of Pipe Leak Hydraulic Simulation

where $\gamma_w$ is the unit weight of water and g is gravitational acceleration.

In hydraulic simulations, a sprinkler is implemented as a fictitious pipe connecting to a fictitious reservoir which has the same elevation as the immediate upstream of the sprinkler. The friction loss, $h_f$, along the fictitious pipe is zero and the head loss, h, is due to the minor loss, $h_m$, calculated by:

$$h = h_m = \frac{1}{\gamma_w C_D^2} Q^2 \tag{6.8}$$

Following the implementation for sprinklers, Figure 6.5 shows the implementation of pipe leakage model in hydraulic simulations. If a pipe leak occurs at point A, a fictitious pipe connecting to a fictitious reservoir with the same elevation as point A is added to point A. The fictitious pipe contains a check valve to prevent water from back-flowing from reservoir to point A. The fictitious pipe diameter is the equivalent diameter corresponding to the leakage area $A_1$ and the pipe friction loss coefficient is taken as infinite to eliminate any potential friction loss along the pipe. The minor loss, $h_m$, and hence head loss, h, is calculated by combining Eqns 6.7 and 6.8, resulting in

$$h = h_m = \frac{1}{2gA_1^2}Q^2 \qquad\qquad (6.9)$$

Comparing Eqn 6.9 with the minor loss equation in hydraulic textbook (Lencastre and Holmes, 1987)

$$h_m = \frac{K}{2gA_1^2}Q^2 \qquad\qquad (6.10)$$

where K is minor loss coefficient, results in K = 1. Therefore, the K value for the fictitious pipe is taken as 1 in the pipe leak hydraulic simulations.

The only unspecified hydraulic parameter in the abovementioned hydraulic model for the pipe leak is the leakage area $A_1$, which is estimated after Shi (2006). Shi (2006) evaluated the characteristics of pipe leakage reported in literature during previous earthquakes, categorized them into 5 different types (i.e., annular disengagement, round crack, longitudinal crack, local loss of pipe wall, and local tear of pipe wall), and provided a set of empirical equations to estimate the leakage area $A_1$ in accordance with pipe dimensions, such as pipe diameter and wall thickness, for different types of leakage. Fore more details on the development of empirical equations, please refer to Shi (2006). Shi (2006) also provide estimation of the occurrence probability of different types of leakage in the pipes composed of different materials, such as cast iron, ductile iron, riveted steel, welded steel, and concrete, as shown in Table 6.1.

Table 6.1.  Occurrence Probability of Different Leak Types

| Pipe Material | Annular Disengagement | Round Crack | Longitudinal Crack | Local Loss of Pipe Wall | Local Tear of Pipe Wall |
|---|---|---|---|---|---|
| **Cast Iron** | 0.3 | 0.5 | 0.1 | 0.1 | N/A |
| **Ductile Iron** | 0.8 | N/A | 0.1 | 0.1 | N/A |
| **Riveted Steel** | 0.6 | N/A | 0.3 | 0.1 | N/A |
| **Welded Steel** | N/A | N/A | N/A | N/A | 1.0 |
| **Concrete** | 1.0 | N/A | N/A | N/A | N/A |

N/A: Not Applicable; this type of leakage does not occur in the pipe composed of the corresponding type of material

GIRAFEE can simulate a pipe leak either deterministically or probabilistically. In deterministic simulations, specific leakage type or leakage area $A_1$, needs to be specified by the users, as opposed to probabilistic simulations, in which GIRAFEE utilizes the occurrence probabilities in Table 6.1 and a uniform random number, $P_2$, between [0,1] to determine the leakage type, and hence leakage area $A_1$. Consider, for example, probabilistic simulation of a leak in a cast iron pipe. If $0 \leq P_2 < 0.3$, annular disengagement type leak occurs; if $0.3 \leq P_2 < 0.3 + 0.5 = 0.8$, round crack type leak occurs; if $0.8 \leq P_2 < 0.8 + 0.1 = 0.9$, longitudinal crack type leak occurs; if $0.9 \leq P_2 \leq 0.9 + 0.1 = 1.0$, local loss of pipe wall occurs; and no local tear of pipe wall may occur in cast iron pipe. Uniform random number $P_2$ is generated for each pipe leak and the type of leakage, and hence, the leakage area $A_1$ is determined accordingly.

### 6.3.3. Treatment of Local Distribution System Damage

The LADWP water supply system contains about 12,000 km of both distribution (diameter < 600 mm) and trunk (diameter ≥ 600 mm) pipelines. There are about 2,800 km pipelines and 1,052 demand nodes, i.e., customers, in the hydraulic network model used by LADWP engineers (LADWP, 2002a) for planning operation and future modification of the system. Most distribution are not modeled explicitly in the hydraulic network model, but are accounted for implicitly by aggregating them into demand nodes. From this perspective, each of the 1,052 demand nodes in the LADWP hydraulic network model represents a small-scale local distribution system. Because of the lack of details on the local distribution systems in the LADWP hydraulic network model, the damage to the local distribution system can not be simulated explicitly using the pipe break and leak model described in the previous sections, and some implicit approaches are necessary.

Shi (2006) describes an implicit approach to account for the damage to local distribution systems using demand fragility curves generated from multi-scale simulations on the LADWP system. It is assumed that each of the 1,052 demand nodes in the LADWP hydraulic network models corresponds to a small-scale local distribution system. As the distribution pipelines are modeled implicitly by demand nodes, the damage to the local distribution systems, which generally accompanies with additional water outflow from the distribution systems, should lead to an increase of the nodal demands in the LADWP hydraulic network models. Monte Carlo simulations on local distribution systems were performed to develop a fragility curve type of relationship between the local distribution line damage, measured by repair rate, i.e., number of repair per kilometers, and the increase of nodal demands in

LADWP hydraulic network models. Finally the developed relationship is applied to adjust the nodal demands in the LADWP hydraulic network models in accordance with the distribution line repair rate after earthquakes. By utilizing the relationship and adjusting nodal demands, the damage to the local distribution systems is accounted for implicitly.

Six LADWP local distribution systems were acquired from LADWP, which are pressure zone 1449, 1000, 579, 426, 448&462, and 205 distribution systems, as shown in Figure 6.6. The six pressure zone distribution systems are spatially distributed over the LADWP system and are considered as a significant amount of sample from the overall LADWP local distribution systems, and hence, are capable of characterizing the behavior of LADWP local distribution systems. Each pressure zone distribution system contains distribution lines as well as trunk lines. Monte Carlo simulations were performed on the six pressure zone distribution systems by adding the distribution line damage, both pipe break and leak, probabilistically, using the simulation process described in the previous sections. The trunk lines in the pressure zone distribution systems were kept undamaged intentionally and the flows in the trunk lines before and after the damages were monitored. It is assumed that the ratio of the flows in the trunk lines before and after the damages is equivalent to the ratio of nodal demands before and after damages, which can not be measured directly as a result of the hydraulic analysis constraints that the demands during the hydraulic analysis must be specified.

Linear regression analysis, based on the simulation results from five of the six pressure zone distribution systems (i.e., 1449, 1000, 579, 426, and 448&462), was performed to develop a relationship between normalized demand, ND, i.e., the ratio
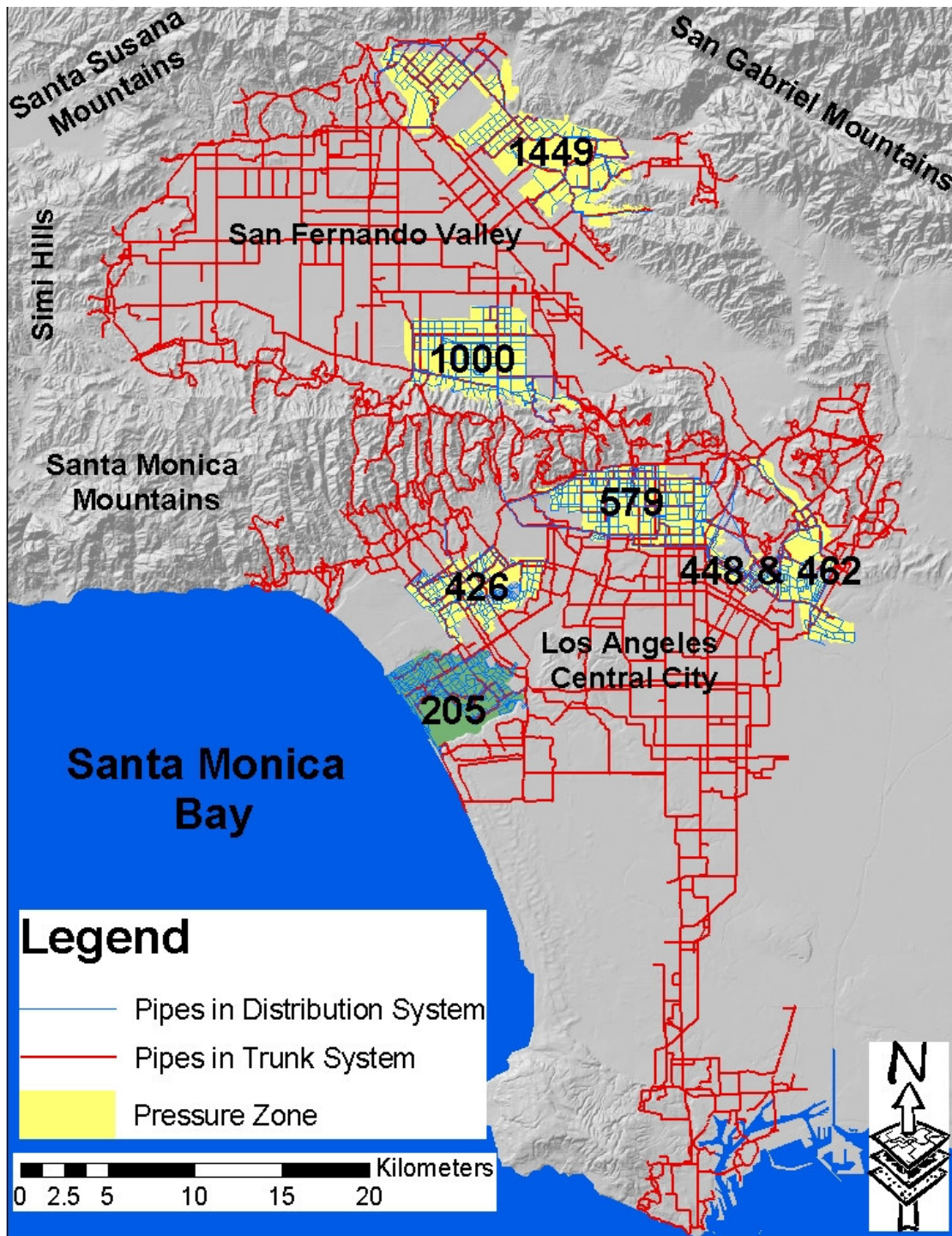
Figure 6.6.  Spatial Distribution of Six Pressure Zone Distribution Systems

of nodal demands after and before damages, and the repair rate, $\lambda$, in units of repair number per kilometers. The regression can be expressed as

$$ND = c + m\lambda \tag{6.11}$$

where c and m are regression constants, further correlated with the mean pressure, $P_m$, of the pressure zone distribution systems, using a similar linear regression process. Two sets of linear regression constants, corresponding to a 90% confidence and mean level, respectively, are implemented in GIRAFFE to estimate the c and m values associated with the $P_m$ in various pressure zones. Since the 90% confidence level regression constants are conservative estimates and account, at least partially, for the data variability that regression analysis was unable to incorporate, one approach is to estimate c and m from $P_m$, as

$$c = 1.1412 + 0.0055 P_m \tag{6.12}$$

$$m = -0.0514 + 0.0347 P_m \tag{6.13}$$

in which $P_m$ is in units of psi.

Another approach is to use the linear regression for the population mean to estimate c and m from $P_m$, as

$$c = 0.9012 + 0.0036 P_m + N(0, \sigma_c) \tag{6.14}$$

$$m = -0.8770 + 0.0248 P_m + N(0, \sigma_m) \tag{6.15}$$

in which N(0, $\sigma_c$) is a normally distributed random variable with 0 mean and $\sigma_c$, standard deviation, and N(0, $\sigma_m$) is a normally distributed random variable with 0 mean and $\sigma_m$, standard deviation. Both $\sigma_c$ and $\sigma_m$ are a function of $P_m$, expressed as

$$\sigma_c = -0.0198 + 0.0015 P_m \tag{6.16}$$

$$\sigma_m = -0.3510 + 0.0094 P_m \tag{6.17}$$

The pressure zone 205 distribution system was analyzed independently to provide a check on the predictive capability of the regression models. Monte Carlo simulations were performed on the pressure zone 205 distribution systems by stochastically adding pipe break and leak to the distribution lines and monitoring the flow ratios in the trunk lines before and after the damages. The ratio of the flows in the trunk lines before and after the damages is assumed equivalent to the ratio of nodal demands before and after damages, and is compared with the ratio predicted using these two sets of regressions (Eqns 6.11, 6.12, and 6.13, or Eqns 6.11, 6.14, 6.15, 6.16, and 6.17), respectively. It was found that the simulation results are consistent with the predictions from both sets of regressions. Details on the distribution system simulations, regression analysis, and regression verifications are provided by Shi (2006).

### 6.3.4. Monte Carlo Simulations

Monte Carlo simulations can be performed using GIRAFFE, which performs each simulation following the flowchart shown in Figure 6.2. In each simulation,

GIRAFFE generates a series of random numbers to determine the occurrence of pipe damages in trunk lines, the types of damage (i.e., break or leak), and the types of leak, as described in the previous sections. Then GIRAFFE implements the hydraulic models for the pipe breaks and leaks in the systems and adjusts the nodal demands to account for the local distribution system damage implicitly. After the damages are implemented, GIRAFFE utilizes the EPANET hydraulic engine to check network connectivity, perform hydraulic analysis, and eliminate negative node pressure until no negative node pressure exists in the system. Finally, GIRAFFE compiles the results from each simulation and provides result statistics, such as mean system serviceability index.

The number of Monte Carlo Simulations can be either specified by users or automatically determined in accordance with the GIRAFFE's self-termination algorithm (Grigoriu, 1995). GIRAFFE monitors the variations of the simulation results, i.e., the mean and coefficient of variation (COV) of system serviceability index, as the number of Monte Carlo simulations increases. If the variation is insignificant, i.e., the mean and COV of the system serviceability index with additional five simulations are both within ±0.02 difference when compared with those without additional five simulations, GIRAFFE considers that sufficient number of Monte Carlo Simulations are performed such that representative simulation results are generated. However, GIRAFFE's self-termination algorithm requires at least fifteen simulations before the program is automatically terminated, and automatically terminates the simulations if the number of simulations exceeds 100. This ultimate termination number was never reached in the simulation performed for this report. The number also can be adjusted.

## 6.4. GIRAFFE Simulations of LADWP System Performance during 1994 Northridge Earthquake

The GIRAFFE capabilities were validated by one of the most severe water system damage case histories, i.e., the performance of the LADWP water supply system during the 1994 Northridge earthquake. This section provides a brief description on the observed LADWP system performance, GIRAFFE simulation procedure, and the comparison between the performance observation and the GIRAFFE simulation results. It is found that GIRAFFE is able to predict the flow patterns and water outage areas reasonably well. The favorable agreement between simulation results and system measurements shows that GIRAFFE is capable of modeling severely damaged water supply systems, and provides confidence in applying GIRAFFE in future studies. A full treatment on the case history, GIRAFFE simulation procedure, and result comparison is given by Shi (2006).

### 6.4.1. LADWP System Performance during the 1994 Northridge Earthquake

The Northridge earthquake ($M_w$ = 6.7) struck the densely-populated Northridge area in Los Angeles at 4:30 a.m. local time on January 17, 1994. The damage to the water supply system resulted from the Northridge earthquake is among the most extensive experienced in the U.S. history, being comparable to the damage sustained after the 1906 San Francisco and 1971 San Fernando earthquakes. The Northridge earthquake caused 70 repairs on trunk lines, 1,013 repairs on distribution lines, and damage to 5 water tanks. Figure 6.7 shows a spatial distribution of the damaged tanks and trunk line repairs. Most damage and repairs, and hence, the water outage occurred in the northern San Fernando Valley (Lund et al., 2005), as shown in
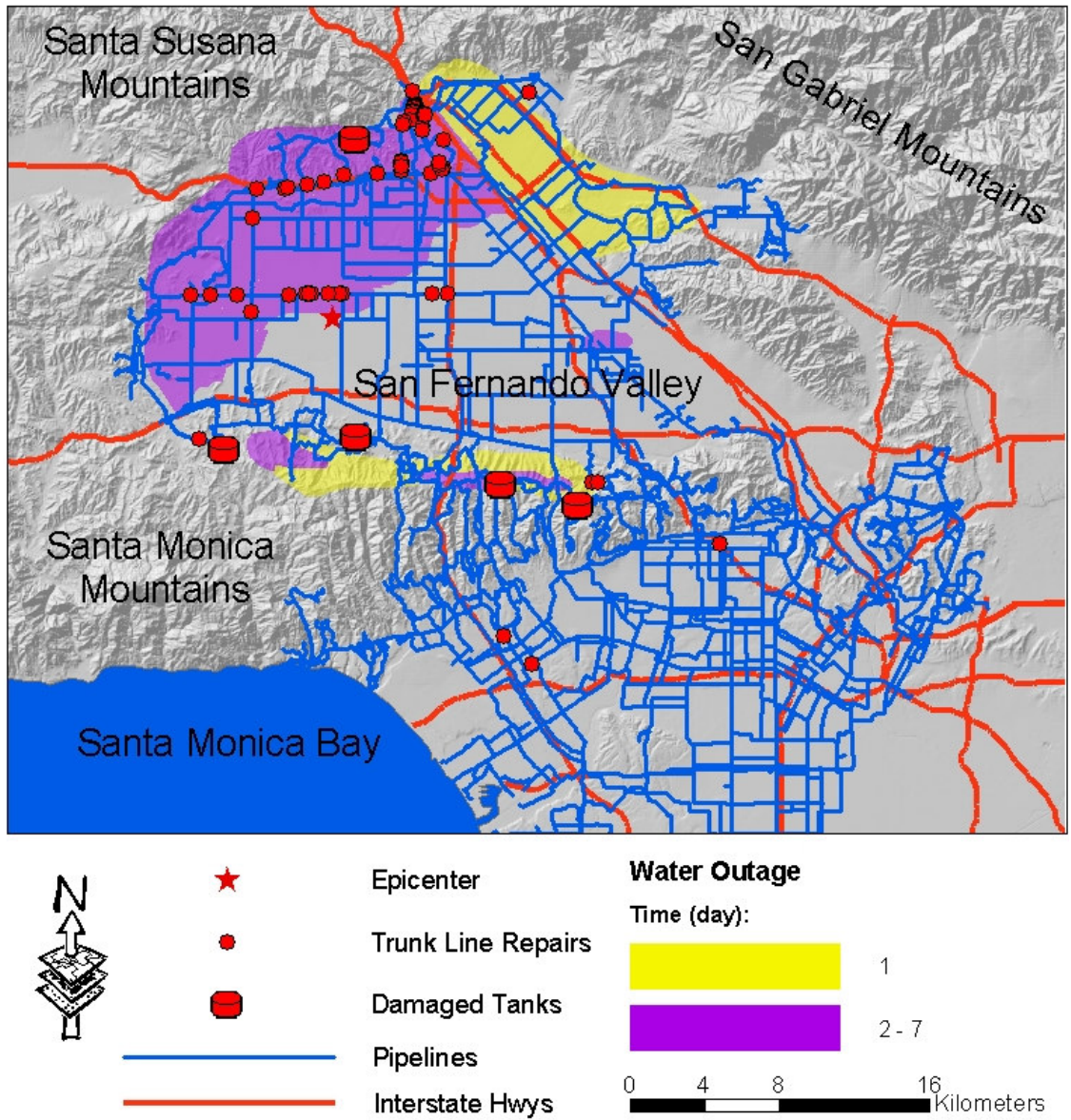
Figure 6.7.   Damaged Tank, Trunk Line Repairs, and Water Outage Areas Induced

by 1994 Northridge Earthquake

Figure 6.7. Approximately 15% of the population was subjected to water outage, and it took about 8 days to restore the disrupted water service after the earthquake. The cost of repairs to the LADWP water systems was about $44 million (Eguchi and Chung, 1995).

To monitor its system performance, LADWP deployed a Supervisory Control and Data Acquisition system (SCADA) covering the whole system. 37 flow meters are located in the San Fernando Valley, where most damage and water outage occurred, and provided first-hand records on how the system behaved before and after the earthquake. The flow meter data were utilized to provide clues on the emergency operations and system reconfiguration after the earthquake and to compare the numerical simulation results. However, as the quality of the 37 monitor data is not consistent among each other, screening process is necessary before their utilization. Three screening criteria are adopted to assure the quality of the monitor data: 1) The meters indicating zero flow before and after the earthquake are considered either malfunctioned or out of service; 2) The meters with a maximum recording flow less than 1000 gpm are discarded; and 3) The constant reading (i.e., constant reading up to the last fourth digit after the decimal point) following the earthquake is considered as malfunction because of the electricity outage after the earthquake. After applying these criteria, thirteen monitor data remain and were utilized further in this study, which is discussed in more details in the following section.

### 6.4.2. GIRAFFE Simulation Procedure

Since most damage and water outage occurred in the San Fernando Valley, the simulation focuses on the northern half of the LADWP system, including six subsystems: Granada Hills (GH), Foothills (FH), Sunland/Tujunga (ST), Valley Floor (VF), Encino Hills (EH), and Santa Monica Mountains (SM) subsystems. Figure 6.8 shows the northern half of the LADWP system, together with a spatial distribution of the thirteen SCADA flow meters. The flow meter readings at River Supply Conduit,
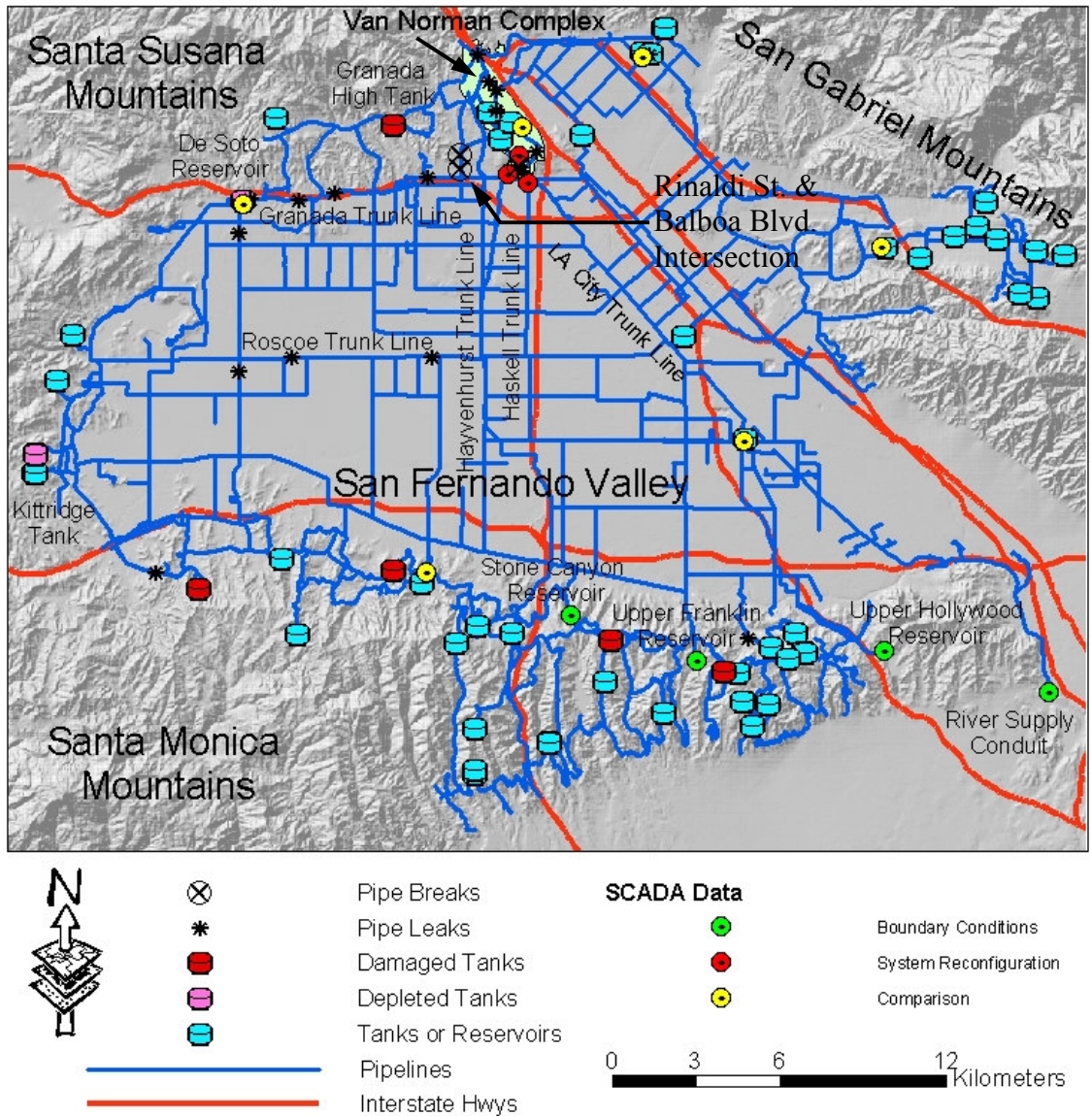
Figure 6.8.   GIRAFFE Simulation of the Northern Half of LADWP System

Upper Hollywood Reservoir Inflow, Upper Franklin Reservoir Inflow, and Stone Canyon Reservoir Inlet, which act as the connectors between the northern and southern halves of the LADWP system, were utilized as boundary conditions for the northern half of the system, as illustrated by green dots in Figure 6.8.

The hydraulic network for the northern half of the system was exported from H2ONET database used by LADWP engineers. Since the Northridge earthquake occurred in January, a typical winter demand is applied in the simulation. The virtual demands at River Supply Conduit, Upper Hollywood Reservoir Inflow, Upper Franklin Reservoir Inflow, and Stone Canyon Reservoir Inlet, representing the water demands of the southern half of the system, were recalibrated in accordance with the actual flow readings at the four locations, respectively.

As mentioned in Chapter 4, the LADWP hydraulic network model was developed for planning purposes and contains only pipelines with relatively large diameter. Therefore, only water tank damage and trunk line repairs are simulated directly. After a careful review on the 70 trunk line repair records, a repair on LA City Trunk Line in the lower Van Norman Complex, and two repairs on Granada Trunk Line and Rinaldi Trunk Line, respectively, in the intersection of Rinaldi St. and Balboa Blvd., as shown in Figure 6.8, are modeled as pipe break, a complete loss of the pipe connectivity. Other repairs are modeled as pipe leak, as described in Section 6.3.2.3. The hydraulic model parameters for the pipe leakage are determined in accordance with the characteristics of the repairs. To simplify the simulation, multiple nearby repairs on the same trunk line are lumped together. For example, twenty-eight repairs on the Granada Trunk Line, except for the one modeled as a pipe break, are simplified as four pipe leaks. Thirteen repairs on the Roscoe Trunk Line are lumped together as two pipe leaks. In total, twenty pipe leaks were used to simulate the trunk line performance after the earthquake, as shown in Figure 6.8.

As illustrated by red dots in Figure 6.8, three flow meters monitoring the flow in LA City, Haskell, and Hayvenhurst Trunk Lines in the lower Van Norman Complex,

respectively, are utilized to provide guidance on how the system was reconfigured shortly after the earthquake. The three flow meter data show that the flows decreased to zero shortly after the earthquake, suggesting that these three pipe segments, which sustained severe damage, were isolated promptly to prevent water loss. Please note that the isolated section in the LA City Trunk Line is located upstream of the connection between the LA City Trunk Line and the LA Reservoir Outlet, the main water source for LA City Trunk Line. Therefore, the isolation had little impact on the water flow southward through the LA City Trunk Line (Please refer to Chapter 4).

Four of the five damaged water tanks were simulated by disconnecting them from the system. The Granada High Tank located in the northern San Fernando Valley collapsed completely during the Northridge earthquake and was removed permanently after the earthquake. The current LADWP hydraulic network model does not include the Granada High Tank, and, it was therefore not simulated in this study. The Kittridge Tank on the western rim of the San Fernando Valley and De Soto Reservoir on the northern rim of the San Fernando Valley, as shown by pink symbols in Figure 6.8, were removed from the GIRAFFE simulation because they were depleted shortly after the earthquake. Hydraulic simulation shows that the Kittridge Tanks and De Soto Reservoir were empty within several hours after the earthquake. The depletion of the tanks and reservoir was confirmed by the LADWP engineers (Vargas, 2005).

The interaction between the water supply and electric power systems was accounted for in the simulation. The longest power outage, i.e., 27 hours (LADWP, 1994), occurred in the northern San Fernando valley, where the most important water system facility, i.e., Van Norman Complex, is located. The power outage rendered the pump stations in the Van Norman Complex inoperable. Accordingly, the pump

stations in the Van Norman Complex were turned off in the simulations after the earthquake.

### 6.4.3. GIRAFFE Simulation Results

Figure 6.9 shows the GIRAFFE simulation results, superimposed by the observed water outage areas. The original no-flow pipes in the intact system and the damage-induced no-flow pipes are color coded by pink and red, respectively. The unsatisfied demands are illustrated by yellow dots. Most damage-induced no-flow pipes and unsatisfied demands occurred in the northern and western San Fernando Valley, consistent with the areas of observed water outage for more than one day.

Figure 6.9 illustrates the locations of 6 SCADA flow meters providing data pertaining to the LA Reservoir Outlet, Encino Reservoir outflow, Granada Trunk Line, Morella & Van Owen Regulation Station, Astoria Pump Station, and Green Verdugo Pump Station, respectively. Figure 6.10 shows comparisons between the GIRAFFE simulation results and the monitored data at each flow meter. In general, the simulation results compare favorably with the monitored data at each location.

The earthquake-induced damage had different effects on the water supply system components at different locations in the system. The earthquake led to flow decrease in some components, such as LA Reservoir Outlet and Morella & Van Owen Regulation Station, or even complete loss of component functionality, such as zero flow in Granada Trunk Line and Astoria Pump Station. On the other hand, some components were little affected by earthquake-induced damage. Consider, for example, Green Verdugo Pump Station, which is located far away from the major damage in the
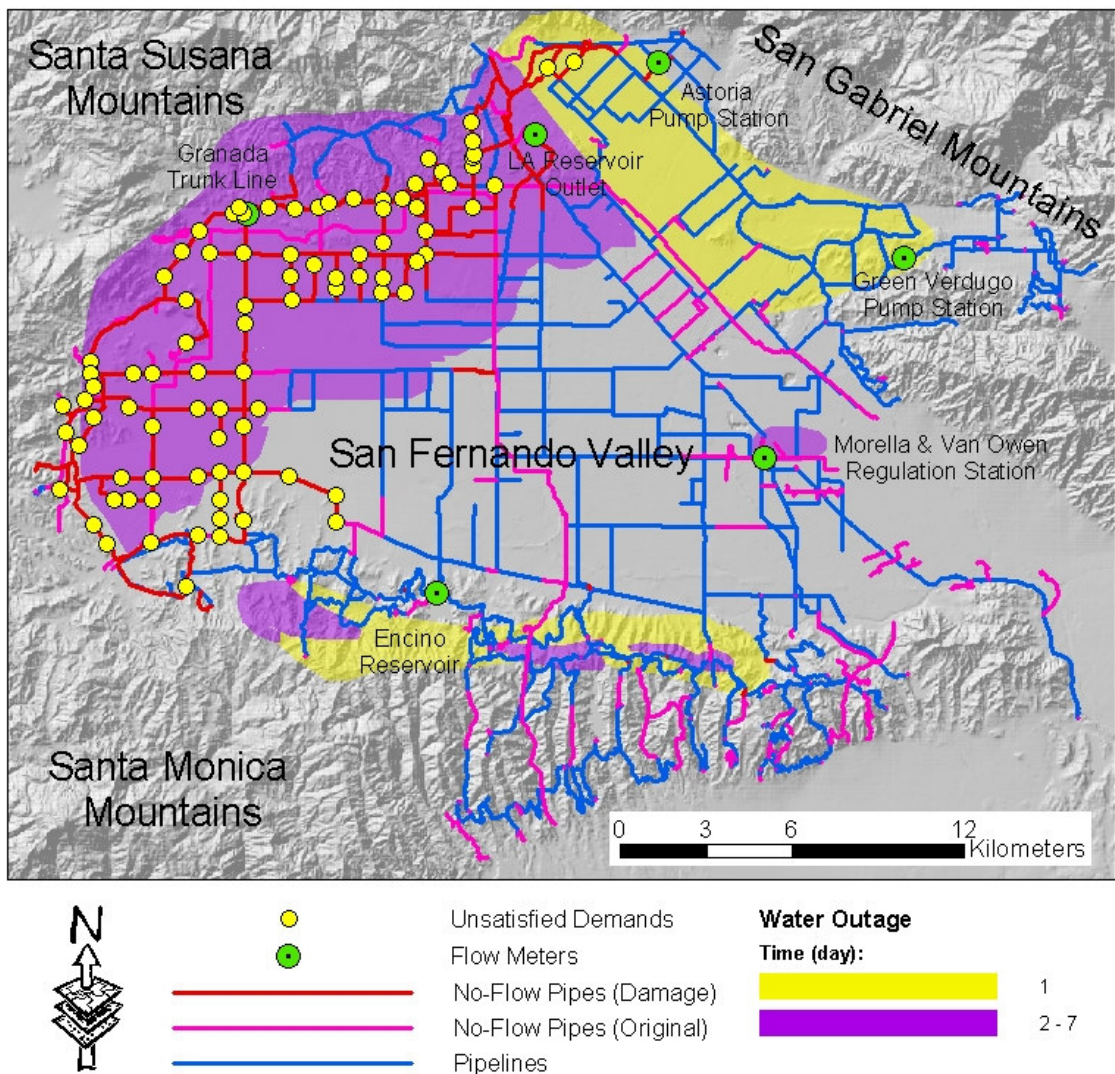
Figure 6.9.  GIRAFFE Simulation Results

San Fernando Valley and was not influenced by the damage. The damage may result in flow increase in some components, such as Encino Reservoir, to compensate the loss of functionality of other damaged components. The Encino Reservoir had to provide more water to the southern San Fernando Valley after the earthquake to compensate for the loss of water that normally flows from the north. Despite of this variability, the difference between the monitored data and simulation results is

213
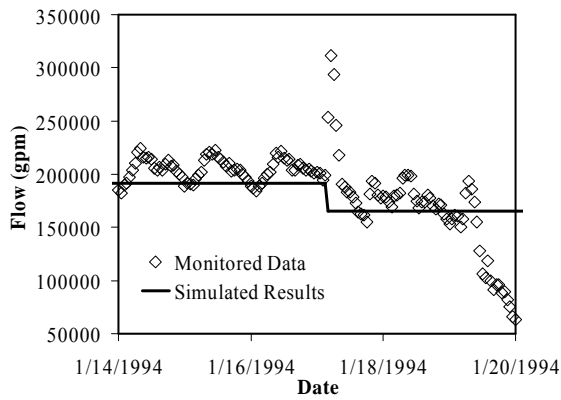
(a) LA Reservoir Outlet
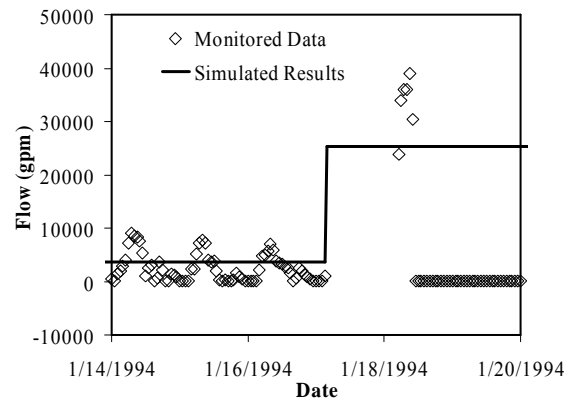
(b) Encino Reservoir Outflow
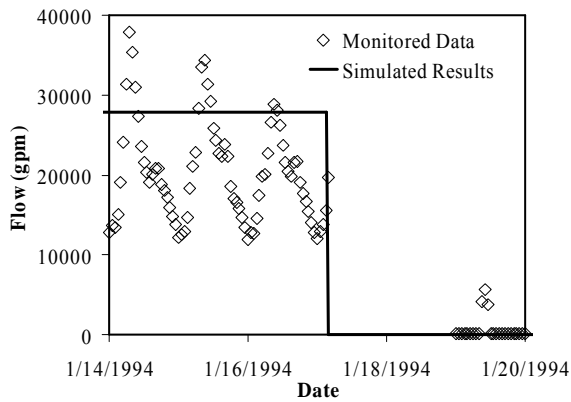
(c) Granada Trunk Line Flow
Station
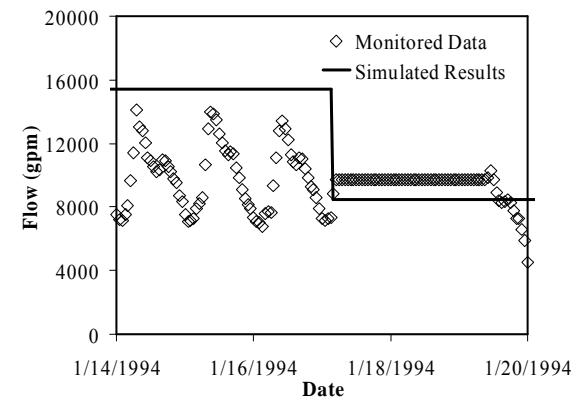
(d) Morella & Van Owen Regulation Station
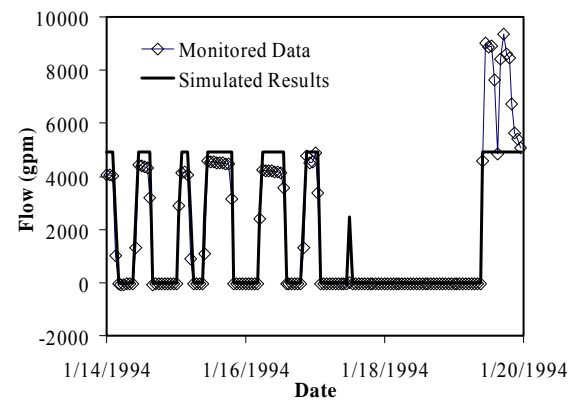
(e) Astoria Pump Station
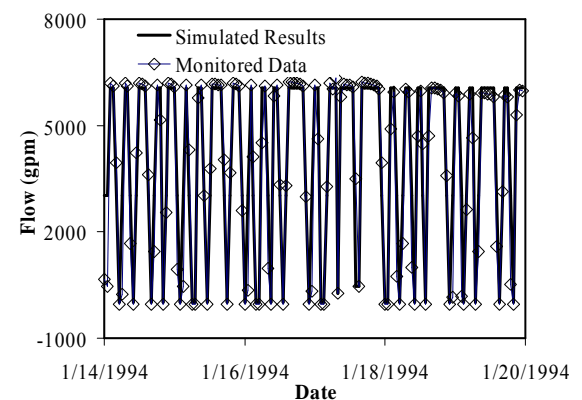
(f) Green Verdugo Pump Station

Figure 6.10.    Comparisons between GIRAFFE Results and Monitored Data

214

generally less than 10%. The favorable agreement between simulation results and system measurements shows that GIRAFFE is capable of modeling severely damaged water supply systems, and provides confidence in applying GIRAFFE in future studies.

## 6.5. Summary

This chapter briefly describes the special hydraulic analysis computer program (GIRAFFE) used in this work. GIRAFFE is able to compensate for the limitations of commercially available hydraulic analysis software in predicting unrealistic negative pressures in a heavily damaged system by eliminating portions of the network containing negative pressures. GIRAFFE simulates trunk line damage explicitly by a Poisson process to model the occurrence of pipe damage and hydraulic models for both pipe break and leak to model the water outflow from the system. In addition, damage to distribution lines is simulated implicitly by adjusting the nodal demands in the trunk line system. GIRAFFE is capable of performing Monte Carlo simulations and compiling the simulation results in a format that can be used in GIS. The LADWP water supply system performance during the 1994 Northridge earthquake was modeled using GIRAFFE, and it was found that GIRAFFE provided simulation results consistent with the observed water outage and the recorded flows in the system after the earthquake. The favorable agreement between simulation results and system measurements shows that GIRAFFE is capable of modeling severely damaged water supply systems, and provides confidence in applying GIRAFFE in future studies.

# CHAPTER 7

# PROBABILISTIC SEISMIC PERFORMANCE EVALUATION OF LADWP WATER SUPPLY SYSTEM

## 7.1. Introduction

The framework for evaluating earthquake effects on lifeline systems outlined in Chapter 2 is applied to evaluate the seismic performance of the LADWP water supply system. This chapter summarizes the implementation of the evaluation framework and presents the evaluation results. It starts with the evaluation procedures employed, assumptions adopted, and input parameters or analysis models utilized, then proceeds to an illustration of the evaluation process using the performance of the LADWP water supply system subjected to one (i.e., the Scenario 175 Verdugo earthquake) of the 59 scenario earthquakes described in Chapter 3. The results of the probabilistic evaluation for the 59 scenario earthquakes are aggregated in the form of risk curves, for both the entire LADWP system and the five water districts, respectively. Key contributing scenario earthquakes for the system risks are identified by deaggregation plots. Finally, the evaluation results are organized such that they can be utilized in the consequence analysis, such as economic loss, community impacts, and emergency response and restoration.

## 7.2. Evaluation Procedures

The basic chain of activities in the seismic performance evaluation of the LADWP water supply system includes the seismic hazard characterizations, system property characterizations, analyses of the interaction between seismic demand and lifeline component or facility response, and the assessment of system response and its consequences for the regional economy and community institutions, which are described in the following subheadings, respectively.

### 7.2.1. Seismic Hazards

For each of the 59 scenario earthquakes described in Chapter 3, ground motions were generated at 572 points in a grid covering the LADWP system and interpolated to develop contour surfaces, which were then corrected for site conditions following the NEHRP-HAZUS approach. The seismic demands on system components, e.g., peak ground velocity for pipelines, were determined from the corrected contour surfaces according to their locations. This allows for the performance evaluation of the system components as well as for the entire system when subjected to the scenario earthquakes. Ground motions, corresponding to mean + $\sigma_{inter-event}$ level, were used in this work. $\sigma_{intra-event}$ describes the variation of ground motion resulting from different earthquake source characteristics, as discussed in Section 3.2.1.5.

Similar processes were applied for the 59 individual scenario earthquakes and the results, together with the corresponding annual frequencies of occurrence, were integrated to develop the risk curves, as discussed in Section 7.4. It is assumed that

when the seismic hazards from the 59 scenario earthquakes match those from the USGS 2002 dataset, the LADWP system seismic performance evaluation using the 59 scenario earthquakes is representative of the system seismic performance according to the USGS 2002 dataset.

### 7.2.2. System Characteristics

The system characteristics of the LADWP water supply system are embodied in a H2ONET hydraulic model, as described in Chapter 4. The H2ONET hydraulic model is provided by LADWP engineers and contains 9,287 nodes and 10,665 links, representing about 2,186 km of pipelines, 1,052 demand nodes, 591 control valves, 110 tanks and reservoirs, 151 local groundwater wells, and 284 pumps. Since the H2ONET hydraulic model was originally developed for planning purposes, it contains only pipelines with relatively large diameter. The H2ONET hydraulic model contains twelve different simulation scenarios representing either the whole or part of the LADWP system with various system valving and control strategies and demand sets simulating either summer or winter demands. Because the summer demand is the highest demand likely to be experienced by the system, the scenario "SUMMER, All thirteen Subsystems without closed valves", which contains the entire LADWP water supply system with the typical summer valving and control strategies and summer demand set, was utilized in the system seismic performance evaluation.

Using the export function in the H2ONET software, the selected scenarios in H2ONET hydraulic model were exported into a standard EPANET format, which is the input data format for GIRAFFE. Two independent hydraulic simulations for the selected scenario were performed using H2ONET and GIRAFFE (i.e., EPANET

hydraulic engine), respectively, and the results were compared. It is found that the overwhelming majority of the links and nodes have identical flows or pressures from both simulations using different software packages. However, because of the inevitable difference in numerical procedures inherent in two different software packages, minor difference exists in a small portion of links and nodes. The maximum flow difference in links is less than 0.38 $m^3$ per minute (100 gpm) or 1% and the maximum pressure difference in nodes is less than 13.8 kPa (2 psi) or 1%. It was verified that GIRAFFE provides virtually identical results for the undamaged LADWP system when comparing with results from H2ONET.

### 7.2.3. System Component Performance Evaluation

This work focuses on seismic wave (TGD) interactions with pipelines, which have an important impact on system performance. The seismic performance evaluation of other components, such as pump stations, regulation stations, ground water wells, and tanks and reservoirs, is not included in this work. Procedures are available for modeling the seismic performance of these facilities by means of fragility curves (ALA, 2001), which relate the probability of reaching or exceeding a particular damage state to a particular level of earthquake hazard. Such procedures can be readily incorporated in future simulations. Localized and relatively minor PGD effects are implicitly covered by the regression relationships between repair rate and PGV, but locally large PGD events are not. Models exist for soil-structure interaction under various PGD scenarios (e.g., O'Rourke, 1998; and O'Rourke and Liu, 1999), and can be easily incorporated in the approach developed in this work. PGD characterization generally depends on explicit information about subsurface soil conditions and ground failure hazards. Moreover, the risk of ground failure at specific locations will be linked

to specific scenario earthquakes because of proximity and level of TGD needed to trigger PGD. Accounting for PGD in a probabilistic format that is consistent with PSHA approach adopted (see Section 2.3.1 and Chapter 3) for TGD is beyond the scope of this work. The framework for PSHA evaluation of lifeline system performance has nonetheless been established, and provides a sound basis for incorporating both PGD and TGD hazards in subsequent development.

Chapter 5 presents models on seismic wave interaction with pipelines, which can be utilized to evaluate the seismic performance of pipelines. However, to apply those models, details are required on seismic wave characteristics, e.g., predominant period and apparent wave velocity, pipeline properties, e.g., cross-sectional area and axial deformation stiffness, and ground conditions, e.g., burial depth, unit weight of soils, and pipe-soil interface friction angle. This information is quite often not available, particular for such a large and complex system as the LADWP system, which contains about 12,000 km pipes covering an area of approximately 1,200 km$^2$. One alternate method, which requires minimal input parameters, for estimating pipeline damage during earthquakes is to use regressions between observed repair rates and measured seismic parameters during previous earthquakes. The regressions adopted in this research are summarized in Sections 7.2.3.1.

As described in Chapter 4, the H2ONET hydraulic model contains only pipelines with relatively large diameter and includes the majority of local distribution lines by aggregating them to demand nodes. The damage to the pipelines included directly in H2ONET model was simulated explicitly, as summarized in Section 7.2.3.2. In contrast, as the H2ONET contains no explicit information on the majority of local

distribution lines, an implicit approach to simulate their damage was applied, as described in Section 7.2.3.3.

## 7.2.3.1. *Regressions for Estimating Pipeline Damage*

The damage to cast iron and ductile iron pipelines was estimated using the regressions developed by Jeon (2002). Empirical data were collected about pipeline repairs and locations of repairs after the 1994 Northridge earthquake and incorporated in a large GIS database, consisting of over 12,000 km of pipelines in greater Los Angeles area and more than 240 strong motion records. Records from over 240 strong motion stations throughout the earthquake-affected area were analyzed with respect to various seismic parameters (Toprak, 1998). The spatial distributions of different seismic parameters were estimated by interpolation and superimposed on the pipeline network and spatially distributed database of pipeline damage. Where possible, pipeline repairs in zones of documented PGD were screened from the repair rates so that the resulting statistics would reflect principally the effects of seismic waves or TGD. Using the GIS software, the repair rate was calculated for areas influenced by specific seismic parameters. Correlations then were developed through regression procedures to obtain the most statistically significant relationships among repair rate and values of different seismic parameters. It was found that the most statistically relevant parameter for correlation with repair rate is PGV. Figure 7.1 shows the linear regressions developed by Toprak (1998) and Jeon (2002) and utilized in this work to calculate the repair rates from PGVs for cast iron and ductile iron pipelines.

Following the procedures developed by Jeon (2002), regressions of repair rate vs. PGV for trunk lines composed of other materials were developed and included in

222
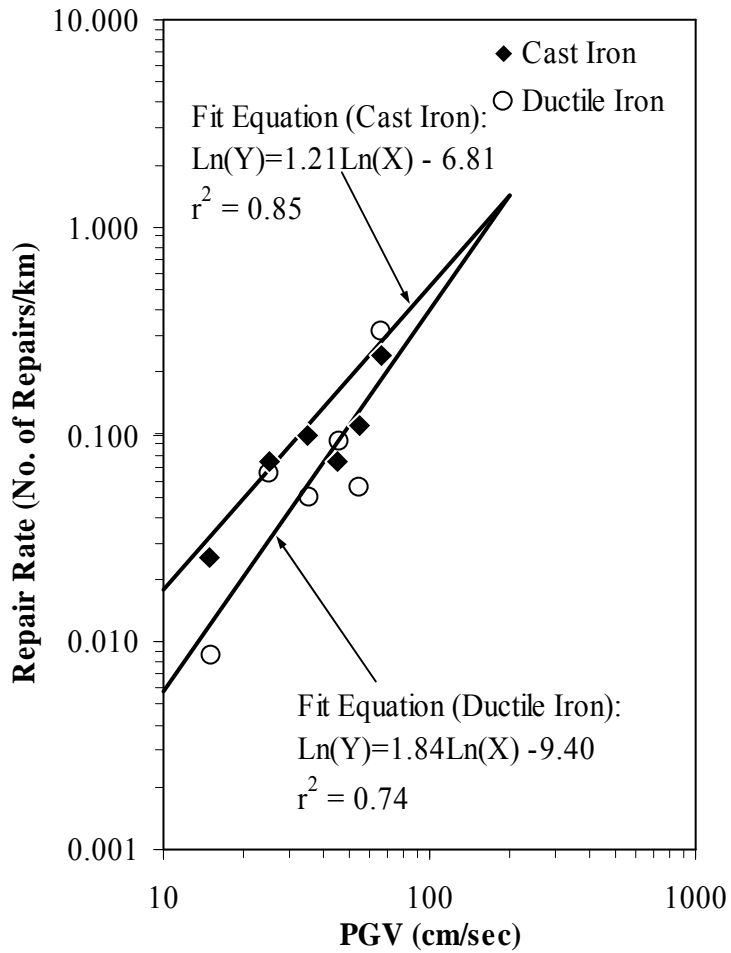
Figure 7.1.   Regressions of Repair Rate vs. PGV for Cast Iron and Ductile Iron

Pipelines (after Jeon, 2002)


Appendix A. Figure 7.2 shows the regressions for concrete, riveted steel, and steel

pipelines.


The repair rates of pipelines composed of different materials were calculated in

accordance with PGV using the regressions shown in Figures 7.1 and 7.2. An equal-

weight average of five repair rates using the five regressions in the figures was applied

to the pipelines (about 7% of total length in the LADWP system) without composition

information available in the H2ONET database.
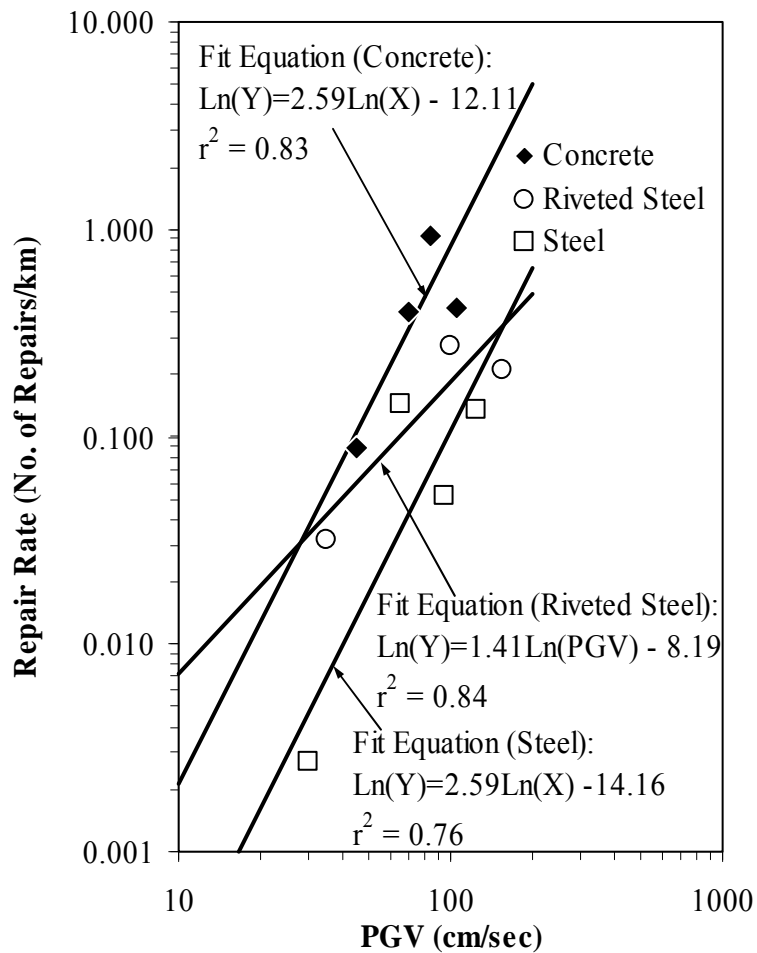
Figure 7.2. Regressions of Repair Rate vs. PGV for Concrete, Riveted Steel and Steel

Pipelines

## 7.2.3.2. *Explicit Trunk Line Damage Simulations*

The occurrence of damage to the pipelines included directly in the H2ONET hydraulic model was simulated by a Poisson process in GIRAFFE. The details on the Poisson process simulation are given in Chapter 6 of this work and by Shi (2006). The repair rate, i.e., number of repairs per km, for each pipe was calculated according to the repair rate vs. peak ground velocity regressions described in Section 7.2.3.1. As

described in Chapter 3, if the pipeline is so long that extends over several PGV contour intervals, the GIS "Intersect" function divides the pipeline into several new short pipes, each of which falls into a single PGV contour interval. The repair rates for these short pipes were calculated individually, using the repair rate vs. PGV regressions, and integrated by a weighted average according to the pipe lengths to obtain the repair rate for the original long pipe. GIRAFFE can simulate multiple damages along one pipe and further divides the pipe damage into either pipe break or leak.

Two different hydraulic models for pipe break and leak were implemented, respectively, in GIRAFFE after the simulation of pipe damage occurrence and the determination of damage category, i.e., pipe break or leak. The pipe leak was further categorized into five types according to pipe materials and the occurrence of leak types was determined stochastically. More details on the hydraulic models and the determination of leak types are given in Chapter 6 and by Shi (2006).

### 7.2.3.3. *Implicit Simulations of Local Distribution Line Damage*

As mentioned in Chapter 4, the H2ONET hydraulic model used in this work was used by LADWP engineers (LADWP, 2002a) for system planning and management purposes, and hence, contains only pipelines with relatively large diameter or water delivery significance. Figure 7.3 shows about 12,000 km pipelines operated by LADWP, as opposed to about 2,800 km pipelines included in the H2ONET database. Most distribution lines in the LADWP system, as color-coded by red in Figure 7.3, are not directly included in the H2ONET hydraulic model, which contains mainly trunk lines, as color-coded by blue in Figure 7.3. Most distribution
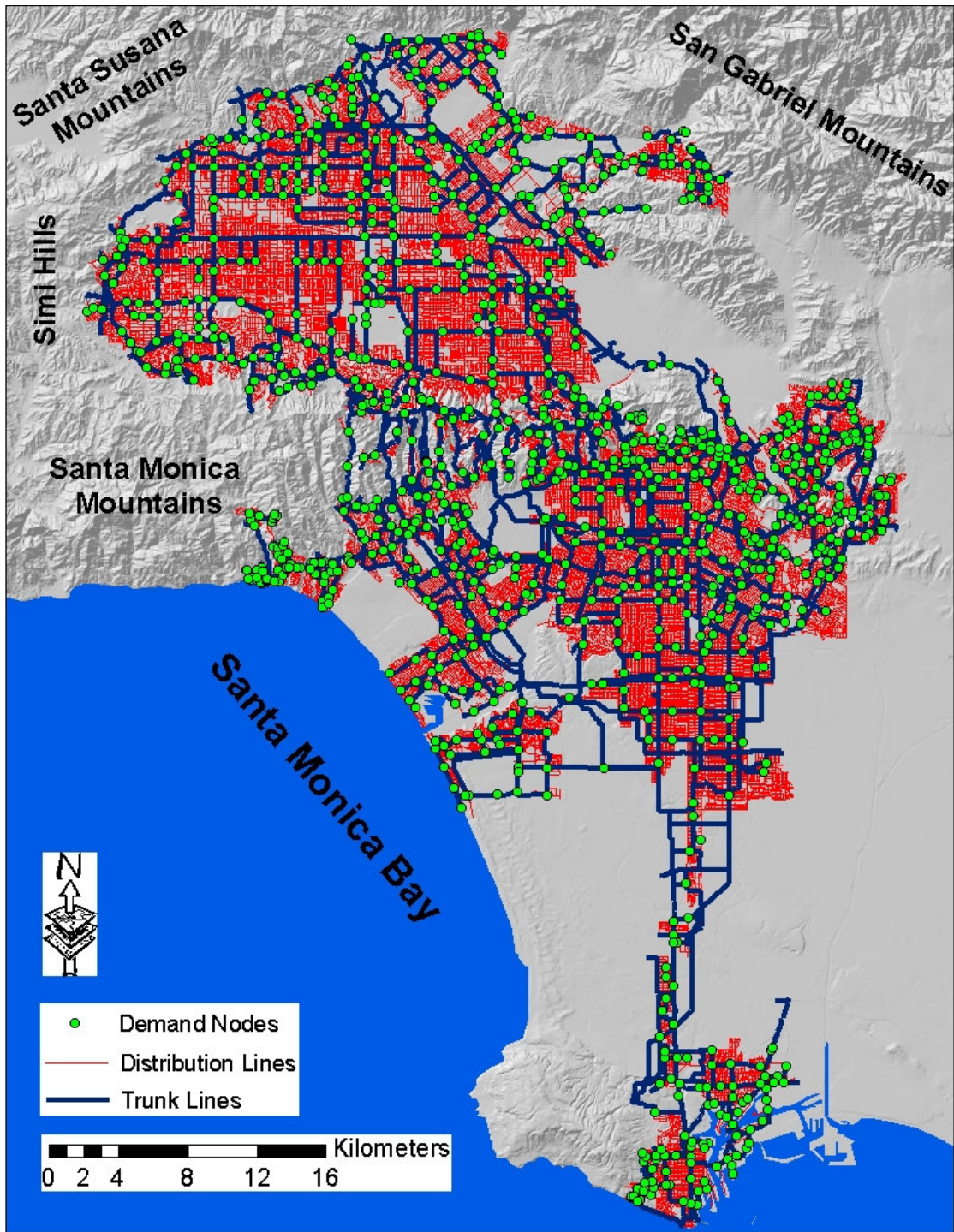
Figure 7.3. Simplifications of LADWP Water Supply System in H2ONET Database

226

lines are accounted for implicitly in the H2ONET database by aggregating them into demand nodes, as shown by green dots in Figure 7.3. From this perspective, each of the 1,052 demand nodes in the LADWP hydraulic network model represents a small-scale local distribution system.

Because of the lack of details on the local distribution systems in the LADWP hydraulic model, the damage to the local distribution system can not be simulated explicitly, as described in Section 7.2.3.2 for trunk lines. The GIRAFFE simulates the damage to local distribution system damage by adjusting the water demands in the demand nodes according to the distribution system damage after earthquakes, as described in Section 6.3.3.

The PGVs to the demand nodes are determined by superimposing the spatial distribution of demand nodes on PGV contour surfaces, as described in Section 3.4.4. A demand node is typical linked to a local distribution system that is sufficiently small that strong motion effects can be modeled with sufficient accuracy by a single representative seismic parameter. The repair rate in the local distribution systems represented by the demand nodes was estimated using the repair rate vs. PGV regressions. Since majority, i.e., 72% (Jeon, 2002), of the local distribution pipelines in the LADWP system is composed of cast iron, the cast iron regression was utilized to estimate the repair rate. The increases in nodal demands were calculated using Eqn 6.11, the regression constants c and m of which were estimated from the mean pressure, $P_m$, of the local distribution systems, using the 90% confidence linear regressions, i.e., Eqns 6.12 and 6.13. Figure 7.4 shows a spatial distribution of $P_m$ for local distribution system. The demand nodes are color-coded by the $P_m$ of the local distribution systems they represent. The high mean pressure occurs in the mountainous
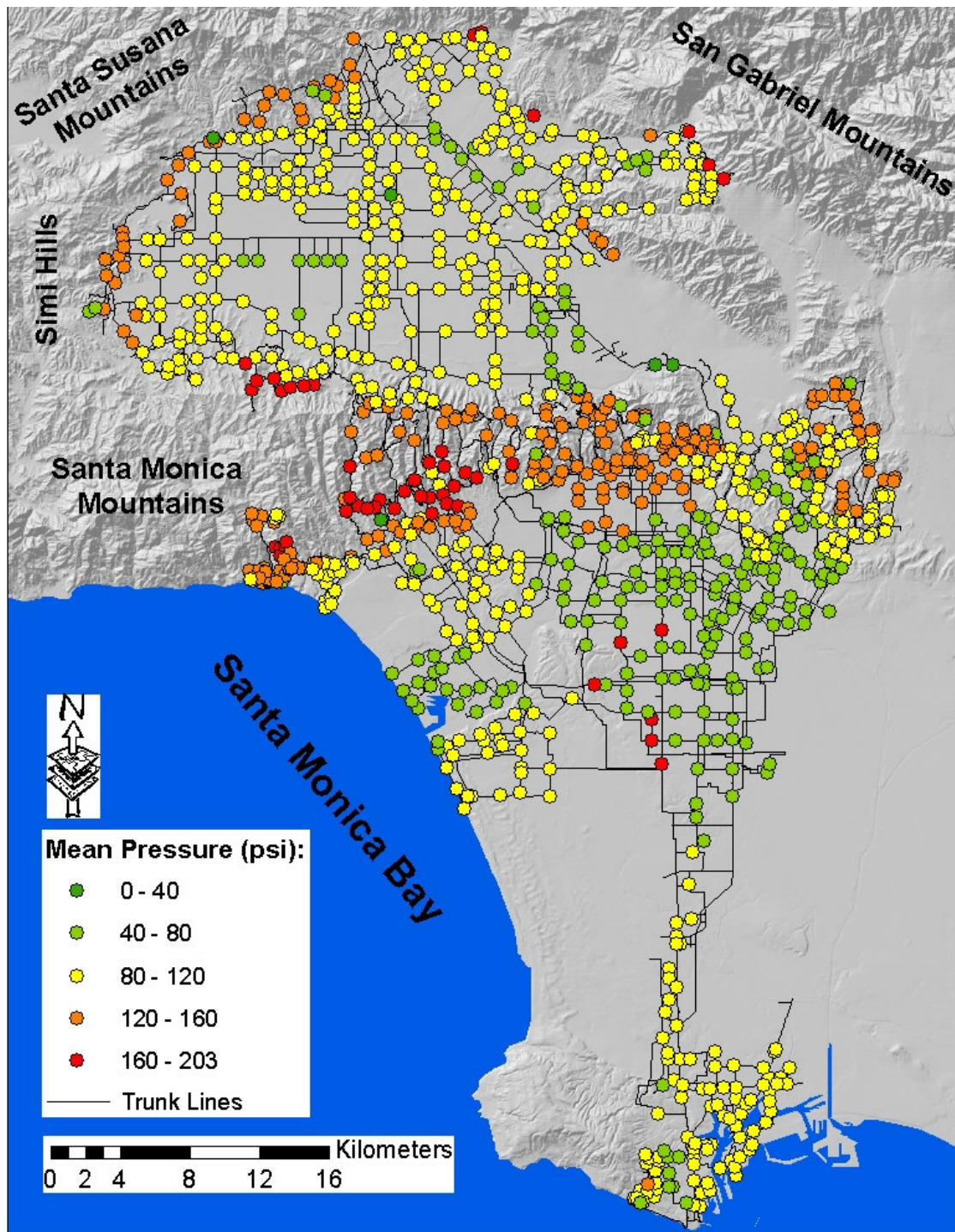
Figure 7.4.   Spatial Distribution of Mean Pressures for Local Distribution Systems

areas, i.e., Santa Susana Mountains, Simi Hills, and Santa Monica Mountains, to accommodate large elevation difference in those areas. Since c and m are linear function of $P_m$ (refer to Eqns 6.12 and 6.13), more nodal demand increases are expected in those areas, given the PGVs or the repair rates are similar in the local distribution systems.

### 7.2.4. System Performance Evaluation

The seismic system performance of the LADWP water system was evaluated using GIRAFFE. Monte Carlo simulations were performed for each of the 59 scenario earthquakes. In each simulation, GIRAFFE simulated the trunk line damage explicitly by implementing the hydraulic models for pipe breaks and leaks, and modeled the damage to local distribution system implicitly by adjusting the nodal demands according to the repair rates in the local distribution systems. Then, GIRAFFE utilized the EPANET hydraulic engine to check network connectivity, perform hydraulic analysis, and eliminate negative node pressures until no negative node pressures are present in the system. Finally, GIRAFFE compiled the results from each simulation and provided result statistics, such as the mean system serviceability index, as defined in Section 6.3.1.

In addition, GIRAFFE was utilized to study the effects of water loss from storage tanks. Leaking and ruptured pipelines will draw down the water levels in tanks and local reservoirs, thereby further reducing flow and pressure in the pipeline network. Evaluating the effects of water losses from tanks and reservoirs may provide a more representative model for post-earthquake performance because it will take

229

water utility crews some time to isolate leaks and pipeline breaks to reduce their impact on local water sources.

For each simulation that accounts for tank water losses, after all negative pressure nodes were eliminated and the simulation results were complied, the water levels of the storage tanks in the system were updated according to the flow rates determined from the hydraulic analysis to simulate the impact of leakage from damaged pipelines for a 24-hour period after the earthquake. The system with the updated tank water level was reanalyzed in GIRAFFE to eliminate additional negative pressure nodes resulting from the loss of storage water in tanks, and the second set of simulation results with a 24-hour period of running tanks was generated. For more details about the implementation of the storage water loss effects in GIRAFFE simulations, please refer to Shi (2006).

The number of Monte Carlo simulations was automatically determined in accordance with the GIRAFFE's self-termination algorithm (Grigoriu, 1995) with a convergence tolerance of $\pm 0.02$ difference for both mean and COV of the system serviceability index. It is found that the Monte Carlo simulations for all 59 scenario earthquakes terminated at a number of fifteen, resulting in 885 simulations in total.

An example of the simulations is given in Section 7.3, using the Scenario 175 Verdugo earthquake. Similar procedures apply for each of the 59 scenario earthquakes and the simulation results from the 59 individual scenario earthquakes are integrated in the form of risk curves, as described in Section 7.4.

### 7.2.5. Social and Economic Consequence Evaluation

The social and economic consequence evaluations for the LADWP water supply system are performed by other MCEER researchers, and are beyond the scope of this report. As described in Chapter 2, Computable General Equilibrium (CGE) models have been developed to assess the economic impacts caused by earthquake-induced lifelines losses (e.g., Rose and Liao, 2003 and 2005; and Rose and Guha, 2003). The community impacts of the seismic-induced lifeline loss have been evaluated by other researchers (e.g., Chang and Miles, 2003; and Chang and Chamberlin, 2004). Davidson and Cagnan (2004) and Cagnan (2005) modeled lifeline system restorations after earthquakes and simulated system repair and recovery operations for both the LADWP water supply and electric power systems. Each of these simulations relies on information about damage states, as provided by the system simulation model developed in this work. For example, input for evaluating regional economic consequence of damage is provided in the form of water availability in the 13 subsystems after earthquakes, as described in Section 7.5.

## 7.3. Evaluation Example: Scenario 175 Verdugo Earthquake

The simulation processes described in Section 7.2 are illustrated using the Scenario 175 Verdugo earthquake. PGV contour surfaces generated in Chapter 3 (refer to Figures 3.12 and 3.13) were utilized to determine the PGV for each trunk line and demand node representing the local distribution system, and the repair rate for each pipe was estimated accordingly. The damage to the pipelines, included directly in the H2ONET database, were simulated explicitly, while those to the local distribution systems were modeled implicitly by adjusting the nodal demands, as described in

Section 6.3.3. The damage scenarios were imposed on the LADWP water system and the hydraulic network analysis was performed using GIRAFFE.

Figure 7.5 shows the spatial distribution of breaks and leaks simulated explicitly for the trunk lines and included in the H2ONET database, superimposed on the PGV contour surfaces. In this simulation, breaks occur in 25 pipes, as shown by red crosses in Figure 7.5, and leakage occurs in 143 pipes, as shown by triangles in Figure 7.5. The pipes with one leak are color-coded by green, as opposed to those with two or three leaks by yellow and red, respectively. Most pipe breaks and leaks occur in the upper right quarter of the figure, corresponding to the high PGV values in those locations. Pipe damage also occurs sparsely in the other parts of the system. It should be recognized that this specific simulation applies to one damage scenario triggered by one of the 59 scenario earthquakes. To capture properly the statistics of performance for a particular scenario earthquake, Monte Carlo simulations were performed, as described in Section 6.3.4.

Figure 7.6 shows the spatial distribution of demand nodes superimposed on the PGV contour surfaces. The demand nodes are color-coded according to the ratio of water demands after the earthquake normalized to those before the earthquake for implicitly modeling the damages to local distribution systems. High normalized demand ratios, indicating severe damage and water losses, occur in the upper right quarter of the figure, corresponding to the high PGV values in those locations. Because of the high mean pressures in the mountainous areas, i.e., Santa Susana Mountains, Simi Hills, and Santa Monica Mountains (please refer to Figure 7.4), high normalized demand ratios are also observed around Santa Monica Mountains and the rims of San Fernando Valley.
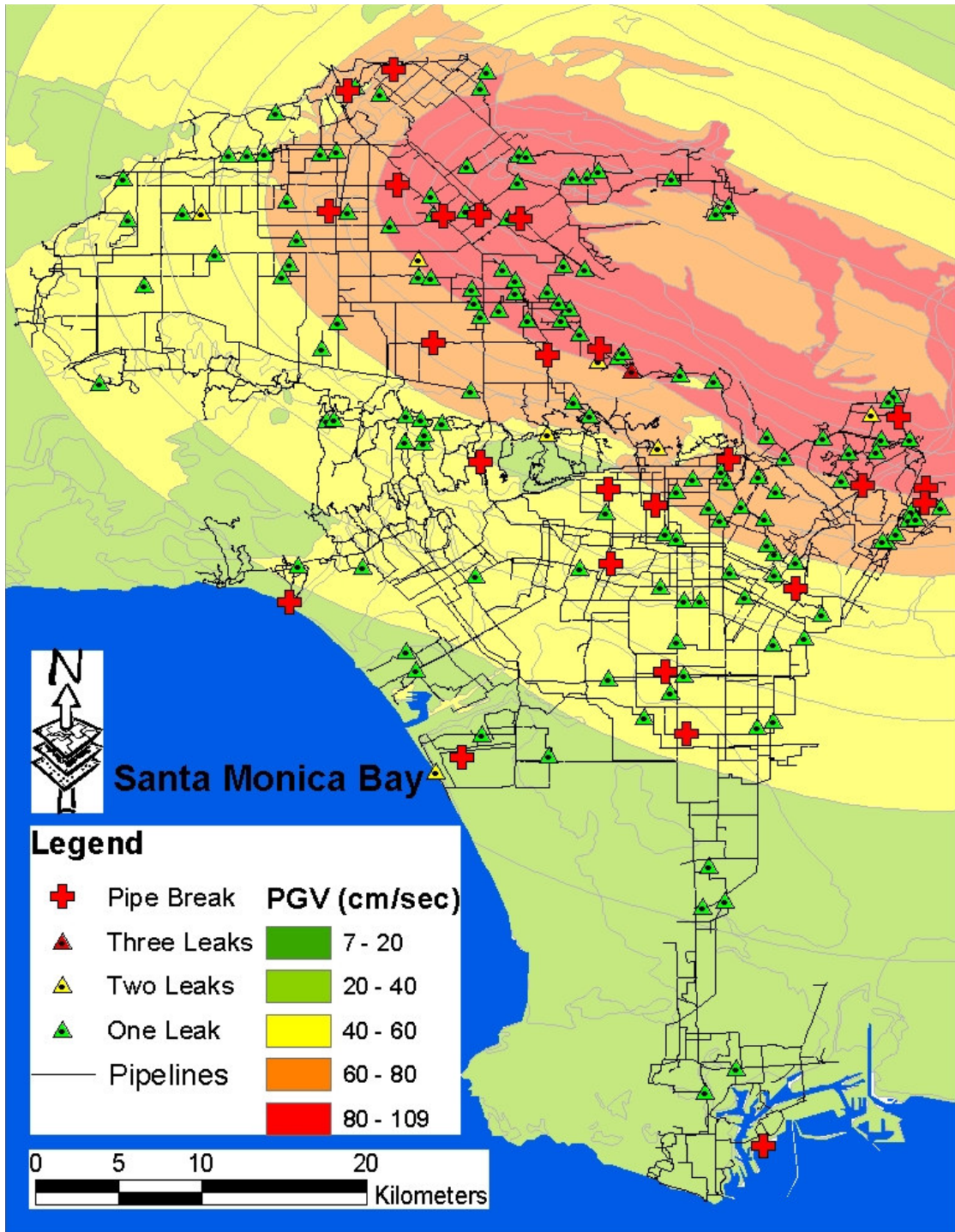
Figure 7.5. Spatial Distribution of Pipe Breaks and Leaks for Scenario 175 Verdugo
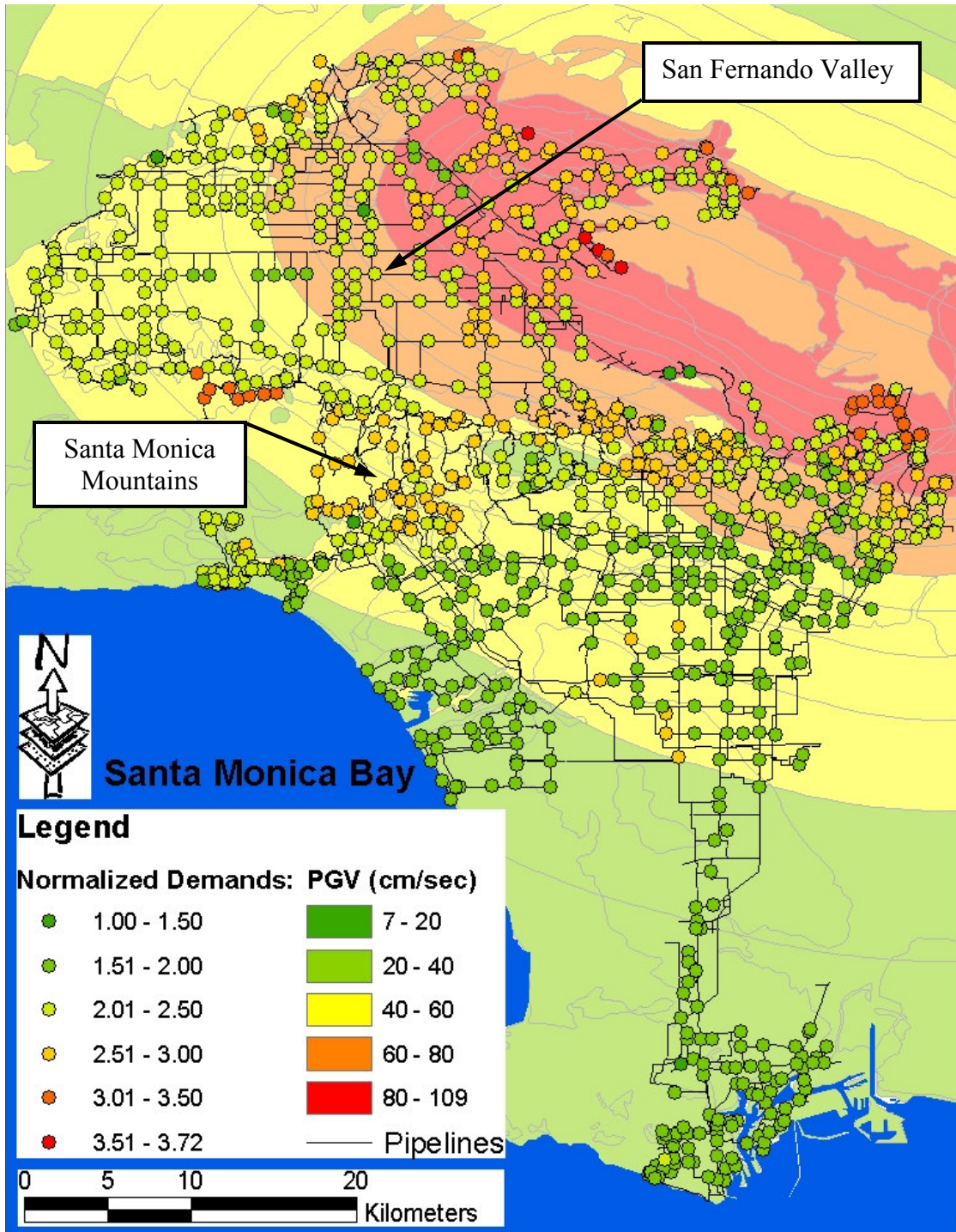
Earthquake

Figure 7.6.   Spatial Distribution of Increasing Demands for Scenario 175 Verdugo

Earthquake

Figure 7.7 shows the spatial distribution of water outage areas after the earthquake according to GIRAFFE simulations. The unsatisfied demand nodes are shown by yellow dots and the pipes with no flow as a result of earthquake-induced damage are shown by red lines. Please note that the pipes with no flows in the undamaged LADWP system to provide redundancy in the system are shown by pink lines. As a results of high PGV values in the upper right quarter of the figure and concentrated damage in those areas, most water outage clusters in the upper right quarter. Sparse water outage also occurs in other parts of the system and the overall system serviceability index (SSI) is 0.81.

Figure 7.8 shows the spatial distribution of water outage areas after a 24-hour period of running tanks using the same legend as Figure 7.7. The system deteriorates rapidly and a significant increase of water outage occurs, particularly in the Santa Monica Mountain areas and the west rim of the San Fernando Valley. As described in Chapter 4, the water in the LADWP system starts from Van Norman Complex and flows from the north to the south. Water is pumped into the storage tanks in the Santa Monica Mountain areas (please refer to Figure 4.2), serving the communities in those high elevation areas by those tanks. Similarly, several water tanks in the west rim of the San Fernando Valley receive water from Granada Trunk Line and/or Rinaldi Trunk Line and provide water to the west rim of the valley. In addition to the impaired capability of those areas to receive water directly from the source, i.e., Van Norman Complex, most tanks are empty after a 24-hour period of outflow, resulting in severe water outage in those areas. Relatively slight increases of water outage are observed in other parts of the system and the overall system serviceability is 0.49.
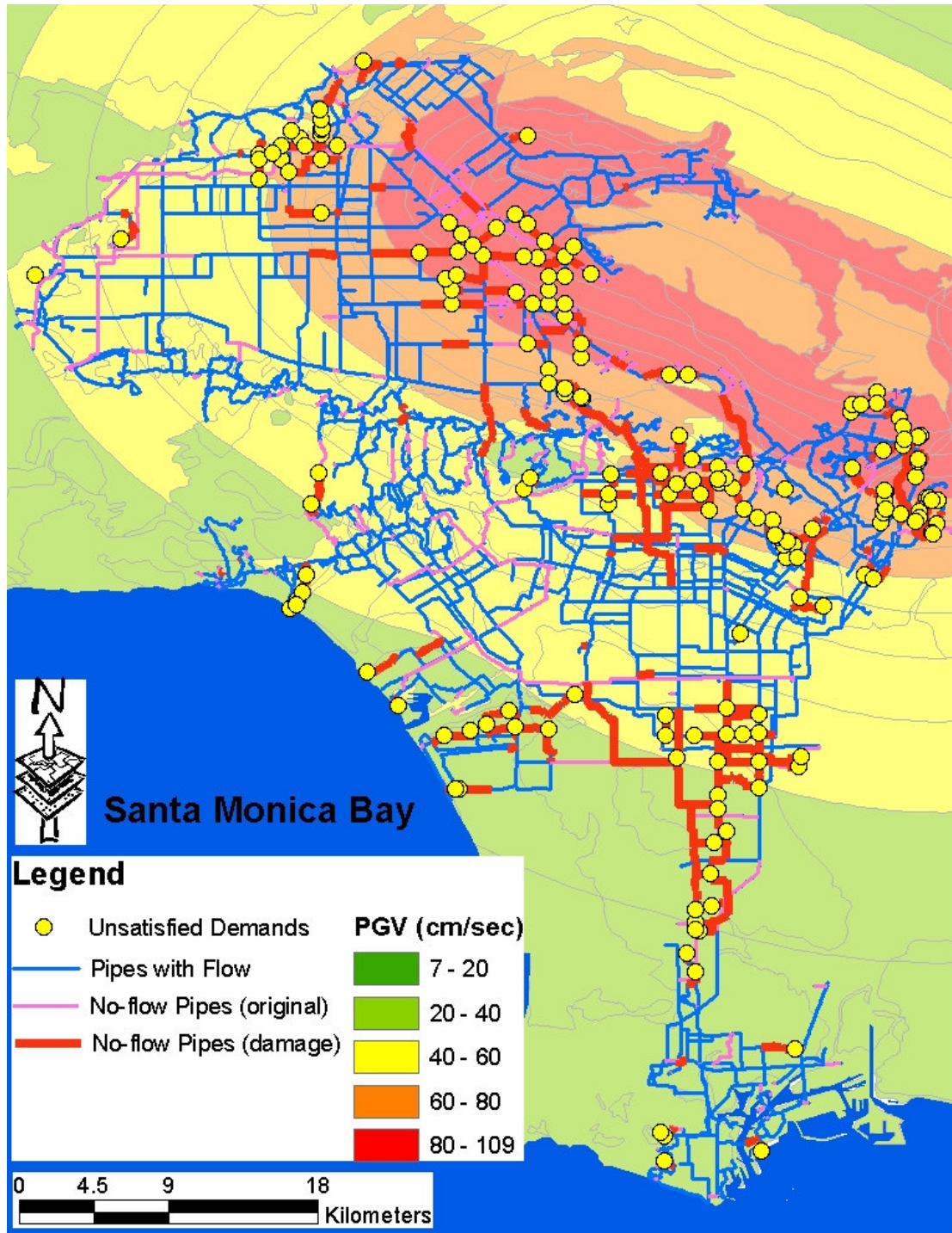
Figure 7.7. Spatial Distribution of Water Outage after Scenario 175 Verdugo
Earthquake
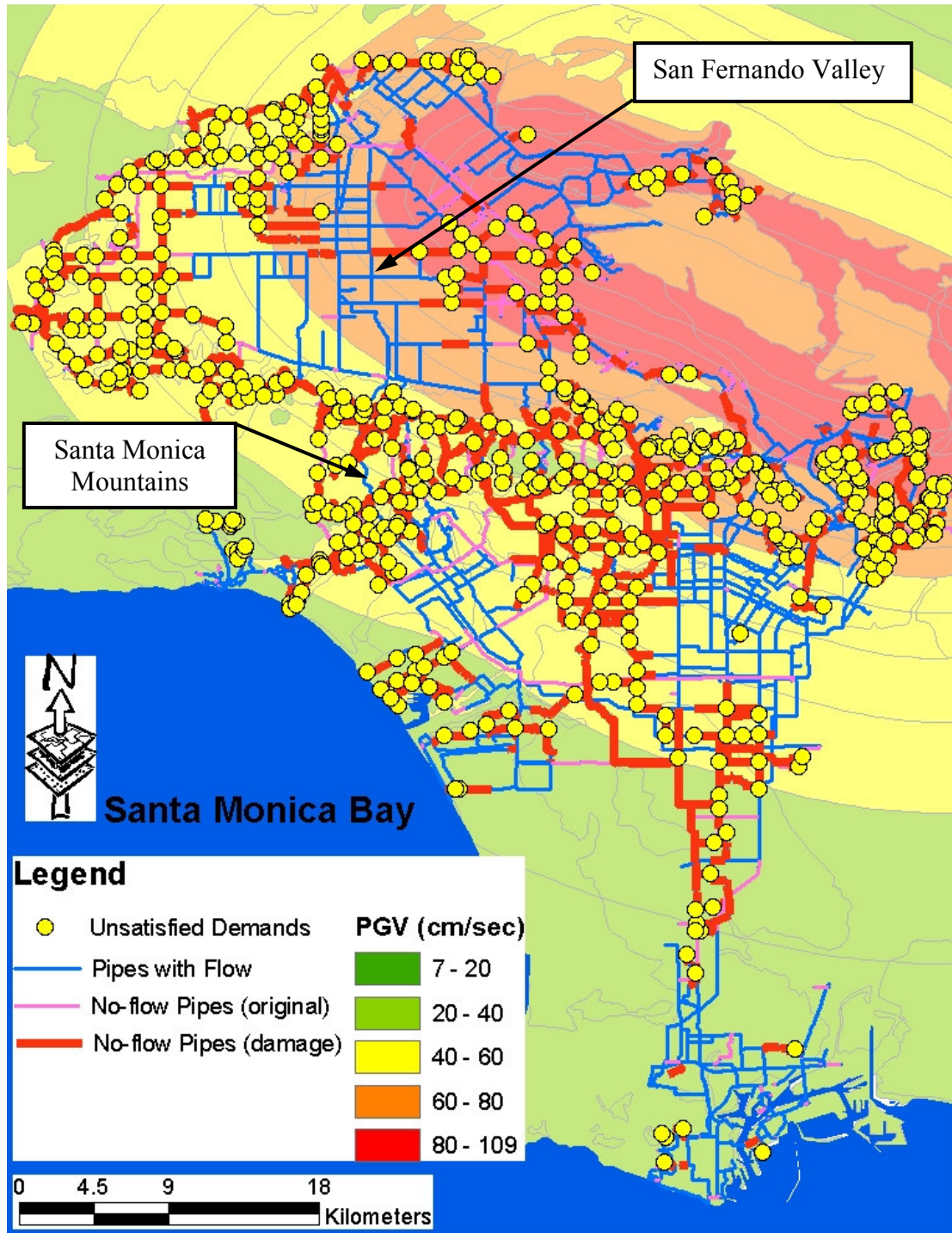
Figure 7.8.   Spatial Distribution of Water Outage after 24-hour Period of Running

Tanks for Scenario 175 Verdugo Earthquake

237

Table 7.1 summarizes the fifteen Monte Carlo simulation results for the Scenario 175 Verdugo earthquake. The mean system serviceability index for the simulations with or without a 24-hour period of running tanks is 0.81 and 0.49, respectively. The losses of storage water in tanks have significant effects on the performance of the system.

Similar Monte Carlo simulations were performed for each of the 59 scenario earthquakes and the results were integrated in the form of risk curves, as described in the next section.

## 7.4. Risk Curves

The simulation results for the 59 scenario earthquakes were integrated in the form of risk curves, plotting the variation of annual exceedance frequency as a function of system serviceability index (SSI). Each scenario earthquake is characterized by an optimized annual frequency of occurrence, as shown in Table 3. 1. Fifteen Monte Carlo simulations were performed for each of the 59 scenario earthquakes, resulting in 885 simulation results. If the fifteen Monte Carlo simulation results are assumed to occur with equal likelihood, i.e., equal annual frequency of occurrence, the annual frequency of occurrence for each set of Monte Carlo simulation results is one fifteenth of that for the associated scenario earthquake. Consider, for example, the Scenario 175 Verdugo earthquake, the annual occurrence frequency of which is 0.000964792. Then, the annual occurrence frequency for a SSI (with the effect of water loss in storage tanks) of 0.55, associated with the first simulation results in Table 7.1, is 0.0000643195. Similarly, the annual occurrence frequency for a SSI of 0.49 or 0.44, associated with the second or third simulation results in Table 7.1,

Table 7.1. Monte Carlo Simulation Results for Scenario 175 Verdugo Earthquake

| Simulation ID | System Serviceability Index (without 24-hour period of running tanks) | System Serviceability Index (with 24-hour period of running tanks) |
|---|---|---|
| 1 | 0.85 | 0.55 |
| 2 | 0.81 | 0.49 |
| 3 | 0.85 | 0.44 |
| 4 | 0.86 | 0.46 |
| 5 | 0.78 | 0.35 |
| 6 | 0.86 | 0.45 |
| 7 | 0.76 | 0.48 |
| 8 | 0.93 | 0.46 |
| 9 | 0.83 | 0.37 |
| 10 | 0.96 | 0.50 |
| 11 | 0.86 | 0.47 |
| 12 | 0.68 | 0.35 |
| 13 | 0.80 | 0.44 |
| 14 | 0.88 | 0.38 |
| 15 | 0.81 | 0.46 |

is also 0.0000643195. The similar process was applied to all 885 simulation results, i.e., SSI, each of which is associated with its own annual occurrence frequency. The 885 SSI were then sorted in an increasing order of SSI, and the annual frequency of exceedance a given SSI, $SSI_0$, is calculated by a summation of the annual occurrence frequencies for those $SSI \leq SSI_0$,

$$F(SSI_0) = \sum_{SSI \leq SSI_0} f(SSI) \qquad (7.1)$$

where $F(SSI_0)$ is the annual frequency of exceeding $SSI_0$, and f(SSI) is the annual occurrence frequency of SSI.

### 7.4.1. System Risk Curves

Figure 7.9 shows the system risk curves plotting the variation of annual exceedance frequency as a function of system serviceability index (SSI) as defined in Section 6.3.1. The system risk curve without a 24-hour period of running tanks is shown by open triangles and that with a 24-hour period of running tanks is shown by open squares. The system risk curve without a 24-hour period of running tanks varies almost linearly in the semi-logarithmetic scale, with a minimum SSI of 0.64 corresponding to an annual frequency of 0.0001, or 10,000-year recurrence interval. The system risk curve with 24-hour running tanks plots to the right of the first curve, indicating much lower SSI values for the same annual exceedance frequency. The linear portion of the curve, with lower SSI values, is approximately parallel to the system risk curve without 24-hour period of running tanks. The difference between the curve without 24-hour period of running tanks and its parallel portion in the curve with 24-hour period of running tanks signifies the effects of running tanks. After 24-hour period of running tanks, the system deteriorates rapidly and the SSI decreases significantly.

The system risk curve with a 24-hour period of running tanks provides an estimate of LADWP system performance after earthquakes that reflects the deteriorating capacity of local tanks and reservoirs, where water levels drop because of pipeline damage after earthquakes. This system risk curve is examined more closely to identify the key scenario earthquakes that significantly influence system risk, as described in the next section.
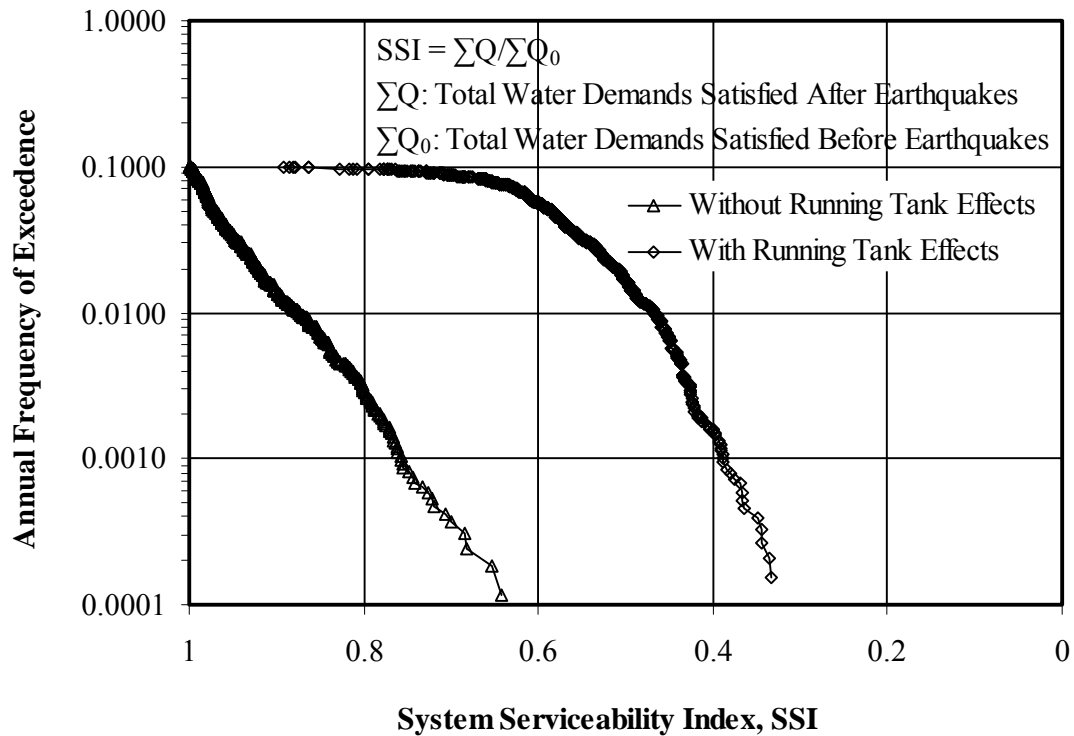
Figure 7.9.  System Risk Curves

## 7.4.2. System Risk Deaggregations

Table 7.2 summarizes the scenario earthquakes that contribute to the system risk at a SSI of 0.42 in the risk curve with a 24-hour period of running tanks, corresponding to a 475-year recurrence interval or 10% probability of exceedance in 50 years. The fourth Column in Table 7.2 indicates the closest distance from the fault to the LADWP service area centroid with geographic coordinates (-118.40787°, 34.11769°), as shown by the green star in Figure 7.10. The annual occurrence frequency in the fifth Column is determined according to the optimized annual occurrence frequency of the scenario and the number of simulations that have the SSI less than the pre-specified value, i.e., 0.42. Consider, for example, Scenario 397 Puente Hills blind thrust earthquake, the optimized annual occurrence frequency of

Table 7.2. Summary of Scenario Contributions to 475-year Recurrence Risks

| Scenario ID | Scenario Name | $M_w$ | Distance (km) | Annual Occurrence Frequency | Contribution (%) |
|---|---|---|---|---|---|
| 397 | Puente Hills blind thrust | 7.1 | 12 | 4.60E-04 | 22.47 |
| 370 | Northridge | 7.0 | 17 | 3.82E-04 | 18.65 |
| 560 | Background Source | 7.0 | 5 | 2.58E-04 | 12.60 |
| 175 | Verdugo | 6.9 | 12 | 2.57E-04 | 12.56 |
| 159 | Newport-Inglewood | 7.1 | 8 | 1.62E-04 | 7.90 |
| 559 | Background Source | 7.0 | 2 | 1.40E-04 | 6.81 |
| 169 | San Gabriel | 7.2 | 25 | 1.02E-04 | 4.98 |
| 562 | Background Source | 7.0 | 11 | 1.02E-04 | 4.96 |
| 561 | Background Source | 7.0 | 11 | 8.60E-05 | 4.20 |
| 166 | Sierra Madre | 7.2 | 19 | 4.97E-05 | 2.42 |
| 202 | Simi-Santa Rosa | 7.0 | 32 | 4.23E-05 | 2.07 |
| 399 | Puente Hills blind thrust | 6.6 | 12 | 5.47E-06 | 0.27 |
| 372 | Northridge | 6.5 | 17 | 1.58E-06 | 0.08 |
| 119 | Hollywood | 6.4 | 3 | 4.43E-07 | 0.02 |
| 177 | Verdugo | 6.4 | 12 | 1.89E-07 | 0.01 |

Note: the table is based on the simulations with a 24-hour period of running tanks and the SSI corresponding to 475-year recurrence risks is 0.42.

which is 0.000863186. Among fifteen Monte Carlo simulations performed for this scenario earthquake, eight of them have SSI less than 0.42, resulting in an annual occurrence frequency of 8/15 of 0.000863186, i.e., 0.000460366, for SSI less than 0.42 because of the Scenario 397 Puente Hills blind thrust earthquake. The contribution in the sixth Column is percentage of the annual occurrence frequency for each scenario earthquake in the fifth Column over the sum of the fifth Column. The table is sorted in a decreasing order of the contribution.

Fifteen scenario earthquakes have contributed to this specific risk level, among which, Puente Hills blind thrust, Northridge, Background source 560, Verdugo, Newport-Inglewood, and Background Source 559 scenario earthquakes have relatively
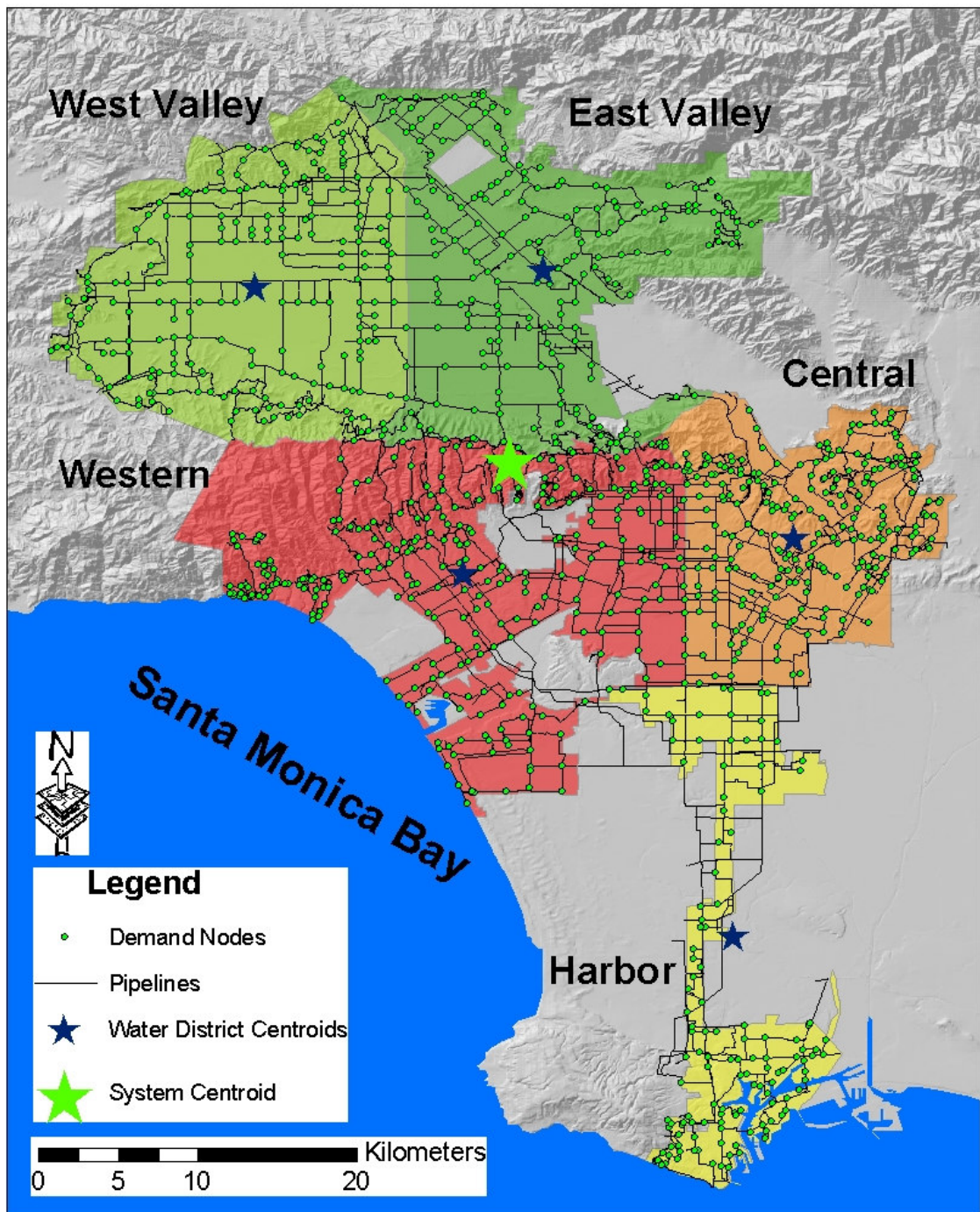
Figure 7.10.   Spatial Distribution of LADWP Water Districts and Their Centroids

significant contributions, i.e., > 5%, to the system risk. Figure 7.11a shows the system risk deaggregation according to earthquake magnitude, $M_w$, and distance. Most scenario earthquakes contributing to the system risk originate on faults located within 30 km from the system centroid, i.e., inside the system service areas, and have magnitude greater than 6.5.

Table 7.3 summarizes the scenario earthquakes that contribute to the system risk at a SSI of 0.51 in the risk curve with a 24-hour period of running tanks, corresponding to a 50-year recurrence interval or 100% probability of exceedance in 50 years. In total 59 scenario earthquakes utilized in this work, 44 scenario earthquakes have contributed to this specific risk level, among which, San Andreas-1857, San Andreas-All Southern Segments, and Northridge scenario earthquakes have relatively significant contributions, i.e., > 5%, to the system risk. Figure 7.11b shows the system risk deaggregation according to $M_w$ and distance. Significant contributions from scenario earthquakes originating from relatively far from the system centroid are observed, particularly those associated with the San Andreas fault, which are about 55 km from the centroid.

Comparisons between Tables 7.2 and 7.3 show that the number of scenario earthquakes that have contributions to the system risk increases significantly as the recurrence interval for the risk decreases from 475 years to 50 years. Comparisons between Figure 7.11a and b show that, as the recurrence interval decreases, or SSI increases, the contributions from scenario earthquakes with relatively large distances from originating faults to the system increase significantly.
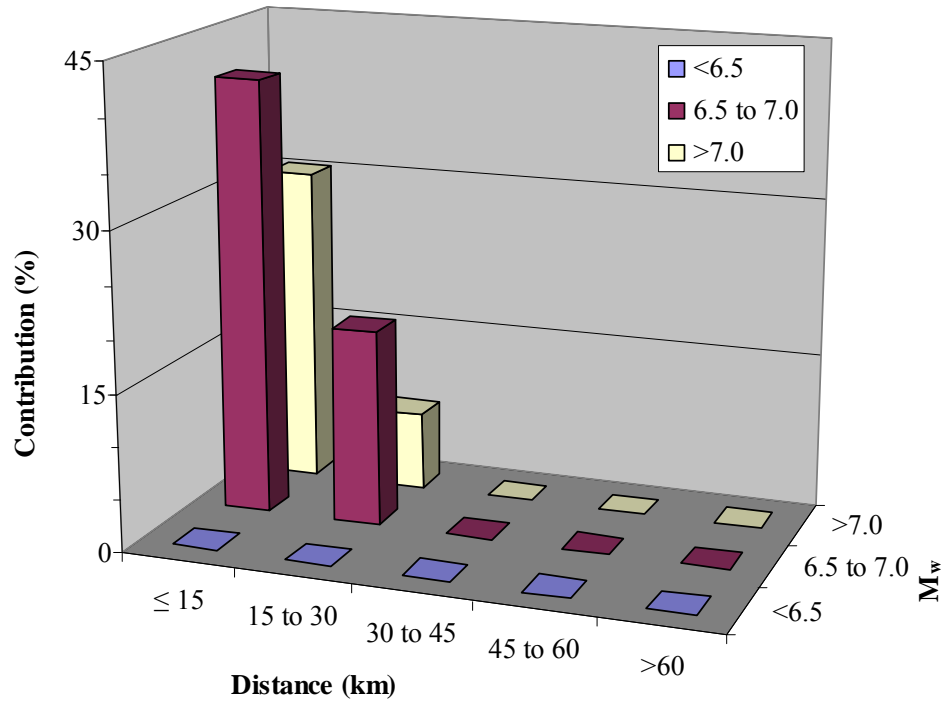
(a) 475-year Recurrence Risks, SSI = 0.42
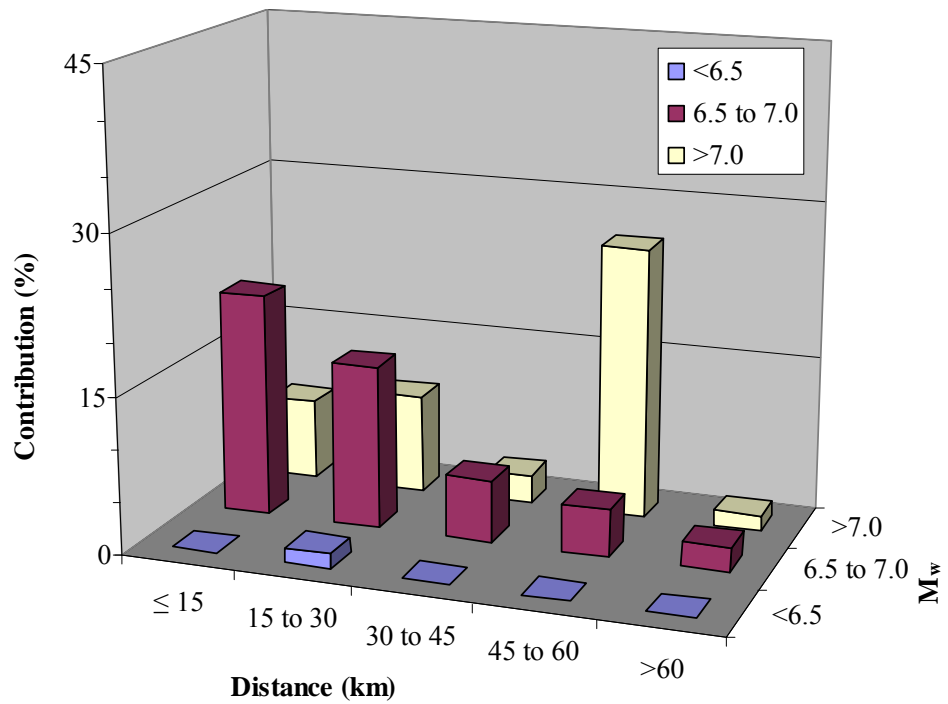


(b) 50-year Recurrence Risks, SSI = 0.51

Figure 7.11. System Risk Deaggregations

Table 7.3.  Summary of Scenario Contributions to 50-year Recurrence Risks

| Scenario ID | Scenario Name | $M_w$ | Distance (km) | Annual Occurrence Frequency | Contribution (%) |
|---|---|---|---|---|---|
| 22 | San Andreas Fault - 1857 | 7.8 | 55 | 3.20E-03 | 16.02 |
| 21 | San Andreas Fault-All southern segments | 8.1 | 55 | 2.00E-03 | 10.00 |
| 370 | Northridge | 7 | 17 | 1.24E-03 | 6.21 |
| 195 | San Cayetano | 7 | 48 | 9.15E-04 | 4.58 |
| 175 | Verdugo | 6.9 | 12 | 9.00E-04 | 4.50 |
| 397 | Puente Hills blind thrust | 7.1 | 12 | 8.63E-04 | 4.32 |
| 561 | Background Source | 7 | 11 | 8.60E-04 | 4.30 |
| 198 | Santa Susana | 6.7 | 23 | 8.04E-04 | 4.02 |
| 559 | Background Source | 7 | 2 | 7.68E-04 | 3.84 |
| 560 | Background Source | 7 | 5 | 7.23E-04 | 3.62 |
| 169 | San Gabriel | 7.2 | 25 | 7.15E-04 | 3.57 |
| 159 | Newport-Inglewood | 7.1 | 8 | 7.02E-04 | 3.51 |
| 166 | Sierra Madre | 7.2 | 19 | 6.95E-04 | 3.48 |
| 562 | Background Source | 7 | 11 | 6.61E-04 | 3.31 |
| 219 | Anacapa-Dume | 7.5 | 32 | 5.62E-04 | 2.81 |
| 191 | Oak Ridge-onshore | 6.5 | 42 | 5.14E-04 | 2.57 |
| 443 | Sierra Madre-San Fernando | 6.7 | 19 | 5.02E-04 | 2.51 |
| 444 | Palos Verdes | 7.3 | 24 | 4.91E-04 | 2.45 |
| 440 | Cucamonga | 6.9 | 63 | 4.12E-04 | 2.06 |
| 19 | San Andreas Fault - Carrizo | 7.4 | 65 | 3.04E-04 | 1.52 |
| 454 | Palos Verdes | 6.3 | 24 | 2.89E-04 | 1.44 |
| 189 | Oak Ridge-onshore | 7 | 42 | 2.75E-04 | 1.38 |
| 174 | Santa Monica | 6.6 | 6 | 2.44E-04 | 1.22 |
| 12 | Elsinore - Whittier | 6.8 | 39 | 2.40E-04 | 1.20 |
| 220 | Anacapa-Dume | 7 | 30 | 2.28E-04 | 1.14 |
| 447 | Palos Verdes | 6.8 | 24 | 1.25E-04 | 0.62 |
| 202 | Simi-Santa Rosa | 7 | 32 | 8.46E-05 | 0.42 |
| 168 | Sierra Madre | 6.7 | 19 | 7.38E-05 | 0.37 |
| 221 | Anacapa-Dume | 7 | 61 | 6.29E-05 | 0.31 |
| 162 | Newport-Inglewood | 6.6 | 8 | 6.00E-05 | 0.30 |
| 399 | Puente Hills blind thrust | 6.6 | 12 | 5.47E-05 | 0.27 |

Note: the table is based on the simulations with a 24-hour period of running tanks and the SSI corresponding to 50-year recurrence risks is 0.51.

Table 7.3.   (Continued)

| Scenario ID | Scenario Name | $M_w$ | Distance (km) | Annual Occurrence Frequency | Contribution (%) |
|---|---|---|---|---|---|
| 446 | Palos Verdes | 6.8 | 41 | 5.47E-05 | 0.27 |
| 120 | Raymond | 6.5 | 17 | 4.94E-05 | 0.25 |
| 371 | Northridge | 6.5 | 25 | 3.84E-05 | 0.19 |
| 161 | Newport-Inglewood | 6.6 | 30 | 3.72E-05 | 0.19 |
| 118 | Holser | 6.5 | 35 | 2.22E-05 | 0.11 |
| 170 | San Gabriel | 6.7 | 25 | 1.99E-05 | 0.10 |
| 372 | Northridge | 6.5 | 17 | 1.11E-05 | 0.06 |
| 388 | Upper Elysian Park | 6.4 | 10 | 8.18E-06 | 0.04 |
| 176 | Verdugo | 6.4 | 14 | 4.19E-06 | 0.02 |
| 119 | Hollywood | 6.4 | 3 | 1.77E-06 | 0.01 |
| 177 | Verdugo | 6.4 | 12 | 7.57E-07 | 0.00 |
| 173 | Malibu Coast | 6.7 | 15 | 3.60E-07 | 0.00 |
| 222 | Anacapa-Dume | 6.5 | 30 | 2.59E-07 | 0.00 |

Note: the table is based on the simulations with a 24-hour period of running tanks and the SSI corresponding to 50-year recurrence risks is 0.51.

### 7.4.3. Risk Curves for Five Water Districts

As described in Chapter 4, the LADWP water supply system can be divided into five water districts: West Valley, East Valley, Western, Central, and Harbor Water Districts. Figure 7.10 shows a spatial distribution of water districts and their centroids by blue stars. The system serviceability indexes (SSI) can be calculated for the 5 water districts, respectively, providing additional information on the spatial distribution of the system risks, as shown in Figure 7.12.

Figure 7.12a shows the risk curves without a 24-hour period of running tanks for five water districts, respectively. The water districts have significantly different risk curves. The most vulnerable one is the Harbor Water District, followed by the Central and Western Water Districts, as opposed to the most robust one, the West Valley Water District. The performance of five water districts is consistent with the
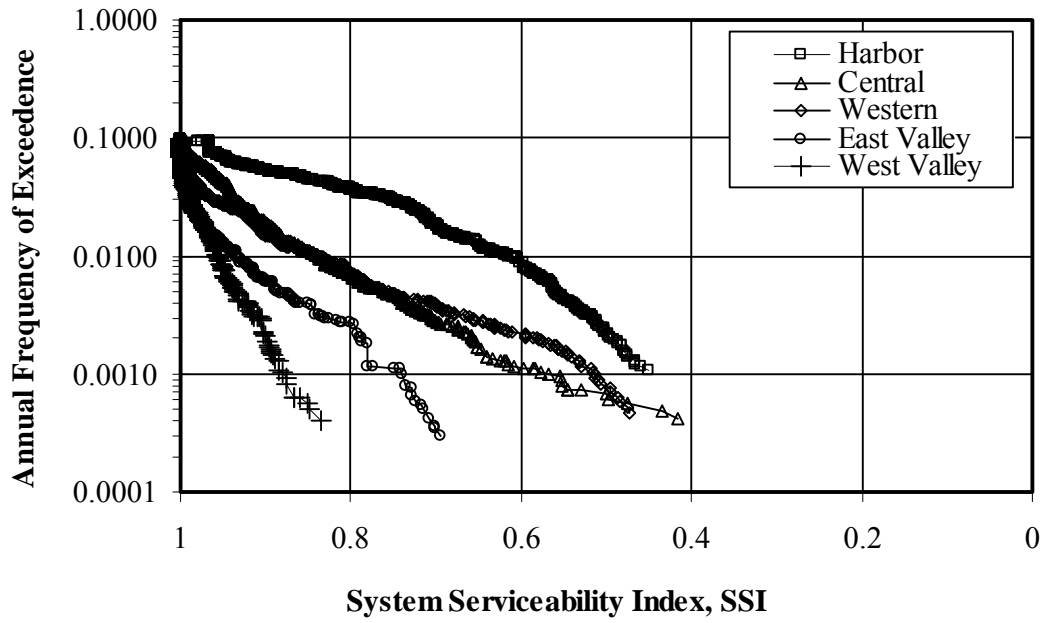
(a) Without 24-hour Period of Running Tanks
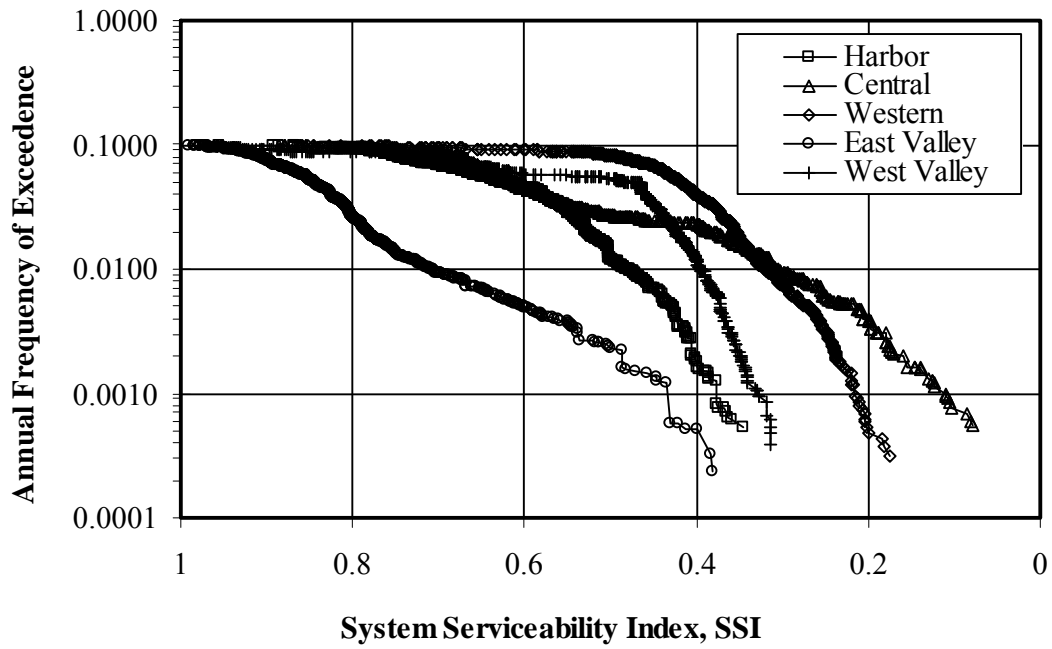


(b) With 24-hour Period of Running Tanks

Figure 7.12.   Risk Curves for Five Water Districts

248

system configuration and water flow pattern of the LADWP water supply system. As described in Chapter 4, the LADWP water supply system is configured such that water flows from the north to the south. Starting from the Van Norman Complex in the northern San Fernando Valley, the water flows through the East Valley and West Valley Water Districts, followed by the Western and Central Water Districts, and finally arrives at the Harbor Water District. Because the West Valley and East Valley Water Districts are located close to the water sources, i.e., Van Norman Complex, the chance of disruption is small when the water is conveyed from the sources to the water districts, resulting in more robust performance of these two water districts. In addition, the mesh type configuration of the pipelines in the San Fernando Valley provides redundancy to the system, and hence, improves the performance of these two water districts. In contrast, the Harbor Water district is located in the far end of the system and the distance that the water has to travel before it reach Harbor Water District is the longest. Therefore, the probability of disruption is relatively large when the water is conveyed from the sources to the district. Additionally, less redundancy in the Harbor Water District contributes to the vulnerable performance of the district.

Figure 7.12b shows the risk curves with a 24-hour period of running tanks for five water districts, respectively. When compared with the risk curves without a 24-hour period of running tanks, all the risk curves move to the right, indicating deterioration of system performance. However, the five water districts deteriorate to various degrees after the 24-hour period of running tanks. The most vulnerable districts are the Western and Central Water Districts, followed by the West Valley and Harbor Water Districts, as opposed to the most robust one, the East Valley Water District. The performance of five water districts is consistent with the locations of the most water storage tanks and the water flow pattern in the LADWP water supply

249

system. As described in Chapter 4 and illustrated by the evaluation example in Section 7.3, most storage tanks are located in the Santa Monica Mountain areas, where the Western and Central Water Districts are located, and west rim of the San Fernando Valley, which is part of the West Valley Water District. A 24-hour running period empties most tanks in these areas and causes significant increases of water outage in these areas, resulting in significant deterioration of system performance in the Western, Central, and West Valley Water Districts. In contrast, only limited numbers of water storage tanks are located in the East Valley and Harbor Water Districts, and hence, the deterioration of the system performance after the 24-hour period of running tanks is not as severe as those of the Western, Central, and West Valley Water Districts. In addition, most water in the East Valley Water District is provided from the Van Norman Complex directly, contributing to the relatively robust performance of the East Valley Water District after the 24-hour period of running tanks.

### 7.4.4. Risk Deaggregations for Five Water Districts

The water district risk curves with a 24-hour period of running tanks are examined closely to identify the key scenario earthquakes that significantly influence water district risks. Risk deaggregations are performed at district risks corresponding to 475-year and 50-year recurrence intervals for five water districts, i.e., the West Valley, East Valley, Western, Central, and Harbor water districts. The details on the risk deaggregations are described in Appendix B, and only the summary is provide in this section.

It is found that the number of scenario earthquakes that have contributions to the water district risk increases significantly as the recurrence interval for the risk

decreases from 475 years to 50 years. Furthermore, as the recurrence interval decreases, or SSI increases, the contributions from scenario earthquakes with relatively large distances from originating faults to the water districts increase significantly. However, it is found that, even for risk with relative large recurrence interval, the Harbor Water District is significantly affected by the scenario earthquakes with relatively large distances from originating faults to the water district because of its southern end position in the system and the long distance that the water has to travel before arriving at the district.

## 7.5. Input Data for Consequence Analysis

An important objective of this work is to provide engineering evaluation results of the LADWP water supply system for social and economic consequence analysis. Computable General Equilibrium (CGE) models are being developed to assess the economic impacts caused by earthquake-induced lifelines losses (Rose, 2005). Figure 7.13 shows the spatial distribution of subsystems utilized in the economic consequence analysis. The engineering evaluation results in the form of water availability, SSI, after earthquakes are complied with respect to the thirteen subsystems, as described in Chapter 4. Since the subsystem Valley Floor (VF) has a service area significantly larger than other twelve subsystems, the subsystem VF is divided into three portions, resulting in a total of fifteen subsystems utilized to determine the SSI. The SSIs in the fifteen subsystems serve as the input data for the CGE models to assess the economic consequence caused by earthquake-induced water supply losses. As described by Rose and Liao (2003 and 2005), water losses in the fifteen subsystems are used to assess the economic consequences arising from water shortage. In brief, the economic impact is evaluated by CGE production functions that
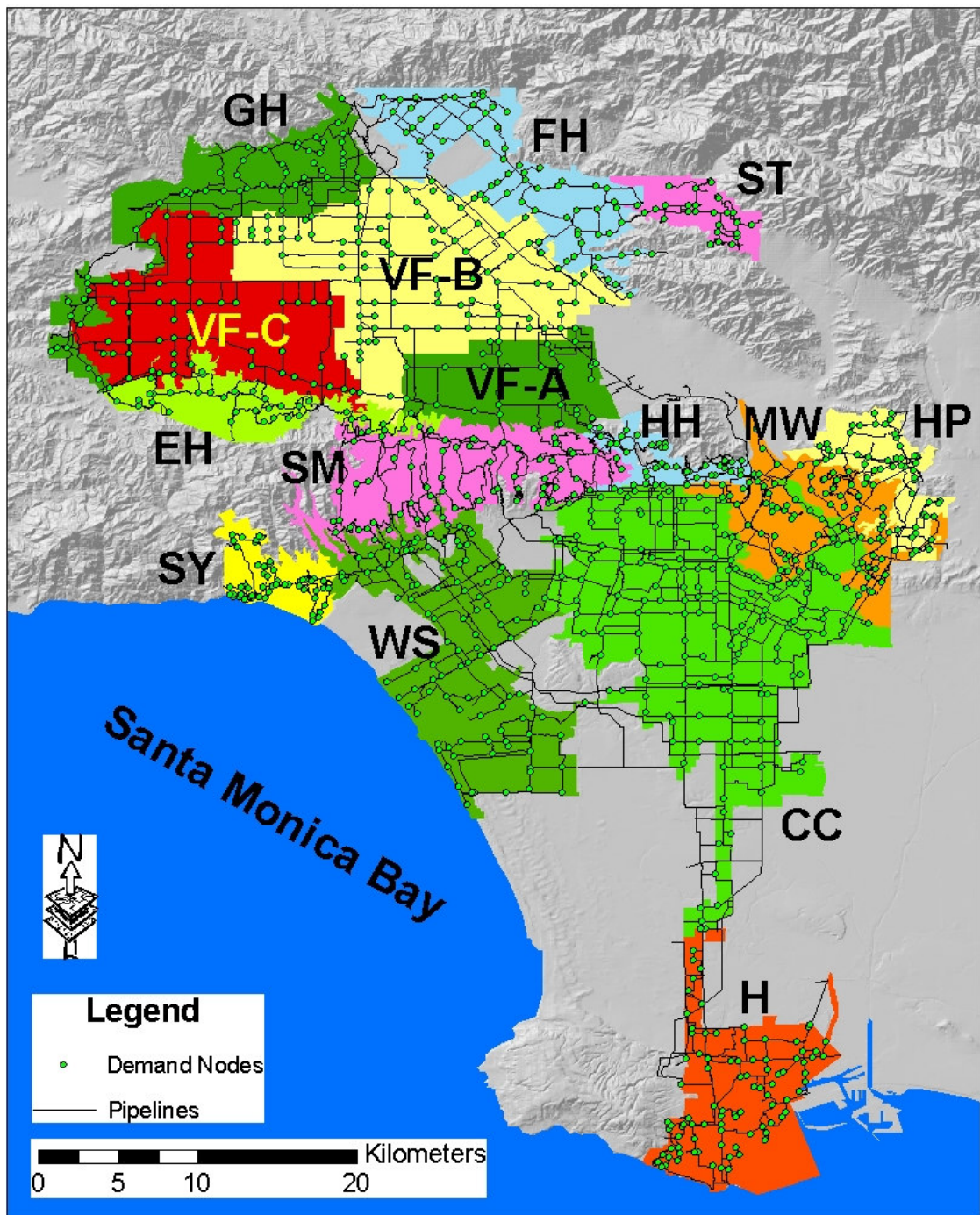
Figure 7.13.   Spatial Distribution of Subsystems Utilized in Economic Analysis

are nonlinear and readily incorporate behavioral content for producer and consumer response in a multi-market context. The behavioral content modeled in CGE models generally includes conservation, input substitution, and import substitution. The CGE model can account for seismic resilience, and their results provide more realistic estimates of economic impacts than those of Input-Output models.

## 7.6.  Summary

A process for the seismic performance evaluation of water supply systems was developed using the LADWP water supply system. The seismic hazards in the LADWP water supply system were characterized by a suite of 59 scenario earthquakes and their annual frequencies of occurrence. Procedures were developed to determine the seismic demands on the system components, which were compiled into a hydraulic network model. The damage to the pipelines during earthquakes was estimated using the regressions between repair rates and PGVs based on performance records from previous earthquakes. The damage to the trunk lines was simulated explicitly. A Poisson process was utilized to simulate the occurrences of trunk line damage. This type of damage was further categorized into leaks and breaks that, in turn, were simulated using pipe leak and break hydraulic models, respectively. The damage of local distribution lines was simulated by increasing the nodal demands such that they represent water losses consistent with earthquake-related repair rates in the local distribution systems.

The seismic system performance of the LADWP water system was evaluated using GIRAFFE. Fifteen Monte Carlo simulations were performed for each of the 59 scenario earthquakes, resulting 885 simulations in total. The number of simulations in

each Monte Carlo analysis was determined by the GIRAFFE self-termination algorithm, which stops the simulation process when the difference in the mean and coefficient of variation of the results are less than 2%. The 885 simulation results were integrated in the form of risk curves, plotting the annual exceedance frequency as a function of system serviceability index (SSI), which is defined as the ratio of the sum of satisfied water demands after an earthquake to that before an earthquake. The effects of the loss of storage water in tanks after earthquakes on system performance were evaluated by simulating the leakage from damaged pipelines for a 24-hour period after the earthquake and comparing risk curves with and without the 24-hour running period. The engineering evaluation results, expressing as the water availability after earthquakes, serve as the key input in the social and economic consequence evaluations performed by the social scientists and economists.

The system risk curve without storage water loss varies almost linearly in the semi-logarithmetic scale, with an SSI of 0.79, which corresponds to an annual frequency of 0.0021, or 475-year recurrence interval. After a 24-hour period of running tanks, the system deteriorates rapidly, and the SSI decreases significantly. The system risk curve with 24-hour running tanks plots to the right of the first curve, indicating much lower SSI values for the same annual exceedance frequency. The linear portion of the curve, with lower SSI values, is approximately parallel to the system risk curve without a 24-hour period of water losses from the tanks. For the condition of tank losses, the system risk curve shows an SSI of 0.42, which corresponds to an annual frequency of 0.0021, or 475-year recurrence interval. The difference between the curve without a 24-hour period of running tanks and its parallel portion in the curve with a 24-hour period of running tanks signifies the effects of water losses from tanks.

The system risk curve with a 24-hour period of running tanks was examined closely to identify the key scenario earthquakes that significantly influence system risk and their characteristics. The risk level corresponding to a 475-year recurrence interval, or 10% probability of exceedance in 50 years, is attributed to fifteen scenario earthquakes, as summarized in the main text. Most scenario earthquakes, contributing to the system risk, originate on faults located within 30 km of the system centroid, i.e., inside the system service areas, and have magnitude greater than 6.5.

The risk level corresponding to a 50-year recurrence interval, or 100% probability of exceedance in 50 years, can be attributed to 44 scenario earthquakes. Significant contributions from scenario earthquakes with relatively large distances from originating faults to the system centroid were observed, particularly those associated with the San Andreas fault, which are about 55 km from the system centroid.

It was found that the number of scenario earthquakes, which have contributions to the system risk, increases significantly as the recurrence interval for the risk decreases from 475 years to 50 years. Furthermore, as the recurrence interval decreases, or SSI increases, the contributions from scenario earthquakes with relatively large distance from the originating faults to the system increase significantly.

The risk curves were also constructed for five water districts to provide additional information about the spatial distribution of system risks. It was found that the water districts have significantly different risk curves. According to the risk curves without storage water loss in tanks, the most vulnerable one is the Harbor Water

District, followed by the Central and Western Water Districts. The most robust district is the West Valley Water District. The performance of five water districts is consistent with their relative positions in the system and with the north to the south water flow pattern in the LADWP water supply system.

For a 24-hour period of water losses from tanks, the SSIs decrease by varying degrees in the water districts. The most vulnerable districts are the Western and Central Water Districts, followed by the West Valley and Harbor Water Districts. The most robust district is the East Valley Water District. The performance of five water districts is consistent with the concentration of the most water storage tanks in the Western, Central, and West Valley Water Districts and with the north to the south water flow pattern in the LADWP water supply system.

The risk curves with a 24-hour period of tank water losses were examined closely to identify the key scenario earthquakes that significantly influence the water district risks. It was found that the number of scenario earthquakes that have contributions to the water district risk increases significantly as the recurrence interval for the risk decreases from 475 years to 50 years. Furthermore, as the recurrence interval decreases, or SSI increases, the contributions from scenario earthquakes with relatively large distances from originating faults to the water districts increase significantly. However, it was found that, even for risks with relatively large recurrence intervals, the Harbor Water District is significantly affected by scenario earthquakes with relatively large distances from originating faults to the water district because of its southern end position in the system and the long distance that the water has to travel before arriving at the district.

# CHAPTER 8

# SUMMARY AND CONCLUSIONS

## 8.1.  Introduction

This report deals with the seismic performance evaluation of water supply systems. An evaluation process is developed for simulating the seismic performance of a large, geographically-distributed, water supply system and characterizing the performance in terms of system reliability and serviceability. The process makes use of probabilistic seismic hazard analysis, theoretical and empirical relations to estimate pipeline response, hydraulic analysis for heavily damaged water systems, and multi-scale simulations of complex water systems. It provides output that is beneficial for system management and decision-making and necessary for economists and social scientists to assess the economic and community impacts of lifeline disruption by earthquakes.

A framework for evaluating the seismic effects on lifeline systems is first introduced and then demonstrated by an application to one of the largest and most complex water supply systems in the world - the water supply system in the greater Los Angeles area operated by the Los Angeles Department of Water and Power (LADWP). The framework contains five basic activities, i.e., seismic hazard characterizations, system property characterizations, system component response evaluation, system response evaluation, and consequence evaluation, each of which

was described. The seismic hazards in the greater Los Angeles area were characterized by a suite of 59 scenario earthquakes and their associated annual occurrence frequencies. The LADWP water supply system was represented by a hydraulic model for component response evaluation and system response evaluation. Models for the seismic wave effects on pipelines were developed to improve the capability of component response evaluation. A special computer program (GIRAFFE), equipped with a negative pressure analysis algorithm and capable of performing Monte Carlo simulations, was utilized to evaluate the system response. The system evaluation results were organized in the form of risk curves and serve as the key input for the consequence analysis.

This chapter summarizes the major research findings associated with each part of this report. The sections that follow are organized to present the research findings corresponding to the research objectives described in Chapter 1. The final section provides some recommendations for future research.

## 8.2. Framework for Earthquake Effects on Lifelines

Lifelines are the systems and facilities that provide services vital to the function of an industrialized society and important to the emergency response and recovery after disastrous events. These systems and facilities include electric power, natural gas and liquid fuels, telecommunications, transportation, waste disposal, and water. In general, each lifeline system is a network within which there are sources, major transmission lines, storage, and distribution or collection system. All lifeline systems share four common characteristics: geographical dispersion, interconnectivity, diversity, and interdependencies.

A framework for evaluating lifeline system seismic performance was presented, and a basic chain of activities that predominates in the framework was identified. The basic chain starts with the characterizations of seismic hazards and system properties, then proceeds to the analyses of interactions between them, from which system response and the evaluation of community impacts follow. Engineering seismologists may estimate the ground shaking hazards at a particular site quantitatively by either deterministic or probabilistic seismic hazard analysis. The lifeline system properties are usually characterized by the utility companies, who own and operate the systems. Geotechnical engineers and structural engineers focus on the evaluation of component response, which are then integrated to provide an evaluation of system performance in terms of system reliability and serviceability, e.g., water availability after earthquakes for water supply systems. The engineering output of the system response evaluation is then utilized in the social and economic consequence evaluation by social scientists and economists.

## 8.3. Seismic Hazard Characterizations of LADWP Systems

The seismic hazard characterization for the Los Angeles area was developed by approximating the aggregate seismic hazard, i.e., USGS 2002 Dataset, in the area that takes into account all currently identified, potential seismic sources in a probabilistic context. The approximation was accomplished by means of 59 scenario earthquakes that were selected to provide probability of exceedance characteristics for strong ground motion similar to those for all currently identified, potential seismic sources in the area (Lee et al., 2005). Scenario earthquakes that generate ground motion without engineering significance in the LADWP water supply system were

screened from the original USGS 2002 dataset. In addition, expert judgments were exercised to screen out other scenario earthquakes in the original USGS 2002 dataset.

The seismic hazard associated with the 59 scenario earthquakes was adjusted to match that of the USGS 2002 dataset over the LADWP water supply system by a multivariate, nonlinear optimization process. The 59 annual occurrence frequencies for the 59 scenario earthquakes are the optimized variables. The target function was selected by minimizing an error function for the sum of the differences between the hazard curves, i.e., the variation of annual exceedance frequency as a function of $S_{A1}$ at equivalent rock sites, from the 59 scenario earthquakes and USGS 2002 dataset at each of the 56 control points spatially distributed over the LADWP water supply system.

Strong ground motions, e.g., PGV, for each of the 59 scenario earthquakes were generated at 572 points in a grid covering the LADWP water supply system. The PGV contour surfaces were interpolated from these 572 points, and site condition corrections were applied according to the NEHRP-HAZUS procedures. With the aid of GIS software, the spatial distribution of the LADWP system components were superimposed on the PGV contour surfaces to determine the seismic demand on each component in accordance with its respective location.

## 8.4. Seismic Body Wave Effects on Pipelines

The earthquake performance of a water supply system is often closely related to the performance of water trunk and transmission lines, whose seismic wave interactions were studied in this chapter. Examinations of near-source strong ground

motion records during previous earthquakes indicate that seismic waves can be approximated by sinusoidal waves, and it is reasonable to simplify the seismic body waves as a single sinusoidal pulse in seismic wave-pipeline interactions.

Depending on the seismic wave characteristics, R, ground conditions, f, and pipeline properties, EA, pipelines behave either flexibly or rigidly in the axial dimension. When f/EAR > 1, the pipeline is axially flexible with respect to ground strain accumulation. No relative displacement occurs between the pipeline and the surrounding soil, and the pipeline deforms coincidentally with the ground surrounding the pipeline, resulting in $\varepsilon_p = \varepsilon_g$ everywhere the pipeline is continuous. The ratio between maximum pipe strain, $\varepsilon_{pmax}$, and maximum ground strain, $\varepsilon_{gmax}$, is equal to 1. When f/EAR < 1, the pipeline is relatively rigid with respect to axial ground strain accumulation, and relative displacement occurs between soil and pipeline. The strain in the continuous pipeline will accumulate linearly at a slope of f/EA. The $\varepsilon_{pmax}$ occurs at the locations corresponding to the amplitude of the sinusoidal seismic wave, and the ratio between $\varepsilon_{pmax}$ and $\varepsilon_{gmax}$ is equal to f/EAR.

The typical range of f/EAR values for water trunk lines, when affected by seismic body waves, is much greater than 1, and the water trunk lines tend to behave as flexible pipes when affected by seismic body waves. Rigid pipe behavior only occurs under extremely adverse conditions, such as where surrounded by liquefied soils, where the f approaches 0, resulting in f/EAR less than 1.

Attention is drawn to the seismic body wave interaction with jointed concrete cylinder pipelines (JCCPs), the performance of which has varied significantly during previous earthquakes. Close examinations of the design and as-built drawings of the

JCCPs reveal that the pullout capacity of the JCCP joints depends on the tensile behavior of the cement mortar at the joints. Moreover, it is not uncommon to observe cracks in the cement mortar and separation at the joints before earthquakes because of shrinkage of mortar cement during curing and subsequent operational loads and movements in the field.

A simplified model for seismic body wave interactions with JCCPs containing existing cracked joints was developed to estimate relative joint displacements. The relative joint displacement at a cracked joint equals the integration of the differential strain between the pipeline and ground from the cracked joint to the positions in the pipe where no relative displacement occurs between the pipe and the soil.

Extensive parametric studies with various ground conditions, seismic body wave parameters, and pipe properties were performed using finite element models. In total, 320 finite element runs were performed, and the results were summarized by a universal relationship between two dimensionless parameters, $\delta_j/\delta_0$ and f/EAR. With known ground conditions, pipeline properties, and seismic wave characteristics, f/EAR and $\delta_0$ can be calculated, and the joint displacement, $\delta_j$, can be estimated directly using the universal relationship.

The continuous JCCPs without existing cracked joints may crack at joints as a result of seismic body wave propagation when $\varepsilon_{pmax}$ exceeds the cracking strain, $\varepsilon_T$, at the mortar joints. The cracking of joints transforms the pipeline from a continuous structure to a segmented one. Therefore, geometric nonlinearity has to be incorporated in the modeling. The relative joint displacement varies as the seismic body waves pass through the pipelines. The two most critical cases for relative joint displacement were

found to be immediately before the joint cracks and when the $\varepsilon_{pmax}$ occurs at the cracked joint. The equations for calculating the corresponding relative joint displacement were derived.

The JCCP response to seismic body waves depends on the relative magnitude of the mortar cracking strain and maximum pipe strain induced by seismic waves. When $\varepsilon_{pmax} \geq \varepsilon_T$, the mortar at the joints may be cracked and the pipe changes from a continuous pipe to a segmented pipe. In contrast, when $\varepsilon_{pmax} < \varepsilon_T$, no joint will be cracked by the seismic body waves and the relative joint displacement only occurs at existing cracked joints. The mortar cracking strain also has significant effect on the magnitude and occurrence frequency of relatively joint displacement. Low $\varepsilon_T$ causes small relative joint displacement to occur frequently with a small interval along the pipeline. In contrast, high $\varepsilon_T$ results in large relative joint displacement concentrated at fewer locations of cracked joints.

Understanding the interaction of seismic waves and JCCPs leads to some design and construction concepts that may improve earthquake performance. The JCCPs may be designed and constructed such that all the joints have zero or very low axial pullout resistance, i.e., $\varepsilon_T = 0$. The zero or low axial pullout resistance allows very small displacements to occur at each joint, with no appreciable strain accumulation along pipe segments or displacement concentrations at existing cracked joints. The absence of mortar cracking strain or low strain capacity may be accomplished by cracking each joint intentionally or reducing the adhesion between mortar and pipe segments by inserting some low adhesion materials, such as Teflon or high density polyethylene (HDPE) at the mortar and pipe segment interface.

The model for seismic body wave interaction with JCCPs was extended for the locally weak joints in pipelines composed of other materials, such as cast iron. A relative joint displacement correction factor, $\delta_d/\delta_j$, was introduced and the relationship between $\delta_d/\delta_j$ and strain ratio, $\varepsilon_u/\varepsilon_{pmax}$ [i.e., $(P_u/EA)/(V_{ap}/C_a)$], was provided. The relative joint displacment at the locally weak joint is a product of the relative joint displacement at the existing cracked joint and the correction factor.

The models for seismic wave interaction with pipelines also have application to other linear structures, such as displacement at flexible connections between subaqueous tunnels and shore facilities when subjected to near-source strong motions.

## 8.5. Prototype for Water Supply System Seismic Performance Evaluation

A process for the seismic performance evaluation of water supply systems was developed using the LADWP water supply system. The seismic hazards in the LADWP water supply system were characterized by a suite of 59 scenario earthquakes and their annual frequencies of occurrence. Procedures were developed to determine the seismic demands on the system components, which were compiled into a hydraulic network model.

The characteristics of the LADWP water supply system are embodied in a H2ONET hydraulic network model. The H2ONET hydraulic network model was developed under the supervision of LADWP engineers. It contains 9,287 nodes and 10,665 links, representing about 2,186 km of pipelines, 1,052 demand nodes, 591 control valves, 110 tanks and reservoirs, 151 local groundwater wells, and 284 pumps.

The H2ONET hydraulic network model was exported to GIRAFFE, which provides virtually identical results for the undamaged LADWP system when comparing with the results from H2ONET.

The damage to the pipelines during earthquakes was estimated using the regressions between repair rates and PGVs based on performance records from previous earthquakes. The damage to the trunk lines was simulated explicitly. A Poisson process was utilized to simulate the occurrences of trunk line damage. This type of damage was further categorized into leaks and breaks that, in turn, were simulated using pipe leak and break hydraulic models, respectively. The damage of local distribution lines was simulated by increasing the nodal demands such that they represent water losses consistent with earthquake-related repair rates in the local distribution systems.

The seismic system performance of the LADWP water system was evaluated using GIRAFFE. Fifteen Monte Carlo simulations were performed for each of the 59 scenario earthquakes, resulting 885 simulations in total. The number of simulations in each Monte Carlo analysis was determined by the GIRAFFE self-termination algorithm, which stops the simulation process when the difference in the mean and coefficient of variation of the results are less than 2%. The 885 simulation results were integrated in the form of risk curves, plotting the annual exceedance frequency as a function of system serviceability index (SSI), which is defined as the ratio of the sum of satisfied water demands after an earthquake to that before an earthquake. The effects of the loss of storage water in tanks after earthquakes on system performance were evaluated by simulating the leakage from damaged pipelines for a 24-hour period after the earthquake and comparing risk curves with and without the 24-hour running

period. The engineering evaluation results, expressing as the water availability after earthquakes, serve as the key input in the social and economic consequence evaluations performed by the social scientists and economists.

## 8.6. Probabilistic Seismic Performance Evaluation of LADWP Water Supply System

The system risk curve without storage water loss varies almost linearly in the semi-logarithmetic scale, with an SSI of 0.79, which corresponds to an annual frequency of 0.0021, or 475-year recurrence interval. After a 24-hour period of running tanks, the system deteriorates rapidly, and the SSI decreases significantly. The system risk curve with 24-hour running tanks plots to the right of the first curve, indicating much lower SSI values for the same annual exceedance frequency. The linear portion of the curve, with lower SSI values, is approximately parallel to the system risk curve without a 24-hour period of water losses from the tanks. For the condition of tank losses, the system risk curve shows an SSI of 0.42, which corresponds to an annual frequency of 0.0021, or 475-year recurrence interval. The difference between the curve without a 24-hour period of running tanks and its parallel portion in the curve with a 24-hour period of running tanks signifies the effects of water losses from tanks.

The system risk curve with a 24-hour period of running tanks was examined closely to identify the key scenario earthquakes that significantly influence system risk and their characteristics. The risk level corresponding to a 475-year recurrence interval, or 10% probability of exceedance in 50 years, is attributed to fifteen scenario earthquakes, as summarized in the main text. Most scenario earthquakes, contributing

to the system risk, originate on faults located within 30 km of the system centroid, i.e., inside the system service areas, and have magnitude greater than 6.5.

The risk level corresponding to a 50-year recurrence interval, or 100% probability of exceedance in 50 years, can be attributed to 44 scenario earthquakes. Significant contributions from scenario earthquakes with relatively large distances from originating faults to the system centroid were observed, particularly those associated with the San Andreas fault, which are about 55 km from the system centroid.

It was found that the number of scenario earthquakes, which have contributions to the system risk, increases significantly as the recurrence interval for the risk decreases from 475 years to 50 years. Furthermore, as the recurrence interval decreases, or SSI increases, the contributions from scenario earthquakes with relatively large distance from the originating faults to the system increase significantly.

The risk curves were also constructed for five water districts to provide additional information about the spatial distribution of system risks. It was found that the water districts have significantly different risk curves. According to the risk curves without storage water loss in tanks, the most vulnerable one is the Harbor Water District, followed by the Central and Western Water Districts. The most robust district is the West Valley Water District. The performance of five water districts is consistent with their relative positions in the system and with the north to the south water flow pattern in the LADWP water supply system.

For a 24-hour period of water losses from tanks, the SSIs decrease by varying degrees in the water districts. The most vulnerable districts are the Western and Central Water Districts, followed by the West Valley and Harbor Water Districts. The most robust district is the East Valley Water District. The performance of five water districts is consistent with the concentration of the most water storage tanks in the Western, Central, and West Valley Water Districts and with the north to the south water flow pattern in the LADWP water supply system.

The risk curves with a 24-hour period of tank water losses were examined closely to identify the key scenario earthquakes that significantly influence the water district risks. It was found that the number of scenario earthquakes that have contributions to the water district risk increases significantly as the recurrence interval for the risk decreases from 475 years to 50 years. Furthermore, as the recurrence interval decreases, or SSI increases, the contributions from scenario earthquakes with relatively large distances from originating faults to the water districts increase significantly. However, it was found that, even for risks with relatively large recurrence intervals, the Harbor Water District is significantly affected by scenario earthquakes with relatively large distances from originating faults to the water district because of its southern end position in the system and the long distance that the water has to travel before arriving at the district.

## 8.7. Future Research

This work focuses on the seismic performance evaluation of pipelines and their impact on the overall system performance. The seismic performance evaluation of other components, such as pump stations, regulation stations, ground water wells, and

tanks and reservoirs, is not included in this work. It is useful to extend this study to incorporate the seismic performance of those components and to integrate their impacts to the overall system reliability and serviceability after earthquakes. The framework and procedures described in this work can be readily adapted to other components, provided that fragility information for those components is developed.

Because of the difficulty in predicting the occurrence of permanent ground deformation and delineating the spatial distribution of permanent ground deformation, the PGD effects on the system component performance during earthquakes are not currently incorporated in this work. It is also valuable to extend this study to incorporate the PGD effects on the seismic performance of system components, as well as the overall system. The framework and procedures described in this work can be easily modified to incorporate PGD effects.

Interdependencies among different lifeline systems are one of the most prominent characteristics of lifeline systems. The damage and disruption of seismic hazards in other systems may affect the system being assessed because of physical proximity and/or operational interaction. For example, the loss of electricity affects water supply systems by rendering pumps and automatic valves inoperable, thereby affecting the flow and pressure in the water supply systems. Therefore, one important component of the framework for lifeline seismic performance evaluation is the interaction of the system under scrutiny with other lifeline systems. Although the interactions among different lifeline systems are beyond the scope of this work, further studies of that issue are highly recommended.

# CHAPTER 9
# REFERENCES

Abrahamson, N. A. and Silva, W. J. (1997). "Empirical Response Spectral Attenuation Relations for Shallow Crustal Earthquakes." *Seismological Research Letters*, Vol. 68, No. 1, 94-127.

American Lifelines Alliance (ALA). (2001). *Seismic Fragility Formulations for Water Systems*.

http://www.americanlifelinesalliance.org/Products_new3.htm#WaterSystems

American Water Works Association (AWWA) (1999). "Prestressed Concrete Pipe, Steel-Cylinder Type." *AWWA Standard C301-99*. AWWA, Denver, CO, 33p.

American Water Works Association (AWWA) (2003). "Concrete Pressure Pipe, Bar-Wrapped, Steel-Cylinder Type." *AWWA Standard C303-02*. AWWA, Denver, CO, 44p.

Atkinson, G. M. and Boore, D. M. (2003). "Empirical Ground-Motion Relations for Subduction Zone Earthquakes and Their Application to Cascadia and Other Regions." *Bulletin of the Seismological Society of America*, Vol. 93, No. 4, 1703-1729.

Autodesk (2005).

http://usa.autodesk.com/adsk/servlet/home?siteID=123112&id=129446

Avram, C., Facaoaru, I., Filimon, I., Mirsu, O., and Tertea, I. (1981). *Concrete Strength and Strains*. Elsevier Scientific Publishing Company, North-Holland, 557p.

Ayala, A. G. and O'Rourke, M. J. (1989). "Effects of the 1985 Michoacan Earthquake on Water System and Other Buried Lifelines in Mexico City." *Technical Report NCEER-89-0009*. Multidisciplinary Center for Earthquake Engineering Research, Buffalo, NY, 110p.

allantyne, D. B., Berg, E., Kennedy, J. Reneau, R., and Wu, D. (1990). "Earthquake Loss Estimation Modeling of the Seattle Water System." *Technical Report*. Kennedy/Jenks/Chilton, Federal Way, WA, 139p.

Bird, J., O'Rourke, T., Bracegirdle, T., Bommer, J., and Tromans, I. (2004). "A Framework for Assessing Earthquake Hazards for Major Pipelines." *Proceedings of International Conference on Terrain and GeohazardsFacing Onshore Oil and Gas Pipelines, GeoPipe 2004*. Thomas Telford, London.

Boore, D. M., Joyner, W. B., and Fumal, T. E. (1997). "Equations for Estimating Horizontal Response Spectra and Peak Acceleration from Western North American Earthquakes: A Summary of Recent Work." *Seismological Research Letters*, Vol. 68, No. 1, 128-153.

Cagnan, Z. (2005). "Post-Earthquake Restoration Modeling For Critical Lifeline Systems." *Ph.D. Dissertation*. Cornell University, Ithaca, NY.

Campbell, K. W. and Bozorgnia, Y. (2003). "Updated Near-Source Ground-Motion (Attenuation) Relations for the Horizontal and Vertical Components of Peak Ground Acceleration and Acceleration Response Spectra." *Bulletin of the Seismological Society of America*, Vol. 93, No. 1, 314-331.

Cao, T., Bryant, W. A., Rowshandel, B., Branum, D., and Wills, C. J. (2003). *The Revised 2002 California Probabilistic Seismic Hazard Maps*. http://www.consrv.ca.gov/CGS/rghm/psha/fault_parameters/pdf/2002_CA_Hazard_Maps.pdf

Carino, N. J. (1974). "The Behavior of a Model of Plain Concrete Subject to Compression-Tension and Tension-Tension Biaxial Stresses." *Ph.D. Dissertation*. Cornell University, Ithaca, NY.

Chang, J.-F. (2006). "P-Y Modeling of Soil-pile Interaction." *Ph.D. Dissertation*. Cornell University, Ithaca, NY.

Chang, S. E. and Chamberlin, C. (2004). "Assessing the Role of Lifeline System in Community Disaster Resilience." *Research Progress and Accomplishments 2003-2004*. Multidisciplinary Center for Earthquake Engineering Research, Buffalo, NY.

Chang, S. E. and Miles, S. B. (2003). "Resilient Community Recovery: Improving Recovery Through Comprehensive Modeling." *Research Progress and Accomplishments 2001-2003*. Multidisciplinary Center for Earthquake Engineering Research, Buffalo, NY.

Chang, S. E., Rose, A., Shinozuka, M., Svekla, W. D., and Tierney, K. J. (2000a). "Modeling Earthquake Impact on Urban Lifeline Systems: Advances and Integration." *Research Progress and Accomplishments: 1999-2000*. Multidisciplinary Center for Earthquake Engineering Research, Buffalo, NY.

Chang, S. E., Seligson, H. A., and Eguchi, R. T. (1996). "Estimation of the Economic Impact of Multiple Lifeline Disruption: Memphis Light, Gas and Water Division Case Study." *Technical Report NCEER-96-0011*. National Center for Earthquake Engineering Research, Buffalo, NY.

Chang, S. E., Shinozuka, M., and Moore II, J. E. (2000b). "Probabilistic Earthquake Scenarios: Extending Risk Analysis Methodologies to Spatially Distributed Systems." *Earthquake Spectra*, Vol. 16, No. 3, 557-572.

Chang, S. E., Svekla, W. D., and Shinozuka, M. (2002). "Linking Infrastructure and Urban Economy: Simulation of Water Disruption Impacts in Earthquakes." *Environment and Planning B*, Vol. 29, No. 2, 281-301.

Chen, Y.-J. and Kulhawy, F. H. (1994). "Case History Evaluation of the Behavior of Drilled Shafts under Axial and Lateral Loading." *EPRI TR-104601*. Electric Power Research Institute, Palo Alto, CA.

Chopra, A.K. (2001). *Dynamics of Structures: Theory and Application to Earthquake Engineering*. 2$^{nd}$ Edition, Prentice Hall, NJ, 729p.

Chopra, A. K. (2005). *Earthquake dynamics of structures: a primer*. Earthquake Engineering Research Institute, Oakland, CA, 129p.

Committee on Gas and Liquid Fuel Lifelines (CGLFL) (1984). *Guidelines for the Seismic Design of Oil and Gas Pipeline Systems*. ASCE, New York, NY, 471p.

Consortium of Organizations for Strong-Motion Observation Systems (COSMOS) (2004). http://db.cosmos-eq.org/scripts/default.plx

Cornell, C. A. (1968). "Engineering Seismic Risk Analysis." *Bulletin of the Seismological Society of America*, Vol. 58, No. 5, 1583-1606.

Davidson R. A. and Cagnan, Z. (2004). "Restoration Modeling of Lifeline Systems." *Research Progress and Accomplishments 2003-2004*. Multidisciplinary Center for Earthquake Engineering Research, Buffalo, NY.

Davis, C. A. (1999). "Case Study of the Granada Trunk Line during Two Near-field Earthquakes." *Proceedings of the 7th US-Japan Workshop on Earthquake Resistant Design of Lifeline Facilities and Countermeasures for Soil Liquefaction*. Seattle, WA, O'Rourke T. D., Bardet, J. P., and Hamada, M., ed., 415-430.

Davis, C. A. (2003). *Personal Communications*.

Davis, C. A. and Bardet, J. P. (1995). "Seismic Performance of Van Norman Water Lifelines." *Lifeline Earthquake Engineering*, *Technical Council on Lifeline Earthquake Engineering Monograph No. 6*. ASCE, Reston, VA, O'Rourke, M. J., ed., 653-659.

Davis, C. A. and Bardet, J. P. (2000). "Responses of Buried Corrugated Metal Pipes to Earthquakes." *Journal of Geotechnical and Geoenvironmental Engineering*, ASCE, Vol. 126, No., 1, 28-39.

Duke, C. M. and Moran, D. F. (1972). "Earthquakes and City Lifelines." *San Fernando Earthquake of February 9, 1971 and Public Policy*. Gate, G. O., ed., Joint Committee on Seismic Safety, California Legislature, San Jose, CA, 132p.

Eguchi, R. T. and Chung, R. M. (1995). "Performance of lifelines during the January 17, 1994 Northridge Earthquake." *Lifeline Earthquake Engineering*, *Technical Council on Lifeline Earthquake Engineering Monograph No. 6*. O'Rourke, M. J., ed., ASCE, Reston, VA, 120-127.

Eidinger, J. M. (1998). "Water-Distribution System." *the Loma Prieta, California, Earthquake of October 17, 1989-Lifelines*. Schiff, A. J., ed., US Geological Survey Professional Paper 1552-A, US State Government Printing Office, Washington D. C., A63 – A86.

Environmental Protection Agency, USA (EPA, 2005).
http://www.epa.gov/ORD/NRMRL/wswrd/epanet.html

Environmental Systems Research Institute, Inc. (ESRI, 1999). *Getting Started with ArcGIS*. Redlands, CA.

Environmental Systems Research Institute, Inc. (ESRI, 2001). *Using ArcGIS Geostatistical Analyst*. Redlands, CA.

Federal Emergency Management Agency (FEMA, 1999). *HAZUS99 Technical Manual*. FEMA, Washington, D. C.

Federal Emergency Management Agency (FEMA, 2003). *FEMA-450: NEHRP Recommended Provisions for Seismic Regulations for New Buildings and Other Structures*. 2003 Edition, Washington, D. C., Developed by the Building Seismic Safety Council (BSSC) for FEMA.

Frankel, A., Mueller, C., Barnhard, T., Perkins, D., Leyendecker, E. V., Dickman, N., Hanson, S., and Hopper, M. (1996). "Documentation for June 1996 National

Seismic Hazard Maps." *Open-File Report 96-532*. US Geological Survey, Denver, CO.

Frankel, A., Petersen, M., Mueller, C., Haller, K., Wheeler, R., Leyendecker, E. V., Wesson, R., Harmsen, S., Cramer, C., Perkins, D., and Rukstales, K. (2002). "Documentation for the 2002 Update of the National Seismic Hazard Maps." *Open-File Report 02-420*. US Geological Survey, Denver, CO.

Gilbert, G. K., Humphrey, R. L., Sewell, J. S., and Soule, F. (1907). "The San Francisco Earthquake and Fire of April 18, 1906 and Their Effects on Structures and Structural Materials." *Bulletin 324*. US Geological Survey, US Government Printing Office, Washington D.C.

Goh, A. T. C., Kulhawy, F. H., and Chua, C. G. (2005). "Bayesian Neural Network Analysis of Undrained Side Resistance of Drilled Shafts." *Journal of Geotechnical and Geoenvironmental Engineering*, ASCE, Vol. 131, No. 1, 84-93.

Goh, S. H. and O'Rourke, T. D. (2000). "Geotechnical Engineering Analysis and Design for Pile Response to Liquefaction-Induced Ground Deformation." *Proceedings of the 12th World Conference on Earthquake Engineering*. Auckland, NZ.

Grigoriu, M. D. (1995). *Applied Non-Gaussian Processes: Examples, Theory, Simulation, Linear Random Vibration, and MATLAB*. PTR Prentice Hall, Englewood Cliffs, NJ, 442p.

Grigoriu, M. D., O'Rourke, T. D., and Khater, M. M. (1989). "Serviceability of the San Francisco Auxiliary Water Supply System." *Proceedings of International Conference on Structural Safety and Reliability*. San Francisco, CA.

Hamada, M. and O'Rourke, T. D. (1992). "Case Studies of Liquefaction and Lifeline Performance during Past Earthquakes." *NCEER-92-0001*. Vol. 1, National Center for Earthquake Engineering Research, Buffalo, NY.

Hamada, M., Isoyama, R., and Wakamatsu, K. (1996). "Liquefaction-induced Ground Displacement and its Related Damage to Lifeline Facilities." *Soils and Foundations*, Vol. 36, Special Issue, 81-98.

Hamada, M. and Wakamatsu, K. (1996). "Liquefaction, Ground Deformation and Their Caused Damage to Structures." *The 1995 Hyogoken-Nanbu Earthquake – Investigation into Damage to Civil Engineering Structures*. Committee of Earthquake Engineering, Japan Society of Civil Engineers.

Harmsen, S. and Frankel, A. (2001). "Geographic Deaggregation of Seismic Hazard in the United States." *Bulletin of the Seismological Society of America*, Vol. 91, No.1, 13-26.

Harmsen, S., Perkins, D., and Frankel, A. (1999). "Deaggregation of Probabilistic Ground Motions in the Central and Eastern United States" *Bulletin of the Seismological Society of America*, Vol. 89, No.1, 1-13.

Holzer, T. L., Bennett, M. J., Ponti, D. J., and Tinsley, J. C. (1999). "Liquefaction and Soil Failure During 1994 Northridge Earthquake." *Journal of Geotechnical and Geoenvironmental Engineering*, ASCE, Vol. 125, No. 6, 438-452.

Hwang, H. H. M., Lin, H., and Shinozuka, M. (1998). "Seismic Performance Assessment of Water Distribution Systems." *Journal of Infrastructure Systems*, ASCE, Vol. 4, No. 3, 118- 125.

Jeon, S-S. (2002). "Earthquake Performance of Pipelines and Residential Buildings and Rehabilitation with Cast-in-place Pipe Lining Systems." *Ph.D. Dissertation*. Cornell University, Ithaca, NY.

Jeon, S-S. and O'Rourke, T. D. (2005). "Northridge Earthquake Effects on Pipelines and Residential Buildings." *Bulletin of the Seismological Society of America*, Vol. 95, No.1, 294-318.

Kramer, S. L. (1996). *Geotechnical Earthquake Engineering*. Prentice Hall, NJ, 653p.

Kubo, K. (1974). "Behavior of Underground water Pipes during an Earthquake." *Proceedings of the 5th World conference on Earthquake Engineering*. Rome, Italy, 569-578.

Kulhawy, F. H. and Chen, Y.-J. (2003). "Evaluation of Undrained Side and Tip Resistances for Drilled Shafts." *Soil and Rock America 2003, Proceedings of the 12th Pan-Am Conference on Soil Mechanics Geotechnical Engineering / the 39th US Rock Mechanics Symposium*. Culligan, P. J., Einstein, H. H., and Whittle, A. J., ed., Cambridge, MA, 1963-1968.

Kulhawy, F. H., Trautmann, C. H., Beech, J. F., O'Rourke, T. D., and McGuire, W. (1983). "Transmission Line Structure Foundations for Uplift-Compression Loading." *EPRI EL-2870*. Electric Power Research Institute, Palo Alto, CA.

Lee, J., Graf, W., Somerville, P., O'Rourke, T. D., and Shinozuka, M. (2005). "Development of Earthquake Scenarios for Use in Earthquake Risk Analysis for Lifeline System." *Report for the Los Angeles Department of Water and Power*. Los Angeles, CA, 34p.

Leontief, W. (1986). *Input-output Economics*. Wiley, NY, 257p.

Los Angeles Department of Water and Power (LADWP) (1994). *January 17, 1994 Northridge Earthquake Major Emergency Report*. Power Operating and Maintenance Division, Operating Engineering Section, Los Angeles, CA.

Los Angeles Department of Water and Power (LADWP) (1996). *Geotechnical Report on Earthquake Damage to the Granada Trunk Line at the Van Norman Complex*. Water Supply Division, Report No. AX500, Los Angeles, CA.

Los Angeles Department of Water and Power (LADWP) (1997). *Response of the High Speed and Bypass Channels to the 1994 Northridge Earthquake and Recommended Repairs*. Water Supply Division, Report No. AX215-47, Los Angeles, CA.

Los Angeles Department of Water and Power (LADWP) (2002a). *H2ONET Hydraulic Model of the LADWP Water Supply System.* Los Angeles, CA.

Los Angeles Department of Water and Power (LADWP) (2002b). *Flow Diagram of the LADWP Water Supply System.* Los Angeles, CA.

Los Angeles Department of Water and Power (LADWP) (2002c). *Water Map of the LADWP Water Supply System.* Los Angeles, CA.

Lund, L. and Cooper, T. (1995). "Water System." *Northridge Earthquake: Lifeline Performance and Post-earthquake Response, Technical Council on Lifeline Earthquake Engineering Monograph No. 8*. Schiff, A.J., ed., ASCE, New York, NY, 96-131.

Lund, L., Davis, C. A., and Adams, M. L. (2005). "Water System Seismic Performance 1994 Northridge – 1995 Kobe Earthquakes." *Proceeding of the 4th Japan-US Workshop on Seismic Measures for Water Supply*. AWWARF/FWWA, Kobe, Japan.

Markov, I., Grigoriu, M., and O'Rourke, T. D. (1994). "An Evaluation of Seismic Serviceability Water Supply Networks with Application to the San Francisco Auxiliary Water Supply System." *Technical Report NCEER-94-0001*. Multidisciplinary Center for Earthquake Engineering Research, Buffalo, NY.

MWH Soft, Inc. (1999). *H2ONET Users Guide*. Pasadena, CA.

Mulligan, G. (2003). *Personal Communications*.

Naeim, F. (2003). *The Seismic Design Handbook*. Kluwer Academic Publishers, Norwell, MA, 830p.

Newmark, N. M. (1967). "Problems in Wave Propagation in Soils and Rocks." *Proceedings of the International Symposium on Wave Propagation and Dynamic Properties of Earth Materials*. University of New Mexico Press, 7-26.

Nigg, J. (1998). *Perceptions of Earthquake Impacts and Loss-Reduction Policy Preferences among Community Residents and Option Leaders*. Disaster Research Center, University of Delaware.

O'Rourke, M. J. and Liu, X. (1999). "Response of Buried Pipelines Subject to Earthquake Effects." *Multidisciplinary Center for Earthquake Engineering Research Monograph Series No. 3*. Multidisciplinary Center for Earthquake Engineering Research, Buffalo, NY.

O'Rourke, T. D. (1998). "An Overview of Geotechnical and Lifeline Earthquake Engineering." *Geotechnical Special Publication No. 75, Proceedings of Geotechnical Earthquake Engineering and Soil Dynamics Conference*. Seattle, WA, Vol. 2, 1392-1426.

O'Rourke, T. D. (2005). *Personal Communications*.

O'Rourke, T. D., Beaujon, P. A., and Scawthorn, C. R. (1992). "Large Ground Deformations and Their Effects on Lifelines Facilities: 1906 San Francisco Earthquake." *Case Studies of Liquefaction and Lifeline Performance during Past Earthquakes, NCEER-92-0002*. O'Rourke, T. D. and Hamada, M., ed., National Center for Earthquake Engineering Research, Buffalo, NY, Vol 2, 1.1-1.130.

O'Rourke, T. D., Bonneau, A. L., Pease, J. W., Shi, P. and Wang, Y. (2006). "Liquefaction and Ground Failures in San Francisco." *Earthquake Spectra*, Vol. 22, 1906 San Francisco Earthquake Special Issue, in press.

O'Rourke, T. D. and Hamada, M. (1992). "Case Studies of Liquefaction and Lifeline Performance During Past Earthquakes." *NCEER-92-0002*. Vol. 2, National Center for Earthquake Engineering Research, Buffalo, NY.

O'Rourke, T. D. , Netravali, A. N., Pendharkar, S. M., Tonkinson, A., Chaudhuri, D., and Toprak, S. (1996). "Evaluating Service Life of Anaerobic Joint Sealing Products and Techniques." *Report No: GRI-96/031.* Gas Research Institute, Chicago, IL.

O'Rourke, T. D., Pease, J. W. (1992). "Large Ground Deformations and Their Effects on Lifelines Facilities: 1989 Loma Prieta Earthquake." *Case Studies of Liquefaction and Lifeline Performance during Past Earthquakes*, *NCEER-92-0002*. O'Rourke, T. D. and Hamada, M., ed., National Center for Earthquake Engineering Research, Buffalo, NY, Vol 2, 5.1-5.85.

O'Rourke, T. D., Stewart, H. E., and Jeon, S-S. (2001). "Geotechnical Aspect of Lifeline Engineering." *Geotechnical Engineering*, ICE, Vol. 149, No. 1, 13-26.

O'Rourke, T. D., and Toprak, S. (1997). "GIS Assessment of Water Supply Damage from the Northridge Earthquake." *Spatial Analysis in Soil Dynamics and Earthquake Engineering*, *Geotechnical Special Publication* No. 67. Frost, J. D., ed., ASCE, Reston, VA, 117-131.

O'Rourke, T. D., Turner, J. E., Jeon, S-S., Stewart, H. E., Wang, Y., and Shi, P. (2005). "Soil-structure Interaction Under Extreme Loading Conditions." *Buchanan Lecture*, Texas A&M University.

O'Rourke, T. D., Wang, Y., and Shi, P. (2004a). "Advances in Lifeline Earthquake Engineering." *Proceedings of the 13th World Conference on Earthquake Engineering.* Vancouver, British Columbia, Canada, Paper No. 5003.

O'Rourke, T. D., Wang, Y., Shi, P., and Jones, S. (2004b). "Seismic Wave Effects on Water Trunk and Transmission Lines." *Proceedings of the 11th International*

*Conference on Soil Dynamics & Earthquake Engineering, and 3rd International Conference on Earthquake Geotechnical Engineering.* Berkeley, CA, Vol. 2, 420-428.

Petersen, M. D., Bryant, W. A., Cramer, C. H., Cao, T., Reichle, M., Frankel, A. D., Lienkaemper, J. J., McCrory, P. A., and Schwartz, D. P. (1996). "Probabilistic Seismic Hazard Assessment for the State of California." *Open-File Report 96-08*. California Department of Conservation, Division of Mines and Geology, Sacramento, CA, *Open-File Report 96-706*. US Geological Survey, Denver, CO.

Prior, J. C. (1935). "Investigation of Bell and Spigot Joints in Cast Iron Water Pipes." *Bulletin 87*. Ohio State University Experiment Station.

Pugh, J. (2003). *Personal Communications*.

Reiter, L. (1990). *Earthquake Hazard Analysis*. Columbia University Press, NY, 254p.

Rose, A. (2005) *Personal Communications.*

Rose, A. and Benavides, J. (1998). "Regional Economic Impacts." *Engineering and Socioeconomic Impacts of Earthquakes, Multidisciplinary Center for Earthquake Engineering Research Monograph Series 2*. Multidisciplinary Center for Earthquake Engineering Research, Buffalo, NY.

Rose, A., Benavides, J., Chang, S., Szczesniak, P., and Lim, D. (1997). "The Regional Economic Impact of an Earthquake: Direct and Indirect Effects of Electricity Lifeline Disruptions." *Journal of Regional Science*, Vol. 37, No. 3, 437-458.

Rose, A. and Guha, G. (2003). "Computable General Equilibrium Modeling of Electric Utility Lifeline Losses from Earthquakes." *Modeling the Spatial Economic Impacts of Natural Hazards*. Chang, S. and Okuyama, Y., ed., Springer. 323p.

Rose, A. and Liao, S.-Y. (2003). "Understanding Sources of Economic Resiliency to Hazards: Modeling the Behavior of Lifeline Service Customers." *Research Progress and Accomplishments 2001-2003*. Multidisciplinary Center for Earthquake Engineering Research, Buffalo, NY.

Rose, A. and Liao, S.-Y. (2005). "Modeling Regional Economic Resiliency to Earthquakes: A Computable General Equilibrium Analysis of Water Service Disruptions." *Journal of Regional Science,* Vol. 45, No. 1, 75-112.

Rossman, L.A. (2000). *EPANET 2 Users Manual*. National Risk Management Research Laboratory, Office of Research and Development, US Environmental Protection Agency, Cincinnati, OH.

Sadigh, S., Chang, C.-Y., Egan, J. A., Makdisi, F., and Youngs, R. R. (1997). "Attenuation Relationships for Shallow Crustal Earthquakes Based on California Strong Motion Data." *Seismological Research Letters*, Vol. 68, No. 1, 180-189.

Sakurai, A. and Takahashi, T. (1969). "Dynamic Stress of Underground Pipelines During Earthquakes." *Proceedings of the 4th World Conference on Earthquake Engineering*. Santiago, Chile, 811-895.

Scawthorn, C., O'Rourke, T. D., and Balckburn, F. T. (2006). "The San Francisco Earthquake and Fire of 1906 – Enduring Lesson for Fire Protection and Water Supply." *Earthquake Spectra*, Vol. 22, 1906 San Francisco Earthquake Special Issue, in press.

Schwartz, D. P. and Coppersmith, K. J. (1984). "Fault Behavior and Characteristic Earthquakes: Examples from the Wasatch and San Andreas Faults." *Journal of Geophysical Research*, Vol. 89, No. B7, 5873-5890.

Shi, P. (2006). "Seismic Response Modeling of Water Supply Systems." *Ph.D. Dissertation*. Cornell University, Ithaca, NY.

Shinozuka, M. and Chang, S. E. (2004). "Evaluating the Disaster Resilience of Power Networks and Grids." *Modeling Spatial Economic Impacts of Disasters*. Chang, S. and Okuyama, Y., ed., Springer, 323p.

Shinozuka, M., Chang, S. E., Cheng, T.-C., Feng, M., O'Rourke, T. D., Saadeghvaziri, M. A., Dong, X., Jin, X., Wang, Y., and Shi, P. (2004). "Resilience of Integrated Power and Water Systems." *Research Progress and Accomplishments 2003-2004*. Multidisciplinary Center for Earthquake Engineering Research, Buffalo, NY.

Shinozuka, M., Feng, M., Dong, X., Chang, S. E., Cheng, T.-C., Jin, X., and Saadeghvaziri, M. A. (2003). "Advances in Seismic Performance Evaluation of Power Systems." *Research Progress and Accomplishments 2001-2003*. Multidisciplinary Center for Earthquake Engineering Research, Buffalo, NY.

Shinozuka, M., and Hwang, H. H. M. (1998). "Seismic Performance of Electric Power System." *Engineering and Socioeconomic Impacts of Earthquake: An Analysis of Electricity of Lifetime Distributions in New Madrid Area*, *Multidisciplinary Center for Earthquake Engineering Research Monograph Series No. 2*. Multidisciplinary Center for Earthquake Engineering Research, Buffalo, NY, 33-43.

Shinzuka, M., Hwang, H., and Murata, M. (1992). "Impact on Water Supply of a Seismically Damaged Water Delivery System." *Lifeline Earthquake Engineering in the Central and Eastern US, Technical Council on Lifeline Earthquake Engineering Monograph No.5*. Ballantyne, D. B., ed., ASCE, Reston, VA, 43-57.

Shinozuka, M. and Koibe, T. (1979). "Estimation of Structural Strains in Underground Lifeline Pipes." *Lifeline Earthquake Engineering – Buried Pipelines, Seismic Risk, and Instrumentation*. PVP-34, ASME, 31-48.

Shinozuka, M., Rose, A., and Eguchi, R. T. (1998). *Engineering and Socioeconomic Impacts of Earthquakes*, *Multidisciplinary Center for Earthquake Engineering Research Monograph Series 2*. Multidisciplinary Center for Earthquake Engineering Research, Buffalo, NY.

Shoven, J. and Whalley, J. (1992). *Applying General Equilibrium*. Cambridge University Press, NY, 299p.

Spudich, P., Joyner, W. B., Lindh, A. G., Boore, D. M., Margaris, B. M., and Fletcher, J. B. (1999). "A Revised Ground Motion Prediction Relation for Use in Extensional Tectonic Regimes." *Bulletin of the Seismological Society of America*, Vol. 89, No. 5, 1156-1170.

Stewart, J. P., Seed, R. B., and Bray, J. D. (1996). "Incidents of Ground Failure from the 1994 Northridge Earthquake." *Bulletin of the Seismological Society of America*, Vol. 86, No.1B, S300-S318.

Tanaka, S. (1996). "Lifeline Seismic Performance Analysis for Water and Electric Power Systems." *Ph.D. Dissertation*. Waseda University, Tokyo, Japan.

Taylor, C. E. (1991). "Seismic Loss Estimation for a Hypothetical Water System." *Technical Council on Lifeline Earthquake Engineering Monograph No.2*. ASCE, Reston, VA.

Thompson, M. (2003). *Personal Communications*.

Toprak, S. (1998). "Earthquake Effects on Buried Lifeline Systems." *Ph.D. Dissertation*. Cornell University, Ithaca, NY.

Trifunac, M. D., Todorovska, M. I., and Lee, V. W. (1998). "The Rinaldi Strong Motion Accelerogram of the Northridge, California, Earthquake of 17 January, 1994." *Earthquake Spectra*, Vol. 14, No. 1, 225-239.

United States Geological Survey (USGS, 2005). http://eqhazmaps.usgs.gov/

Vargas, V. (2005). *Personal Communications*.

Wald, D., Heaton, T. H., and Hudnut, K. W. (1996). "The Slip History of the 1994 Northridge, California, Earthquake Determined from Strong-motion, Teleseismic, GPS, and Leveling Data." *Bulletin of the Seismological Society of America*, 1996, 86 No. 1B, S49-S70.

Wills, C. J., Petersen, M., Bryant, W. A., Reichle, M., Saucedo, G. J., Tan, S., Taylor, G., and Treiman, J. (2000). "A Site-Conditions Map for California Based on Geology and Shear-Wave Velocity." *Bulletin of the Seismological Society of America*, Vol. 90, No. 6B, S187-S208.

Wu, C., Fok, E., Fotinos, G., Tseng, W., and Oberholtzer, G. (2003). "Seismic Assessment and Retrofit Concepts of the BART Transbay Tube." *Advancing Mitigation Technologies and Disaster Response for Lifeline Systems, Proceedings of the 6th US Conference and Workshop on Lifeline Earthquake Engineering*. Long Beach, CA, 203-212.

Yeats, R. S., Sieh, K., and Allen, C. R. (1997). *Geology of Earthquakes*. Oxford University Press, NY, 568p.

Youngs, R. R., Chiou, S. J., Silva, W. J., and Humphrey, J. R. (1997). "Strong Ground Motion Attenuation Relationships for Subduction Zone Earthquakes." *Seismological Research Letters*, Vol. 68, No. 1, 58-73.

# APPENDIX A

# TRUNK LINE REPAIRS DURING 1994 NORTHRIDGE EARTHQUAKE AND REGRESSION ANALYSIS

## A.1.  Introduction

This appendix describes a database containing trunk line (diameter $\geq$ 610 mm) repairs during the 1994 Northridge earthquake and regression analysis based on this database. It starts with the collection of trunk line repair information from four water agencies affected by the 1994 Northridge earthquake, followed by an effort to determine the zones of documented permanent ground deformation (PGD) and to screen trunk line repairs in those zones so that the resulting statistics reflect principally the effects of transient ground deformation (TGD). It then proceeds to regression analysis for concrete, steel, and riveted steel trunk lines, using the strong ground motion data and regression procedures developed by O'Rourke et al., (2001) and Jeon (2002).

## A.2.  Trunk Line Repair Database

The database contains repairs on trunk lines operated by four water agencies, i.e., the Los Angeles Department of Water and Power (LADWP), Metropolitan Water District (MWD), Calleguas Municipal Water District (CMWD), and Castaic Lake Water Agency (CLWA). In total, 125 repairs in 1094.9 km of trunk line were collected

287
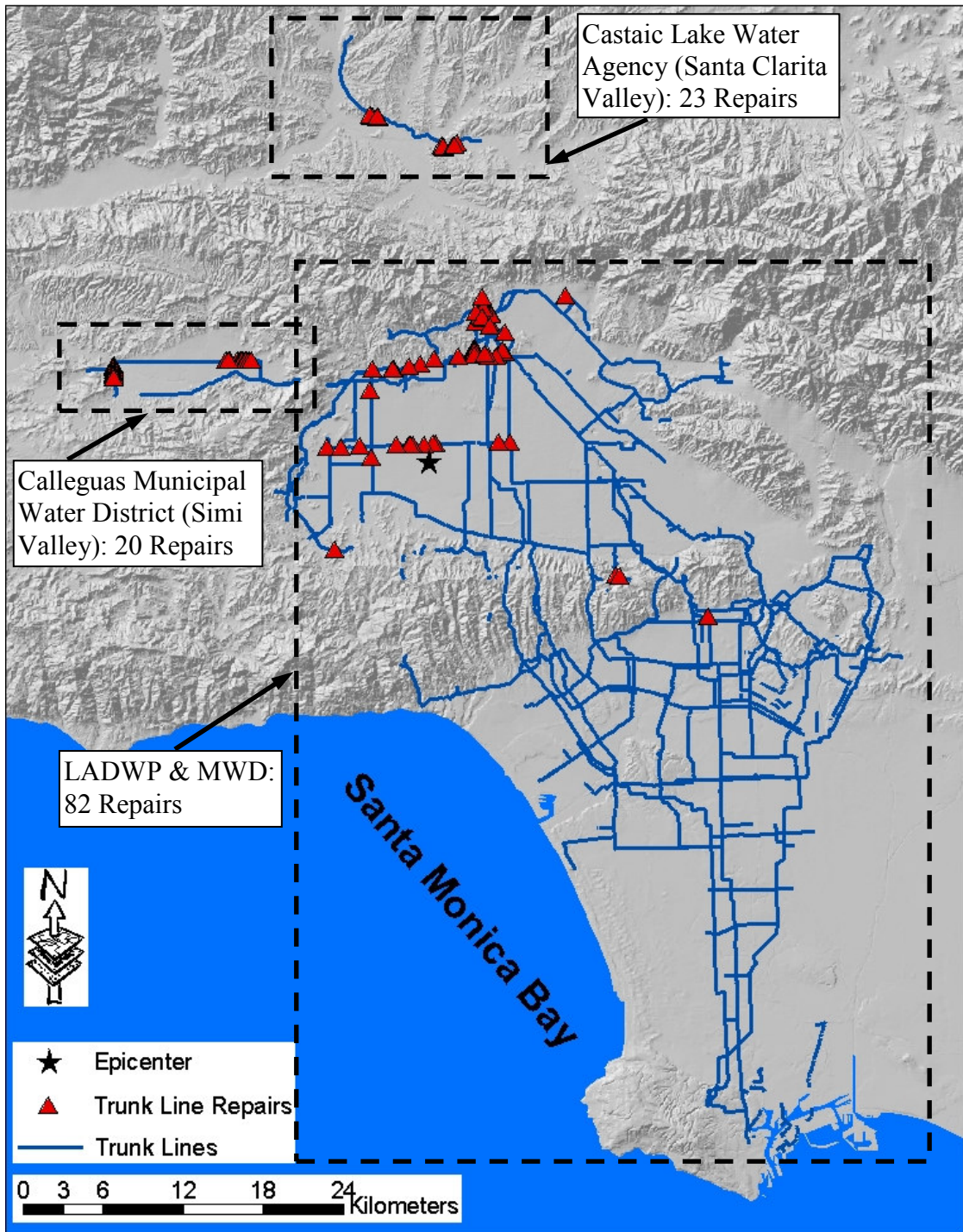
Figure A.1. Spatial Distribution of Trunk Line Repairs during 1994 Northridge

Earthquake

in the database. Figure A.1 shows the spatial distribution of the trunk line repairs during the 1994 Northridge earthquake and trunk lines operated by these four agencies. More description of the collection of the data and details on each trunk line repair is provided in the following subheadings:

### A.2.1. LADWP and MWD Trunk Line Repairs

The trunk line repair database for the LADWP and MWD system was first compiled by Toprak (1998), who obtained relevant information from LADWP, MWD, State of California Office of Emergency Services (OES), and EQE, Inc. The database was further updated with the aid of LADWP engineers (Davis, 2003). The Northridge earthquake caused 82 repairs in trunk lines operated by both agencies, 70 for 781.5 km of the LADWP trunk lines and 12 for 262.4 km of the MWD trunk lines. Tables A.1 and A.2 summarize characteristics of the repairs for the LADWP and MWD trunk lines, respectively. The tables include repair location, pipe diameter, pipe material, joint details, damage description, and type of repairs. Information about the LADWP and MWD trunk lines was obtained from the LADWP hydraulic model (LADWP, 2002a). The database does not include damage to corrugated metal pipes, which were used as drainage conduits throughout the Van Norman Complex and are described by Davis and Bardet (2000). Please note that the Rinaldi Trunk Line is owned by MWD, but rented and operated by LADWP. Therefore, seven repairs in the Rinaldi Trunk Line are considered as LADWP trunk line repairs. The "NA" in Tables A.1 and other tables in this appendix indicates that sufficient data are not available.

Significant effort was made to identify zones of PGD in the LADWP/MWD system. O'Rourke et al. (2001) identified five high distribution line repair zones in the

Table A.1.   Summary of LADWP Trunk Line Repairs during 1994 Northridge Earthquake

| No. | Pipeline | Location | Diameter (mm) | Material | Joint Connection | Damage Description | Repair | Cause[2] |
|---|---|---|---|---|---|---|---|---|
| 1 | Granada Trunk Line | Upper Debris Basin under Dike | 1257 | Steel | Welded bell and spigot | Crack at joint, approximate 300 mm long | Rewelded joint inside | PGD |
| 2 | Granada Trunk Line | Upper Debris Basin under Dike | 1257 | Steel | Welded bell and spigot | Crack at joint, approximate 300 mm long | Rewelded joint inside | PGD |
| 3 | Granada Trunk Line | Upper Debris Basin Sta. 3+68 | 1257 | Steel | Welded butt strap | Jagged tears, folded inward 76 mm, separated several tens mm, identified as major break by Davis (1999) | Welded 6-mm butt strap inside | PGD |
| 4 | Granada Trunk Line | Upper Debris Basin Sta. 3+72 | 1257 | Steel | Welded butt strap | Jagged tears, folded inward 76 mm, separated several tens mm, lateral offset several tens mm to 300 mm, identified as major break by Davis (1999) | Welded 6-mm butt strap inside | PGD |
| 5 | Granada Trunk Line | Upper Debris Basin Sta. 6+21 | 1257 | Steel | Welded bell and spigot | Spigot flared inward 13 mm, compression | Welded 6-mm butt strap inside | PGD |
| 6 | Granada Trunk Line | Upper Debris Basin Sta. 0+00 Relocated Line | 1257 | Steel | Welded butt strap | Folded inward and separated, identified as major break by Davis (1999) | Welded 6-mm butt strap inside | PGD |
| 7 | Granada Trunk Line | Upper Debris Basin Sta. 0+3.4 Relocated Line | 1257 | Steel | Welded butt strap | Jagged tears, folded inward 76 mm, separated several tens mm, identified as major break by Davis (1999) | Welded 6-mm butt strap inside | PGD |
| 8 | Granada Trunk Line | Upper Debris Basin Sta. 0+4.4 Relocated Line | 1257 | Steel | Welded butt strap | Folded inward and separated | Welded 6-mm butt strap inside | PGD |
| 9 | Granada Trunk Line | Utility Corridor, Sta 0+91.70 | 1257 | Steel | Mechanical coupling | 292 mm residual compressional displacement, coupling compressed 305 mm, slammed together, and separated 12 mm | WEKO-SEAL | PGD |
| 10 | Granada Trunk Line | Utility Corridor, Sta. 3+39 to 3+48 | 1257 | Steel | Welded bell and spigot | 50 to 76 mm inside bulge, buckling at joint | No repair | PGD |

Table A.1.   (Continued)

| No. | Pipeline | Location | Diameter (mm) | Material | Joint Connection | Damage Description | Repair | Cause[2] |
|---|---|---|---|---|---|---|---|---|
| 11 | Granada Trunk Line | Utility Corridor, Sta. 3+60 | 1257 | Steel | Mechanical coupling | 50 mm compressional displacement | No repair | PGD |
| 12 | Granada Trunk Line | Utility Corridor, Sta. 5+40 | 1257 | Steel | Welded bell and spigot | Cement mortar failure | No repair | PGD |
| 13 | Granada Trunk Line | Utility Corridor, Sta. 6+98.4 | 1257 | Steel | Mechanical coupling | 76 mm extensional displacement | No repair | PGD |
| 14 | Granada Trunk Line | Utility Corridor, Sta. 9+68.4 | 1257 | Steel | Mechanical coupling | 76 mm extensional displacement | No repair | PGD |
| 15 | Granada Trunk Line | Utility Corridor, Sta. 13+28.5 | 1257 | Steel | Mechanical coupling | 102 mm extensional displacement | No repair | PGD |
| 16 | Granada Trunk Line | Utility Corridor, Sta. 16+49.9 | 1257 | Steel | Mechanical coupling | 50 mm extensional displacement | No repair | PGD |
| 17 | Granada Trunk Line | Utility Corridor, Sta. 17+40 | 1257 | Steel | Welded butt strap | Cement mortar failure | No repair | PGD |
| 18 | Granada Trunk Line | Utility Corridor, Sta. 26+89.18 | 1257 | Steel | Mechanical coupling | 76 mm extensional displacement | No repair | PGD |
| 19 | Granada Trunk Line | Utility Corridor, Sta. 39+60 | 1257 | Steel | Mechanical coupling | 30 mm extensional displacement | WEKO-SEAL | PGD |
| 20 | Granada Trunk Line | Balboa Blvd. at Valve between Woodley and Colvin | 1257 | Steel | Mechanical coupling | Damaged and leaking, extensional movement | Butt strap | PGD |

Table A.1. (Continued)

| No. | Pipeline | Location | Diameter (mm) | Material | Joint Connection | Damage Description | Repair | Cause[2] |
|---|---|---|---|---|---|---|---|---|
| 21 | Granada Trunk Line | 17200 Balboa Blvd at Lorillard | 1257 | Steel | Welded bell and spigot | Joint fracture, extensional movement | Butt strap | PGD |
| 22 | Granada Trunk Line | 11661 Balboa Blvd. | 1257 | Steel | Mechanical coupling | Pulled apart 508 mm, extensional movement | Pipe sleeve and butt straps | PGD |
| 23 | Granada Trunk Line | Balboa Blvd. Sta. 115+80 | 1257 | Steel | Welded bell and spigot | Separated joint, tension | Butt strap | PGD |
| 24 | Granada Trunk Line | Balboa Blvd. Sta. 129+56 | 1257 | Steel | Welded bell and spigot | Pipe telescoped inside itself, compression | Pipe sleeve and butt straps | PGD |
| 25 | Granada Trunk Line | East of Shoshone | 1220 | Concrete | Bell and spigot | NA[1] | NA[1] | PGD |
| 26 | Granada Trunk Line | Wilbur | 1220 | Concrete | Bell and spigot | NA[1] | NA[1] | TGD |
| 27 | Granada Trunk Line | Tampa Ave. at 118 Frwy | 1220 | Concrete | Bell and spigot | Joint fracture, joint fractured along side existing weld | Welded fracture | TGD |
| 28 | Granada Trunk Line | Desoto Reservoir, North side | 1220 | Concrete | Bell and spigot | Joint fracture, joint fractured along side existing weld | Welded fracture | TGD |
| 29 | Granada Trunk Line | Between Melvin & Winnetka | 1220 | Concrete | Bell and spigot | NA[1] | NA[1] | TGD |
| 30 | Rinaldi Trunk Line | 11700 Balboa Blvd. | 1727 | Steel | Welded joint | Pulled apart 508 mm, extensional movement | Pipe sleeve and butt straps | PGD |

Table A.1. (Continued)

| No. | Pipeline | Location | Diameter (mm) | Material | Joint Connection | Damage Description | Repair | Cause[2] |
|---|---|---|---|---|---|---|---|---|
| 31 | Rinaldi Trunk Line | Balboa Blvd. 91 m North of above | 1727 | Steel | Welded joint | Extensional movement | Butt strap | PGD |
| 32 | Rinaldi Trunk Line | Balboa Blvd. Sta. 62+12 | 1727 | Steel | Welded bell and spigot | 13 mm separation, extensional movement | Butt strap | PGD |
| 33 | Rinaldi Trunk Line | Balboa Blvd. Sta. 65+87 | 1727 | Steel | Welded bell and spigot | Cement mortar failure | NA[1] | PGD |
| 34 | Rinaldi Trunk Line | Balboa Blvd. Sta. 63+72 | 1753 | Steel | Welded bell and spigot | 102 mm separation, extensional movement | Butt strap | PGD |
| 35 | Rinaldi Trunk Line | 11539 Balboa Blvd. | 1727 | Steel | Welded joint | Compression | Pipe sleeve and butt straps | PGD |
| 36 | Rinaldi Trunk Line | West of Winnetka St. Sta. 1219+10 (west of Melvin) | 1372 | Concrete | Bell and spigot | Multiple cracks in 4.9-m section of pipe, cracked at a cut-off wall | WEKO-SEAL (DWP) and 2.4-m external steel band (MWD) | TGD |
| 37 | Hayvenhurst Trunk Line | Rinaldi & Woodley NE corner | 1372 | Riveted Steel | Riveted | Sheared rivets, up to 25 mm compressional movement | Cut out and welded new | PGD |
| 38 | Van Ness Trunk Line Sta. 124+55 | Hollywood Freeway | NA[1] | Steel | Welded joint | NA[1] | WEKO-SEAL | PGD |
| 39 | Van Norman P.S. Discharge Line | Pier supports | 1372 | Steel | Welded bell and spigot | Ring girder collapse, displaced pier supports, no damage to pipe connections, only pipe damage came from pipe falling on concrete pier after girder collapse | No repair | PGD |
| 40 | Van Norman P.S. Discharge Line | North of Olden St. Trunk Line | 1372 | Steel | Welded bell and spigot | Compression buckle, 50 mm lateral offset | Pipe sleeve and butt straps | PGD |

293

Table A.1. (Continued)

| No. | Pipeline | Location | Diameter (mm) | Material | Joint Connection | Damage Description | Repair | Cause[2] |
|---|---|---|---|---|---|---|---|---|
| 41 | Van Norman P.S. Discharge Line | Between Foothill and Olden St. Trunk Line's | 1372 | Steel | Mechanical coupling | Compression, bow, wrinkle and rip in gasket, pipe shell bowed | NA[1] | PGD |
| 42 | Van Norman P.S. Discharge Line | Between Foothill and Olden St. Trunk Line's | 305 | Steel | NA[1] | Compression, shear | Realigned and replace butterfly valve | PGD |
| 43 | Backwash Pond #6 Drain | West side, pond 4 | 610 | Steel | Welded bell and spigot | Compression, rotation, shear, compound deformation | Pipe sleeve and butt straps | PGD |
| 44 | LA Reservoir Outlet | Butterfly valve at vault below dam | 3048 | Steel | Mechanical coupling | Leak at coupling | Tightened coupling | PGD |
| 45 | LA Reservoir Outlet | At City Trunk Line | 3048 | Steel | Mechanical coupling | Leak at coupling, tear in gasket | Replace mechanical coupling | PGD |
| 46 | Stone Canyon Inlet | 762-mm main at Hayvenhurst Trunk Line | 1524 | Steel | Mechanical coupling | Leak at coupling, ruptured gasket | Replace coupling w/ butt strap | PGD |
| 47 | Stone Canyon Inlet | 1219-mm butterfly valve at LAR outlet | 1524 | Steel | Mechanical coupling | Leak at coupling, ruptured gasket | Replace coupling w/ butt strap | PGD |
| 48 | Reseda Trunk Line | Asuncion St. (1.5 blocks North of Rinaldi) | 762 | Steel | Welded joint | NA[1] | NA[1] | TGD |
| 49 | Roscoe Trunk Line | Reseda Blvd. | 1016 | Steel | Welded joint | No observable pipe movement | Butt strap | TGD |
| 50 | Roscoe Trunk Line | Reseda Blvd., 140 m West, 18546 Roscoe Blvd | 1016 | Steel | Welded joint | No observable pipe movement | Butt strap | TGD |

Table A.1.  (Continued)

| No. | Pipeline | Location | Diameter (mm) | Material | Joint Connection | Damage Description | Repair | Cause[2] |
|---|---|---|---|---|---|---|---|---|
| 51 | Roscoe Trunk Line | Oakdale, 18 m West | 1067 | Riveted Steel | Riveted | No observable pipe movement | NA[1] | TGD |
| 52 | Roscoe Trunk Line | Wilbur Ave. 53 m East 18844 Roscoe Blvd. | 1016 | Steel | Welded joint | No observable pipe movement | Butt strap | TGD |
| 53 | Roscoe Trunk Line | Fallbrook Ave. West Side | 914 | Riveted Steel | Riveted | No observable pipe movement | NA[1] | TGD |
| 54 | Roscoe Trunk Line | Shirley Ave. 46 m East | 991 | Riveted Steel | Riveted | No observable pipe movement | NA[1] | TGD |
| 55 | Roscoe Trunk Line | Tampa | 1016 | Steel | Welded joint | No observable pipe movement | Butt strap | TGD |
| 56 | Roscoe Trunk Line | Calvin | 1016 | Riveted Steel | Riveted | No observable pipe movement | NA[1] | TGD |
| 57 | Roscoe Trunk Line | Haskel Ave | 1524 | Steel | Welded joint | NA[1] | NA[1] | TGD |
| 58 | Roscoe Trunk Line | Woodley Ave | 1321 | Steel | Welded joint | NA[1] | NA[1] | TGD |
| 59 | Roscoe Trunk Line | Canoga Ave | 1295 | Riveted Steel | Riveted | NA[1] | NA[1] | TGD |
| 60 | Roscoe Trunk Line | Faralone Ave. 171 m West 22259 Roscoe Blvd. | 1372 | Riveted Steel | Riveted | NA[1] | NA[1] | TGD |

Table A.1.  (Continued)

| No. | Pipeline | Location | Diameter (mm) | Material | Joint Connection | Damage Description | Repair | Cause[2] |
|---|---|---|---|---|---|---|---|---|
| 61 | Roscoe Trunk Line | Oakdale, 58 m West | 1067 | Riveted Steel | Riveted | NA[1] | NA[1] | TGD |
| 62 | Desoto Trunk Line | Ingomar | 1067 | Steel | Welded joint | NA[1] | NA[1] | TGD |
| 63 | Desoto Trunk Line | Devonshire | 1372 | Steel | Welded joint | NA[1] | NA[1] | TGD |
| 64 | City Trunk Line | Lower San Fernando Dam | 1829 | Riveted Steel | Riveted | Tear at longitudinal seam | Welded plate strap | TGD |
| 65 | Susana Trunk Line | Penstock Pump Station | 1372 | Steel | Welded joint | 102 mm flange gasket tapped off | Repaired gasket | TGD |
| 66 | NA[1] | 2438-mm butterfly valve east of Van Norman Pump Station #2 | 3048 | Steel | Mechanical coupling | Leak at coupling | Tightened coupling | PGD |
| 67 | NA[1] | Near Maclay Reservior | 914 | NA[1] | NA[1] | NA[1] | NA[1] | TGD |
| 68 | NA[1] | Near Topanga Tank | 914 | Steel | NA[1] | NA[1] | NA[1] | PGD |
| 69 | NA[1] | Near Cold Water Canyon Tank | 610 | NA[1] | NA[1] | NA[1] | NA[1] | TGD |
| 70 | NA[1] | Near Cold Water Canyon Tank | 610 | NA[1] | NA[1] | NA[1] | NA[1] | TGD |

1: Sufficient data are not available.
2: Permanent ground deformation (PGD) inferred from published field observations and mapped PGD zones (O'Rourke et al., 2001; LADWP, 1996; Stewart et al., 1996; and Holzer et al., 1999). Transient ground deformation (TGD) inferred where PGD observations were absent.

Table A.2.   Summary of MWD Trunk Line Repairs during 1994 Northridge Earthquake

| No. | Pipeline | Location | Diameter (mm) | Material | Joint Connection | Damage Description | Repair | Cause[2] |
|---|---|---|---|---|---|---|---|---|
| 1 | Sepulveda Feeder | One block south to Bull Creek | 3848 | Concrete | Bell and spigot | NA[1] | NA[1] | PGD |
| 2 | LA-25 | Debris Basin, 1st joint past flow structure | 1524 | Steel | Mechanical coupling | Extension, approximately 102 mm movement | WEKO-SEAL | PGD |
| 3 | LA-25 | At bend | 1524 | Steel | Welded joint | Weld fracture | Rewelded fracture | TGD |
| 4 | LA-25 | At concrete cradle | 2438 | Steel | Welded joint | Flexure, rotation, 102 mm compression, compound deformation | Butt strap | TGD |
| 5 | LA-25 (MWD Overflow Conduit) | Concrete double box | 1524×1524 | Concrete | Bell and spigot | Extension, 165 mm separation at connection w/ discharge structure and 50 mm break in box culvert | Steel plate bolted in place across gap and welded in corners, voids filled with concrete | PGD |
| 6 | LA-35T | Valve structure | 1524 | Steel | Mechanical coupling | Coupling displaced, differential movement between valve structure and tunnel manifold caused problem | Coupling middle ring welded over gap in pipe between pipeline and valve thimble | PGD |
| 7 | LA-35T | Upper Debris Basin | 1549 | Steel | Mechanical coupling | Permanent, horizontal and vertical displacement | Cut out small section of pipe and welded in new, sleeve coupling repositioned and bolted. | PGD |
| 8 | Balboa Influent Conduit (MWD) | Jensen, between manifold and vent | 2159 | Steel | welded bell and spigot | Fracture and rupture, at welded slip joint | Cut out, replaced with 2 fabricated sections and 3 butt straps | PGD |

Table A.2. (Continued)

| No. | Pipeline | Location | Diameter (mm) | Material | Joint Connection | Damage Description | Repair | Cause[2] |
|---|---|---|---|---|---|---|---|---|
| 9 | Balboa Influent Box (MWD) | Jensen, just before flash mixers | 3810 | Concrete | Bell and spigot | Separation, 13 mm movement before entering flash mixer and cracks along top of sidewall | Hydracure from inside | PGD |
| 10 | Effluent Conduit (MWD) | Jensen, at finish water reservoir #1 | 3048 | Concrete | Bell and spigot | Smashed, continued leaking after repairs | NA[1] | PGD |
| 11 | East Valley Feeder (MWD) | Woodley and Rinaldi at flood channel | 1219 | Concrete | Bell and spigot | Compression, break near bell and spigot away from encasement | Internal band with O-rings | PGD |
| 12 | East Valley Feeder (MWD) | Odessa and Rinaldi | 1219 | Concrete | Bell and spigot | Extension, break near bell and spigot at encasement where pipe goes under flood control channel | Welded bar to fill gap in joint, filled joint with mortar flush wit inside gap | PGD |

1: Sufficient data are not available.

2: Permanent ground deformation (PGD) inferred from published field observations and mapped PGD zones (O'Rourke et al., 2001; LADWP, 1996; Stewart et al., 1996; and Holzer et al., 1999). Transient ground deformation (TGD) inferred where PGD observations were absent.

298

system and attributed the repairs in those zones to their geotechnical characteristics, such as soft clay deposits susceptible to lateral movement and lurching, sands and interbedded clay/silts susceptible to liquefaction, and steep slopes with soils and fills susceptible to slumping and landslides. The trunk line repairs located in those zones are considered related to PGD, and hence, were screened from the regression analysis, as described in Section A.3. In addition, PGDs observed by LADWP engineers (LADWP, 1996) or documented in the literature (Stewart et al., 1996; and Holzer et al., 1999) were used to screen trunk line repairs, located in the zones of PGD, from the regression analysis. The trunk line repairs that were located in the zones of PGD are indicated by "PGD" in the last column of Tables A.1 and A.2.

The damage summarized for MWD pipelines in Table A.2 was assessed from data collected and published by Davis and Bardet (1995) and observations and unpublished data collected after the earthquake by O'Rourke (2005) and Davis (2003). Of special interest is the damage to LA-25. This line provides a tie-in between the Jensen Filtration Plant finished reservoirs and LADWP system that would be used in situations where flow from the Los Angeles Aqueducts is impeded or temporarily stopped. The connection is normally closed. Figure A.2 shows a photo of damage (No. 4 in Table A.2) at a welded slip joint of a 2438-mm-diameter pipe at a concrete cradle. The welded slip joint has failed in compression and ruptured near the crown of the pipe. A very careful inspection of the site was made for evidence of PGD, and none was found (O'Rourke, 2005).

Figure A.2.   Welded Slip Joint Damage in LA-25

## A.2.2.  CMWD Trunk Line Repairs

Contact was made with engineers of the Calleguas Municipal Water District (CMWD), which operates the water supply system in Simi Valley. Information about the trunk line characteristics, geographic location of trunk lines and Northridge earthquake repairs, types of repairs, and soil conditions near repair locations was provided by CMWD engineers (Pugh, 2003; and Mulligan, 2003). The database contains twenty repairs in 33.5 km of concrete trunk line. Table A.3 summarizes characteristics of the repairs, including their location, pipe diameter, pipe material, joint details, damage description, and type of repairs.

Table A.3.   Summary of CMWD Trunk Line Repairs during 1994 Northridge Earthquake

| No. | Pipeline | Location | Diameter (mm) | Material | Joint Connection | Damage Description | Repair | Cause[1] |
|---|---|---|---|---|---|---|---|---|
| 1 | Calleguas Conduit North Branch | Madera Rd | 1981 | Concrete | Bell and spigot | Weld cracks or ruptures at joint | Welded joint | PGD |
| 2 | Calleguas Conduit North Branch | Madera Rd | 1981 | Concrete | Bell and spigot | Weld cracks or ruptures at joint | Welded joint | PGD |
| 3 | Calleguas Conduit North Branch | Madera Rd | 1981 | Concrete | Bell and spigot | Weld cracks or ruptures at joint | Welded joint | PGD |
| 4 | Calleguas Conduit North Branch | Madera Rd | 1981 | Concrete | Bell and spigot | Weld cracks or ruptures at joint | Welded joint | PGD |
| 5 | Calleguas Conduit North Branch | Madera Rd | 1981 | Concrete | Bell and spigot | Weld cracks or ruptures at joint | Welded joint | PGD |
| 6 | Calleguas Conduit North Branch | Madera Rd | 1981 | Concrete | Bell and spigot | Weld cracks or ruptures at joint | Welded joint | PGD |
| 7 | Calleguas Conduit North Branch | Madera Rd | 1981 | Concrete | Bell and spigot | Weld cracks or ruptures at joint | Welded joint | PGD |
| 8 | Calleguas Conduit North Branch | Madera Rd | 1981 | Concrete | Bell and spigot | Weld cracks or ruptures at joint | Welded joint | PGD |
| 9 | Calleguas Conduit North Branch | Fig St | 1981 | Concrete | Bell and spigot | Weld cracks or ruptures at joint | Welded joint | PGD |
| 10 | Calleguas Conduit North Branch | Fig St | 1981 | Concrete | Bell and spigot | Weld cracks or ruptures at joint | Welded joint | PGD |

Table A.3. (Continued)

| No. | Pipeline | Location | Diameter (mm) | Material | Joint Connection | Damage Description | Repair | Cause[1] |
|---|---|---|---|---|---|---|---|---|
| 11 | Calleguas Conduit North Branch | Fig St | 1981 | Concrete | Bell and spigot | Weld cracks or ruptures at joint | Welded joint | PGD |
| 12 | Calleguas Conduit North Branch | Fig St | 1981 | Concrete | Bell and spigot | Weld cracks or ruptures at joint | Welded joint | PGD |
| 13 | Calleguas Conduit North Branch | Fig St | 1981 | Concrete | Bell and spigot | Pulled out of rubber gasket | Welded joint | TGD |
| 14 | Calleguas Conduit North Branch | Cochran St and Stearns St | 1981 | Concrete | Bell and spigot | Pulled out of rubber gasket | Welded joint | TGD |
| 15 | Calleguas Conduit North Branch | Cochran St and Stearns St | 1981 | Concrete | Bell and spigot | Pulled out of rubber gasket | Welded joint | TGD |
| 16 | Calleguas Conduit North Branch | Stow St | 1981 | Concrete | Bell and spigot | Pulled out of rubber gasket | Welded joint | TGD |
| 17 | Calleguas Conduit North Branch | Stow St | 1981 | Concrete | Bell and spigot | Pulled out of rubber gasket | Welded joint | TGD |
| 18 | Calleguas Conduit North Branch | Stow St | 1981 | Concrete | Bell and spigot | Pulled out of rubber gasket | Welded joint | TGD |
| 19 | Calleguas Conduit North Branch | Stow St | 1981 | Concrete | Bell and spigot | Pulled out of rubber gasket | Welded joint | TGD |
| 20 | Calleguas Conduit North Branch | Stow St | 1981 | Concrete | Bell and spigot | Pulled out of rubber gasket | Welded joint | TGD |

1: Permanent ground deformation (PGD) inferred from published field observations and mapped PGD zones (O'Rourke et al., 2001; LADWP, 1996; Stewart et al., 1996; and Holzer et al., 1999). Transient ground deformation (TGD) inferred where PGD observations were absent.

Among the twenty repairs reported, significant ground and pipeline movement was observed near the locations of twelve repairs (Pugh, 2003), as indicated by "PGD" in the last column of Table A.3. Therefore, these twelve repairs are screened from the regression analysis. The remaining eight trunk line repairs were further checked with the zones of PGD documented in the literature (Stewart et al., 1996; and Holzer et al., 1999), and interviews were conducted with engineers who supervised repairs after the Northridge earthquake (O'Rourke, 2005). In addition, subsurface investigation data near these repairs were reviewed for the presence of liquefiable soils. None of the eight trunk line repairs were located in zones of observed PGD or in zones where significant deposits of liquefiable sand could be identified from the subsurface exploration data.

### A.2.3.  CLWA Trunk Line Repairs

Contact was made with engineers of the Castaic Lake Water Agency (CLWA), which operates the water supply system in Santa Clarita Valley. Information about the trunk line characteristics, geographic location of trunk lines and Northridge earthquake repairs, and type of repairs was provided by CLWA engineers (Thompson, 2003) in the form of repair project completion and certification reports prepared for the Federal Emergency Management Agency (FEMA), as well as pipeline plan and profile drawings. The database contains 23 repairs in 17.4 km of concrete trunk lines. Table A.4 summarizes characteristics of the repairs, including their location, pipe diameter, pipe material, joint details, damage description, and type of repairs.

The 23 trunk line repairs were checked with zones of PGD documented in literature (Stewart et al., 1996; and Holzer et al., 1999). None of the 23 trunk line

Table A.4.   Summary of CLWA Trunk Line Repairs during 1994 Northridge Earthquake

| No. | Pipeline | Location | Diameter (mm) | Material | Joint Connection | Damage Description | Repair | Cause[2] |
|---|---|---|---|---|---|---|---|---|
| 1 | Castaic Conduit | Vicinity of Rye Canyon Rd., Sta. 244 +33 | 1372 | Concrete | Bell and spigot | NA[1] | Remortared joints | TGD |
| 2 | Castaic Conduit | Vicinity of Rye Canyon Rd., Sta. 246 +11 | 1372 | Concrete | Bell and spigot | NA[1] | Remortared joints | TGD |
| 3 | Castaic Conduit | Vicinity of Rye Canyon Rd., Sta. 246 +43 | 1372 | Concrete | Bell and spigot | NA[1] | Remortared joints | TGD |
| 4 | Castaic Conduit | Vicinity of Rye Canyon Rd., Sta. 246 +75 | 1372 | Concrete | Bell and spigot | NA[1] | Remortared joints | TGD |
| 5 | Honby Lateral | 23560 Lyons Ave., Sta. 73 +91 | 838 | Concrete | Bell and spigot | Joint pulled apart or jammed together | Repaired with welding with backing rod | TGD |
| 6 | Honby Lateral | 23560 Lyons Ave., Sta. 74 +32 | 838 | Concrete | Bell and spigot | Joint pulled apart or jammed together | Repaired with welding with backing rod | TGD |
| 7 | Honby Lateral | 23560 Lyons Ave., Sta. 82 +12 | 838 | Concrete | Bell and spigot | Joint pulled apart | Joints were welded bell-end with backing rod | TGD |
| 8 | Honby Lateral | 23560 Lyons Ave., Sta. 82 +60 | 838 | Concrete | Bell and spigot | Joint pulled apart | Joints were welded bell-end with backing rod | TGD |
| 9 | Honby Lateral | 23560 Lyons Ave., Sta. 125 +87 | 838 | Concrete | Bell and spigot | Joint pulled apart | Joints were welded bell-end with backing rod | TGD |
| 10 | Honby Lateral | 23560 Lyons Ave., Sta. 126 +23 | 838 | Concrete | Bell and spigot | Joint separated | Joints were welded bell-end with backing rod | TGD |

304

Table A.4. (Continued)

| No. | Pipeline | Location | Diameter (mm) | Material | Joint Connection | Damage Description | Repair | Cause[2] |
|-----|----------|----------|---------------|----------|------------------|--------------------|--------|----------|
| 11 | Honby Lateral | Sta. 112 + 25 | 838 | Concrete | Bell and spigot | Joint pulled apart, pipe wrap broken and coating damaged | Replace pipe section and close with butt strap at joints | TGD |
| 12 | Honby Lateral | Sta. 112 + 50 | 838 | Concrete | Bell and spigot | Weld Joint jammed | Replace pipe section and close with butt strap at joints | TGD |
| 13 | Honby Lateral | Sta. 114 + 00 | 838 | Concrete | Bell and spigot | Air Relief fitting and piping damaged | Replace pipe section and close with butt strap at joints | TGD |
| 14 | Honby Lateral | Sta. 114 + 75 | 838 | Concrete | Bell and spigot | Joint separated | Replace pipe section and close with butt strap at joints | TGD |
| 15 | Castaic Conduit | Vicinity of Rye Canyon Rd., Sta. 262 +08 | 1372 | Concrete | Bell and spigot | Joint separated | Butt strap joint | TGD |
| 16 | Castaic Conduit | Vicinity of Rye Canyon Rd., Sta. 262 +40 | 1372 | Concrete | Bell and spigot | Joint separated | Butt strap joint | TGD |
| 17 | Castaic Conduit | Vicinity of Rye Canyon Rd., Sta. 263 +00 | 1372 | Concrete | Bell and spigot | Joint separated | Butt strap joint | TGD |
| 18 | Castaic Conduit | Vicinity of Rye Canyon Rd., Sta. 263 +32 | 1372 | Concrete | Bell and spigot | Joint separated | Butt strap joint | TGD |
| 19 | Castaic Conduit | Vicinity of Rye Canyon Rd., Sta. 258 +32 | 1372 | Concrete | Bell and spigot | Joint deformed | Deformed joint section removed and replaced inside the pipe | TGD |
| 20 | Castaic Conduit | Vicinity of Rye Canyon Rd., Sta. 258 +65 | 1372 | Concrete | Bell and spigot | Joint deformed | Deformed joint section removed and replaced inside the pipe | TGD |

Table A.4. (Continued)

| No. | Pipeline | Location | Diameter (mm) | Material | Joint Connection | Damage Description | Repair | Cause[2] |
|-----|----------|----------|---------------|----------|------------------|--------------------|--------|----------|
| 21 | Castaic Conduit | Vicinity of Rye Canyon Rd., Sta. 239 +10 | 1372 | Concrete | Bell and spigot | Joint jammed and pipe line deformed | Replace pipe section and close with butt strap at joints | TGD |
| 22 | Castaic Conduit | Vicinity of Rye Canyon Rd., Sta. 239 +50 | 1372 | Concrete | Bell and spigot | Joint pulled apart and pipe line deformed | Replace pipe section and close with butt strap at joints | TGD |
| 23 | Castaic Conduit | 23560 Lyons Ave., Sta. 257 + 60 | 1372 | Concrete | Bell and spigot | Joint pulled apart and gasket pulled out of seat | Repaired with welding with backing rod | TGD |

1: Sufficient data are not available.
2: Permanent ground deformation (PGD) inferred from published field observations and mapped PGD zones (O'Rourke et al., 2001; LADWP, 1996; Stewart et al., 1996; and Holzer et al., 1999). Transient ground deformation (TGD) inferred where PGD observations were absent.

repairs were located in zones of reported PGD. Because evidence for soil movement and potentially liquefiable soils was absent along the trunk line rights of way, the 23 trunk line repairs were included in the regression analysis.

## A.3. Regression Analysis

The regression procedures utilized in this work follow those developed by O'Rourke and Toprak (1997), Toprak (1998), O'Rourke et al. (2001), and Jeon (2002). Empirical data were collected about distribution pipeline repairs and locations of repairs after the 1994 Northridge earthquake and incorporated in a large GIS database, consisting of over 12,000 km of pipelines in the greater Los Angeles area and more than 240 strong motion records. Records from over 240 strong motion stations throughout the earthquake-affected area were analyzed with respect to various seismic parameters (Toprak, 1998). The spatial distributions of different seismic parameters were estimated by interpolation and superimposed on the pipeline network and spatially distributed database of pipeline damage. Where possible, pipeline repairs in zones of documented PGD were screened from the repair rates so that the resulting statistics would reflect principally the effects of seismic waves or TGD. Using the GIS software, the repair rate was calculated for areas influenced by specific seismic parameters. Correlations then were developed through regression analysis to obtain the most statistically significant relationships among repair rate and values of different seismic parameters. It was found that the most statistically relevant parameter for correlation with repair rate is PGV. The most statistically meaningful regression between repair rate and PGV was developed by varying the PGV bins to achieve the highest coefficient of determination, $r^2$, in the regression analysis.

Using the spatial distribution of PGV developed by Jeon (2002) and the trunk line repair database described in Section A.2, regressions between trunk line repair rate, number of repairs per km pipe length, and PGV are developed for concrete, steel, and riveted steel trunk lines, which are described in the following subheadings:

### A.3.1.  Concrete Trunk Lines

After screening the repairs in the PGD zones, 36 repairs in the 141.9 km of pipeline were included in the regressions for concrete trunk lines. Table A. 5 summarizes characteristics of the 36 repairs. Figure A. 3 shows the spatial distributions of concrete trunk lines and their repairs during the 1994 Northridge earthquake, superimposed on the PGV spatial distribution by Jeon (2002). Regression analysis using the repair rates and PGV values summarized in Table A. 6 results in the following regression equation with the highest $r^2$ (i.e., 0.83):

$$\ln(\lambda) = 2.59 \times \ln(V_p) - 12.11 \qquad\qquad (A.1)$$

where $\lambda$ is the repair rate in units of repair number per km length pipeline, and $V_p$ is peak ground velocity in units of cm/sec.

### A.3.2.  Steel Trunk Lines

After screening the repairs in the PGD zones, twelve repairs in 468.8 km of pipeline were included in the regressions for steel trunk lines. Table A. 7 summarizes characteristics of the twelve repairs. Figure A. 4 shows the spatial distributions of steel trunk lines and their repairs during the 1994 Northridge earthquake, superimposed on

Table A.5.   Summary of Repairs in Concrete Trunk Lines after PGD Screening

| No. | Pipeline | Location | Diameter (mm) | Material | Joint Connection | Damage Description | Repair | Owner |
|---|---|---|---|---|---|---|---|---|
| 1 | Castaic Conduit | Vicinity of Rye Canyon Rd., Sta. 244 +33 | 1372 | Concrete | Bell and spigot | NA[1] | Remortared joints | CLWA |
| 2 | Castaic Conduit | Vicinity of Rye Canyon Rd., Sta. 246 +11 | 1372 | Concrete | Bell and spigot | NA[1] | Remortared joints | CLWA |
| 3 | Castaic Conduit | Vicinity of Rye Canyon Rd., Sta. 246 +43 | 1372 | Concrete | Bell and spigot | NA[1] | Remortared joints | CLWA |
| 4 | Castaic Conduit | Vicinity of Rye Canyon Rd., Sta. 246 +75 | 1372 | Concrete | Bell and spigot | NA[1] | Remortared joints | CLWA |
| 5 | Honby Lateral | 23560 Lyons Ave., Sta. 73 +91 | 838 | Concrete | Bell and spigot | Joint pulled apart or jammed together | Repaired with welding with backing rod | CLWA |
| 6 | Honby Lateral | 23560 Lyons Ave., Sta. 74 +32 | 838 | Concrete | Bell and spigot | Joint pulled apart or jammed together | Repaired with welding with backing rod | CLWA |
| 7 | Honby Lateral | 23560 Lyons Ave., Sta. 82 +12 | 838 | Concrete | Bell and spigot | Joint pulled apart | Joints were welded bell-end with backing rod | CLWA |
| 8 | Honby Lateral | 23560 Lyons Ave., Sta. 82 +60 | 838 | Concrete | Bell and spigot | Joint pulled apart | Joints were welded bell-end with backing rod | CLWA |
| 9 | Honby Lateral | 23560 Lyons Ave., Sta. 125 +87 | 838 | Concrete | Bell and spigot | Joint pulled apart | Joints were welded bell-end with backing rod | CLWA |
| 10 | Honby Lateral | 23560 Lyons Ave., Sta. 126 +23 | 838 | Concrete | Bell and spigot | Joint separated | Joints were welded bell-end with backing rod | CLWA |

Table A.5. (Continued)

| No. | Pipeline | Location | Diameter (mm) | Material | Joint Connection | Damage Description | Repair | Owner |
|-----|----------|----------|---------------|----------|------------------|--------------------|--------|-------|
| 11 | Honby Lateral | Sta. 112 + 25 | 838 | Concrete | Bell and spigot | Joint pulled apart, pipe wrap broken and coating damaged | Replace pipe section and close with butt strap at joints | CLWA |
| 12 | Honby Lateral | Sta. 112 + 50 | 838 | Concrete | Bell and spigot | Weld Joint jammed | Replace pipe section and close with butt strap at joints | CLWA |
| 13 | Honby Lateral | Sta. 114 + 00 | 838 | Concrete | Bell and spigot | Air Relief fitting and piping damaged | Replace pipe section and close with butt strap at joints | CLWA |
| 14 | Honby Lateral | Sta. 114 + 75 | 838 | Concrete | Bell and spigot | Joint separated | Replace pipe section and close with butt strap at joints | CLWA |
| 15 | Castaic Conduit | Vicinity of Rye Canyon Rd., Sta. 262 +08 | 1372 | Concrete | Bell and spigot | Joint separated | Butt strap joint | CLWA |
| 16 | Castaic Conduit | Vicinity of Rye Canyon Rd., Sta. 262 +40 | 1372 | Concrete | Bell and spigot | Joint separated | Butt strap joint | CLWA |
| 17 | Castaic Conduit | Vicinity of Rye Canyon Rd., Sta. 263 +00 | 1372 | Concrete | Bell and spigot | Joint separated | Butt strap joint | CLWA |
| 18 | Castaic Conduit | Vicinity of Rye Canyon Rd., Sta. 263 +32 | 1372 | Concrete | Bell and spigot | Joint separated | Butt strap joint | CLWA |
| 19 | Castaic Conduit | Vicinity of Rye Canyon Rd., Sta. 258 +32 | 1372 | Concrete | Bell and spigot | Joint deformed | Deformed joint section removed and replaced inside the pipe | CLWA |
| 20 | Castaic Conduit | Vicinity of Rye Canyon Rd., Sta. 258 +65 | 1372 | Concrete | Bell and spigot | Joint deformed | Deformed joint section removed and replaced inside the pipe | CLWA |

310

Table A.5. (Continued)

| No. | Pipeline | Location | Diameter (mm) | Material | Joint Connection | Damage Description | Repair | Owner |
|-----|----------|----------|---------------|----------|------------------|--------------------|--------|-------|
| 21 | Castaic Conduit | Vicinity of Rye Canyon Rd., Sta. 239 +10 | 1372 | Concrete | Bell and spigot | Joint jammed and pipe line deformed | Replace pipe section and close with butt strap at joints | CLWA |
| 22 | Castaic Conduit | Vicinity of Rye Canyon Rd., Sta. 239 +50 | 1372 | Concrete | Bell and spigot | Joint pulled apart and pipe line deformed | Replace pipe section and close with butt strap at joints | CLWA |
| 23 | Castaic Conduit | 23560 Lyons Ave., Sta. 257 + 60 | 1372 | Concrete | Bell and spigot | Joint pulled apart and gasket pulled out of seat | Repaired with welding with backing rod | CLWA |
| 24 | Calleguas Conduit North Branch | Fig St | 1981 | Concrete | Bell and spigot | Pulled out of rubber gasket | Welded joint | CMWD |
| 25 | Calleguas Conduit North Branch | Cochran St and Stearns St | 1981 | Concrete | Bell and spigot | Pulled out of rubber gasket | Welded joint | CMWD |
| 26 | Calleguas Conduit North Branch | Cochran St and Stearns St | 1981 | Concrete | Bell and spigot | Pulled out of rubber gasket | Welded joint | CMWD |
| 27 | Calleguas Conduit North Branch | Stow St | 1981 | Concrete | Bell and spigot | Pulled out of rubber gasket | Welded joint | CMWD |
| 28 | Calleguas Conduit North Branch | Stow St | 1981 | Concrete | Bell and spigot | Pulled out of rubber gasket | Welded joint | CMWD |
| 29 | Calleguas Conduit North Branch | Stow St | 1981 | Concrete | Bell and spigot | Pulled out of rubber gasket | Welded joint | CMWD |
| 30 | Calleguas Conduit North Branch | Stow St | 1981 | Concrete | Bell and spigot | Pulled out of rubber gasket | Welded joint | CMWD |

311

Table A.5. (Continued)

| No. | Pipeline | Location | Diameter (mm) | Material | Joint Connection | Damage Description | Repair | Owner |
|-----|----------|----------|---------------|----------|------------------|--------------------|--------|-------|
| 31 | Calleguas Conduit North Branch | Stow St | 1981 | Concrete | Bell and spigot | Pulled out of rubber gasket | Welded joint | CMWD |
| 32 | Granada Trunk Line | Wilbur | 1220 | Concrete | Bell and spigot | NA[1] | NA[1] | LADWP |
| 33 | Granada Trunk Line | Tampa Ave. at 118 Frwy | 1220 | Concrete | Bell and spigot | Joint fracture, joint fractured along side existing weld | Welded fracture | LADWP |
| 34 | Granada Trunk Line | Desoto Reservoir, North side | 1220 | Concrete | Bell and spigot | Joint fracture, joint fractured along side existing weld | Welded fracture | LADWP |
| 35 | Granada Trunk Line | Between Melvin & Winnetka | 1220 | Concrete | Bell and spigot | NA[1] | NA[1] | LADWP |
| 36 | Rinaldi Trunk Line | West of Winnetka St. Sta. 1219+10 (west of Melvin) | 1372 | Concrete | Bell and spigot | Multiple cracks in 4.9-m section of pipe, cracked at a cut-off wall | WEKO-SEAL (DWP) and 2.4-m external steel band (MWD) | LADWP |

1: Sufficient data are not available.
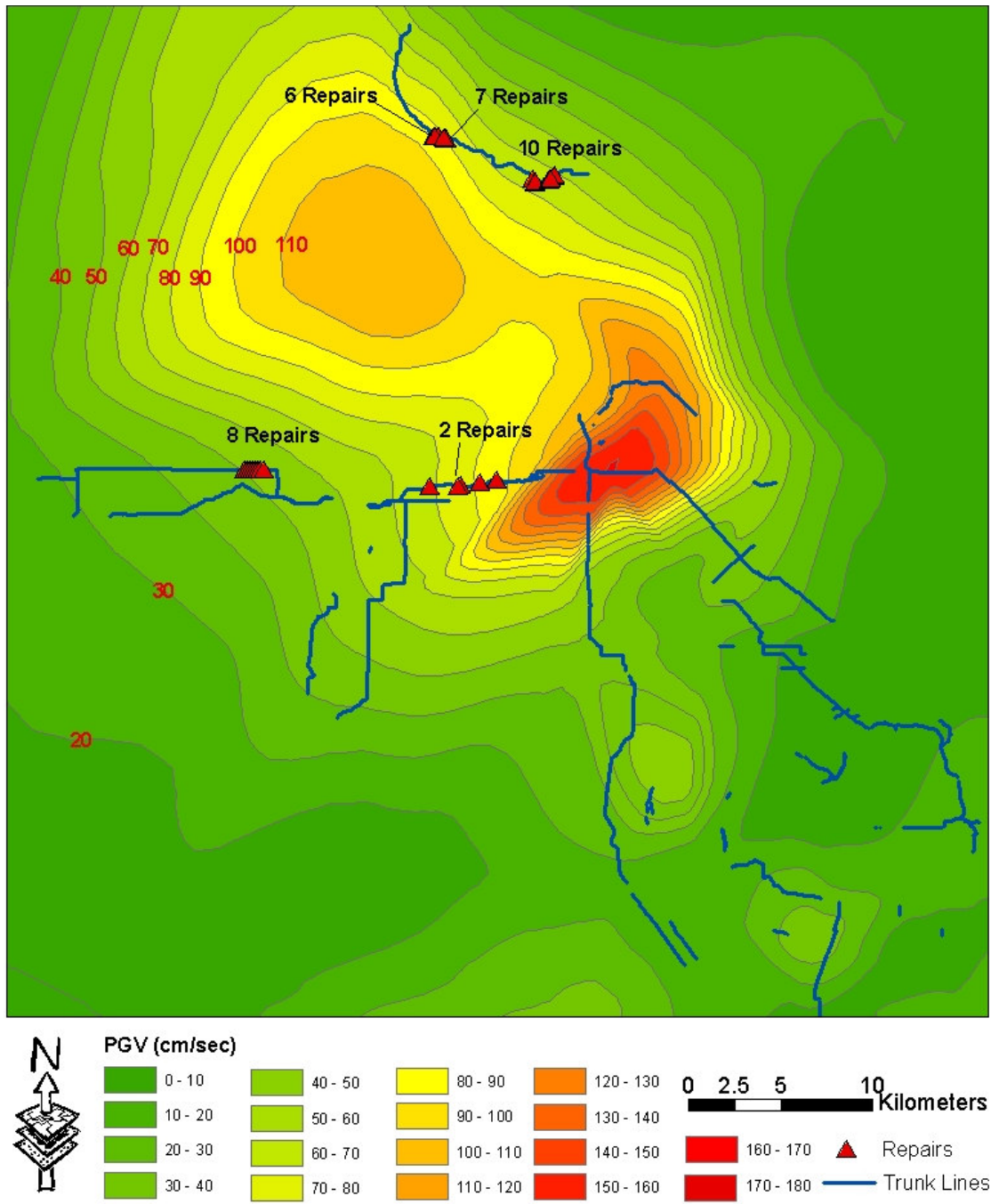
Figure A.3.   Concrete Trunk Line Performance during 1994 Northridge Earthquake

Table A.6.   Summary of Concrete Trunk Line Repair Rate According to PGV

| PGV Bin (cm/sec) | Representative PGV (cm/sec) | Pipe Length (km) | Repair No | Repair Rate (Repair No. / km) |
|---|---|---|---|---|
| 30-60 | 45 | 91.3 | 8 | 0.09 |
| 60-80 | 70 | 27.7 | 11 | 0.40 |
| 80-90 | 85 | 9.7 | 9 | 0.93 |
| 90-120 | 105 | 13.2 | 8 | 0.61 |

the PGV spatial distribution by Jeon (2002). Regression analysis using the repair rates and PGV values summarized in Table A. 8 results in the following regression equation with the highest $r^2$ (i.e., 0.76):

$$\ln(\lambda) = 2.59 \times \ln(V_p) - 14.16 \tag{A.2}$$

### A.3.3.  Riveted Steel Trunk Lines

After screening the repairs in the PGD zones, eight repairs in 114.5 km of pipeline were included in the regressions for steel trunk lines. Table A. 9 summarizes characteristics of the eight repairs. Figure A. 5 shows the spatial distributions of riveted steel trunk lines and their repairs during the 1994 Northridge earthquake, superimposed on the PGV spatial distribution by Jeon (2002). Regression analysis using the repair rates and PGV values summarized in Table A. 10 results in the following regression equation with the highest $r^2$ (i.e., 0.84):

$$\ln(\lambda) = 1.41 \times \ln(V_p) - 8.19 \tag{A.3}$$

Table A.7. Summary of Repairs in Steel Trunk Lines after PGD Screening

| No. | Pipeline | Location | Diameter (mm) | Material | Joint Connection | Damage Description | Repair | Owner |
|---|---|---|---|---|---|---|---|---|
| 1 | Reseda Trunk Line | Asuncion St. (1.5 blocks North of Rinaldi) | 762 | Steel | Welded joint | NA[1] | NA[1] | LADWP |
| 2 | Roscoe Trunk Line | Reseda Blvd. | 1016 | Steel | Welded joint | No observable pipe movement | Butt strap | LADWP |
| 3 | Roscoe Trunk Line | Reseda Blvd., 140 m West, 18546 Roscoe Blvd | 1016 | Steel | Welded joint | No observable pipe movement | Butt strap | LADWP |
| 4 | Roscoe Trunk Line | Wilbur Ave. 53 m East 18844 Roscoe Blvd. | 1016 | Steel | Welded joint | No observable pipe movement | Butt strap | LADWP |
| 5 | Roscoe Trunk Line | Tampa | 1016 | Steel | Welded joint | No observable pipe movement | Butt strap | LADWP |
| 6 | Roscoe Trunk Line | Haskel Ave | 1524 | Steel | Welded joint | NA[1] | NA[1] | LADWP |
| 7 | Roscoe Trunk Line | Woodley Ave | 1321 | Steel | Welded joint | NA[1] | NA[1] | LADWP |
| 8 | Desoto Trunk Line | Ingomar | 1067 | Steel | Welded joint | NA[1] | NA[1] | LADWP |
| 9 | Desoto Trunk Line | Devonshire | 1372 | Steel | Welded joint | NA[1] | NA[1] | LADWP |
| 10 | Susana Trunk Line | Penstock Pumping Station | 1372 | Steel | Welded joint | 102 mm flange gasket tapped off | Repaired gasket | LADWP |
| 11 | LA-25 | At bend | 1524 | Steel | Welded joint | Weld fracture | Rewelded fracture | MWD |
| 12 | LA-25 | At concrete cradle | 2438 | Steel | Welded joint | Flexure, rotation, 102 mm compression, compound deformation | Butt strap | MWD |

1: Sufficient data are not available.
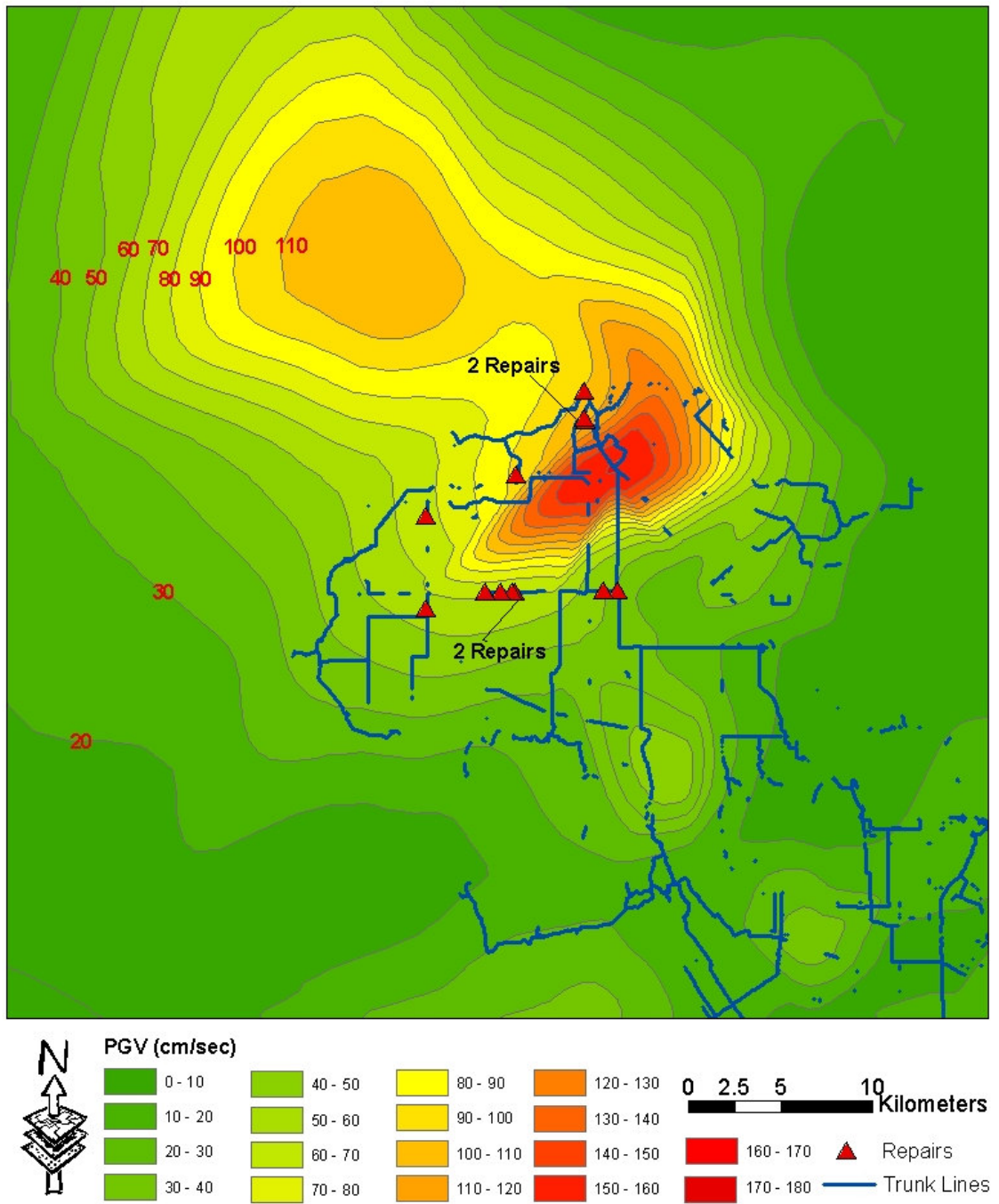
Figure A.4.   Steel Trunk Line Performance during 1994 Northridge Earthquake

Table A.8. Summary of Steel Trunk Line Repair Rate According to PGV

| PGV Bin (cm/sec) | Representative PGV (cm/sec) | Pipe Length (km) | Repair No | Repair Rate (Repair No. / km) |
|---|---|---|---|---|
| 10-50 | 30 | 371.2 | 1 | 0.003 |
| 50-80 | 65 | 56.1 | 7 | 0.13 |
| 80-110 | 95 | 19.3 | 1 | 0.05 |
| 110-140 | 125 | 22.2 | 3 | 0.14 |

## A.3.4. Comparison of Regressions for Different Trunk Lines

Figure A.6 summarizes the regressions for concrete, riveted steel, and steel trunk lines. It is obvious that the repair rate increases as the PGV increases. Inspections of the regressions in Figure A.6 show that there is an approximate 10-fold increase in repair rate for concrete trunk lines relative to steel trunk lines.

Table A.9. Summary of Repairs in Riveted Steel Trunk Lines after PGD Screening

| No. | Pipeline | Location | Diameter (mm) | Material | Joint Connection | Damage Description | Repair | Owner |
|---|---|---|---|---|---|---|---|---|
| 1 | Roscoe Trunk Line | Oakdale, 18 m West | 1067 | Riveted Steel | Riveted | No observable pipe movement | NA[1] | LADWP |
| 2 | Roscoe Trunk Line | Fallbrook Ave. West Side | 914 | Riveted Steel | Riveted | No observable pipe movement | NA[1] | LADWP |
| 3 | Roscoe Trunk Line | Shirley Ave. 46 m East | 991 | Riveted Steel | Riveted | No observable pipe movement | NA[1] | LADWP |
| 4 | Roscoe Trunk Line | Calvin | 1016 | Riveted Steel | Riveted | No observable pipe movement | NA[1] | LADWP |
| 5 | Roscoe Trunk Line | Canoga Ave | 1295 | Riveted Steel | Riveted | NA[1] | NA[1] | LADWP |
| 6 | Roscoe Trunk Line | Faralone Ave. 171 m West 22259 Roscoe Blvd. | 1372 | Riveted Steel | Riveted | NA[1] | NA[1] | LADWP |
| 7 | Roscoe Trunk Line | Oakdale, 58 m West | 1067 | Riveted Steel | Riveted | NA[1] | NA[1] | LADWP |
| 8 | City Trunk Line | Lower San Fernando Dam | 1829 | Riveted Steel | Riveted | Tear at longitudinal seam | Welded plate strap | LADWP |

1: Sufficient data are not available.
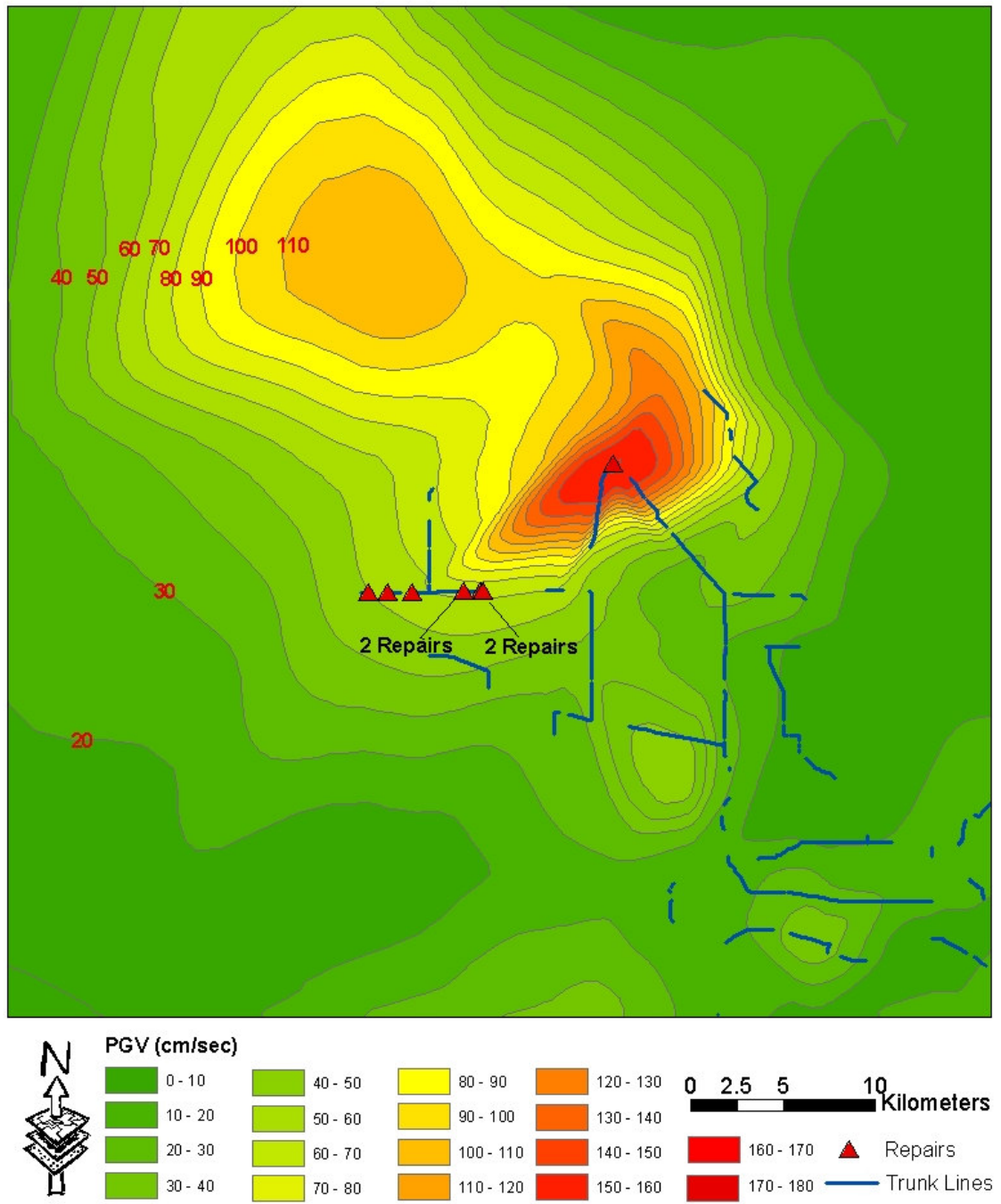
Figure A.5. Riveted Steel Trunk Line Performance during 1994 Northridge

Earthquake

Table A.10.   Summary of Riveted Steel Trunk Line Repair Rate According to PGV

| PGV Bin (cm/sec) | Representative PGV (cm/sec) | Pipe Length (km) | Repair No | Repair Rate (Repair No. / km) |
|---|---|---|---|---|
| 0-70 | 35 | 95.1 | 3 | 0.03 |
| 70-130 | 100 | 14.6 | 4 | 0.27 |
| 130-180 | 155 | 4.8 | 1 | 0.21 |
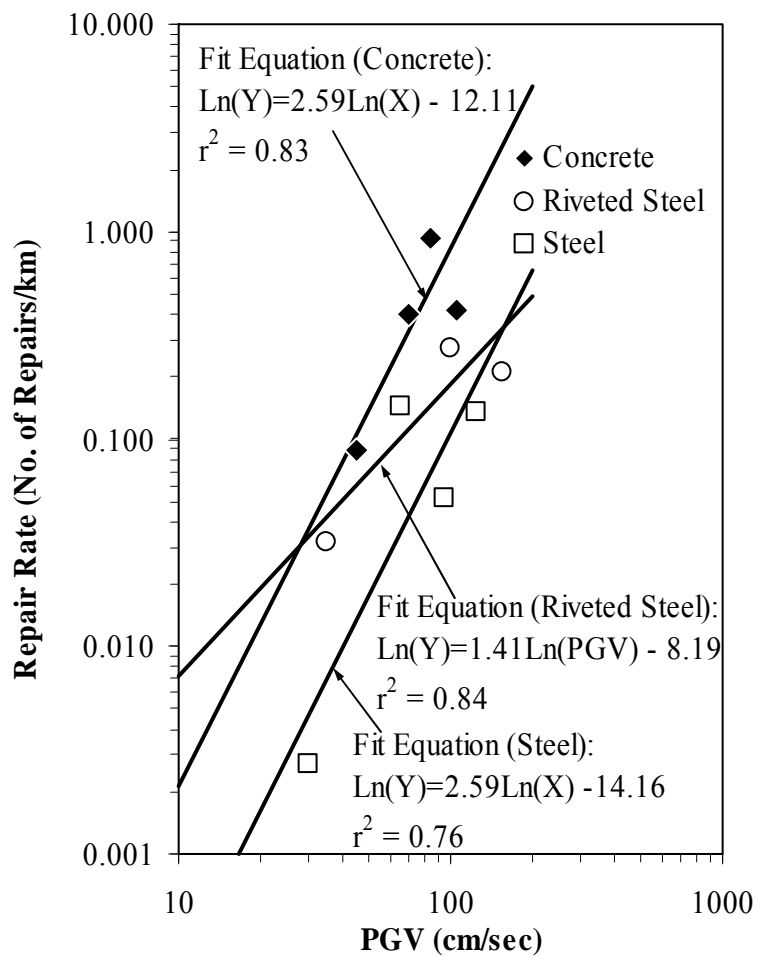


Figure A.6.   Regressions of Repair Rate vs. PGV for Concrete, Riveted Steel and Steel Pipelines

# APPENDIX B

# RISK DEAGGREGATIONS FOR FIVE WATER DISTRICTS

## B.1. Introduction

The water district risk curves with a 24-hour period of water losses from tanks are examined closely to identify the key scenario earthquakes that significantly influence water district risks. Risk deaggregations are performed at district risks corresponding to 475-year and 50-year recurrence intervals for five water districts, i.e., the West Valley, East Valley, Western, Central, and Harbor water districts, as described in the following subheadings:

## B.2. West Valley

Table B.1 summarizes the scenario earthquakes that contribute to the district risk at a system serviceability index (SSI) of 0.35 in the risk curve for the West Valley Water District, corresponding to a 475-year recurrence interval or 10% probability of exceedance in 50 years. The fourth Column in Table B.1 indicates the closest distance from the fault to the West Valley Water District centroid with geographic coordinates (-118.55175°, 34.21725°), as shown by the blue star in Figure 7.10. The table is sorted in a decreasing order of the contribution. Fifteen scenario earthquakes have contributed to this specific risk level, among which, Northridge, Background Source

Table B.1.  Summary of Scenario Contributions to 475-year Recurrence Risks in West Valley Water District

| Scenario ID | Scenario Name | $M_w$ | Distance (km) | Annual Occurrence Frequency | Contribution (%) |
|---|---|---|---|---|---|
| 370 | Northridge | 7.0 | 11 | 6.69E-04 | 32.76 |
| 561 | Background Source | 7.0 | 0 | 2.58E-04 | 12.63 |
| 198 | Santa Susana | 6.7 | 9 | 2.01E-04 | 9.84 |
| 21 | San Andreas Fault-All southern segments | 8.1 | 50 | 2.00E-04 | 9.80 |
| 175 | Verdugo | 6.9 | 13 | 1.93E-04 | 9.45 |
| 443 | Sierra Madre-San Fernando | 6.7 | 12 | 1.25E-04 | 6.15 |
| 202 | Simi-Santa Rosa | 7.0 | 16 | 8.46E-05 | 4.15 |
| 559 | Background Source | 7.0 | 9 | 6.98E-05 | 3.42 |
| 219 | Anacapa-Dume | 7.5 | 29 | 6.24E-05 | 3.06 |
| 159 | Newport-Inglewood | 7.1 | 24 | 5.40E-05 | 2.64 |
| 562 | Background Source | 7.0 | 22 | 5.09E-05 | 2.49 |
| 166 | Sierra Madre | 7.2 | 25 | 4.97E-05 | 2.43 |
| 203 | Simi-Santa Rosa | 6.5 | 16 | 1.91E-05 | 0.94 |
| 372 | Northridge | 6.5 | 11 | 4.74E-06 | 0.23 |
| 177 | Verdugo | 6.4 | 13 | 1.89E-07 | 0.01 |

Note: the table is based on the simulations with a 24-hour period of running tanks and the SSI corresponding to 475-year recurrence risks is 0.35.

561 scenario, Santa Susana, San Andreas Fault-All Southern Segments, Verdugo, and Sierra Madre-San Fernando scenario earthquakes have relatively significant contributions, i.e., > 5%, to the water district risk. Figure B.1a shows the water district risk deaggregation according to $M_w$ and distance. About 75% of the water district risk is contributed from the scenario earthquakes originating on faults located within 15 km from the water district centroid and having magnitude between 6.5 and 7.0.

Table B.2 summarizes the scenario earthquakes that contribute to the district risk at a SSI of 0.42 in the risk curve with a 24-hour period of running tanks, corresponding to a 50-year recurrence interval or 100% probability of exceedance in 50 years. In total 59 scenario earthquakes utilized in this work, 47 scenario

(a) 475-year Recurrence Risks, SSI = 0.35



(b) 50-year Recurrence Risks, SSI = 0.42

Figure B.1.   Risk Deaggregations for West Valley Water District

Table B.2. Summary of Scenario Contributions to 50-year Recurrence Risks in West Valley Water District

| Scenario ID | Scenario Name | $M_w$ | Distance (km) | Annual Occurrence Frequency | Contribution (%) |
|---|---|---|---|---|---|
| 22 | San Andreas Fault - 1857 | 7.8 | 50 | 3.20E-03 | 16.02 |
| 198 | Santa Susana | 6.7 | 9 | 2.01E-03 | 10.05 |
| 21 | San Andreas Fault-All southern segments | 8.1 | 50 | 1.60E-03 | 8.00 |
| 370 | Northridge | 7 | 11 | 1.43E-03 | 7.16 |
| 189 | Oak Ridge-onshore | 7 | 25 | 1.38E-03 | 6.88 |
| 561 | Background Source | 7 | 0 | 1.12E-03 | 5.59 |
| 195 | San Cayetano | 7 | 30 | 9.15E-04 | 4.58 |
| 559 | Background Source | 7 | 9 | 7.68E-04 | 3.84 |
| 175 | Verdugo | 6.9 | 13 | 7.08E-04 | 3.54 |
| 443 | Sierra Madre-San Fernando | 6.7 | 12 | 6.27E-04 | 3.14 |
| 169 | San Gabriel | 7.2 | 20 | 6.13E-04 | 3.06 |
| 219 | Anacapa-Dume | 7.5 | 29 | 5.62E-04 | 2.81 |
| 166 | Sierra Madre | 7.2 | 25 | 4.47E-04 | 2.24 |
| 196 | San Cayetano | 6.5 | 30 | 4.02E-04 | 2.01 |
| 560 | Background Source | 7 | 16 | 3.10E-04 | 1.55 |
| 19 | San Andreas Fault - Carrizo | 7.4 | 53 | 3.04E-04 | 1.52 |
| 444 | Palos Verdes | 7.3 | 30 | 2.80E-04 | 1.40 |
| 18 | San Andreas Fault - Mojave | 7.3 | 50 | 2.75E-04 | 1.38 |
| 159 | Newport-Inglewood | 7.1 | 24 | 2.70E-04 | 1.35 |
| 191 | Oak Ridge-onshore | 6.5 | 25 | 2.57E-04 | 1.29 |
| 562 | Background Source | 7 | 22 | 2.54E-04 | 1.27 |
| 202 | Simi-Santa Rosa | 7 | 16 | 2.54E-04 | 1.27 |
| 23 | San Andreas Fault - Southern 2 segments | 7.7 | 97 | 2.24E-04 | 1.12 |
| 220 | Anacapa-Dume | 7 | 29 | 1.90E-04 | 0.95 |
| 397 | Puente Hills blind thrust | 7.1 | 29 | 1.73E-04 | 0.86 |
| 141 | Newport-Inglewood offshore | 7.1 | 92 | 1.70E-04 | 0.85 |
| 171 | San Gabriel | 6.7 | 21 | 1.69E-04 | 0.85 |
| 447 | Palos Verdes | 6.8 | 30 | 1.66E-04 | 0.83 |
| 221 | Anacapa-Dume | 7 | 54 | 1.26E-04 | 0.63 |

Note: the table is based on the simulations with a 24-hour period of running tanks and the SSI corresponding to 50-year recurrence risks is 0.42.

Table B.2. (Continued)

| Scenario ID | Scenario Name | $M_w$ | Distance (km) | Annual Occurrence Frequency | Contribution (%) |
|---|---|---|---|---|---|
| 371 | Northridge | 6.5 | 12 | 1.15E-04 | 0.58 |
| 174 | Santa Monica | 6.6 | 21 | 1.05E-04 | 0.52 |
| 203 | Simi-Santa Rosa | 6.5 | 16 | 7.65E-05 | 0.38 |
| 122 | Clamshell-Sawpit | 6.5 | 32 | 7.09E-05 | 0.35 |
| 446 | Palos Verdes | 6.8 | 56 | 5.47E-05 | 0.27 |
| 162 | Newport-Inglewood | 6.6 | 24 | 5.00E-05 | 0.25 |
| 378 | Channel Island Thrust | 7.5 | 71 | 3.41E-05 | 0.17 |
| 399 | Puente Hills blind thrust | 6.6 | 29 | 2.74E-05 | 0.14 |
| 372 | Northridge | 6.5 | 11 | 2.05E-05 | 0.10 |
| 170 | San Gabriel | 6.7 | 20 | 1.99E-05 | 0.10 |
| 168 | Sierra Madre | 6.7 | 25 | 1.48E-05 | 0.07 |
| 118 | Holser | 6.5 | 21 | 1.11E-05 | 0.06 |
| 177 | Verdugo | 6.4 | 13 | 1.33E-06 | 0.01 |
| 176 | Verdugo | 6.4 | 24 | 1.05E-06 | 0.01 |
| 398 | Puente Hills blind thrust | 6.6 | 52 | 6.93E-07 | 0.00 |
| 173 | Malibu Coast | 6.7 | 20 | 5.40E-07 | 0.00 |
| 119 | Hollywood | 6.4 | 20 | 4.43E-07 | 0.00 |
| 222 | Anacapa-Dume | 6.5 | 29 | 8.63E-08 | 0.00 |

Note: the table is based on the simulations with a 24-hour period of running tanks and the SSI corresponding to 50-year recurrence risks is 0.42.

earthquakes have contributed to this specific risk level, among which, San Andreas-1857, Santa Susana, San Andreas-All Southern Segments, Northridge, Oak Ridge-onshore, and Background Source 561 scenario earthquakes have relatively significant contributions, i.e., > 5%, to the system risk. Figure B.1b shows the district risk deaggregation according to $M_w$ and distance. Significant contributions from scenario earthquakes with relatively large distances from originating faults to the district centroid are observed, particularly those associated with the San Andreas fault, which are about 50 km from the centroid.

Comparisons between Tables B.1 and B.2 show that the number of scenario earthquakes that have contributions to the water district risk increases significantly as the recurrence interval for the risk decreases from 475 years to 50 years. Comparisons between Figure B.1a and b show that, as the recurrence interval decreases, or SSI increases, the contributions from scenario earthquakes with relatively large distances from originating faults to the water district increase significantly.

## B.3.  East Valley

Table B.3 summarizes the scenario earthquakes that contribute to the district risk at a SSI of 0.49 in the risk curve for the East Valley Water District, corresponding to a 475-year recurrence interval or 10% probability of exceedance in 50 years. The fourth Column in Table B.3 indicates the closest distance from the fault to the East Valley Water District centroid with geographic coordinates (-118.38873°, 34.22718°), as shown by the blue star in Figure 7.10. The table is sorted in a decreasing order of the contribution. Fifteen scenario earthquakes have contributed to this specific risk level, among which, San Andreas fault-1857, Santa Susana, Sierra Madre-San Fernando, San Gabriel, Northridge, and Background Source 561 scenario earthquakes have relatively significant contributions, i.e., > 5%, to the water district risk. Figure B.2a shows the water district risk deaggregation according to $M_w$ and distance. About 40% of the water district risk is contributed from the San Andrea fault-1857, which is located about 43 km from the water district centorid. The remaining contributions to the district risk are mostly from scenario earthquakes originating on faults located within 30 km from the water district centroid.
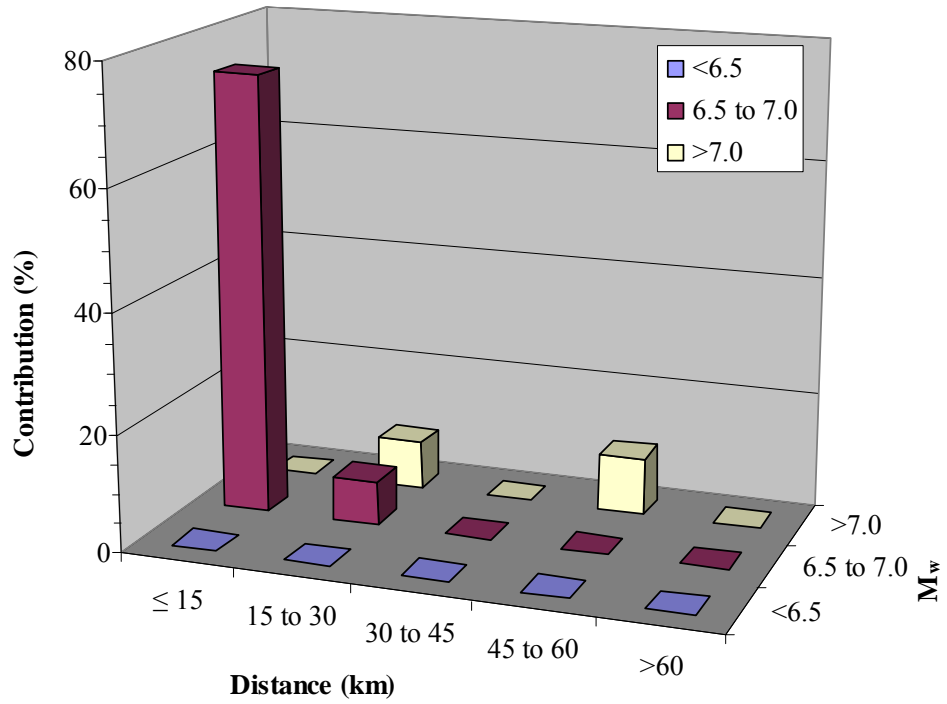
Table B.3. Summary of Scenario Contributions to 475-year Recurrence Risks in East Valley Water District

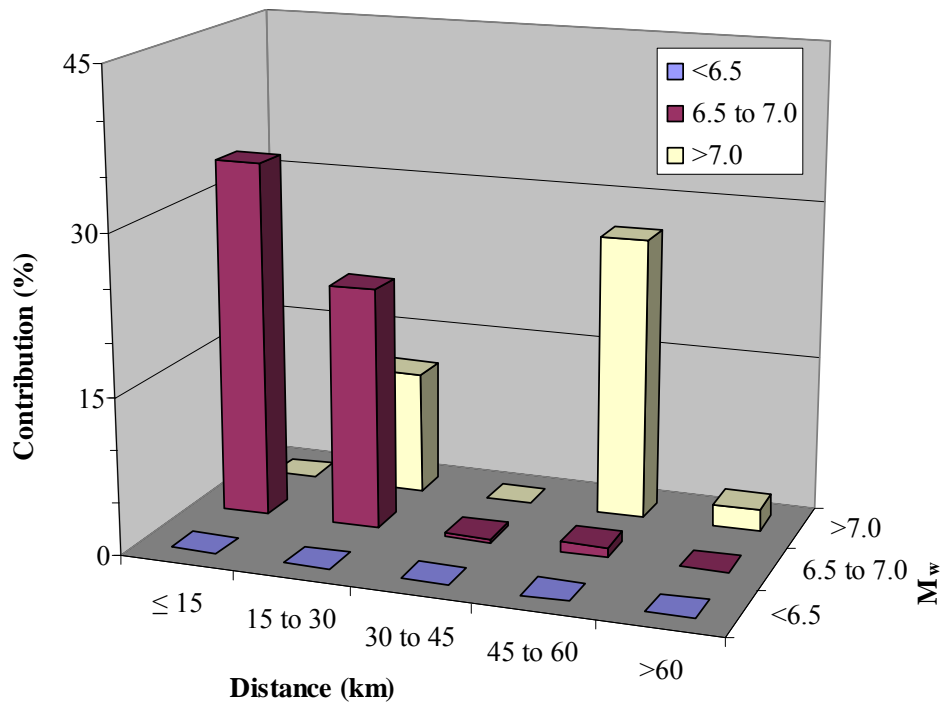| Scenario ID | Scenario Name | $M_w$ | Distance (km) | Annual Occurrence Frequency | Contribution (%) |
|---|---|---|---|---|---|
| 22 | San Andreas Fault - 1857 | 7.8 | 43 | 6.41E-04 | 39.87 |
| 198 | Santa Susana | 6.7 | 15 | 2.01E-04 | 12.50 |
| 443 | Sierra Madre-San Fernando | 6.7 | 6 | 1.88E-04 | 11.71 |
| 169 | San Gabriel | 7.2 | 14 | 1.02E-04 | 6.35 |
| 370 | Northridge | 7.0 | 6 | 9.55E-05 | 5.94 |
| 561 | Background Source | 7.0 | 1 | 8.60E-05 | 5.35 |
| 175 | Verdugo | 6.9 | 1 | 6.43E-05 | 4.00 |
| 397 | Puente Hills blind thrust | 7.1 | 21 | 5.75E-05 | 3.58 |
| 159 | Newport-Inglewood | 7.1 | 20 | 5.40E-05 | 3.36 |
| 166 | Sierra Madre | 7.2 | 11 | 4.97E-05 | 3.09 |
| 202 | Simi-Santa Rosa | 7.0 | 28 | 4.23E-05 | 2.63 |
| 168 | Sierra Madre | 6.7 | 11 | 1.48E-05 | 0.92 |
| 162 | Newport-Inglewood | 6.6 | 20 | 1.00E-05 | 0.62 |
| 176 | Verdugo | 6.4 | 10 | 1.05E-06 | 0.07 |
| 177 | Verdugo | 6.4 | 1 | 1.89E-07 | 0.01 |

Note: the table is based on the simulations with a 24-hour period of running tanks and the SSI corresponding to 475-year recurrence risks is 0.49.


Table B.4 summarizes the scenario earthquakes that contribute to the district risk at a SSI of 0.78 in the risk curve with a 24-hour period of running tanks, corresponding to a 50-year recurrence interval or 100% probability of exceedance in 50 years. In total 59 scenario earthquakes utilized in this work, 46 scenario earthquakes have contributed to this specific risk level, among which, San Andreas-1857, Santa Susana, San Andreas-All Southern Segments, Northridge, and San Gabriel scenario earthquakes have relatively significant contributions, i.e., > 5%, to the system risk. Figure B.2b shows the district risk deaggregation according to $M_w$ and distance. Significant contributions from scenario earthquakes with relatively large distances from originating faults to water district centroid are observed, particularly
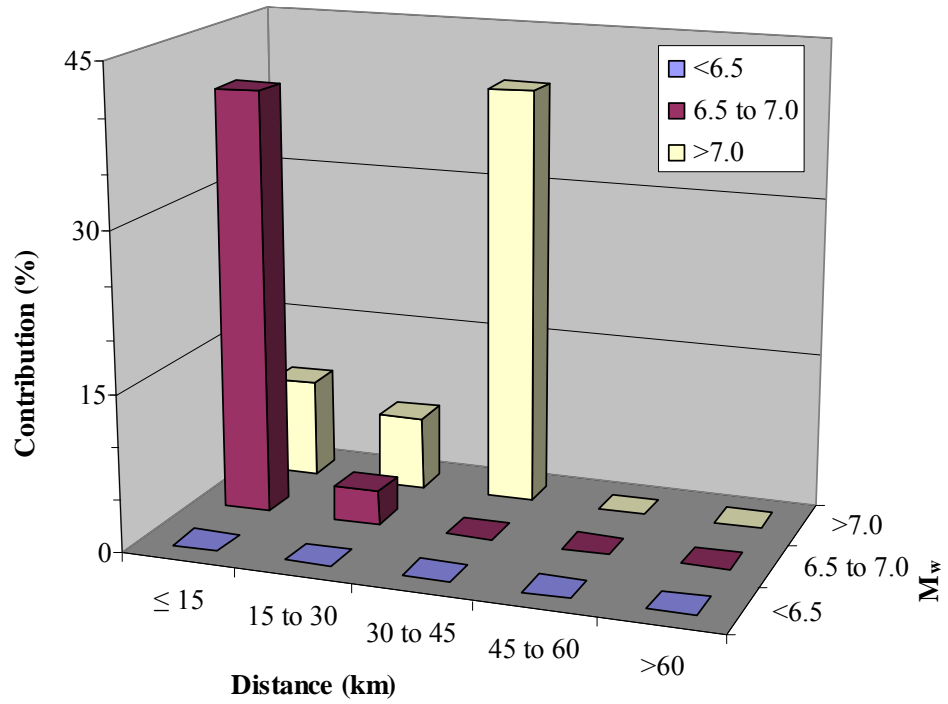
(a) 475-year Recurrence Risks, SSI = 0.49
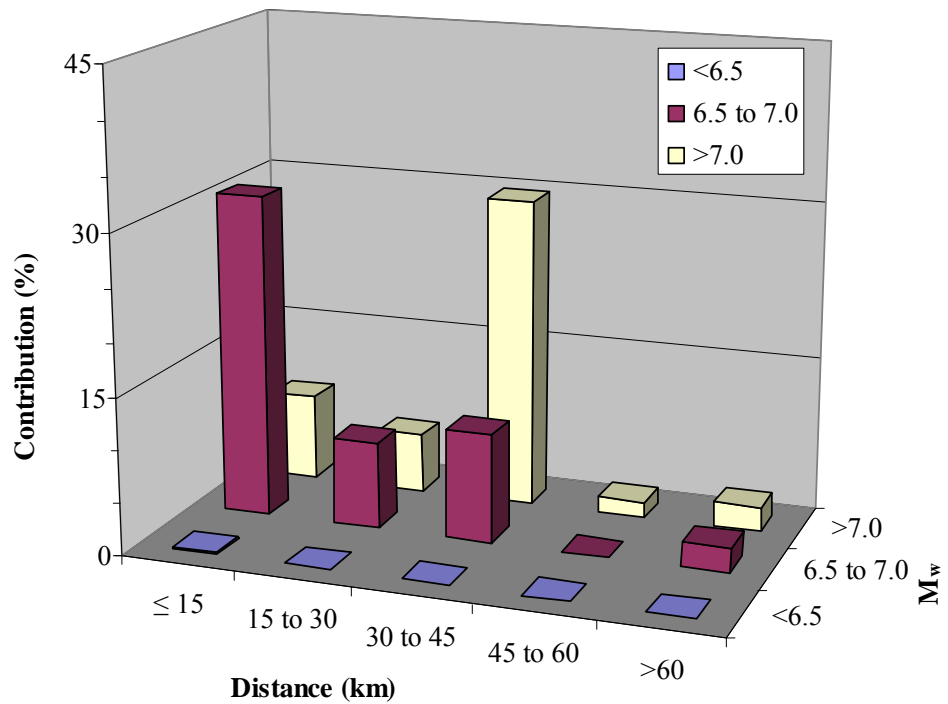


(b) 50-year Recurrence Risks, SSI = 0.78

Figure B.2.   Risk Deaggregations for East Valley Water District

Table B.4.  Summary of Scenario Contributions to 50-year Recurrence Risks in East Valley Water District

| Scenario ID | Scenario Name | $M_w$ | Distance (km) | Annual Occurrence Frequency | Contribution (%) |
|---|---|---|---|---|---|
| 22 | San Andreas Fault - 1857 | 7.8 | 43 | 3.85E-03 | 19.23 |
| 198 | Santa Susana | 6.7 | 15 | 1.61E-03 | 8.04 |
| 21 | San Andreas Fault-All southern segments | 8.1 | 43 | 1.40E-03 | 7.00 |
| 370 | Northridge | 7 | 6 | 1.34E-03 | 6.69 |
| 169 | San Gabriel | 7.2 | 14 | 1.02E-03 | 5.10 |
| 175 | Verdugo | 6.9 | 1 | 9.65E-04 | 4.82 |
| 561 | Background Source | 7 | 1 | 8.60E-04 | 4.30 |
| 397 | Puente Hills blind thrust | 7.1 | 21 | 8.06E-04 | 4.03 |
| 443 | Sierra Madre-San Fernando | 6.7 | 6 | 7.53E-04 | 3.76 |
| 166 | Sierra Madre | 7.2 | 11 | 6.46E-04 | 3.23 |
| 219 | Anacapa-Dume | 7.5 | 39 | 5.62E-04 | 2.81 |
| 189 | Oak Ridge-onshore | 7 | 36 | 5.51E-04 | 2.75 |
| 559 | Background Source | 7 | 10 | 4.88E-04 | 2.44 |
| 12 | Elsinore - Whittier | 6.8 | 43 | 4.80E-04 | 2.40 |
| 195 | San Cayetano | 7 | 41 | 4.58E-04 | 2.29 |
| 440 | Cucamonga | 6.9 | 62 | 4.12E-04 | 2.06 |
| 560 | Background Source | 7 | 17 | 3.62E-04 | 1.81 |
| 562 | Background Source | 7 | 23 | 3.56E-04 | 1.78 |
| 159 | Newport-Inglewood | 7.1 | 20 | 3.24E-04 | 1.62 |
| 19 | San Andreas Fault - Carrizo | 7.4 | 53 | 3.04E-04 | 1.52 |
| 167 | Sierra Madre | 6.7 | 38 | 2.93E-04 | 1.47 |
| 171 | San Gabriel | 6.7 | 23 | 2.54E-04 | 1.27 |
| 202 | Simi-Santa Rosa | 7 | 28 | 2.54E-04 | 1.27 |
| 145 | Coronado Bank | 7.6 | 115 | 2.33E-04 | 1.17 |
| 220 | Anacapa-Dume | 7 | 39 | 2.28E-04 | 1.14 |
| 141 | Newport-Inglewood offshore | 7.1 | 83 | 1.70E-04 | 0.85 |
| 444 | Palos Verdes | 7.3 | 36 | 1.40E-04 | 0.70 |
| 174 | Santa Monica | 6.6 | 18 | 1.40E-04 | 0.70 |
| 168 | Sierra Madre | 6.7 | 11 | 1.18E-04 | 0.59 |
| 371 | Northridge | 6.5 | 16 | 1.15E-04 | 0.58 |
| 120 | Raymond | 6.5 | 19 | 9.88E-05 | 0.49 |

Note: the table is based on the simulations with a 24-hour period of running tanks and the SSI corresponding to 50-year recurrence Risks is 0.78.

Table B.4.   (Continued)

| Scenario ID | Scenario Name | $M_w$ | Distance (km) | Annual Occurrence Frequency | Contribution (%) |
|---|---|---|---|---|---|
| 447 | Palos Verdes | 6.8 | 36 | 8.32E-05 | 0.42 |
| 378 | Channel Island Thrust | 7.5 | 85 | 6.82E-05 | 0.34 |
| 162 | Newport-Inglewood | 6.6 | 61 | 6.00E-05 | 0.30 |
| 118 | Holser | 6.5 | 25 | 4.44E-05 | 0.22 |
| 399 | Puente Hills blind thrust | 6.6 | 21 | 2.74E-05 | 0.14 |
| 170 | San Gabriel | 6.7 | 14 | 1.99E-05 | 0.10 |
| 203 | Simi-Santa Rosa | 6.5 | 28 | 1.91E-05 | 0.10 |
| 388 | Upper Elysian Park | 6.4 | 15 | 1.64E-05 | 0.08 |
| 372 | Northridge | 6.5 | 6 | 9.48E-06 | 0.05 |
| 176 | Verdugo | 6.4 | 10 | 8.39E-06 | 0.04 |
| 398 | Puente Hills blind thrust | 6.6 | 41 | 1.39E-06 | 0.01 |
| 177 | Verdugo | 6.4 | 1 | 1.33E-06 | 0.01 |
| 119 | Hollywood | 6.4 | 14 | 8.86E-07 | 0.00 |
| 173 | Malibu Coast | 6.7 | 25 | 7.20E-07 | 0.00 |
| 222 | Anacapa-Dume | 6.5 | 39 | 8.63E-08 | 0.00 |

Note: the table is based on the simulations with a 24-hour period of running tanks and the SSI corresponding to 50-year recurrence risks is 0.78.

those associated with the San Andreas fault, which are about 43 km from the centroid.

Comparisons between Tables B.3 and B.4 show that the number of scenario earthquakes that have contributions to the water district risk increases significantly as the recurrence interval for the risk decreases from 475 years to 50 years. Comparisons between Figure B.2a and b show that, as the recurrence interval decreases, or SSI increases, the contributions from scenario earthquakes with relatively large distances from originating faults to the water district increase significantly.

## B.4. Western

Table B.5 summarizes the scenario earthquakes that contribute to the district risk at a SSI of 0.24 in the risk curve for the Western Water District, corresponding to a 475-year recurrence interval or 10% probability of exceedance in 50 years. The fourth Column in Table B.5 indicates the closest distance from the fault to the Western Water District centroid with geographic coordinates (-118.43397°, 34.05516°), as shown by the blue star in Figure 7.10. The table is sorted in a decreasing order of the contribution. Sixteen scenario earthquakes have contributed to this specific risk level, among which, Puente Hills blind thrust fault, Newport-Inglewood, Background Source 562 scenario, San Andreas fault-Southern 2 Segments, Palos Verdes, and Anacapa-Dume earthquakes have relatively significant contributions, i.e., > 5%, to the water district risk. Figure B.3a shows the water district risk deaggregation according to $M_w$ and distance. About 75% of the water district risk is contributed from the scenario earthquakes originating on faults located within 30 km from the water district centroid and having magnitude larger than 6.5.

Table B.6 summarizes the scenario earthquakes that contribute to the district risk at a SSI of 0.35 in the risk curve with a 24-hour period of running tanks, corresponding to a 50-year recurrence interval or 100% probability of exceedance in 50 years. In total 59 scenario earthquakes utilized in this work, 43 scenario earthquakes have contributed to this specific risk level, among which, San Andreas-1857, San Andreas-All Southern Segments, and Northridge scenario earthquakes have relatively significant contributions, i.e., > 5%, to the system risk. Figure B.3b shows the district risk deaggregation according to $M_w$ and distance. Significant contributions from scenario earthquakes with relative large distances from originating faults to water

Table B.5.   Summary of Scenario Contributions to 475-year Recurrence Risks in
Western Water District

| Scenario ID | Scenario Name | $M_w$ | Distance (km) | Annual Occurrence Frequency | Contribution (%) |
|---|---|---|---|---|---|
| 397 | Puente Hills blind thrust | 7.1 | 12 | 5.18E-04 | 24.73 |
| 159 | Newport-Inglewood | 7.1 | 4 | 2.70E-04 | 12.88 |
| 562 | Background Source | 7.0 | 4 | 2.54E-04 | 12.14 |
| 23 | San Andreas Fault - Southern 2 segments | 7.7 | 90 | 2.24E-04 | 10.71 |
| 451 | Palos Verdes | 6.3 | 43 | 2.18E-04 | 10.42 |
| 444 | Palos Verdes | 7.3 | 18 | 1.40E-04 | 6.69 |
| 219 | Anacapa-Dume | 7.5 | 25 | 1.25E-04 | 5.96 |
| 560 | Background Source | 7.0 | 2 | 1.03E-04 | 4.93 |
| 161 | Newport-Inglewood | 6.6 | 26 | 7.43E-05 | 3.55 |
| 175 | Verdugo | 6.9 | 20 | 6.43E-05 | 3.07 |
| 166 | Sierra Madre | 7.2 | 27 | 4.97E-05 | 2.37 |
| 174 | Santa Monica | 6.6 | 0 | 3.49E-05 | 1.67 |
| 399 | Puente Hills blind thrust | 6.6 | 12 | 1.09E-05 | 0.52 |
| 170 | San Gabriel | 6.7 | 32 | 6.65E-06 | 0.32 |
| 119 | Hollywood | 6.4 | 4 | 4.43E-07 | 0.02 |
| 173 | Malibu Coast | 6.7 | 10 | 1.80E-07 | 0.01 |

Note: the table is based on the simulations with a 24-hour period of running tanks and the SSI corresponding to 475-year recurrence risks is 0.24.

district centroid are observed, particularly those associated with the San Andreas fault, which are about 62 km from the centroid.

Comparisons between Tables B.5 and B.6 show that the number of scenario earthquakes that have contributions to the water district risk increases significantly as the recurrence interval for the risk decreases from 475 years to 50 years. Comparisons between Figure B.3a and b show that, as the recurrence interval decreases, or SSI increases, the contributions from scenario earthquakes with relatively large distances from originating faults to the water district increase significantly.

(a) 475-year Recurrence Risks, SSI = 0.24



(b) 50-year Recurrence Risks, SSI = 0.35

Figure B.3.   Risk Deaggregations for Western Water District

Table B.6.   Summary of Scenario Contributions to 50-year Recurrence Risks in Western Water District

| Scenario ID | Scenario Name | $M_w$ | Distance (km) | Annual Occurrence Frequency | Contribution (%) |
|---|---|---|---|---|---|
| 22 | San Andreas Fault - 1857 | 7.8 | 62 | 3.20E-03 | 16.02 |
| 21 | San Andreas Fault-All southern segments | 8.1 | 62 | 2.20E-03 | 11.01 |
| 370 | Northridge | 7 | 24 | 1.05E-03 | 5.25 |
| 444 | Palos Verdes | 7.3 | 18 | 9.81E-04 | 4.91 |
| 195 | San Cayetano | 7 | 52 | 9.15E-04 | 4.58 |
| 559 | Background Source | 7 | 9 | 9.07E-04 | 4.54 |
| 397 | Puente Hills blind thrust | 7.1 | 12 | 8.63E-04 | 4.32 |
| 159 | Newport-Inglewood | 7.1 | 4 | 8.10E-04 | 4.05 |
| 560 | Background Source | 7 | 2 | 7.23E-04 | 3.62 |
| 219 | Anacapa-Dume | 7.5 | 25 | 6.87E-04 | 3.43 |
| 23 | San Andreas Fault - Southern 2 segments | 7.7 | 90 | 6.73E-04 | 3.37 |
| 562 | Background Source | 7 | 4 | 6.61E-04 | 3.31 |
| 175 | Verdugo | 6.9 | 20 | 6.43E-04 | 3.22 |
| 198 | Santa Susana | 6.7 | 29 | 6.03E-04 | 3.01 |
| 561 | Background Source | 7 | 18 | 6.02E-04 | 3.01 |
| 189 | Oak Ridge-onshore | 7 | 46 | 5.51E-04 | 2.75 |
| 166 | Sierra Madre | 7.2 | 27 | 5.46E-04 | 2.73 |
| 220 | Anacapa-Dume | 7 | 25 | 3.80E-04 | 1.90 |
| 447 | Palos Verdes | 6.8 | 18 | 3.33E-04 | 1.66 |
| 174 | Santa Monica | 6.6 | 0 | 3.14E-04 | 1.57 |
| 169 | San Gabriel | 7.2 | 32 | 3.06E-04 | 1.53 |
| 454 | Palos Verdes | 6.3 | 18 | 2.89E-04 | 1.44 |
| 161 | Newport-Inglewood | 6.6 | 26 | 2.23E-04 | 1.12 |
| 451 | Palos Verdes | 6.3 | 43 | 2.18E-04 | 1.09 |
| 19 | San Andreas Fault - Carrizo | 7.4 | 71 | 1.52E-04 | 0.76 |
| 162 | Newport-Inglewood | 6.6 | 4 | 1.50E-04 | 0.75 |
| 120 | Raymond | 6.5 | 21 | 1.48E-04 | 0.74 |
| 453 | Palos Verdes | 6.3 | 20 | 1.38E-04 | 0.69 |
| 145 | Coronado Bank | 7.6 | 99 | 1.17E-04 | 0.58 |
| 378 | Channel Island Thrust | 7.5 | 77 | 1.02E-04 | 0.51 |
| 202 | Simi-Santa Rosa | 7 | 36 | 8.46E-05 | 0.42 |

Note: the table is based on the simulations with a 24-hour period of running tanks and the SSI corresponding to 50-year recurrence risks is 0.35.

Table B.6. (Continued)

| Scenario ID | Scenario Name | $M_w$ | Distance (km) | Annual Occurrence Frequency | Contribution (%) |
|---|---|---|---|---|---|
| 443 | Sierra Madre-San Fernando | 6.7 | 26 | 6.27E-05 | 0.31 |
| 168 | Sierra Madre | 6.7 | 27 | 5.91E-05 | 0.30 |
| 399 | Puente Hills blind thrust | 6.6 | 12 | 5.47E-05 | 0.27 |
| 388 | Upper Elysian Park | 6.4 | 14 | 2.45E-05 | 0.12 |
| 371 | Northridge | 6.5 | 31 | 1.92E-05 | 0.10 |
| 170 | San Gabriel | 6.7 | 32 | 1.33E-05 | 0.07 |
| 372 | Northridge | 6.5 | 24 | 9.48E-06 | 0.05 |
| 176 | Verdugo | 6.4 | 21 | 6.29E-06 | 0.03 |
| 119 | Hollywood | 6.4 | 4 | 3.54E-06 | 0.02 |
| 173 | Malibu Coast | 6.7 | 10 | 1.80E-06 | 0.01 |
| 177 | Verdugo | 6.4 | 20 | 5.68E-07 | 0.00 |
| 222 | Anacapa-Dume | 6.5 | 25 | 8.63E-08 | 0.00 |

Note: the table is based on the simulations with a 24-hour period of running tanks and the SSI corresponding to 50-year recurrence risks is 0.35.

## B.5. Central

Table B.7 summarizes the scenario earthquakes that contribute to the district risk at a SSI of 0.17 in the risk curve for the Central Water District, corresponding to a 475-year recurrence interval or 10% probability of exceedance in 50 years. The fourth Column in Table B.7 indicates the closest distance from the fault to the Central Water District centroid with geographic coordinates (-118.24667°, 34.07510°), as shown by the blue star in Figure 7.10. The table is sorted in a decreasing order of the contribution. Seventeen scenario earthquakes have contributed to this specific risk level, among which, Cucamonga, Puente Hills blind thrust fault, Newport-Inglewood offshore, Elsinore-Whittier, Santa Susana, and Background Source 560 scenario earthquakes have relatively significant contributions, i.e., > 5%, to the water district risk. Figure B.4a shows the water district risk deaggregation according to $M_w$ and
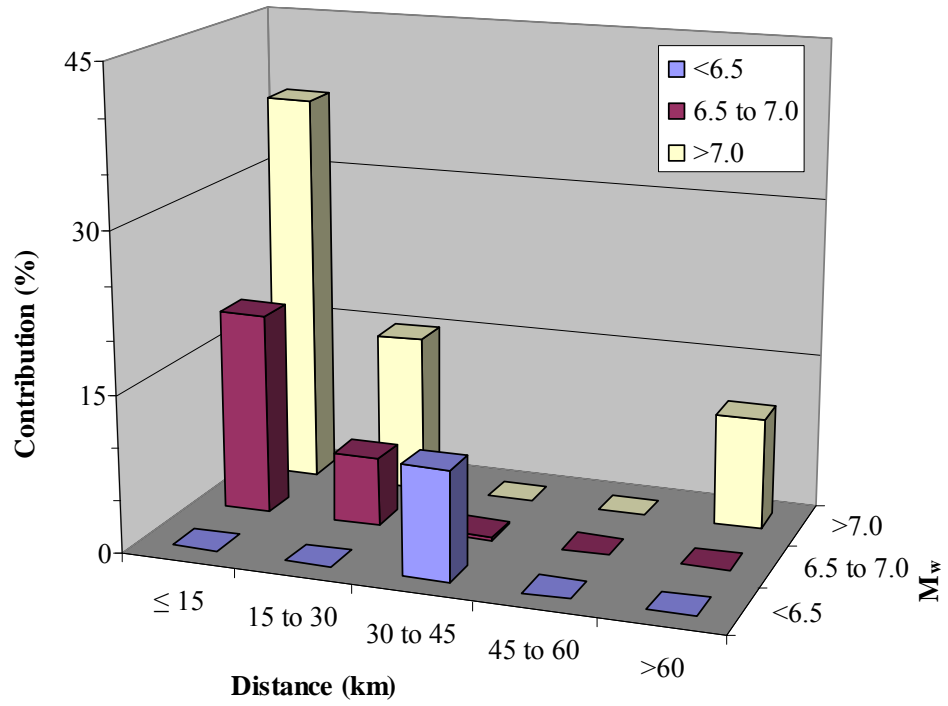
Table B.7.   Summary of Scenario Contributions to 475-year Recurrence Risks in Central Water District

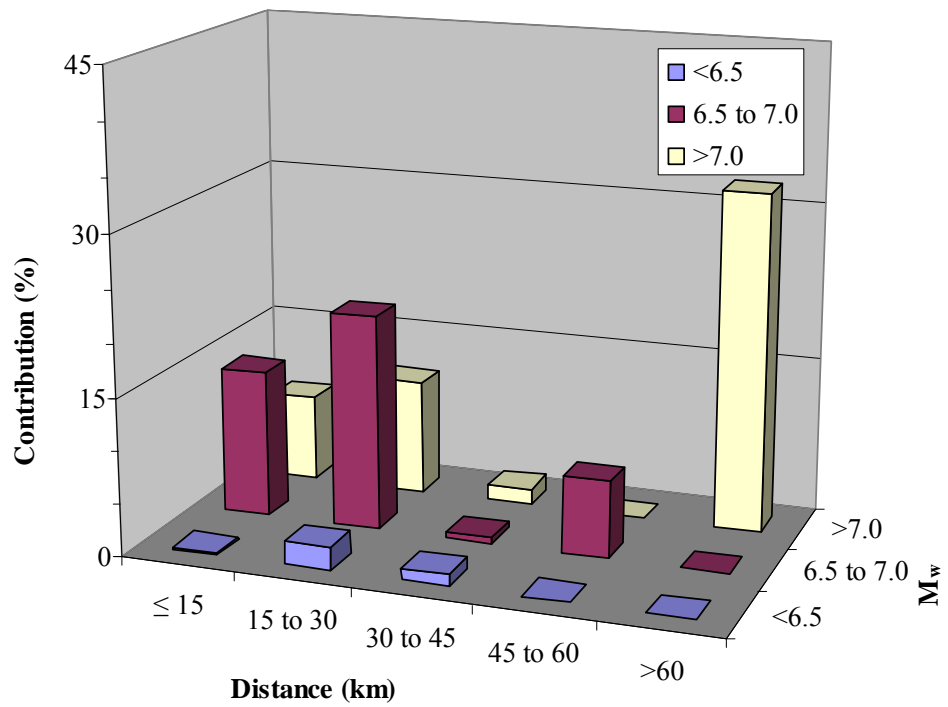| Scenario ID | Scenario Name | $M_w$ | Distance (km) | Annual Occurrence Frequency | Contribution (%) |
|---|---|---|---|---|---|
| 440 | Cucamonga | 6.9 | 48 | 4.12E-04 | 19.95 |
| 397 | Puente Hills blind thrust | 7.1 | 4 | 3.45E-04 | 16.72 |
| 141 | Newport-Inglewood offshore | 7.1 | 62 | 3.41E-04 | 16.49 |
| 12 | Elsinore - Whittier | 6.8 | 24 | 2.40E-04 | 11.61 |
| 198 | Santa Susana | 6.7 | 36 | 2.01E-04 | 9.73 |
| 560 | Background Source | 7.0 | 0 | 1.55E-04 | 7.50 |
| 169 | San Gabriel | 7.2 | 27 | 1.02E-04 | 4.94 |
| 370 | Northridge | 7.0 | 26 | 9.55E-05 | 4.62 |
| 175 | Verdugo | 6.9 | 9 | 6.43E-05 | 3.11 |
| 166 | Sierra Madre | 7.2 | 16 | 4.97E-05 | 2.40 |
| 202 | Simi-Santa Rosa | 7.0 | 48 | 4.23E-05 | 2.05 |
| 388 | Upper Elysian Park | 6.4 | 0 | 8.18E-06 | 0.40 |
| 399 | Puente Hills blind thrust | 6.6 | 4 | 5.47E-06 | 0.26 |
| 372 | Northridge | 6.5 | 26 | 3.16E-06 | 0.15 |
| 398 | Puente Hills blind thrust | 6.6 | 20 | 6.93E-07 | 0.03 |
| 173 | Malibu Coast | 6.7 | 27 | 1.80E-07 | 0.01 |
| 222 | Anacapa-Dume | 6.5 | 42 | 8.63E-08 | 0.00 |

Note: the table is based on the simulations with a 24-hour period of running tanks and the SSI corresponding to 475-year recurrence risks is 0.17.

distance. Most water district risk is contributed from the scenario earthquakes with $M_w$ larger than 6.5.

Table B.8 summarizes the scenario earthquakes that contribute to the district risk at a SSI of 0.38 in the risk curve with a 24-hour period of running tanks, corresponding to a 50-year recurrence interval or 100% probability of exceedance in 50 years. In total 59 scenario earthquakes utilized in this work, 51 scenario earthquakes have contributed to this specific risk level, among which, Cucamonga,
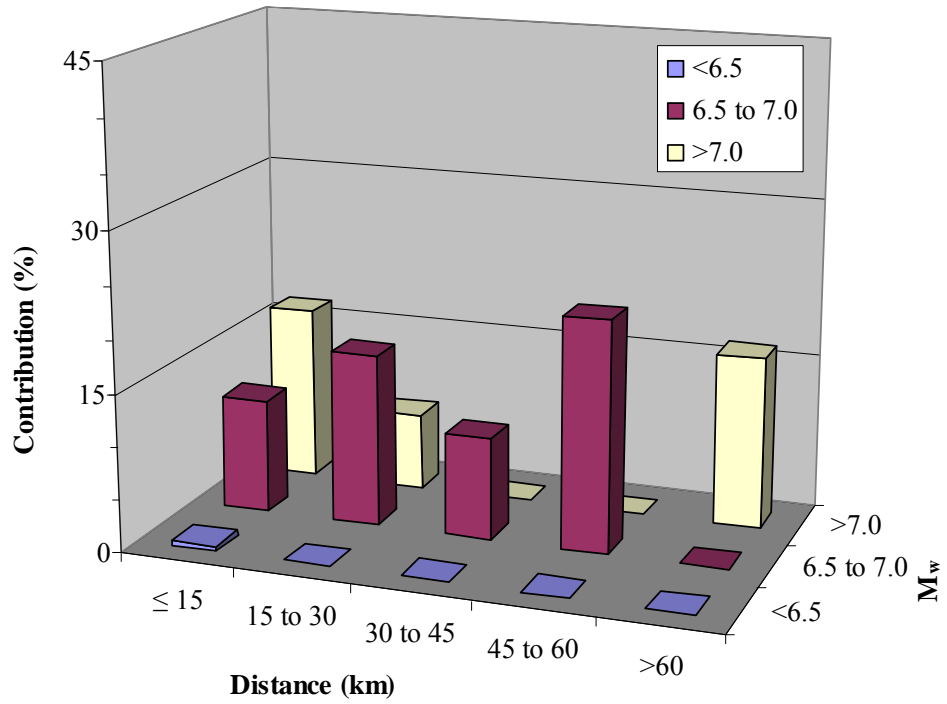
(a) 475-year Recurrence Risks, SSI = 0.17
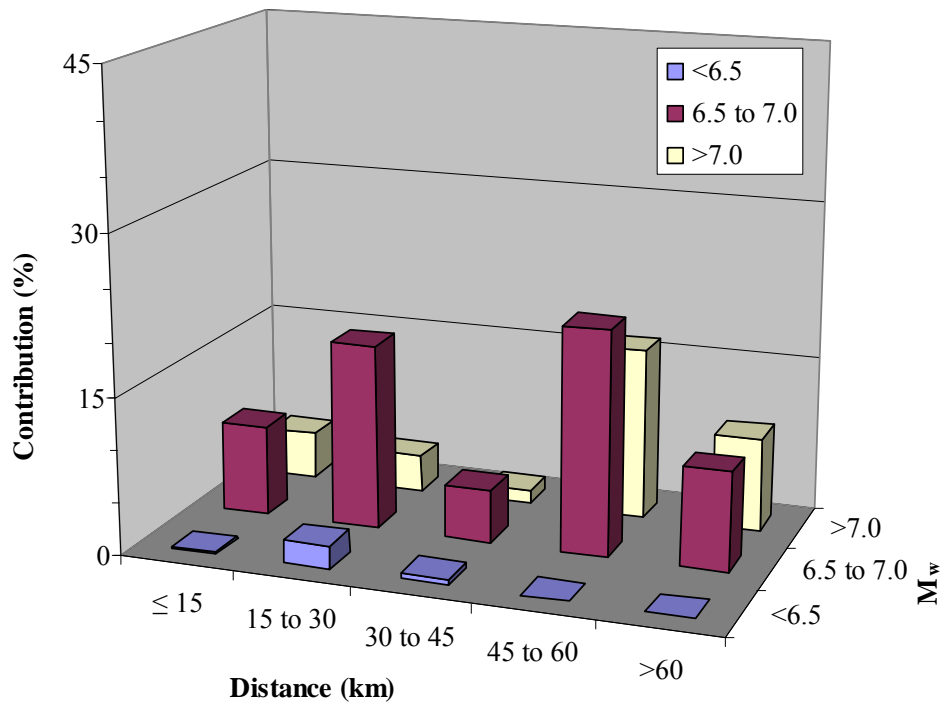


(b) 50-year Recurrence Risks, SSI = 0.38

Figure B.4.   Risk Deaggregations for Central Water District

Table B.8.   Summary of Scenario Contributions to 50-year Recurrence Risks in Central Water District

| Scenario ID | Scenario Name | $M_w$ | Distance (km) | Annual Occurrence Frequency | Contribution (%) |
|---|---|---|---|---|---|
| 440 | Cucamonga | 6.9 | 48 | 2.47E-03 | 12.36 |
| 22 | San Andreas Fault - 1857 | 7.8 | 52 | 1.92E-03 | 9.61 |
| 195 | San Cayetano | 7 | 61 | 1.83E-03 | 9.15 |
| 189 | Oak Ridge-onshore | 7 | 56 | 1.38E-03 | 6.88 |
| 167 | Sierra Madre | 6.7 | 26 | 1.17E-03 | 5.86 |
| 12 | Elsinore - Whittier | 6.8 | 24 | 9.60E-04 | 4.80 |
| 397 | Puente Hills blind thrust | 7.1 | 4 | 8.06E-04 | 4.03 |
| 21 | San Andreas Fault-All southern segments | 8.1 | 52 | 8.00E-04 | 4.00 |
| 141 | Newport-Inglewood offshore | 7.1 | 62 | 6.81E-04 | 3.41 |
| 23 | San Andreas Fault - Southern 2 segments | 7.7 | 73 | 6.73E-04 | 3.37 |
| 198 | Santa Susana | 6.7 | 36 | 6.03E-04 | 3.01 |
| 18 | San Andreas Fault - Mojave | 7.3 | 52 | 5.50E-04 | 2.75 |
| 19 | San Andreas Fault - Carrizo | 7.4 | 72 | 4.56E-04 | 2.28 |
| 454 | Palos Verdes | 6.3 | 29 | 4.33E-04 | 2.17 |
| 560 | Background Source | 7 | 0 | 4.13E-04 | 2.07 |
| 169 | San Gabriel | 7.2 | 27 | 4.08E-04 | 2.04 |
| 370 | Northridge | 7 | 26 | 3.82E-04 | 1.91 |
| 559 | Background Source | 7 | 7 | 3.49E-04 | 1.74 |
| 561 | Background Source | 7 | 20 | 3.44E-04 | 1.72 |
| 175 | Verdugo | 6.9 | 9 | 3.22E-04 | 1.61 |
| 562 | Background Source | 7 | 8 | 3.05E-04 | 1.53 |
| 120 | Raymond | 6.5 | 6 | 2.96E-04 | 1.48 |
| 191 | Oak Ridge-onshore | 6.5 | 56 | 2.57E-04 | 1.29 |
| 219 | Anacapa-Dume | 7.5 | 42 | 2.50E-04 | 1.25 |
| 174 | Santa Monica | 6.6 | 16 | 2.09E-04 | 1.05 |
| 202 | Simi-Santa Rosa | 7 | 48 | 1.69E-04 | 0.85 |
| 160 | Newport-Inglewood | 6.6 | 40 | 1.58E-04 | 0.79 |
| 166 | Sierra Madre | 7.2 | 16 | 1.49E-04 | 0.75 |
| 122 | Clamshell-Sawpit | 6.5 | 26 | 1.42E-04 | 0.71 |

Note: the table is based on the simulations with a 24-hour period of running tanks and the SSI corresponding to 50-year recurrence risks is 0.38.

Table B.8. (Continued)

| Scenario ID | Scenario Name | $M_w$ | Distance (km) | Annual Occurrence Frequency | Contribution (%) |
|---|---|---|---|---|---|
| 444 | Palos Verdes | 7.3 | 29 | 1.40E-04 | 0.70 |
| 443 | Sierra Madre-San Fernando | 6.7 | 23 | 1.25E-04 | 0.63 |
| 220 | Anacapa-Dume | 7 | 42 | 1.14E-04 | 0.57 |
| 446 | Palos Verdes | 6.8 | 35 | 1.09E-04 | 0.55 |
| 159 | Newport-Inglewood | 7.1 | 13 | 1.08E-04 | 0.54 |
| 452 | Palos Verdes | 6.3 | 32 | 9.59E-05 | 0.48 |
| 168 | Sierra Madre | 6.7 | 16 | 8.86E-05 | 0.44 |
| 221 | Anacapa-Dume | 7 | 75 | 6.29E-05 | 0.31 |
| 447 | Palos Verdes | 6.8 | 29 | 4.16E-05 | 0.21 |
| 161 | Newport-Inglewood | 6.6 | 22 | 3.72E-05 | 0.19 |
| 399 | Puente Hills blind thrust | 6.6 | 4 | 2.19E-05 | 0.11 |
| 170 | San Gabriel | 6.7 | 27 | 1.99E-05 | 0.10 |
| 371 | Northridge | 6.5 | 37 | 1.92E-05 | 0.10 |
| 388 | Upper Elysian Park | 6.4 | 0 | 1.64E-05 | 0.08 |
| 162 | Newport-Inglewood | 6.6 | 13 | 1.00E-05 | 0.05 |
| 372 | Northridge | 6.5 | 26 | 7.90E-06 | 0.04 |
| 119 | Hollywood | 6.4 | 4 | 3.54E-06 | 0.02 |
| 176 | Verdugo | 6.4 | 9 | 3.15E-06 | 0.02 |
| 398 | Puente Hills blind thrust | 6.6 | 20 | 2.77E-06 | 0.01 |
| 173 | Malibu Coast | 6.7 | 27 | 5.40E-07 | 0.00 |
| 222 | Anacapa-Dume | 6.5 | 42 | 4.31E-07 | 0.00 |
| 177 | Verdugo | 6.4 | 13 | 3.79E-07 | 0.00 |

Note: the table is based on the simulations with a 24-hour period of running tanks and the SSI corresponding to 50-year recurrence risks is 0.38.

San Andreas fault-1857, San Cayetano, Oak Ridge-onshore, and Sierra Madre scenario earthquakes have relatively significant contributions, i.e., > 5%, to the district risk. Figure B.4b shows the district risk deaggregation according to $M_w$ and distance. Most water district risk is contributed from the scenario earthquakes with $M_w \geq 6.5$.

Comparisons between Tables B.7 and B.8 show that the number of scenario earthquakes that have contributions to the water district risk increases significantly as the recurrence interval for the risk decreases from 475 years to 50 years. Although it is not as obvious as that for the West Valley, East Valley, and Western Water Districts, comparisons between Figure B.4a and b show that, as the recurrence interval decreases, or SSI increases, the contributions increase from scenario earthquakes with relatively large distances from originating faults to the water district.

## B.6. Harbor

Table B.9 summarizes the scenario earthquakes that contribute to the district risk at a SSI of 0.41 in the risk curve for the Harbor Water District, corresponding to a 475-year recurrence interval or 10% probability of exceedance in 50 years. The fourth Column in Table B.9 indicates the closest distance from the fault to the Harbor Water District centroid with geographic coordinates (-118.28105°, 33.84948°), as shown by the blue star in Figure 7.10. The table is sorted in a decreasing order of the contribution. Fifteen scenario earthquakes have contributed to this specific risk level, among which, San Cayetano, Newport-Inglewood, Palos Verdes, Verdugo, Newport-Inglewood offshore scenario earthquakes have relatively significant contributions, i.e., > 5%, to the water district risk. Figure B.5a shows the water district risk deaggregation according to $M_w$ and distance. Scenario earthquakes with various distances to the district centroid contribute to the water district risk significantly. This is consistent with the system configuration and water flow pattern of the LADWP water supply system. The Harbor Water District is positioned in the southern end of the system and water has to travel from the north to the south, going through the whole system, before it arrives at the Harbor Water District. Disruption occurred during the conveyance,

Table B.9. Summary of Scenario Contributions to 475-year Recurrence Risks in Harbor Water District

| Scenario ID | Scenario Name | $M_w$ | Distance (km) | Annual Occurrence Frequency | Contribution (%) |
|---|---|---|---|---|---|
| 195 | San Cayetano | 7.0 | 79 | 4.58E-04 | 21.93 |
| 159 | Newport-Inglewood | 7.1 | 4 | 3.24E-04 | 15.52 |
| 444 | Palos Verdes | 7.3 | 7 | 2.80E-04 | 13.44 |
| 175 | Verdugo | 6.9 | 34 | 1.93E-04 | 9.25 |
| 141 | Newport-Inglewood offshore | 7.1 | 44 | 1.70E-04 | 8.17 |
| 446 | Palos Verdes | 6.8 | 9 | 1.09E-04 | 5.24 |
| 169 | San Gabriel | 7.2 | 52 | 1.02E-04 | 4.89 |
| 452 | Palos Verdes | 6.3 | 7 | 9.59E-05 | 4.60 |
| 370 | Northridge | 7.0 | 49 | 9.55E-05 | 4.58 |
| 397 | Puente Hills blind thrust | 7.1 | 17 | 5.75E-05 | 2.76 |
| 562 | Background Source | 7.0 | 19 | 5.09E-05 | 2.44 |
| 447 | Palos Verdes | 6.8 | 7 | 4.16E-05 | 1.99 |
| 220 | Anacapa-Dume | 7.0 | 40 | 3.80E-05 | 1.82 |
| 162 | Newport-Inglewood | 6.6 | 4 | 1.00E-05 | 0.48 |
| 399 | Puente Hills blind thrust | 6.6 | 17 | 5.47E-06 | 0.26 |
| 398 | Puente Hills blind thrust | 6.6 | 20 | 6.93E-07 | 0.03 |

Note: the table is based on the simulations with a 24-hour period of running tanks and the SSI corresponding to 475-year recurrence risks is 0.41.

which may result from the faults located close to the northern portion of the system but distant from the Harbor district, has significant impacts on the performance of the Harbor Water District.

Table B.10 summarizes the scenario earthquakes that contribute to the district risk at a SSI of 0.53 in the risk curve with a 24-hour period of running tanks, corresponding to a 50-year recurrence interval or 100% probability of exceedance in 50 years. In total 59 scenario earthquakes utilized in this work, 51 scenario earthquakes have contributed to this specific risk level, among which, San Andreas-

(a) 475-year Recurrence Risks, SSI = 0.41



(b) 50-year Recurrence Risks, SSI = 0.53

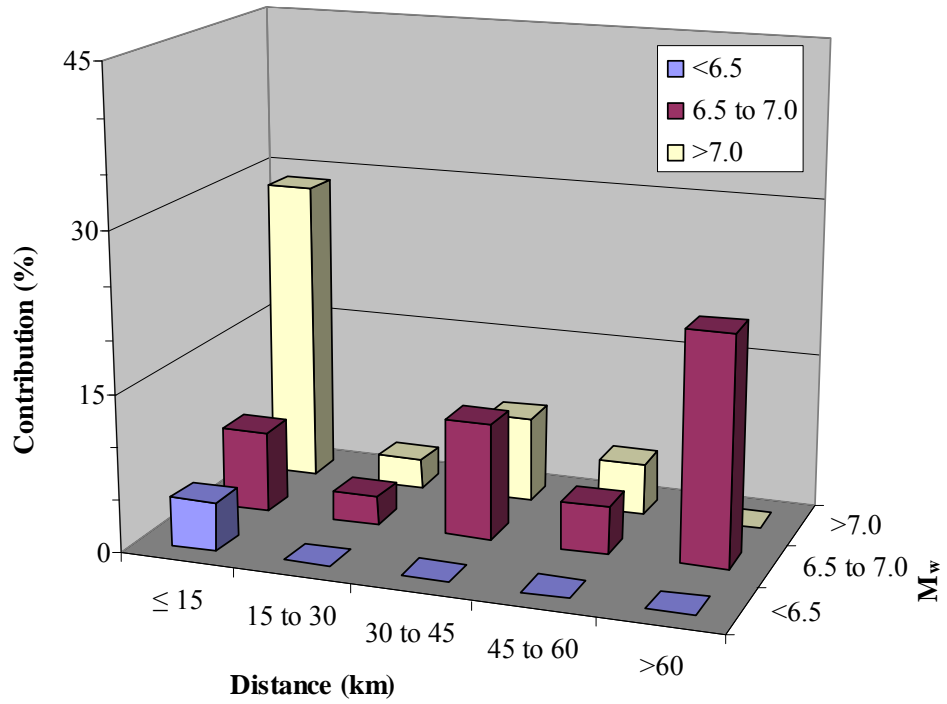Figure B.5.   Risk Deaggregations for Harbor Water District

Table B.10. Summary of Scenario Contributions to 50-year Recurrence Risks in Harbor Water District

| Scenario ID | Scenario Name | $M_w$ | Distance (km) | Annual Occurrence Frequency | Contribution (%) |
|---|---|---|---|---|---|
| 22 | San Andreas Fault - 1857 | 7.8 | 76 | 4.49E-03 | 22.43 |
| 21 | San Andreas Fault-All southern segments | 8.1 | 76 | 1.20E-03 | 6.00 |
| 444 | Palos Verdes | 7.3 | 7 | 9.81E-04 | 4.91 |
| 167 | Sierra Madre | 6.7 | 44 | 8.80E-04 | 4.40 |
| 159 | Newport-Inglewood | 7.1 | 4 | 8.10E-04 | 4.05 |
| 397 | Puente Hills blind thrust | 7.1 | 17 | 8.06E-04 | 4.03 |
| 141 | Newport-Inglewood offshore | 7.1 | 44 | 6.81E-04 | 3.41 |
| 23 | San Andreas Fault - Southern 2 segments | 7.7 | 87 | 6.73E-04 | 3.37 |
| 562 | Background Source | 7 | 19 | 6.10E-04 | 3.05 |
| 370 | Northridge | 7 | 49 | 5.73E-04 | 2.87 |
| 453 | Palos Verdes | 6.3 | 8 | 5.53E-04 | 2.77 |
| 560 | Background Source | 7 | 25 | 5.16E-04 | 2.58 |
| 175 | Verdugo | 6.9 | 34 | 5.15E-04 | 2.57 |
| 446 | Palos Verdes | 6.8 | 9 | 4.92E-04 | 2.46 |
| 559 | Background Source | 7 | 32 | 4.88E-04 | 2.44 |
| 12 | Elsinore - Whittier | 6.8 | 28 | 4.80E-04 | 2.40 |
| 195 | San Cayetano | 7 | 79 | 4.58E-04 | 2.29 |
| 219 | Anacapa-Dume | 7.5 | 40 | 4.37E-04 | 2.18 |
| 160 | Newport-Inglewood | 6.6 | 22 | 3.16E-04 | 1.58 |
| 19 | San Andreas Fault - Carrizo | 7.4 | 96 | 3.04E-04 | 1.52 |
| 166 | Sierra Madre | 7.2 | 41 | 2.98E-04 | 1.49 |
| 454 | Palos Verdes | 6.3 | 17 | 2.89E-04 | 1.44 |
| 189 | Oak Ridge-onshore | 7 | 73 | 2.75E-04 | 1.38 |
| 161 | Newport-Inglewood | 6.6 | 4 | 2.23E-04 | 1.12 |
| 451 | Palos Verdes | 6.3 | 16 | 2.18E-04 | 1.09 |
| 169 | San Gabriel | 7.2 | 52 | 2.04E-04 | 1.02 |
| 198 | Santa Susana | 6.7 | 55 | 2.01E-04 | 1.00 |
| 120 | Raymond | 6.5 | 31 | 1.98E-04 | 0.99 |
| 452 | Palos Verdes | 6.3 | 7 | 1.92E-04 | 0.96 |
| 174 | Santa Monica | 6.6 | 26 | 1.74E-04 | 0.87 |
| 561 | Background Source | 7 | 42 | 1.72E-04 | 0.86 |

Note: the table is based on the simulations with a 24-hour period of running tanks and the SSI corresponding to 50-year recurrence risks is 0.53.

Table B.10.  (Continued)

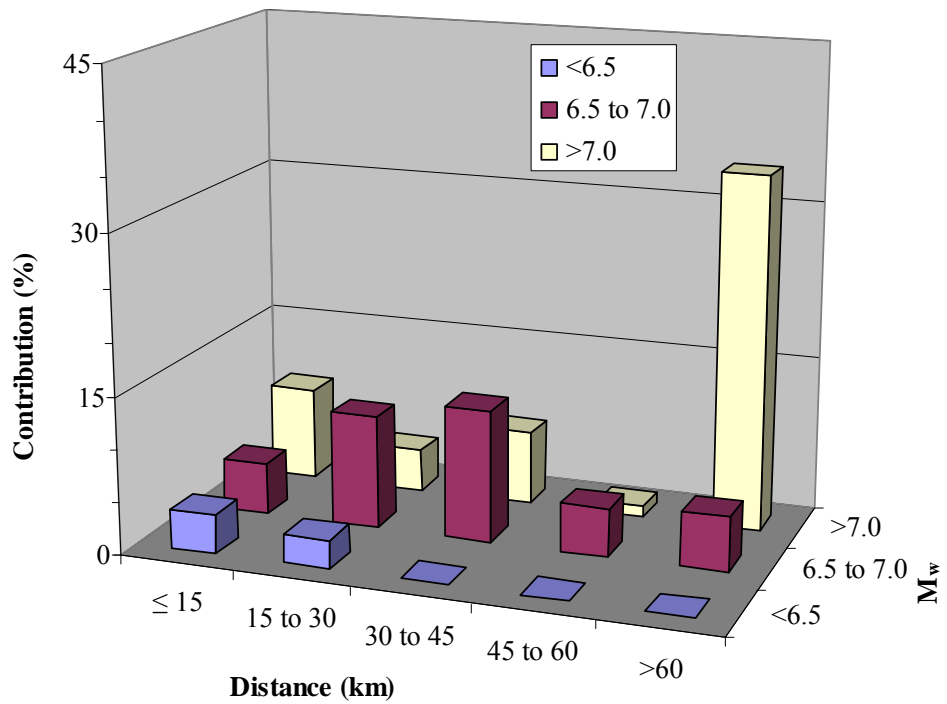| Scenario ID | Scenario Name | $M_w$ | Distance (km) | Annual Occurrence Frequency | Contribution (%) |
|---|---|---|---|---|---|
| 202 | Simi-Santa Rosa | 7 | 63 | 1.69E-04 | 0.85 |
| 447 | Palos Verdes | 6.8 | 7 | 1.66E-04 | 0.83 |
| 122 | Clamshell-Sawpit | 6.5 | 45 | 1.42E-04 | 0.71 |
| 443 | Sierra Madre-San Fernando | 6.7 | 47 | 1.25E-04 | 0.63 |
| 378 | Channel Island Thrust | 7.5 | 92 | 1.02E-04 | 0.51 |
| 162 | Newport-Inglewood | 6.6 | 4 | 1.00E-04 | 0.50 |
| 171 | San Gabriel | 6.7 | 64 | 8.47E-05 | 0.42 |
| 220 | Anacapa-Dume | 7 | 40 | 7.60E-05 | 0.38 |
| 221 | Anacapa-Dume | 7 | 73 | 6.29E-05 | 0.31 |
| 399 | Puente Hills blind thrust | 6.6 | 17 | 6.02E-05 | 0.30 |
| 168 | Sierra Madre | 6.7 | 41 | 4.43E-05 | 0.22 |
| 388 | Upper Elysian Park | 6.4 | 24 | 2.04E-05 | 0.10 |
| 170 | San Gabriel | 6.7 | 52 | 1.33E-05 | 0.07 |
| 372 | Northridge | 6.5 | 49 | 6.32E-06 | 0.03 |
| 398 | Puente Hills blind thrust | 6.6 | 20 | 2.08E-06 | 0.01 |
| 119 | Hollywood | 6.4 | 29 | 1.77E-06 | 0.01 |
| 176 | Verdugo | 6.4 | 34 | 1.05E-06 | 0.01 |
| 173 | Malibu Coast | 6.7 | 31 | 7.20E-07 | 0.00 |
| 177 | Verdugo | 6.4 | 37 | 5.68E-07 | 0.00 |
| 222 | Anacapa-Dume | 6.5 | 40 | 1.73E-07 | 0.00 |

Note: the table is based on the simulations with a 24-hour period of running tanks and the SSI corresponding to 50-year recurrence risks is 0.53.


1857 and San Andreas-All Southern Segments scenario earthquakes have relatively significant contributions, i.e., > 5%, to the system risk. Figure B.5b shows the district risk deaggregation according to $M_w$ and distance. Significant contributions from scenario earthquakes with relative large distances from originating faults to the water district centroid are observed, particularly those associated with the San Andreas fault, which are about 76 km from the centroid.

Comparisons between Tables B.9 and B.10 show that the number of scenario earthquakes that have contributions to the water district risk increases significantly as the recurrence interval for the risk decreases from 475 years to 50 years. Although it is not as obvious as that for the West Valley, East Valley, and Western Water Districts, comparisons between Figure B.5a and b show that, as the recurrence interval decreases, or SSI increases, the contributions increase from scenario earthquakes with relatively large distances from originating faults to the water district.

# MCEER Technical Reports

MCEER publishes technical reports on a variety of subjects written by authors funded through MCEER. These reports are available from both MCEER Publications and the National Technical Information Service (NTIS). Requests for reports should be directed to MCEER Publications, MCEER, University at Buffalo, State University of New York, Red Jacket Quadrangle, Buffalo, New York 14261. Reports can also be requested through NTIS, 5285 Port Royal Road, Springfield, Virginia 22161. NTIS accession numbers are shown in parenthesis, if available.

NCEER-87-0001 "First-Year Program in Research, Education and Technology Transfer," 3/5/87, (PB88-134275, A04, MF-A01).

NCEER-87-0002 "Experimental Evaluation of Instantaneous Optimal Algorithms for Structural Control," by R.C. Lin, T.T. Soong and A.M. Reinhorn, 4/20/87, (PB88-134341, A04, MF-A01).

NCEER-87-0003 "Experimentation Using the Earthquake Simulation Facilities at University at Buffalo," by A.M. Reinhorn and R.L. Ketter, to be published.

NCEER-87-0004 "The System Characteristics and Performance of a Shaking Table," by J.S. Hwang, K.C. Chang and G.C. Lee, 6/1/87, (PB88-134259, A03, MF-A01). This report is available only through NTIS (see address given above).

NCEER-87-0005 "A Finite Element Formulation for Nonlinear Viscoplastic Material Using a Q Model," by O. Gyebi and G. Dasgupta, 11/2/87, (PB88-213764, A08, MF-A01).

NCEER-87-0006 "Symbolic Manipulation Program (SMP) - Algebraic Codes for Two and Three Dimensional Finite Element Formulations," by X. Lee and G. Dasgupta, 11/9/87, (PB88-218522, A05, MF-A01).

NCEER-87-0007 "Instantaneous Optimal Control Laws for Tall Buildings Under Seismic Excitations," by J.N. Yang, A. Akbarpour and P. Ghaemmaghami, 6/10/87, (PB88-134333, A06, MF-A01). This report is only available through NTIS (see address given above).

NCEER-87-0008 "IDARC: Inelastic Damage Analysis of Reinforced Concrete Frame - Shear-Wall Structures," by Y.J. Park, A.M. Reinhorn and S.K. Kunnath, 7/20/87, (PB88-134325, A09, MF-A01). This report is only available through NTIS (see address given above).

NCEER-87-0009 "Liquefaction Potential for New York State: A Preliminary Report on Sites in Manhattan and Buffalo," by M. Budhu, V. Vijayakumar, R.F. Giese and L. Baumgras, 8/31/87, (PB88-163704, A03, MF-A01). This report is available only through NTIS (see address given above).

NCEER-87-0010 "Vertical and Torsional Vibration of Foundations in Inhomogeneous Media," by A.S. Veletsos and K.W. Dotson, 6/1/87, (PB88-134291, A03, MF-A01). This report is only available through NTIS (see address given above).

NCEER-87-0011 "Seismic Probabilistic Risk Assessment and Seismic Margins Studies for Nuclear Power Plants," by Howard H.M. Hwang, 6/15/87, (PB88-134267, A03, MF-A01). This report is only available through NTIS (see address given above).

NCEER-87-0012 "Parametric Studies of Frequency Response of Secondary Systems Under Ground-Acceleration Excitations," by Y. Yong and Y.K. Lin, 6/10/87, (PB88-134309, A03, MF-A01). This report is only available through NTIS (see address given above).

NCEER-87-0013 "Frequency Response of Secondary Systems Under Seismic Excitation," by J.A. HoLung, J. Cai and Y.K. Lin, 7/31/87, (PB88-134317, A05, MF-A01). This report is only available through NTIS (see address given above).

NCEER-87-0014 "Modelling Earthquake Ground Motions in Seismically Active Regions Using Parametric Time Series Methods," by G.W. Ellis and A.S. Cakmak, 8/25/87, (PB88-134283, A08, MF-A01). This report is only available through NTIS (see address given above).

NCEER-87-0015 "Detection and Assessment of Seismic Structural Damage," by E. DiPasquale and A.S. Cakmak, 8/25/87, (PB88-163712, A05, MF-A01). This report is only available through NTIS (see address given above).

NCEER-87-0016    "Pipeline Experiment at Parkfield, California," by J. Isenberg and E. Richardson, 9/15/87, (PB88-163720, A03, MF-A01). This report is available only through NTIS (see address given above).

NCEER-87-0017    "Digital Simulation of Seismic Ground Motion," by M. Shinozuka, G. Deodatis and T. Harada, 8/31/87, (PB88-155197, A04, MF-A01). This report is available only through NTIS (see address given above).

NCEER-87-0018    "Practical Considerations for Structural Control: System Uncertainty, System Time Delay and Truncation of Small Control Forces," J.N. Yang and A. Akbarpour, 8/10/87, (PB88-163738, A08, MF-A01). This report is only available through NTIS (see address given above).

NCEER-87-0019    "Modal Analysis of Nonclassically Damped Structural Systems Using Canonical Transformation," by J.N. Yang, S. Sarkani and F.X. Long, 9/27/87, (PB88-187851, A04, MF-A01).

NCEER-87-0020    "A Nonstationary Solution in Random Vibration Theory," by J.R. Red-Horse and P.D. Spanos, 11/3/87, (PB88-163746, A03, MF-A01).

NCEER-87-0021    "Horizontal Impedances for Radially Inhomogeneous Viscoelastic Soil Layers," by A.S. Veletsos and K.W. Dotson, 10/15/87, (PB88-150859, A04, MF-A01).

NCEER-87-0022    "Seismic Damage Assessment of Reinforced Concrete Members," by Y.S. Chung, C. Meyer and M. Shinozuka, 10/9/87, (PB88-150867, A05, MF-A01). This report is available only through NTIS (see address given above).

NCEER-87-0023    "Active Structural Control in Civil Engineering," by T.T. Soong, 11/11/87, (PB88-187778, A03, MF-A01).

NCEER-87-0024    "Vertical and Torsional Impedances for Radially Inhomogeneous Viscoelastic Soil Layers," by K.W. Dotson and A.S. Veletsos, 12/87, (PB88-187786, A03, MF-A01).

NCEER-87-0025    "Proceedings from the Symposium on Seismic Hazards, Ground Motions, Soil-Liquefaction and Engineering Practice in Eastern North America," October 20-22, 1987, edited by K.H. Jacob, 12/87, (PB88-188115, A23, MF-A01). This report is available only through NTIS (see address given above).

NCEER-87-0026    "Report on the Whittier-Narrows, California, Earthquake of October 1, 1987," by J. Pantelic and A. Reinhorn, 11/87, (PB88-187752, A03, MF-A01). This report is available only through NTIS (see address given above).

NCEER-87-0027    "Design of a Modular Program for Transient Nonlinear Analysis of Large 3-D Building Structures," by S. Srivastav and J.F. Abel, 12/30/87, (PB88-187950, A05, MF-A01). This report is only available through NTIS (see address given above).

NCEER-87-0028    "Second-Year Program in Research, Education and Technology Transfer," 3/8/88, (PB88-219480, A04, MF-A01).

NCEER-88-0001    "Workshop on Seismic Computer Analysis and Design of Buildings With Interactive Graphics," by W. McGuire, J.F. Abel and C.H. Conley, 1/18/88, (PB88-187760, A03, MF-A01). This report is only available through NTIS (see address given above).

NCEER-88-0002    "Optimal Control of Nonlinear Flexible Structures," by J.N. Yang, F.X. Long and D. Wong, 1/22/88, (PB88-213772, A06, MF-A01).

NCEER-88-0003    "Substructuring Techniques in the Time Domain for Primary-Secondary Structural Systems," by G.D. Manolis and G. Juhn, 2/10/88, (PB88-213780, A04, MF-A01).

NCEER-88-0004    "Iterative Seismic Analysis of Primary-Secondary Systems," by A. Singhal, L.D. Lutes and P.D. Spanos, 2/23/88, (PB88-213798, A04, MF-A01).

NCEER-88-0005    "Stochastic Finite Element Expansion for Random Media," by P.D. Spanos and R. Ghanem, 3/14/88, (PB88-213806, A03, MF-A01).

NCEER-88-0006    "Combining Structural Optimization and Structural Control," by F.Y. Cheng and C.P. Pantelides, 1/10/88, (PB88-213814, A05, MF-A01).

NCEER-88-0007    "Seismic Performance Assessment of Code-Designed Structures," by H.H-M. Hwang, J-W. Jaw and H-J. Shau, 3/20/88, (PB88-219423, A04, MF-A01). This report is only available through NTIS (see address given above).

NCEER-88-0008    "Reliability Analysis of Code-Designed Structures Under Natural Hazards," by H.H-M. Hwang, H. Ushiba and M. Shinozuka, 2/29/88, (PB88-229471, A07, MF-A01). This report is only available through NTIS (see address given above).

NCEER-88-0009    "Seismic Fragility Analysis of Shear Wall Structures," by J-W Jaw and H.H-M. Hwang, 4/30/88, (PB89-102867, A04, MF-A01).

NCEER-88-0010    "Base Isolation of a Multi-Story Building Under a Harmonic Ground Motion - A Comparison of Performances of Various Systems," by F-G Fan, G. Ahmadi and I.G. Tadjbakhsh, 5/18/88, (PB89-122238, A06, MF-A01). This report is only available through NTIS (see address given above).

NCEER-88-0011    "Seismic Floor Response Spectra for a Combined System by Green's Functions," by F.M. Lavelle, L.A. Bergman and P.D. Spanos, 5/1/88, (PB89-102875, A03, MF-A01).

NCEER-88-0012    "A New Solution Technique for Randomly Excited Hysteretic Structures," by G.Q. Cai and Y.K. Lin, 5/16/88, (PB89-102883, A03, MF-A01).

NCEER-88-0013    "A Study of Radiation Damping and Soil-Structure Interaction Effects in the Centrifuge," by K. Weissman, supervised by J.H. Prevost, 5/24/88, (PB89-144703, A06, MF-A01).

NCEER-88-0014    "Parameter Identification and Implementation of a Kinematic Plasticity Model for Frictional Soils," by J.H. Prevost and D.V. Griffiths, to be published.

NCEER-88-0015    "Two- and Three- Dimensional Dynamic Finite Element Analyses of the Long Valley Dam," by D.V. Griffiths and J.H. Prevost, 6/17/88, (PB89-144711, A04, MF-A01).

NCEER-88-0016    "Damage Assessment of Reinforced Concrete Structures in Eastern United States," by A.M. Reinhorn, M.J. Seidel, S.K. Kunnath and Y.J. Park, 6/15/88, (PB89-122220, A04, MF-A01). This report is only available through NTIS (see address given above).

NCEER-88-0017    "Dynamic Compliance of Vertically Loaded Strip Foundations in Multilayered Viscoelastic Soils," by S. Ahmad and A.S.M. Israil, 6/17/88, (PB89-102891, A04, MF-A01).

NCEER-88-0018    "An Experimental Study of Seismic Structural Response With Added Viscoelastic Dampers," by R.C. Lin, Z. Liang, T.T. Soong and R.H. Zhang, 6/30/88, (PB89-122212, A05, MF-A01).  This report is available only through NTIS (see address given above).

NCEER-88-0019    "Experimental Investigation of Primary - Secondary System Interaction," by G.D. Manolis, G. Juhn and A.M. Reinhorn, 5/27/88, (PB89-122204, A04, MF-A01).

NCEER-88-0020    "A Response Spectrum Approach For Analysis of Nonclassically Damped Structures," by J.N. Yang, S. Sarkani and F.X. Long, 4/22/88, (PB89-102909, A04, MF-A01).

NCEER-88-0021    "Seismic Interaction of Structures and Soils: Stochastic Approach," by A.S. Veletsos and A.M. Prasad, 7/21/88, (PB89-122196, A04, MF-A01). This report is only available through NTIS (see address given above).

NCEER-88-0022    "Identification of the Serviceability Limit State and Detection of Seismic Structural Damage," by E. DiPasquale and A.S. Cakmak, 6/15/88, (PB89-122188, A05, MF-A01).  This report is available only through NTIS (see address given above).

NCEER-88-0023    "Multi-Hazard Risk Analysis: Case of a Simple Offshore Structure," by B.K. Bhartia and E.H. Vanmarcke, 7/21/88, (PB89-145213, A05, MF-A01).

NCEER-88-0024    "Automated Seismic Design of Reinforced Concrete Buildings," by Y.S. Chung, C. Meyer and M. Shinozuka, 7/5/88, (PB89-122170, A06, MF-A01). This report is available only through NTIS (see address given above).

NCEER-88-0025    "Experimental Study of Active Control of MDOF Structures Under Seismic Excitations," by L.L. Chung, R.C. Lin, T.T. Soong and A.M. Reinhorn, 7/10/88, (PB89-122600, A04, MF-A01).

NCEER-88-0026    "Earthquake Simulation Tests of a Low-Rise Metal Structure," by J.S. Hwang, K.C. Chang, G.C. Lee and R.L. Ketter, 8/1/88, (PB89-102917, A04, MF-A01).

NCEER-88-0027    "Systems Study of Urban Response and Reconstruction Due to Catastrophic Earthquakes," by F. Kozin and H.K. Zhou, 9/22/88, (PB90-162348, A04, MF-A01).

NCEER-88-0028    "Seismic Fragility Analysis of Plane Frame Structures," by H.H-M. Hwang and Y.K. Low, 7/31/88, (PB89-131445, A06, MF-A01).

NCEER-88-0029    "Response Analysis of Stochastic Structures," by A. Kardara, C. Bucher and M. Shinozuka, 9/22/88, (PB89-174429, A04, MF-A01).

NCEER-88-0030    "Nonnormal Accelerations Due to Yielding in a Primary Structure," by D.C.K. Chen and L.D. Lutes, 9/19/88, (PB89-131437, A04, MF-A01).

NCEER-88-0031    "Design Approaches for Soil-Structure Interaction," by A.S. Veletsos, A.M. Prasad and Y. Tang, 12/30/88, (PB89-174437, A03, MF-A01). This report is available only through NTIS (see address given above).

NCEER-88-0032    "A Re-evaluation of Design Spectra for Seismic Damage Control," by C.J. Turkstra and A.G. Tallin, 11/7/88, (PB89-145221, A05, MF-A01).

NCEER-88-0033    "The Behavior and Design of Noncontact Lap Splices Subjected to Repeated Inelastic Tensile Loading," by V.E. Sagan, P. Gergely and R.N. White, 12/8/88, (PB89-163737, A08, MF-A01).

NCEER-88-0034    "Seismic Response of Pile Foundations," by S.M. Mamoon, P.K. Banerjee and S. Ahmad, 11/1/88, (PB89-145239, A04, MF-A01).

NCEER-88-0035    "Modeling of R/C Building Structures With Flexible Floor Diaphragms (IDARC2)," by A.M. Reinhorn, S.K. Kunnath and N. Panahshahi, 9/7/88, (PB89-207153, A07, MF-A01).

NCEER-88-0036    "Solution of the Dam-Reservoir Interaction Problem Using a Combination of FEM, BEM with Particular Integrals, Modal Analysis, and Substructuring," by C-S. Tsai, G.C. Lee and R.L. Ketter, 12/31/88, (PB89-207146, A04, MF-A01).

NCEER-88-0037    "Optimal Placement of Actuators for Structural Control," by F.Y. Cheng and C.P. Pantelides, 8/15/88, (PB89-162846, A05, MF-A01).

NCEER-88-0038    "Teflon Bearings in Aseismic Base Isolation: Experimental Studies and Mathematical Modeling," by A. Mokha, M.C. Constantinou and A.M. Reinhorn, 12/5/88, (PB89-218457, A10, MF-A01). This report is available only through NTIS (see address given above).

NCEER-88-0039    "Seismic Behavior of Flat Slab High-Rise Buildings in the New York City Area," by P. Weidlinger and M. Ettouney, 10/15/88, (PB90-145681, A04, MF-A01).

NCEER-88-0040    "Evaluation of the Earthquake Resistance of Existing Buildings in New York City," by P. Weidlinger and M. Ettouney, 10/15/88, to be published.

NCEER-88-0041    "Small-Scale Modeling Techniques for Reinforced Concrete Structures Subjected to Seismic Loads," by W. Kim, A. El-Attar and R.N. White, 11/22/88, (PB89-189625, A05, MF-A01).

NCEER-88-0042    "Modeling Strong Ground Motion from Multiple Event Earthquakes," by G.W. Ellis and A.S. Cakmak, 10/15/88, (PB89-174445, A03, MF-A01).

NCEER-88-0043    "Nonstationary Models of Seismic Ground Acceleration," by M. Grigoriu, S.E. Ruiz and E. Rosenblueth, 7/15/88, (PB89-189617, A04, MF-A01).

NCEER-88-0044    "SARCF User's Guide: Seismic Analysis of Reinforced Concrete Frames," by Y.S. Chung, C. Meyer and M. Shinozuka, 11/9/88, (PB89-174452, A08, MF-A01).

NCEER-88-0045    "First Expert Panel Meeting on Disaster Research and Planning," edited by J. Pantelic and J. Stoyle, 9/15/88, (PB89-174460, A05, MF-A01).

NCEER-88-0046    "Preliminary Studies of the Effect of Degrading Infill Walls on the Nonlinear Seismic Response of Steel Frames," by C.Z. Chrysostomou, P. Gergely and J.F. Abel, 12/19/88, (PB89-208383, A05, MF-A01).

NCEER-88-0047    "Reinforced Concrete Frame Component Testing Facility - Design, Construction, Instrumentation and Operation," by S.P. Pessiki, C. Conley, T. Bond, P. Gergely and R.N. White, 12/16/88, (PB89-174478, A04, MF-A01).

NCEER-89-0001    "Effects of Protective Cushion and Soil Compliancy on the Response of Equipment Within a Seismically Excited Building," by J.A. HoLung, 2/16/89, (PB89-207179, A04, MF-A01).

NCEER-89-0002    "Statistical Evaluation of Response Modification Factors for Reinforced Concrete Structures," by H.H-M. Hwang and J-W. Jaw, 2/17/89, (PB89-207187, A05, MF-A01).

NCEER-89-0003    "Hysteretic Columns Under Random Excitation," by G-Q. Cai and Y.K. Lin, 1/9/89, (PB89-196513, A03, MF-A01).

NCEER-89-0004    "Experimental Study of `Elephant Foot Bulge' Instability of Thin-Walled Metal Tanks," by Z-H. Jia and R.L. Ketter, 2/22/89, (PB89-207195, A03, MF-A01).

NCEER-89-0005    "Experiment on Performance of Buried Pipelines Across San Andreas Fault," by J. Isenberg, E. Richardson and T.D. O'Rourke, 3/10/89, (PB89-218440, A04, MF-A01). This report is available only through NTIS (see address given above).

NCEER-89-0006    "A Knowledge-Based Approach to Structural Design of Earthquake-Resistant Buildings," by M. Subramani, P. Gergely, C.H. Conley, J.F. Abel and A.H. Zaghw, 1/15/89, (PB89-218465, A06, MF-A01).

NCEER-89-0007    "Liquefaction Hazards and Their Effects on Buried Pipelines," by T.D. O'Rourke and P.A. Lane, 2/1/89, (PB89-218481, A09, MF-A01).

NCEER-89-0008    "Fundamentals of System Identification in Structural Dynamics," by H. Imai, C-B. Yun, O. Maruyama and M. Shinozuka, 1/26/89, (PB89-207211, A04, MF-A01).

NCEER-89-0009    "Effects of the 1985 Michoacan Earthquake on Water Systems and Other Buried Lifelines in Mexico," by A.G. Ayala and M.J. O'Rourke, 3/8/89, (PB89-207229, A06, MF-A01).

NCEER-89-R010    "NCEER Bibliography of Earthquake Education Materials," by K.E.K. Ross, Second Revision, 9/1/89, (PB90-125352, A05, MF-A01). This report is replaced by NCEER-92-0018.

NCEER-89-0011    "Inelastic Three-Dimensional Response Analysis of Reinforced Concrete Building Structures (IDARC-3D), Part I - Modeling," by S.K. Kunnath and A.M. Reinhorn, 4/17/89, (PB90-114612, A07, MF-A01). This report is available only through NTIS (see address given above).

NCEER-89-0012    "Recommended Modifications to ATC-14," by C.D. Poland and J.O. Malley, 4/12/89, (PB90-108648, A15, MF-A01).

NCEER-89-0013    "Repair and Strengthening of Beam-to-Column Connections Subjected to Earthquake Loading," by M. Corazao and A.J. Durrani, 2/28/89, (PB90-109885, A06, MF-A01).

NCEER-89-0014    "Program EXKAL2 for Identification of Structural Dynamic Systems," by O. Maruyama, C-B. Yun, M. Hoshiya and M. Shinozuka, 5/19/89, (PB90-109877, A09, MF-A01).

NCEER-89-0015    "Response of Frames With Bolted Semi-Rigid Connections, Part I - Experimental Study and Analytical Predictions," by P.J. DiCorso, A.M. Reinhorn, J.R. Dickerson, J.B. Radziminski and W.L. Harper, 6/1/89, to be published.

NCEER-89-0016    "ARMA Monte Carlo Simulation in Probabilistic Structural Analysis," by P.D. Spanos and M.P. Mignolet, 7/10/89, (PB90-109893, A03, MF-A01).

NCEER-89-P017    "Preliminary Proceedings from the Conference on Disaster Preparedness - The Place of Earthquake Education in Our Schools," Edited by K.E.K. Ross, 6/23/89, (PB90-108606, A03, MF-A01).

NCEER-89-0017    "Proceedings from the Conference on Disaster Preparedness - The Place of Earthquake Education in Our Schools," Edited by K.E.K. Ross, 12/31/89, (PB90-207895, A012, MF-A02). This report is available only through NTIS (see address given above).

NCEER-89-0018    "Multidimensional Models of Hysteretic Material Behavior for Vibration Analysis of Shape Memory Energy Absorbing Devices, by E.J. Graesser and F.A. Cozzarelli, 6/7/89, (PB90-164146, A04, MF-A01).

NCEER-89-0019    "Nonlinear Dynamic Analysis of Three-Dimensional Base Isolated Structures (3D-BASIS)," by S. Nagarajaiah, A.M. Reinhorn and M.C. Constantinou, 8/3/89, (PB90-161936, A06, MF-A01). This report has been replaced by NCEER-93-0011.

NCEER-89-0020    "Structural Control Considering Time-Rate of Control Forces and Control Rate Constraints," by F.Y. Cheng and C.P. Pantelides, 8/3/89, (PB90-120445, A04, MF-A01).

NCEER-89-0021    "Subsurface Conditions of Memphis and Shelby County," by K.W. Ng, T-S. Chang and H-H.M. Hwang, 7/26/89, (PB90-120437, A03, MF-A01).

NCEER-89-0022    "Seismic Wave Propagation Effects on Straight Jointed Buried Pipelines," by K. Elhmadi and M.J. O'Rourke, 8/24/89, (PB90-162322, A10, MF-A02).

NCEER-89-0023    "Workshop on Serviceability Analysis of Water Delivery Systems," edited by M. Grigoriu, 3/6/89, (PB90-127424, A03, MF-A01).

NCEER-89-0024    "Shaking Table Study of a 1/5 Scale Steel Frame Composed of Tapered Members," by K.C. Chang, J.S. Hwang and G.C. Lee, 9/18/89, (PB90-160169, A04, MF-A01).

NCEER-89-0025    "DYNA1D: A Computer Program for Nonlinear Seismic Site Response Analysis - Technical Documentation," by Jean H. Prevost, 9/14/89, (PB90-161944, A07, MF-A01). This report is available only through NTIS (see address given above).

NCEER-89-0026    "1:4 Scale Model Studies of Active Tendon Systems and Active Mass Dampers for Aseismic Protection," by A.M. Reinhorn, T.T. Soong, R.C. Lin, Y.P. Yang, Y. Fukao, H. Abe and M. Nakai, 9/15/89, (PB90-173246, A10, MF-A02). This report is available only through NTIS (see address given above).

NCEER-89-0027    "Scattering of Waves by Inclusions in a Nonhomogeneous Elastic Half Space Solved by Boundary Element Methods," by P.K. Hadley, A. Askar and A.S. Cakmak, 6/15/89, (PB90-145699, A07, MF-A01).

NCEER-89-0028    "Statistical Evaluation of Deflection Amplification Factors for Reinforced Concrete Structures," by H.H.M. Hwang, J-W. Jaw and A.L. Ch'ng, 8/31/89, (PB90-164633, A05, MF-A01).

NCEER-89-0029    "Bedrock Accelerations in Memphis Area Due to Large New Madrid Earthquakes," by H.H.M. Hwang, C.H.S. Chen and G. Yu, 11/7/89, (PB90-162330, A04, MF-A01).

NCEER-89-0030    "Seismic Behavior and Response Sensitivity of Secondary Structural Systems," by Y.Q. Chen and T.T. Soong, 10/23/89, (PB90-164658, A08, MF-A01).

NCEER-89-0031    "Random Vibration and Reliability Analysis of Primary-Secondary Structural Systems," by Y. Ibrahim, M. Grigoriu and T.T. Soong, 11/10/89, (PB90-161951, A04, MF-A01).

NCEER-89-0032    "Proceedings from the Second U.S. - Japan Workshop on Liquefaction, Large Ground Deformation and Their Effects on Lifelines, September 26-29, 1989," Edited by T.D. O'Rourke and M. Hamada, 12/1/89, (PB90-209388, A22, MF-A03).

NCEER-89-0033    "Deterministic Model for Seismic Damage Evaluation of Reinforced Concrete Structures," by J.M. Bracci, A.M. Reinhorn, J.B. Mander and S.K. Kunnath, 9/27/89, (PB91-108803, A06, MF-A01).

NCEER-89-0034    "On the Relation Between Local and Global Damage Indices," by E. DiPasquale and A.S. Cakmak, 8/15/89, (PB90-173865, A05, MF-A01).

NCEER-89-0035    "Cyclic Undrained Behavior of Nonplastic and Low Plasticity Silts," by A.J. Walker and H.E. Stewart, 7/26/89, (PB90-183518, A10, MF-A01).

NCEER-89-0036    "Liquefaction Potential of Surficial Deposits in the City of Buffalo, New York," by M. Budhu, R. Giese and L. Baumgrass, 1/17/89, (PB90-208455, A04, MF-A01).

NCEER-89-0037    "A Deterministic Assessment of Effects of Ground Motion Incoherence," by A.S. Veletsos and Y. Tang, 7/15/89, (PB90-164294, A03, MF-A01).

NCEER-89-0038    "Workshop on Ground Motion Parameters for Seismic Hazard Mapping," July 17-18, 1989, edited by R.V. Whitman, 12/1/89, (PB90-173923, A04, MF-A01).

NCEER-89-0039    "Seismic Effects on Elevated Transit Lines of the New York City Transit Authority," by C.J. Costantino, C.A. Miller and E. Heymsfield, 12/26/89, (PB90-207887, A06, MF-A01).

NCEER-89-0040    "Centrifugal Modeling of Dynamic Soil-Structure Interaction," by K. Weissman, Supervised by J.H. Prevost, 5/10/89, (PB90-207879, A07, MF-A01).

NCEER-89-0041    "Linearized Identification of Buildings With Cores for Seismic Vulnerability Assessment," by I-K. Ho and A.E. Aktan, 11/1/89, (PB90-251943, A07, MF-A01).

NCEER-90-0001    "Geotechnical and Lifeline Aspects of the October 17, 1989 Loma Prieta Earthquake in San Francisco," by T.D. O'Rourke, H.E. Stewart, F.T. Blackburn and T.S. Dickerman, 1/90, (PB90-208596, A05, MF-A01).

NCEER-90-0002    "Nonnormal Secondary Response Due to Yielding in a Primary Structure," by D.C.K. Chen and L.D. Lutes, 2/28/90, (PB90-251976, A07, MF-A01).

NCEER-90-0003    "Earthquake Education Materials for Grades K-12," by K.E.K. Ross, 4/16/90, (PB91-251984, A05, MF-A05). This report has been replaced by NCEER-92-0018.

NCEER-90-0004    "Catalog of Strong Motion Stations in Eastern North America," by R.W. Busby, 4/3/90, (PB90-251984, A05, MF-A01).

NCEER-90-0005    "NCEER Strong-Motion Data Base: A User Manual for the GeoBase Release (Version 1.0 for the Sun3)," by P. Friberg and K. Jacob, 3/31/90 (PB90-258062, A04, MF-A01).

NCEER-90-0006    "Seismic Hazard Along a Crude Oil Pipeline in the Event of an 1811-1812 Type New Madrid Earthquake," by H.H.M. Hwang and C-H.S. Chen, 4/16/90, (PB90-258054, A04, MF-A01).

NCEER-90-0007    "Site-Specific Response Spectra for Memphis Sheahan Pumping Station," by H.H.M. Hwang and C.S. Lee, 5/15/90, (PB91-108811, A05, MF-A01).

NCEER-90-0008    "Pilot Study on Seismic Vulnerability of Crude Oil Transmission Systems," by T. Ariman, R. Dobry, M. Grigoriu, F. Kozin, M. O'Rourke, T. O'Rourke and M. Shinozuka, 5/25/90, (PB91-108837, A06, MF-A01).

NCEER-90-0009    "A Program to Generate Site Dependent Time Histories: EQGEN," by G.W. Ellis, M. Srinivasan and A.S. Cakmak, 1/30/90, (PB91-108829, A04, MF-A01).

NCEER-90-0010    "Active Isolation for Seismic Protection of Operating Rooms," by M.E. Talbott, Supervised by M. Shinozuka, 6/8/9, (PB91-110205, A05, MF-A01).

NCEER-90-0011 "Program LINEARID for Identification of Linear Structural Dynamic Systems," by C-B. Yun and M. Shinozuka, 6/25/90, (PB91-110312, A08, MF-A01).

NCEER-90-0012 "Two-Dimensional Two-Phase Elasto-Plastic Seismic Response of Earth Dams," by A.N. Yiagos, Supervised by J.H. Prevost, 6/20/90, (PB91-110197, A13, MF-A02).

NCEER-90-0013 "Secondary Systems in Base-Isolated Structures: Experimental Investigation, Stochastic Response and Stochastic Sensitivity," by G.D. Manolis, G. Juhn, M.C. Constantinou and A.M. Reinhorn, 7/1/90, (PB91-110320, A08, MF-A01).

NCEER-90-0014 "Seismic Behavior of Lightly-Reinforced Concrete Column and Beam-Column Joint Details," by S.P. Pessiki, C.H. Conley, P. Gergely and R.N. White, 8/22/90, (PB91-108795, A11, MF-A02).

NCEER-90-0015 "Two Hybrid Control Systems for Building Structures Under Strong Earthquakes," by J.N. Yang and A. Danielians, 6/29/90, (PB91-125393, A04, MF-A01).

NCEER-90-0016 "Instantaneous Optimal Control with Acceleration and Velocity Feedback," by J.N. Yang and Z. Li, 6/29/90, (PB91-125401, A03, MF-A01).

NCEER-90-0017 "Reconnaissance Report on the Northern Iran Earthquake of June 21, 1990," by M. Mehrain, 10/4/90, (PB91-125377, A03, MF-A01).

NCEER-90-0018 "Evaluation of Liquefaction Potential in Memphis and Shelby County," by T.S. Chang, P.S. Tang, C.S. Lee and H. Hwang, 8/10/90, (PB91-125427, A09, MF-A01).

NCEER-90-0019 "Experimental and Analytical Study of a Combined Sliding Disc Bearing and Helical Steel Spring Isolation System," by M.C. Constantinou, A.S. Mokha and A.M. Reinhorn, 10/4/90, (PB91-125385, A06, MF-A01). This report is available only through NTIS (see address given above).

NCEER-90-0020 "Experimental Study and Analytical Prediction of Earthquake Response of a Sliding Isolation System with a Spherical Surface," by A.S. Mokha, M.C. Constantinou and A.M. Reinhorn, 10/11/90, (PB91-125419, A05, MF-A01).

NCEER-90-0021 "Dynamic Interaction Factors for Floating Pile Groups," by G. Gazetas, K. Fan, A. Kaynia and E. Kausel, 9/10/90, (PB91-170381, A05, MF-A01).

NCEER-90-0022 "Evaluation of Seismic Damage Indices for Reinforced Concrete Structures," by S. Rodriguez-Gomez and A.S. Cakmak, 9/30/90, PB91-171322, A06, MF-A01).

NCEER-90-0023 "Study of Site Response at a Selected Memphis Site," by H. Desai, S. Ahmad, E.S. Gazetas and M.R. Oh, 10/11/90, (PB91-196857, A03, MF-A01).

NCEER-90-0024 "A User's Guide to Strongmo: Version 1.0 of NCEER's Strong-Motion Data Access Tool for PCs and Terminals," by P.A. Friberg and C.A.T. Susch, 11/15/90, (PB91-171272, A03, MF-A01).

NCEER-90-0025 "A Three-Dimensional Analytical Study of Spatial Variability of Seismic Ground Motions," by L-L. Hong and A.H.-S. Ang, 10/30/90, (PB91-170399, A09, MF-A01).

NCEER-90-0026 "MUMOID User's Guide - A Program for the Identification of Modal Parameters," by S. Rodriguez-Gomez and E. DiPasquale, 9/30/90, (PB91-171298, A04, MF-A01).

NCEER-90-0027 "SARCF-II User's Guide - Seismic Analysis of Reinforced Concrete Frames," by S. Rodriguez-Gomez, Y.S. Chung and C. Meyer, 9/30/90, (PB91-171280, A05, MF-A01).

NCEER-90-0028 "Viscous Dampers: Testing, Modeling and Application in Vibration and Seismic Isolation," by N. Makris and M.C. Constantinou, 12/20/90 (PB91-190561, A06, MF-A01).

NCEER-90-0029 "Soil Effects on Earthquake Ground Motions in the Memphis Area," by H. Hwang, C.S. Lee, K.W. Ng and T.S. Chang, 8/2/90, (PB91-190751, A05, MF-A01).

NCEER-91-0001    "Proceedings from the Third Japan-U.S. Workshop on Earthquake Resistant Design of Lifeline Facilities and Countermeasures for Soil Liquefaction, December 17-19, 1990," edited by T.D. O'Rourke and M. Hamada, 2/1/91, (PB91-179259, A99, MF-A04).

NCEER-91-0002    "Physical Space Solutions of Non-Proportionally Damped Systems," by M. Tong, Z. Liang and G.C. Lee, 1/15/91, (PB91-179242, A04, MF-A01).

NCEER-91-0003    "Seismic Response of Single Piles and Pile Groups," by K. Fan and G. Gazetas, 1/10/91, (PB92-174994, A04, MF-A01).

NCEER-91-0004    "Damping of Structures: Part 1 - Theory of Complex Damping," by Z. Liang and G. Lee, 10/10/91, (PB92-197235, A12, MF-A03).

NCEER-91-0005    "3D-BASIS - Nonlinear Dynamic Analysis of Three Dimensional Base Isolated Structures: Part II," by S. Nagarajaiah, A.M. Reinhorn and M.C. Constantinou, 2/28/91, (PB91-190553, A07, MF-A01). This report has been replaced by NCEER-93-0011.

NCEER-91-0006    "A Multidimensional Hysteretic Model for Plasticity Deforming Metals in Energy Absorbing Devices," by E.J. Graesser and F.A. Cozzarelli, 4/9/91, (PB92-108364, A04, MF-A01).

NCEER-91-0007    "A Framework for Customizable Knowledge-Based Expert Systems with an Application to a KBES for Evaluating the Seismic Resistance of Existing Buildings," by E.G. Ibarra-Anaya and S.J. Fenves, 4/9/91, (PB91-210930, A08, MF-A01).

NCEER-91-0008    "Nonlinear Analysis of Steel Frames with Semi-Rigid Connections Using the Capacity Spectrum Method," by G.G. Deierlein, S-H. Hsieh, Y-J. Shen and J.F. Abel, 7/2/91, (PB92-113828, A05, MF-A01).

NCEER-91-0009    "Earthquake Education Materials for Grades K-12," by K.E.K. Ross, 4/30/91, (PB91-212142, A06, MF-A01). This report has been replaced by NCEER-92-0018.

NCEER-91-0010    "Phase Wave Velocities and Displacement Phase Differences in a Harmonically Oscillating Pile," by N. Makris and G. Gazetas, 7/8/91, (PB92-108356, A04, MF-A01).

NCEER-91-0011    "Dynamic Characteristics of a Full-Size Five-Story Steel Structure and a 2/5 Scale Model," by K.C. Chang, G.C. Yao, G.C. Lee, D.S. Hao and Y.C. Yeh," 7/2/91, (PB93-116648, A06, MF-A02).

NCEER-91-0012    "Seismic Response of a 2/5 Scale Steel Structure with Added Viscoelastic Dampers," by K.C. Chang, T.T. Soong, S-T. Oh and M.L. Lai, 5/17/91, (PB92-110816, A05, MF-A01).

NCEER-91-0013    "Earthquake Response of Retaining Walls; Full-Scale Testing and Computational Modeling," by S. Alampalli and A-W.M. Elgamal, 6/20/91, to be published.

NCEER-91-0014    "3D-BASIS-M: Nonlinear Dynamic Analysis of Multiple Building Base Isolated Structures," by P.C. Tsopelas, S. Nagarajaiah, M.C. Constantinou and A.M. Reinhorn, 5/28/91, (PB92-113885, A09, MF-A02).

NCEER-91-0015    "Evaluation of SEAOC Design Requirements for Sliding Isolated Structures," by D. Theodossiou and M.C. Constantinou, 6/10/91, (PB92-114602, A11, MF-A03).

NCEER-91-0016    "Closed-Loop Modal Testing of a 27-Story Reinforced Concrete Flat Plate-Core Building," by H.R. Somaprasad, T. Toksoy, H. Yoshiyuki and A.E. Aktan, 7/15/91, (PB92-129980, A07, MF-A02).

NCEER-91-0017    "Shake Table Test of a 1/6 Scale Two-Story Lightly Reinforced Concrete Building," by A.G. El-Attar, R.N. White and P. Gergely, 2/28/91, (PB92-222447, A06, MF-A02).

NCEER-91-0018    "Shake Table Test of a 1/8 Scale Three-Story Lightly Reinforced Concrete Building," by A.G. El-Attar, R.N. White and P. Gergely, 2/28/91, (PB93-116630, A08, MF-A02).

NCEER-91-0019    "Transfer Functions for Rigid Rectangular Foundations," by A.S. Veletsos, A.M. Prasad and W.H. Wu, 7/31/91, to be published.

NCEER-91-0020  "Hybrid Control of Seismic-Excited Nonlinear and Inelastic Structural Systems," by J.N. Yang, Z. Li and A. Danielians, 8/1/91, (PB92-143171, A06, MF-A02).

NCEER-91-0021  "The NCEER-91 Earthquake Catalog: Improved Intensity-Based Magnitudes and Recurrence Relations for U.S. Earthquakes  East of New Madrid," by L. Seeber and J.G. Armbruster, 8/28/91, (PB92-176742, A06, MF-A02).

NCEER-91-0022  "Proceedings from the Implementation of Earthquake Planning and Education in Schools: The Need for Change - The Roles of the Changemakers," by K.E.K. Ross and F. Winslow, 7/23/91, (PB92-129998, A12, MF-A03).

NCEER-91-0023  "A Study of Reliability-Based Criteria for Seismic Design of Reinforced Concrete Frame Buildings," by H.H.M. Hwang and H-M. Hsu, 8/10/91, (PB92-140235, A09, MF-A02).

NCEER-91-0024  "Experimental Verification of a Number of Structural System Identification Algorithms," by R.G. Ghanem, H. Gavin and M. Shinozuka, 9/18/91, (PB92-176577, A18, MF-A04).

NCEER-91-0025  "Probabilistic Evaluation of Liquefaction Potential," by H.H.M. Hwang and C.S. Lee," 11/25/91, (PB92-143429, A05, MF-A01).

NCEER-91-0026  "Instantaneous Optimal Control for Linear, Nonlinear and Hysteretic Structures - Stable Controllers," by J.N. Yang and Z. Li, 11/15/91, (PB92-163807, A04, MF-A01).

NCEER-91-0027  "Experimental and Theoretical Study of a Sliding Isolation System for Bridges," by M.C. Constantinou, A. Kartoum, A.M. Reinhorn and P. Bradford, 11/15/91, (PB92-176973, A10, MF-A03).

NCEER-92-0001  "Case Studies of Liquefaction and Lifeline Performance During Past Earthquakes, Volume 1: Japanese Case Studies," Edited by M. Hamada and T. O'Rourke, 2/17/92, (PB92-197243, A18, MF-A04).

NCEER-92-0002  "Case Studies of Liquefaction and Lifeline Performance During Past Earthquakes, Volume 2: United States Case Studies," Edited by T. O'Rourke and M. Hamada, 2/17/92, (PB92-197250, A20, MF-A04).

NCEER-92-0003  "Issues in Earthquake Education," Edited by K. Ross, 2/3/92, (PB92-222389, A07, MF-A02).

NCEER-92-0004  "Proceedings from the First U.S. - Japan Workshop on Earthquake Protective Systems for Bridges," Edited by I.G. Buckle, 2/4/92, (PB94-142239, A99, MF-A06).

NCEER-92-0005  "Seismic Ground Motion from a Haskell-Type Source in a Multiple-Layered Half-Space," A.P. Theoharis, G. Deodatis and M. Shinozuka, 1/2/92, to be published.

NCEER-92-0006  "Proceedings from the Site Effects Workshop," Edited by R. Whitman, 2/29/92, (PB92-197201, A04, MF-A01).

NCEER-92-0007  "Engineering Evaluation of Permanent Ground Deformations Due to Seismically-Induced Liquefaction," by M.H. Baziar, R. Dobry and A-W.M. Elgamal, 3/24/92, (PB92-222421, A13, MF-A03).

NCEER-92-0008  "A Procedure for the Seismic Evaluation of Buildings in the Central and Eastern United States," by C.D. Poland and J.O. Malley, 4/2/92, (PB92-222439, A20, MF-A04).

NCEER-92-0009  "Experimental and Analytical Study of a Hybrid Isolation System Using Friction Controllable Sliding Bearings," by M.Q. Feng, S. Fujii and M. Shinozuka, 5/15/92, (PB93-150282, A06, MF-A02).

NCEER-92-0010  "Seismic Resistance of Slab-Column Connections in Existing Non-Ductile Flat-Plate Buildings," by A.J. Durrani and Y. Du, 5/18/92, (PB93-116812, A06, MF-A02).

NCEER-92-0011  "The Hysteretic and Dynamic Behavior of Brick Masonry Walls Upgraded by Ferrocement Coatings Under Cyclic Loading and Strong Simulated Ground Motion," by H. Lee and S.P. Prawel, 5/11/92, to be published.

NCEER-92-0012  "Study of Wire Rope Systems for Seismic Protection of Equipment in Buildings," by G.F. Demetriades, M.C. Constantinou and A.M. Reinhorn, 5/20/92, (PB93-116655, A08, MF-A02).

NCEER-92-0013    "Shape Memory Structural Dampers: Material Properties, Design and Seismic Testing," by P.R. Witting and F.A. Cozzarelli, 5/26/92, (PB93-116663, A05, MF-A01).

NCEER-92-0014    "Longitudinal Permanent Ground Deformation Effects on Buried Continuous Pipelines," by M.J. O'Rourke, and C. Nordberg, 6/15/92, (PB93-116671, A08, MF-A02).

NCEER-92-0015    "A Simulation Method for Stationary Gaussian Random Functions Based on the Sampling Theorem," by M. Grigoriu and S. Balopoulou, 6/11/92, (PB93-127496, A05, MF-A01).

NCEER-92-0016    "Gravity-Load-Designed Reinforced Concrete Buildings: Seismic Evaluation of Existing Construction and Detailing Strategies for Improved Seismic Resistance," by G.W. Hoffmann, S.K. Kunnath, A.M. Reinhorn and J.B. Mander, 7/15/92, (PB94-142007, A08, MF-A02).

NCEER-92-0017    "Observations on Water System and Pipeline Performance in the Limón Area of Costa Rica Due to the April 22, 1991 Earthquake," by M. O'Rourke and D. Ballantyne, 6/30/92, (PB93-126811, A06, MF-A02).

NCEER-92-0018    "Fourth Edition of Earthquake Education Materials for Grades K-12," Edited by K.E.K. Ross, 8/10/92, (PB93-114023, A07, MF-A02).

NCEER-92-0019    "Proceedings from the Fourth Japan-U.S. Workshop on Earthquake Resistant Design of Lifeline Facilities and Countermeasures for Soil Liquefaction," Edited by M. Hamada and T.D. O'Rourke, 8/12/92, (PB93-163939, A99, MF-E11).

NCEER-92-0020    "Active Bracing System: A Full Scale Implementation of Active Control," by A.M. Reinhorn, T.T. Soong, R.C. Lin, M.A. Riley, Y.P. Wang, S. Aizawa and M. Higashino, 8/14/92, (PB93-127512, A06, MF-A02).

NCEER-92-0021    "Empirical Analysis of Horizontal Ground Displacement Generated by Liquefaction-Induced Lateral Spreads," by S.F. Bartlett and T.L. Youd, 8/17/92, (PB93-188241, A06, MF-A02).

NCEER-92-0022    "IDARC Version 3.0: Inelastic Damage Analysis of Reinforced Concrete Structures," by S.K. Kunnath, A.M. Reinhorn and R.F. Lobo, 8/31/92, (PB93-227502, A07, MF-A02).

NCEER-92-0023    "A Semi-Empirical Analysis of Strong-Motion Peaks in Terms of Seismic Source, Propagation Path and Local Site Conditions, by M. Kamiyama, M.J. O'Rourke and R. Flores-Berrones, 9/9/92, (PB93-150266, A08, MF-A02).

NCEER-92-0024    "Seismic Behavior of Reinforced Concrete Frame Structures with Nonductile Details, Part I: Summary of Experimental Findings of Full Scale Beam-Column Joint Tests," by A. Beres, R.N. White and P. Gergely, 9/30/92, (PB93-227783, A05, MF-A01).

NCEER-92-0025    "Experimental Results of Repaired and Retrofitted Beam-Column Joint Tests in Lightly Reinforced Concrete Frame Buildings," by A. Beres, S. El-Borgi, R.N. White and P. Gergely, 10/29/92, (PB93-227791, A05, MF-A01).

NCEER-92-0026    "A Generalization of Optimal Control Theory: Linear and Nonlinear Structures," by J.N. Yang, Z. Li and S. Vongchavalitkul, 11/2/92, (PB93-188621, A05, MF-A01).

NCEER-92-0027    "Seismic Resistance of Reinforced Concrete Frame Structures Designed Only for Gravity Loads: Part I - Design and Properties of a One-Third Scale Model Structure," by J.M. Bracci, A.M. Reinhorn and J.B. Mander, 12/1/92, (PB94-104502, A08, MF-A02).

NCEER-92-0028    "Seismic Resistance of Reinforced Concrete Frame Structures Designed Only for Gravity Loads: Part II - Experimental Performance of Subassemblages," by L.E. Aycardi, J.B. Mander and A.M. Reinhorn, 12/1/92, (PB94-104510, A08, MF-A02).

NCEER-92-0029    "Seismic Resistance of Reinforced Concrete Frame Structures Designed Only for Gravity Loads: Part III - Experimental Performance and Analytical Study of a Structural Model," by J.M. Bracci, A.M. Reinhorn and J.B. Mander, 12/1/92, (PB93-227528, A09, MF-A01).

NCEER-92-0030    "Evaluation of Seismic Retrofit of Reinforced Concrete Frame Structures: Part I - Experimental Performance of Retrofitted Subassemblages," by D. Choudhuri, J.B. Mander and A.M. Reinhorn, 12/8/92, (PB93-198307, A07, MF-A02).

NCEER-92-0031    "Evaluation of Seismic Retrofit of Reinforced Concrete Frame Structures: Part II - Experimental Performance and Analytical Study of a Retrofitted Structural Model," by J.M. Bracci, A.M. Reinhorn and J.B. Mander, 12/8/92, (PB93-198315, A09, MF-A03).

NCEER-92-0032    "Experimental and Analytical Investigation of Seismic Response of Structures with Supplemental Fluid Viscous Dampers," by M.C. Constantinou and M.D. Symans, 12/21/92, (PB93-191435, A10, MF-A03). This report is available only through NTIS (see address given above).

NCEER-92-0033    "Reconnaissance Report on the Cairo, Egypt Earthquake of October 12, 1992," by M. Khater, 12/23/92, (PB93-188621, A03, MF-A01).

NCEER-92-0034    "Low-Level Dynamic Characteristics of Four Tall Flat-Plate Buildings in New York City," by H. Gavin, S. Yuan, J. Grossman, E. Pekelis and K. Jacob, 12/28/92, (PB93-188217, A07, MF-A02).

NCEER-93-0001    "An Experimental Study on the Seismic Performance of Brick-Infilled Steel Frames With and Without Retrofit," by J.B. Mander, B. Nair, K. Wojtkowski and J. Ma, 1/29/93, (PB93-227510, A07, MF-A02).

NCEER-93-0002    "Social Accounting for Disaster Preparedness and Recovery Planning," by S. Cole, E. Pantoja and V. Razak, 2/22/93, (PB94-142114, A12, MF-A03).

NCEER-93-0003    "Assessment of 1991 NEHRP Provisions for Nonstructural Components and Recommended Revisions," by T.T. Soong, G. Chen, Z. Wu, R-H. Zhang and M. Grigoriu, 3/1/93, (PB93-188639, A06, MF-A02).

NCEER-93-0004    "Evaluation of Static and Response Spectrum Analysis Procedures of SEAOC/UBC for Seismic Isolated Structures," by C.W. Winters and M.C. Constantinou, 3/23/93, (PB93-198299, A10, MF-A03).

NCEER-93-0005    "Earthquakes in the Northeast - Are We Ignoring the Hazard? A Workshop on Earthquake Science and Safety for Educators," edited by K.E.K. Ross, 4/2/93, (PB94-103066, A09, MF-A02).

NCEER-93-0006    "Inelastic Response of Reinforced Concrete Structures with Viscoelastic Braces," by R.F. Lobo, J.M. Bracci, K.L. Shen, A.M. Reinhorn and T.T. Soong, 4/5/93, (PB93-227486, A05, MF-A02).

NCEER-93-0007    "Seismic Testing of Installation Methods for Computers and Data Processing Equipment," by K. Kosar, T.T. Soong, K.L. Shen, J.A. HoLung and Y.K. Lin, 4/12/93, (PB93-198299, A07, MF-A02).

NCEER-93-0008    "Retrofit of Reinforced Concrete Frames Using Added Dampers," by A. Reinhorn, M. Constantinou and C. Li, to be published.

NCEER-93-0009    "Seismic Behavior and Design Guidelines for Steel Frame Structures with Added Viscoelastic Dampers," by K.C. Chang, M.L. Lai, T.T. Soong, D.S. Hao and Y.C. Yeh, 5/1/93, (PB94-141959, A07, MF-A02).

NCEER-93-0010    "Seismic Performance of Shear-Critical Reinforced Concrete Bridge Piers," by J.B. Mander, S.M. Waheed, M.T.A. Chaudhary and S.S. Chen, 5/12/93, (PB93-227494, A08, MF-A02).

NCEER-93-0011    "3D-BASIS-TABS: Computer Program for Nonlinear Dynamic Analysis of Three Dimensional Base Isolated Structures," by S. Nagarajaiah, C. Li, A.M. Reinhorn and M.C. Constantinou, 8/2/93, (PB94-141819, A09, MF-A02).

NCEER-93-0012    "Effects of Hydrocarbon Spills from an Oil Pipeline Break on Ground Water," by O.J. Helweg and H.H.M. Hwang, 8/3/93, (PB94-141942, A06, MF-A02).

NCEER-93-0013    "Simplified Procedures for Seismic Design of Nonstructural Components and Assessment of Current Code Provisions," by M.P. Singh, L.E. Suarez, E.E. Matheu and G.O. Maldonado, 8/4/93, (PB94-141827, A09, MF-A02).

NCEER-93-0014    "An Energy Approach to Seismic Analysis and Design of Secondary Systems," by G. Chen and T.T. Soong, 8/6/93, (PB94-142767, A11, MF-A03).

NCEER-93-0015    "Proceedings from School Sites: Becoming Prepared for Earthquakes - Commemorating the Third Anniversary of the Loma Prieta Earthquake," Edited by F.E. Winslow and K.E.K. Ross, 8/16/93, (PB94-154275, A16, MF-A02).

NCEER-93-0016    "Reconnaissance Report of Damage to Historic Monuments in Cairo, Egypt Following the October 12, 1992 Dahshur Earthquake," by D. Sykora, D. Look, G. Croci, E. Karaesmen and E. Karaesmen, 8/19/93, (PB94-142221, A08, MF-A02).

NCEER-93-0017    "The Island of Guam Earthquake of August 8, 1993," by S.W. Swan and S.K. Harris, 9/30/93, (PB94-141843, A04, MF-A01).

NCEER-93-0018    "Engineering Aspects of the October 12, 1992 Egyptian Earthquake," by A.W. Elgamal, M. Amer, K. Adalier and A. Abul-Fadl, 10/7/93, (PB94-141983, A05, MF-A01).

NCEER-93-0019    "Development of an Earthquake Motion Simulator and its Application in Dynamic Centrifuge Testing," by I. Krstelj, Supervised by J.H. Prevost, 10/23/93, (PB94-181773, A-10, MF-A03).

NCEER-93-0020    "NCEER-Taisei Corporation Research Program on Sliding Seismic Isolation Systems for Bridges: Experimental and Analytical Study of a Friction Pendulum System (FPS)," by M.C. Constantinou, P. Tsopelas, Y-S. Kim and S. Okamoto, 11/1/93, (PB94-142775, A08, MF-A02).

NCEER-93-0021    "Finite Element Modeling of Elastomeric Seismic Isolation Bearings," by L.J. Billings, Supervised by R. Shepherd, 11/8/93, to be published.

NCEER-93-0022    "Seismic Vulnerability of Equipment in Critical Facilities: Life-Safety and Operational Consequences," by K. Porter, G.S. Johnson, M.M. Zadeh, C. Scawthorn and S. Eder, 11/24/93, (PB94-181765, A16, MF-A03).

NCEER-93-0023    "Hokkaido Nansei-oki, Japan Earthquake of July 12, 1993, by P.I. Yanev and C.R. Scawthorn, 12/23/93, (PB94-181500, A07, MF-A01).

NCEER-94-0001    "An Evaluation of Seismic Serviceability of Water Supply Networks with Application to the San Francisco Auxiliary Water Supply System," by I. Markov, Supervised by M. Grigoriu and T. O'Rourke, 1/21/94, (PB94-204013, A07, MF-A02).

NCEER-94-0002    "NCEER-Taisei Corporation Research Program on Sliding Seismic Isolation Systems for Bridges: Experimental and Analytical Study of Systems Consisting of Sliding Bearings, Rubber Restoring Force Devices and Fluid Dampers," Volumes I and II, by P. Tsopelas, S. Okamoto, M.C. Constantinou, D. Ozaki and S. Fujii, 2/4/94, (PB94-181740, A09, MF-A02 and PB94-181757, A12, MF-A03).

NCEER-94-0003    "A Markov Model for Local and Global Damage Indices in Seismic Analysis," by S. Rahman and M. Grigoriu, 2/18/94, (PB94-206000, A12, MF-A03).

NCEER-94-0004    "Proceedings from the NCEER Workshop on Seismic Response of Masonry Infills," edited by D.P. Abrams, 3/1/94, (PB94-180783, A07, MF-A02).

NCEER-94-0005    "The Northridge, California Earthquake of January 17, 1994: General Reconnaissance Report," edited by J.D. Goltz, 3/11/94, (PB94-193943, A10, MF-A03).

NCEER-94-0006    "Seismic Energy Based Fatigue Damage Analysis of Bridge Columns: Part I - Evaluation of Seismic Capacity," by G.A. Chang and J.B. Mander, 3/14/94, (PB94-219185, A11, MF-A03).

NCEER-94-0007    "Seismic Isolation of Multi-Story Frame Structures Using Spherical Sliding Isolation Systems," by T.M. Al-Hussaini, V.A. Zayas and M.C. Constantinou, 3/17/94, (PB94-193745, A09, MF-A02).

NCEER-94-0008    "The Northridge, California Earthquake of January 17, 1994: Performance of Highway Bridges," edited by I.G. Buckle, 3/24/94, (PB94-193851, A06, MF-A02).

NCEER-94-0009    "Proceedings of the Third U.S.-Japan Workshop on Earthquake Protective Systems for Bridges," edited by I.G. Buckle and I. Friedland, 3/31/94, (PB94-195815, A99, MF-A06).

NCEER-94-0010    "3D-BASIS-ME: Computer Program for Nonlinear Dynamic Analysis of Seismically Isolated Single and Multiple Structures and Liquid Storage Tanks," by P.C. Tsopelas, M.C. Constantinou and A.M. Reinhorn, 4/12/94, (PB94-204922, A09, MF-A02).

NCEER-94-0011    "The Northridge, California Earthquake of January 17, 1994: Performance of Gas Transmission Pipelines," by T.D. O'Rourke and M.C. Palmer, 5/16/94, (PB94-204989, A05, MF-A01).

NCEER-94-0012    "Feasibility Study of Replacement Procedures and Earthquake Performance Related to Gas Transmission Pipelines," by T.D. O'Rourke and M.C. Palmer, 5/25/94, (PB94-206638, A09, MF-A02).

NCEER-94-0013    "Seismic Energy Based Fatigue Damage Analysis of Bridge Columns: Part II - Evaluation of Seismic Demand," by G.A. Chang and J.B. Mander, 6/1/94, (PB95-18106, A08, MF-A02).

NCEER-94-0014    "NCEER-Taisei Corporation Research Program on Sliding Seismic Isolation Systems for Bridges: Experimental and Analytical Study of a System Consisting of Sliding Bearings and Fluid Restoring Force/Damping Devices," by P. Tsopelas and M.C. Constantinou, 6/13/94, (PB94-219144, A10, MF-A03).

NCEER-94-0015    "Generation of Hazard-Consistent Fragility Curves for Seismic Loss Estimation Studies," by H. Hwang and J-R. Huo, 6/14/94, (PB95-181996, A09, MF-A02).

NCEER-94-0016    "Seismic Study of Building Frames with Added Energy-Absorbing Devices," by W.S. Pong, C.S. Tsai and G.C. Lee, 6/20/94, (PB94-219136, A10, A03).

NCEER-94-0017    "Sliding Mode Control for Seismic-Excited Linear and Nonlinear Civil Engineering Structures," by J. Yang, J. Wu, A. Agrawal and Z. Li, 6/21/94, (PB95-138483, A06, MF-A02).

NCEER-94-0018    "3D-BASIS-TABS Version 2.0: Computer Program for Nonlinear Dynamic Analysis of Three Dimensional Base Isolated Structures," by A.M. Reinhorn, S. Nagarajaiah, M.C. Constantinou, P. Tsopelas and R. Li, 6/22/94, (PB95-182176, A08, MF-A02).

NCEER-94-0019    "Proceedings of the International Workshop on Civil Infrastructure Systems: Application of Intelligent Systems and Advanced Materials on Bridge Systems," Edited by G.C. Lee and K.C. Chang, 7/18/94, (PB95-252474, A20, MF-A04).

NCEER-94-0020    "Study of Seismic Isolation Systems for Computer Floors," by V. Lambrou and M.C. Constantinou, 7/19/94, (PB95-138533, A10, MF-A03).

NCEER-94-0021    "Proceedings of the U.S.-Italian Workshop on Guidelines for Seismic Evaluation and Rehabilitation of Unreinforced Masonry Buildings," Edited by D.P. Abrams and G.M. Calvi, 7/20/94, (PB95-138749, A13, MF-A03).

NCEER-94-0022    "NCEER-Taisei Corporation Research Program on Sliding Seismic Isolation Systems for Bridges: Experimental and Analytical Study of a System Consisting of Lubricated PTFE Sliding Bearings and Mild Steel Dampers," by P. Tsopelas and M.C. Constantinou, 7/22/94, (PB95-182184, A08, MF-A02).

NCEER-94-0023    "Development of Reliability-Based Design Criteria for Buildings Under Seismic Load," by Y.K. Wen, H. Hwang and M. Shinozuka, 8/1/94, (PB95-211934, A08, MF-A02).

NCEER-94-0024    "Experimental Verification of Acceleration Feedback Control Strategies for an Active Tendon System," by S.J. Dyke, B.F. Spencer, Jr., P. Quast, M.K. Sain, D.C. Kaspari, Jr. and T.T. Soong, 8/29/94, (PB95-212320, A05, MF-A01).

NCEER-94-0025    "Seismic Retrofitting Manual for Highway Bridges," Edited by I.G. Buckle and I.F. Friedland, published by the Federal Highway Administration (PB95-212676, A15, MF-A03).

NCEER-94-0026    "Proceedings from the Fifth U.S.-Japan Workshop on Earthquake Resistant Design of Lifeline Facilities and Countermeasures Against Soil Liquefaction," Edited by T.D. O'Rourke and M. Hamada, 11/7/94, (PB95-220802, A99, MF-E08).

NCEER-95-0001 "Experimental and Analytical Investigation of Seismic Retrofit of Structures with Supplemental Damping: Part 1 - Fluid Viscous Damping Devices," by A.M. Reinhorn, C. Li and M.C. Constantinou, 1/3/95, (PB95-266599, A09, MF-A02).

NCEER-95-0002 "Experimental and Analytical Study of Low-Cycle Fatigue Behavior of Semi-Rigid Top-And-Seat Angle Connections," by G. Pekcan, J.B. Mander and S.S. Chen, 1/5/95, (PB95-220042, A07, MF-A02).

NCEER-95-0003 "NCEER-ATC Joint Study on Fragility of Buildings," by T. Anagnos, C. Rojahn and A.S. Kiremidjian, 1/20/95, (PB95-220026, A06, MF-A02).

NCEER-95-0004 "Nonlinear Control Algorithms for Peak Response Reduction," by Z. Wu, T.T. Soong, V. Gattulli and R.C. Lin, 2/16/95, (PB95-220349, A05, MF-A01).

NCEER-95-0005 "Pipeline Replacement Feasibility Study: A Methodology for Minimizing Seismic and Corrosion Risks to Underground Natural Gas Pipelines," by R.T. Eguchi, H.A. Seligson and D.G. Honegger, 3/2/95, (PB95-252326, A06, MF-A02).

NCEER-95-0006 "Evaluation of Seismic Performance of an 11-Story Frame Building During the 1994 Northridge Earthquake," by F. Naeim, R. DiSulio, K. Benuska, A. Reinhorn and C. Li, to be published.

NCEER-95-0007 "Prioritization of Bridges for Seismic Retrofitting," by N. Basöz and A.S. Kiremidjian, 4/24/95, (PB95-252300, A08, MF-A02).

NCEER-95-0008 "Method for Developing Motion Damage Relationships for Reinforced Concrete Frames," by A. Singhal and A.S. Kiremidjian, 5/11/95, (PB95-266607, A06, MF-A02).

NCEER-95-0009 "Experimental and Analytical Investigation of Seismic Retrofit of Structures with Supplemental Damping: Part II - Friction Devices," by C. Li and A.M. Reinhorn, 7/6/95, (PB96-128087, A11, MF-A03).

NCEER-95-0010 "Experimental Performance and Analytical Study of a Non-Ductile Reinforced Concrete Frame Structure Retrofitted with Elastomeric Spring Dampers," by G. Pekcan, J.B. Mander and S.S. Chen, 7/14/95, (PB96-137161, A08, MF-A02).

NCEER-95-0011 "Development and Experimental Study of Semi-Active Fluid Damping Devices for Seismic Protection of Structures," by M.D. Symans and M.C. Constantinou, 8/3/95, (PB96-136940, A23, MF-A04).

NCEER-95-0012 "Real-Time Structural Parameter Modification (RSPM): Development of Innervated Structures," by Z. Liang, M. Tong and G.C. Lee, 4/11/95, (PB96-137153, A06, MF-A01).

NCEER-95-0013 "Experimental and Analytical Investigation of Seismic Retrofit of Structures with Supplemental Damping: Part III - Viscous Damping Walls," by A.M. Reinhorn and C. Li, 10/1/95, (PB96-176409, A11, MF-A03).

NCEER-95-0014 "Seismic Fragility Analysis of Equipment and Structures in a Memphis Electric Substation," by J-R. Huo and H.H.M. Hwang, 8/10/95, (PB96-128087, A09, MF-A02).

NCEER-95-0015 "The Hanshin-Awaji Earthquake of January 17, 1995: Performance of Lifelines," Edited by M. Shinozuka, 11/3/95, (PB96-176383, A15, MF-A03).

NCEER-95-0016 "Highway Culvert Performance During Earthquakes," by T.L. Youd and C.J. Beckman, available as NCEER-96-0015.

NCEER-95-0017 "The Hanshin-Awaji Earthquake of January 17, 1995: Performance of Highway Bridges," Edited by I.G. Buckle, 12/1/95, to be published.

NCEER-95-0018 "Modeling of Masonry Infill Panels for Structural Analysis," by A.M. Reinhorn, A. Madan, R.E. Valles, Y. Reichmann and J.B. Mander, 12/8/95, (PB97-110886, MF-A01, A06).

NCEER-95-0019 "Optimal Polynomial Control for Linear and Nonlinear Structures," by A.K. Agrawal and J.N. Yang, 12/11/95, (PB96-168737, A07, MF-A02).

NCEER-95-0020   "Retrofit of Non-Ductile Reinforced Concrete Frames Using Friction Dampers," by R.S. Rao, P. Gergely and R.N. White, 12/22/95, (PB97-133508, A10, MF-A02).

NCEER-95-0021   "Parametric Results for Seismic Response of Pile-Supported Bridge Bents," by G. Mylonakis, A. Nikolaou and G. Gazetas, 12/22/95, (PB97-100242, A12, MF-A03).

NCEER-95-0022   "Kinematic Bending Moments in Seismically Stressed Piles," by A. Nikolaou, G. Mylonakis and G. Gazetas, 12/23/95, (PB97-113914, MF-A03, A13).

NCEER-96-0001   "Dynamic Response of Unreinforced Masonry Buildings with Flexible Diaphragms," by A.C. Costley and D.P. Abrams," 10/10/96, (PB97-133573, MF-A03, A15).

NCEER-96-0002   "State of the Art Review: Foundations and Retaining Structures," by I. Po Lam, to be published.

NCEER-96-0003   "Ductility of Rectangular Reinforced Concrete Bridge Columns with Moderate Confinement," by N. Wehbe, M. Saiidi, D. Sanders and B. Douglas, 11/7/96, (PB97-133557, A06, MF-A02).

NCEER-96-0004   "Proceedings of the Long-Span Bridge Seismic Research Workshop," edited by I.G. Buckle and I.M. Friedland, to be published.

NCEER-96-0005   "Establish Representative Pier Types for Comprehensive Study: Eastern United States," by J. Kulicki and Z. Prucz, 5/28/96, (PB98-119217, A07, MF-A02).

NCEER-96-0006   "Establish Representative Pier Types for Comprehensive Study: Western United States," by R. Imbsen, R.A. Schamber and T.A. Osterkamp, 5/28/96, (PB98-118607, A07, MF-A02).

NCEER-96-0007   "Nonlinear Control Techniques for Dynamical Systems with Uncertain Parameters," by R.G. Ghanem and M.I. Bujakov, 5/27/96, (PB97-100259, A17, MF-A03).

NCEER-96-0008   "Seismic Evaluation of a 30-Year Old Non-Ductile Highway Bridge Pier and Its Retrofit," by J.B. Mander, B. Mahmoodzadegan, S. Bhadra and S.S. Chen, 5/31/96, (PB97-110902, MF-A03, A10).

NCEER-96-0009   "Seismic Performance of a Model Reinforced Concrete Bridge Pier Before and After Retrofit," by J.B. Mander, J.H. Kim and C.A. Ligozio, 5/31/96, (PB97-110910, MF-A02, A10).

NCEER-96-0010   "IDARC2D Version 4.0: A Computer Program for the Inelastic Damage Analysis of Buildings," by R.E. Valles, A.M. Reinhorn, S.K. Kunnath, C. Li and A. Madan, 6/3/96, (PB97-100234, A17, MF-A03).

NCEER-96-0011   "Estimation of the Economic Impact of Multiple Lifeline Disruption: Memphis Light, Gas and Water Division Case Study," by S.E. Chang, H.A. Seligson and R.T. Eguchi, 8/16/96, (PB97-133490, A11, MF-A03).

NCEER-96-0012   "Proceedings from the Sixth Japan-U.S. Workshop on Earthquake Resistant Design of Lifeline Facilities and Countermeasures Against Soil Liquefaction, Edited by M. Hamada and T. O'Rourke, 9/11/96, (PB97-133581, A99, MF-A06).

NCEER-96-0013   "Chemical Hazards, Mitigation and Preparedness in Areas of High Seismic Risk: A Methodology for Estimating the Risk of Post-Earthquake Hazardous Materials Release," by H.A. Seligson, R.T. Eguchi, K.J. Tierney and K. Richmond, 11/7/96, (PB97-133565, MF-A02, A08).

NCEER-96-0014   "Response of Steel Bridge Bearings to Reversed Cyclic Loading," by J.B. Mander, D-K. Kim, S.S. Chen and G.J. Premus, 11/13/96, (PB97-140735, A12, MF-A03).

NCEER-96-0015   "Highway Culvert Performance During Past Earthquakes," by T.L. Youd and C.J. Beckman, 11/25/96, (PB97-133532, A06, MF-A01).

NCEER-97-0001   "Evaluation, Prevention and Mitigation of Pounding Effects in Building Structures," by R.E. Valles and A.M. Reinhorn, 2/20/97, (PB97-159552, A14, MF-A03).

NCEER-97-0002   "Seismic Design Criteria for Bridges and Other Highway Structures," by C. Rojahn, R. Mayes, D.G. Anderson, J. Clark, J.H. Hom, R.V. Nutt and M.J. O'Rourke, 4/30/97, (PB97-194658, A06, MF-A03).

NCEER-97-0003    "Proceedings of the U.S.-Italian Workshop on Seismic Evaluation and Retrofit," Edited by D.P. Abrams and G.M. Calvi, 3/19/97, (PB97-194666, A13, MF-A03).

NCEER-97-0004    "Investigation of Seismic Response of Buildings with Linear and Nonlinear Fluid Viscous Dampers," by A.A. Seleemah and M.C. Constantinou, 5/21/97, (PB98-109002, A15, MF-A03).

NCEER-97-0005    "Proceedings of the Workshop on Earthquake Engineering Frontiers in Transportation Facilities," edited by G.C. Lee and I.M. Friedland, 8/29/97, (PB98-128911, A25, MR-A04).

NCEER-97-0006    "Cumulative Seismic Damage of Reinforced Concrete Bridge Piers," by S.K. Kunnath, A. El-Bahy, A. Taylor and W. Stone, 9/2/97, (PB98-108814, A11, MF-A03).

NCEER-97-0007    "Structural Details to Accommodate Seismic Movements of Highway Bridges and Retaining Walls," by R.A. Imbsen, R.A. Schamber, E. Thorkildsen, A. Kartoum, B.T. Martin, T.N. Rosser and J.M. Kulicki, 9/3/97, (PB98-108996, A09, MF-A02).

NCEER-97-0008    "A Method for Earthquake Motion-Damage Relationships with Application to Reinforced Concrete Frames," by A. Singhal and A.S. Kiremidjian, 9/10/97, (PB98-108988, A13, MF-A03).

NCEER-97-0009    "Seismic Analysis and Design of Bridge Abutments Considering Sliding and Rotation," by K. Fishman and R. Richards, Jr., 9/15/97, (PB98-108897, A06, MF-A02).

NCEER-97-0010    "Proceedings of the FHWA/NCEER Workshop on the National Representation of Seismic Ground Motion for New and Existing Highway Facilities," edited by I.M. Friedland, M.S. Power and R.L. Mayes, 9/22/97, (PB98-128903, A21, MF-A04).

NCEER-97-0011    "Seismic Analysis for Design or Retrofit of Gravity Bridge Abutments," by K.L. Fishman, R. Richards, Jr. and R.C. Divito, 10/2/97, (PB98-128937, A08, MF-A02).

NCEER-97-0012    "Evaluation of Simplified Methods of Analysis for Yielding Structures," by P. Tsopelas, M.C. Constantinou, C.A. Kircher and A.S. Whittaker, 10/31/97, (PB98-128929, A10, MF-A03).

NCEER-97-0013    "Seismic Design of Bridge Columns Based on Control and Repairability of Damage," by C-T. Cheng and J.B. Mander, 12/8/97, (PB98-144249, A11, MF-A03).

NCEER-97-0014    "Seismic Resistance of Bridge Piers Based on Damage Avoidance Design," by J.B. Mander and C-T. Cheng, 12/10/97, (PB98-144223, A09, MF-A02).

NCEER-97-0015    "Seismic Response of Nominally Symmetric Systems with Strength Uncertainty," by S. Balopoulou and M. Grigoriu, 12/23/97, (PB98-153422, A11, MF-A03).

NCEER-97-0016    "Evaluation of Seismic Retrofit Methods for Reinforced Concrete Bridge Columns," by T.J. Wipf, F.W. Klaiber and F.M. Russo, 12/28/97, (PB98-144215, A12, MF-A03).

NCEER-97-0017    "Seismic Fragility of Existing Conventional Reinforced Concrete Highway Bridges," by C.L. Mullen and A.S. Cakmak, 12/30/97, (PB98-153406, A08, MF-A02).

NCEER-97-0018    "Loss Asssessment of Memphis Buildings," edited by D.P. Abrams and M. Shinozuka, 12/31/97, (PB98-144231, A13, MF-A03).

NCEER-97-0019    "Seismic Evaluation of Frames with Infill Walls Using Quasi-static Experiments," by K.M. Mosalam, R.N. White and P. Gergely, 12/31/97, (PB98-153455, A07, MF-A02).

NCEER-97-0020    "Seismic Evaluation of Frames with Infill Walls Using Pseudo-dynamic Experiments," by K.M. Mosalam, R.N. White and P. Gergely, 12/31/97, (PB98-153430, A07, MF-A02).

NCEER-97-0021    "Computational Strategies for Frames with Infill Walls: Discrete and Smeared Crack Analyses and Seismic Fragility," by K.M. Mosalam, R.N. White and P. Gergely, 12/31/97, (PB98-153414, A10, MF-A02).

NCEER-97-0022 "Proceedings of the NCEER Workshop on Evaluation of Liquefaction Resistance of Soils," edited by T.L. Youd and I.M. Idriss, 12/31/97, (PB98-155617, A15, MF-A03).

MCEER-98-0001 "Extraction of Nonlinear Hysteretic Properties of Seismically Isolated Bridges from Quick-Release Field Tests," by Q. Chen, B.M. Douglas, E.M. Maragakis and I.G. Buckle, 5/26/98, (PB99-118838, A06, MF-A01).

MCEER-98-0002 "Methodologies for Evaluating the Importance of Highway Bridges," by A. Thomas, S. Eshenaur and J. Kulicki, 5/29/98, (PB99-118846, A10, MF-A02).

MCEER-98-0003 "Capacity Design of Bridge Piers and the Analysis of Overstrength," by J.B. Mander, A. Dutta and P. Goel, 6/1/98, (PB99-118853, A09, MF-A02).

MCEER-98-0004 "Evaluation of Bridge Damage Data from the Loma Prieta and Northridge, California Earthquakes," by N. Basoz and A. Kiremidjian, 6/2/98, (PB99-118861, A15, MF-A03).

MCEER-98-0005 "Screening Guide for Rapid Assessment of Liquefaction Hazard at Highway Bridge Sites," by T. L. Youd, 6/16/98, (PB99-118879, A06, not available on microfiche).

MCEER-98-0006 "Structural Steel and Steel/Concrete Interface Details for Bridges," by P. Ritchie, N. Kauhl and J. Kulicki, 7/13/98, (PB99-118945, A06, MF-A01).

MCEER-98-0007 "Capacity Design and Fatigue Analysis of Confined Concrete Columns," by A. Dutta and J.B. Mander, 7/14/98, (PB99-118960, A14, MF-A03).

MCEER-98-0008 "Proceedings of the Workshop on Performance Criteria for Telecommunication Services Under Earthquake Conditions," edited by A.J. Schiff, 7/15/98, (PB99-118952, A08, MF-A02).

MCEER-98-0009 "Fatigue Analysis of Unconfined Concrete Columns," by J.B. Mander, A. Dutta and J.H. Kim, 9/12/98, (PB99-123655, A10, MF-A02).

MCEER-98-0010 "Centrifuge Modeling of Cyclic Lateral Response of Pile-Cap Systems and Seat-Type Abutments in Dry Sands," by A.D. Gadre and R. Dobry, 10/2/98, (PB99-123606, A13, MF-A03).

MCEER-98-0011 "IDARC-BRIDGE: A Computational Platform for Seismic Damage Assessment of Bridge Structures," by A.M. Reinhorn, V. Simeonov, G. Mylonakis and Y. Reichman, 10/2/98, (PB99-162919, A15, MF-A03).

MCEER-98-0012 "Experimental Investigation of the Dynamic Response of Two Bridges Before and After Retrofitting with Elastomeric Bearings," by D.A. Wendichansky, S.S. Chen and J.B. Mander, 10/2/98, (PB99-162927, A15, MF-A03).

MCEER-98-0013 "Design Procedures for Hinge Restrainers and Hinge Sear Width for Multiple-Frame Bridges," by R. Des Roches and G.L. Fenves, 11/3/98, (PB99-140477, A13, MF-A03).

MCEER-98-0014 "Response Modification Factors for Seismically Isolated Bridges," by M.C. Constantinou and J.K. Quarshie, 11/3/98, (PB99-140485, A14, MF-A03).

MCEER-98-0015 "Proceedings of the U.S.-Italy Workshop on Seismic Protective Systems for Bridges," edited by I.M. Friedland and M.C. Constantinou, 11/3/98, (PB2000-101711, A22, MF-A04).

MCEER-98-0016 "Appropriate Seismic Reliability for Critical Equipment Systems: Recommendations Based on Regional Analysis of Financial and Life Loss," by K. Porter, C. Scawthorn, C. Taylor and N. Blais, 11/10/98, (PB99-157265, A08, MF-A02).

MCEER-98-0017 "Proceedings of the U.S. Japan Joint Seminar on Civil Infrastructure Systems Research," edited by M. Shinozuka and A. Rose, 11/12/98, (PB99-156713, A16, MF-A03).

MCEER-98-0018 "Modeling of Pile Footings and Drilled Shafts for Seismic Design," by I. PoLam, M. Kapuskar and D. Chaudhuri, 12/21/98, (PB99-157257, A09, MF-A02).

MCEER-99-0001 "Seismic Evaluation of a Masonry Infilled Reinforced Concrete Frame by Pseudodynamic Testing," by S.G. Buonopane and R.N. White, 2/16/99, (PB99-162851, A09, MF-A02).

MCEER-99-0002 "Response History Analysis of Structures with Seismic Isolation and Energy Dissipation Systems: Verification Examples for Program SAP2000," by J. Scheller and M.C. Constantinou, 2/22/99, (PB99-162869, A08, MF-A02).

MCEER-99-0003 "Experimental Study on the Seismic Design and Retrofit of Bridge Columns Including Axial Load Effects," by A. Dutta, T. Kokorina and J.B. Mander, 2/22/99, (PB99-162877, A09, MF-A02).

MCEER-99-0004 "Experimental Study of Bridge Elastomeric and Other Isolation and Energy Dissipation Systems with Emphasis on Uplift Prevention and High Velocity Near-source Seismic Excitation," by A. Kasalanati and M. C. Constantinou, 2/26/99, (PB99-162885, A12, MF-A03).

MCEER-99-0005 "Truss Modeling of Reinforced Concrete Shear-flexure Behavior," by J.H. Kim and J.B. Mander, 3/8/99, (PB99-163693, A12, MF-A03).

MCEER-99-0006 "Experimental Investigation and Computational Modeling of Seismic Response of a 1:4 Scale Model Steel Structure with a Load Balancing Supplemental Damping System," by G. Pekcan, J.B. Mander and S.S. Chen, 4/2/99, (PB99-162893, A11, MF-A03).

MCEER-99-0007 "Effect of Vertical Ground Motions on the Structural Response of Highway Bridges," by M.R. Button, C.J. Cronin and R.L. Mayes, 4/10/99, (PB2000-101411, A10, MF-A03).

MCEER-99-0008 "Seismic Reliability Assessment of Critical Facilities: A Handbook, Supporting Documentation, and Model Code Provisions," by G.S. Johnson, R.E. Sheppard, M.D. Quilici, S.J. Eder and C.R. Scawthorn, 4/12/99, (PB2000-101701, A18, MF-A04).

MCEER-99-0009 "Impact Assessment of Selected MCEER Highway Project Research on the Seismic Design of Highway Structures," by C. Rojahn, R. Mayes, D.G. Anderson, J.H. Clark, D'Appolonia Engineering, S. Gloyd and R.V. Nutt, 4/14/99, (PB99-162901, A10, MF-A02).

MCEER-99-0010 "Site Factors and Site Categories in Seismic Codes," by R. Dobry, R. Ramos and M.S. Power, 7/19/99, (PB2000-101705, A08, MF-A02).

MCEER-99-0011 "Restrainer Design Procedures for Multi-Span Simply-Supported Bridges," by M.J. Randall, M. Saiidi, E. Maragakis and T. Isakovic, 7/20/99, (PB2000-101702, A10, MF-A02).

MCEER-99-0012 "Property Modification Factors for Seismic Isolation Bearings," by M.C. Constantinou, P. Tsopelas, A. Kasalanati and E. Wolff, 7/20/99, (PB2000-103387, A11, MF-A03).

MCEER-99-0013 "Critical Seismic Issues for Existing Steel Bridges," by P. Ritchie, N. Kauhl and J. Kulicki, 7/20/99, (PB2000-101697, A09, MF-A02).

MCEER-99-0014 "Nonstructural Damage Database," by A. Kao, T.T. Soong and A. Vender, 7/24/99, (PB2000-101407, A06, MF-A01).

MCEER-99-0015 "Guide to Remedial Measures for Liquefaction Mitigation at Existing Highway Bridge Sites," by H.G. Cooke and J. K. Mitchell, 7/26/99, (PB2000-101703, A11, MF-A03).

MCEER-99-0016 "Proceedings of the MCEER Workshop on Ground Motion Methodologies for the Eastern United States," edited by N. Abrahamson and A. Becker, 8/11/99, (PB2000-103385, A07, MF-A02).

MCEER-99-0017 "Quindío, Colombia Earthquake of January 25, 1999: Reconnaissance Report," by A.P. Asfura and P.J. Flores, 10/4/99, (PB2000-106893, A06, MF-A01).

MCEER-99-0018 "Hysteretic Models for Cyclic Behavior of Deteriorating Inelastic Structures," by M.V. Sivaselvan and A.M. Reinhorn, 11/5/99, (PB2000-103386, A08, MF-A02).

MCEER-99-0019    "Proceedings of the 7th U.S.- Japan Workshop on Earthquake Resistant Design of Lifeline Facilities and Countermeasures Against Soil Liquefaction," edited by T.D. O'Rourke, J.P. Bardet and M. Hamada, 11/19/99, (PB2000-103354, A99, MF-A06).

MCEER-99-0020    "Development of Measurement Capability for Micro-Vibration Evaluations with Application to Chip Fabrication Facilities," by G.C. Lee, Z. Liang, J.W. Song, J.D. Shen and W.C. Liu, 12/1/99, (PB2000-105993, A08, MF-A02).

MCEER-99-0021    "Design and Retrofit Methodology for Building Structures with Supplemental Energy Dissipating Systems," by G. Pekcan, J.B. Mander and S.S. Chen, 12/31/99, (PB2000-105994, A11, MF-A03).

MCEER-00-0001    "The Marmara, Turkey Earthquake of August 17, 1999: Reconnaissance Report," edited by C. Scawthorn; with major contributions by M. Bruneau, R. Eguchi, T. Holzer, G. Johnson, J. Mander, J. Mitchell, W. Mitchell, A. Papageorgiou, C. Scaethorn, and G. Webb, 3/23/00, (PB2000-106200, A11, MF-A03).

MCEER-00-0002    "Proceedings of the MCEER Workshop for Seismic Hazard Mitigation of Health Care Facilities," edited by G.C. Lee, M. Ettouney, M. Grigoriu, J. Hauer and J. Nigg, 3/29/00, (PB2000-106892, A08, MF-A02).

MCEER-00-0003    "The Chi-Chi, Taiwan Earthquake of September 21, 1999: Reconnaissance Report," edited by G.C. Lee and C.H. Loh, with major contributions by G.C. Lee, M. Bruneau, I.G. Buckle, S.E. Chang, P.J. Flores, T.D. O'Rourke, M. Shinozuka, T.T. Soong, C-H. Loh, K-C. Chang, Z-J. Chen, J-S. Hwang, M-L. Lin, G-Y. Liu, K-C. Tsai, G.C. Yao and C-L. Yen, 4/30/00, (PB2001-100980, A10, MF-A02).

MCEER-00-0004    "Seismic Retrofit of End-Sway Frames of Steel Deck-Truss Bridges with a Supplemental Tendon System: Experimental and Analytical Investigation," by G. Pekcan, J.B. Mander and S.S. Chen, 7/1/00, (PB2001-100982, A10, MF-A02).

MCEER-00-0005    "Sliding Fragility of Unrestrained Equipment in Critical Facilities," by W.H. Chong and T.T. Soong, 7/5/00, (PB2001-100983, A08, MF-A02).

MCEER-00-0006    "Seismic Response of Reinforced Concrete Bridge Pier Walls in the Weak Direction," by N. Abo-Shadi, M. Saiidi and D. Sanders, 7/17/00, (PB2001-100981, A17, MF-A03).

MCEER-00-0007    "Low-Cycle Fatigue Behavior of Longitudinal Reinforcement in Reinforced Concrete Bridge Columns," by J. Brown and S.K. Kunnath, 7/23/00, (PB2001-104392, A08, MF-A02).

MCEER-00-0008    "Soil Structure Interaction of Bridges for Seismic Analysis," I. PoLam and H. Law, 9/25/00, (PB2001-105397, A08, MF-A02).

MCEER-00-0009    "Proceedings of the First MCEER Workshop on Mitigation of Earthquake Disaster by Advanced Technologies (MEDAT-1), edited by M. Shinozuka, D.J. Inman and T.D. O'Rourke, 11/10/00, (PB2001-105399, A14, MF-A03).

MCEER-00-0010    "Development and Evaluation of Simplified Procedures for Analysis and Design of Buildings with Passive Energy Dissipation Systems, Revision 01," by O.M. Ramirez, M.C. Constantinou, C.A. Kircher, A.S. Whittaker, M.W. Johnson, J.D. Gomez and C. Chrysostomou, 11/16/01, (PB2001-105523, A23, MF-A04).

MCEER-00-0011    "Dynamic Soil-Foundation-Structure Interaction Analyses of Large Caissons," by C-Y. Chang, C-M. Mok, Z-L. Wang, R. Settgast, F. Waggoner, M.A. Ketchum, H.M. Gonnermann and C-C. Chin, 12/30/00, (PB2001-104373, A07, MF-A02).

MCEER-00-0012    "Experimental Evaluation of Seismic Performance of Bridge Restrainers," by A.G. Vlassis, E.M. Maragakis and M. Saiid Saiidi, 12/30/00, (PB2001-104354, A09, MF-A02).

MCEER-00-0013    "Effect of Spatial Variation of Ground Motion on Highway Structures," by M. Shinozuka, V. Saxena and G. Deodatis, 12/31/00, (PB2001-108755, A13, MF-A03).

MCEER-00-0014    "A Risk-Based Methodology for Assessing the Seismic Performance of Highway Systems," by S.D. Werner, C.E. Taylor, J.E. Moore, II, J.S. Walton and S. Cho, 12/31/00, (PB2001-108756, A14, MF-A03).

MCEER-01-0001 "Experimental Investigation of P-Delta Effects to Collapse During Earthquakes," by D. Vian and M. Bruneau, 6/25/01, (PB2002-100534, A17, MF-A03).

MCEER-01-0002 "Proceedings of the Second MCEER Workshop on Mitigation of Earthquake Disaster by Advanced Technologies (MEDAT-2)," edited by M. Bruneau and D.J. Inman, 7/23/01, (PB2002-100434, A16, MF-A03).

MCEER-01-0003 "Sensitivity Analysis of Dynamic Systems Subjected to Seismic Loads," by C. Roth and M. Grigoriu, 9/18/01, (PB2003-100884, A12, MF-A03).

MCEER-01-0004 "Overcoming Obstacles to Implementing Earthquake Hazard Mitigation Policies: Stage 1 Report," by D.J. Alesch and W.J. Petak, 12/17/01, (PB2002-107949, A07, MF-A02).

MCEER-01-0005 "Updating Real-Time Earthquake Loss Estimates: Methods, Problems and Insights," by C.E. Taylor, S.E. Chang and R.T. Eguchi, 12/17/01, (PB2002-107948, A05, MF-A01).

MCEER-01-0006 "Experimental Investigation and Retrofit of Steel Pile Foundations and Pile Bents Under Cyclic Lateral Loadings," by A. Shama, J. Mander, B. Blabac and S. Chen, 12/31/01, (PB2002-107950, A13, MF-A03).

MCEER-02-0001 "Assessment of Performance of Bolu Viaduct in the 1999 Duzce Earthquake in Turkey" by P.C. Roussis, M.C. Constantinou, M. Erdik, E. Durukal and M. Dicleli, 5/8/02, (PB2003-100883, A08, MF-A02).

MCEER-02-0002 "Seismic Behavior of Rail Counterweight Systems of Elevators in Buildings," by M.P. Singh, Rildova and L.E. Suarez, 5/27/02. (PB2003-100882, A11, MF-A03).

MCEER-02-0003 "Development of Analysis and Design Procedures for Spread Footings," by G. Mylonakis, G. Gazetas, S. Nikolaou and A. Chauncey, 10/02/02, (PB2004-101636, A13, MF-A03, CD-A13).

MCEER-02-0004 "Bare-Earth Algorithms for Use with SAR and LIDAR Digital Elevation Models," by C.K. Huyck, R.T. Eguchi and B. Houshmand, 10/16/02, (PB2004-101637, A07, CD-A07).

MCEER-02-0005 "Review of Energy Dissipation of Compression Members in Concentrically Braced Frames," by K.Lee and M. Bruneau, 10/18/02, (PB2004-101638, A10, CD-A10).

MCEER-03-0001 "Experimental Investigation of Light-Gauge Steel Plate Shear Walls for the Seismic Retrofit of Buildings" by J. Berman and M. Bruneau, 5/2/03, (PB2004-101622, A10, MF-A03, CD-A10).

MCEER-03-0002 "Statistical Analysis of Fragility Curves," by M. Shinozuka, M.Q. Feng, H. Kim, T. Uzawa and T. Ueda, 6/16/03, (PB2004-101849, A09, CD-A09).

MCEER-03-0003 "Proceedings of the Eighth U.S.-Japan Workshop on Earthquake Resistant Design f Lifeline Facilities and Countermeasures Against Liquefaction," edited by M. Hamada, J.P. Bardet and T.D. O'Rourke, 6/30/03, (PB2004-104386, A99, CD-A99).

MCEER-03-0004 "Proceedings of the PRC-US Workshop on Seismic Analysis and Design of Special Bridges," edited by L.C. Fan and G.C. Lee, 7/15/03, (PB2004-104387, A14, CD-A14).

MCEER-03-0005 "Urban Disaster Recovery: A Framework and Simulation Model," by S.B. Miles and S.E. Chang, 7/25/03, (PB2004-104388, A07, CD-A07).

MCEER-03-0006 "Behavior of Underground Piping Joints Due to Static and Dynamic Loading," by R.D. Meis, M. Maragakis and R. Siddharthan, 11/17/03, (PB2005-102194, A13, MF-A03, CD-A00).

MCEER-04-0001 "Experimental Study of Seismic Isolation Systems with Emphasis on Secondary System Response and Verification of Accuracy of Dynamic Response History Analysis Methods," by E. Wolff and M. Constantinou, 1/16/04 (PB2005-102195, A99, MF-E08, CD-A00).

MCEER-04-0002 "Tension, Compression and Cyclic Testing of Engineered Cementitious Composite Materials," by K. Kesner and S.L. Billington, 3/1/04, (PB2005-102196, A08, CD-A08).

MCEER-04-0003 "Cyclic Testing of Braces Laterally Restrained by Steel Studs to Enhance Performance During Earthquakes," by O.C. Celik, J.W. Berman and M. Bruneau, 3/16/04, (PB2005-102197, A13, MF-A03, CD-A00).

MCEER-04-0004 "Methodologies for Post Earthquake Building Damage Detection Using SAR and Optical Remote Sensing: Application to the August 17, 1999 Marmara, Turkey Earthquake," by C.K. Huyck, B.J. Adams, S. Cho, R.T. Eguchi, B. Mansouri and B. Houshmand, 6/15/04, (PB2005-104888, A10, CD-A00).

MCEER-04-0005 "Nonlinear Structural Analysis Towards Collapse Simulation: A Dynamical Systems Approach," by M.V. Sivaselvan and A.M. Reinhorn, 6/16/04, (PB2005-104889, A11, MF-A03, CD-A00).

MCEER-04-0006 "Proceedings of the Second PRC-US Workshop on Seismic Analysis and Design of Special Bridges," edited by G.C. Lee and L.C. Fan, 6/25/04, (PB2005-104890, A16, CD-A00).

MCEER-04-0007 "Seismic Vulnerability Evaluation of Axially Loaded Steel Built-up Laced Members," by K. Lee and M. Bruneau, 6/30/04, (PB2005-104891, A16, CD-A00).

MCEER-04-0008 "Evaluation of Accuracy of Simplified Methods of Analysis and Design of Buildings with Damping Systems for Near-Fault and for Soft-Soil Seismic Motions," by E.A. Pavlou and M.C. Constantinou, 8/16/04, (PB2005-104892, A08, MF-A02, CD-A00).

MCEER-04-0009 "Assessment of Geotechnical Issues in Acute Care Facilities in California," by M. Lew, T.D. O'Rourke, R. Dobry and M. Koch, 9/15/04, (PB2005-104893, A08, CD-A00).

MCEER-04-0010 "Scissor-Jack-Damper Energy Dissipation System," by A.N. Sigaher-Boyle and M.C. Constantinou, 12/1/04 (PB2005-108221).

MCEER-04-0011 "Seismic Retrofit of Bridge Steel Truss Piers Using a Controlled Rocking Approach," by M. Pollino and M. Bruneau, 12/20/04 (PB2006-105795).

MCEER-05-0001 "Experimental and Analytical Studies of Structures Seismically Isolated with an Uplift-Restraint Isolation System," by P.C. Roussis and M.C. Constantinou, 1/10/05 (PB2005-108222).

MCEER-05-0002 "A Versatile Experimentation Model for Study of Structures Near Collapse Applied to Seismic Evaluation of Irregular Structures," by D. Kusumastuti, A.M. Reinhorn and A. Rutenberg, 3/31/05 (PB2006-101523).

MCEER-05-0003 "Proceedings of the Third PRC-US Workshop on Seismic Analysis and Design of Special Bridges," edited by L.C. Fan and G.C. Lee, 4/20/05, (PB2006-105796).

MCEER-05-0004 "Approaches for the Seismic Retrofit of Braced Steel Bridge Piers and Proof-of-Concept Testing of an Eccentrically Braced Frame with Tubular Link," by J.W. Berman and M. Bruneau, 4/21/05 (PB2006-101524).

MCEER-05-0005 "Simulation of Strong Ground Motions for Seismic Fragility Evaluation of Nonstructural Components in Hospitals," by A. Wanitkorkul and A. Filiatrault, 5/26/05 (PB2006-500027).

MCEER-05-0006 "Seismic Safety in California Hospitals: Assessing an Attempt to Accelerate the Replacement or Seismic Retrofit of Older Hospital Facilities," by D.J. Alesch, L.A. Arendt and W.J. Petak, 6/6/05 (PB2006-105794).

MCEER-05-0007 "Development of Seismic Strengthening and Retrofit Strategies for Critical Facilities Using Engineered Cementitious Composite Materials," by K. Kesner and S.L. Billington, 8/29/05 (PB2006-111701).

MCEER-05-0008 "Experimental and Analytical Studies of Base Isolation Systems for Seismic Protection of Power Transformers," by N. Murota, M.Q. Feng and G-Y. Liu, 9/30/05 (PB2006-111702).

MCEER-05-0009 "3D-BASIS-ME-MB: Computer Program for Nonlinear Dynamic Analysis of Seismically Isolated Structures," by P.C. Tsopelas, P.C. Roussis, M.C. Constantinou, R. Buchanan and A.M. Reinhorn, 10/3/05 (PB2006-111703).

MCEER-05-0010 "Steel Plate Shear Walls for Seismic Design and Retrofit of Building Structures," by D. Vian and M. Bruneau, 12/15/05 (PB2006-111704).

MCEER-05-0011   "The Performance-Based Design Paradigm," by M.J. Astrella and A. Whittaker, 12/15/05 (PB2006-111705).

MCEER-06-0001   "Seismic Fragility of Suspended Ceiling Systems," H. Badillo-Almaraz, A.S. Whittaker, A.M. Reinhorn and G.P. Cimellaro, 2/4/06 (PB2006-111706).

MCEER-06-0002   "Multi-Dimensional Fragility of Structures," by G.P. Cimellaro, A.M. Reinhorn and M. Bruneau, 3/1/06 (PB2007-106974, A09, MF-A02, CD A00).

MCEER-06-0003   "Built-Up Shear Links as Energy Dissipators for Seismic Protection of Bridges," by P. Dusicka, A.M. Itani and I.G. Buckle, 3/15/06 (PB2006-111708).

MCEER-06-0004   "Analytical Investigation of the Structural Fuse Concept," by R.E. Vargas and M. Bruneau, 3/16/06 (PB2006-111709).

MCEER-06-0005   "Experimental Investigation of the Structural Fuse Concept," by R.E. Vargas and M. Bruneau, 3/17/06 (PB2006-111710).

MCEER-06-0006   "Further Development of Tubular Eccentrically Braced Frame Links for the Seismic Retrofit of Braced Steel Truss Bridge Piers," by J.W. Berman and M. Bruneau, 3/27/06 (PB2007-105147).

MCEER-06-0007   "REDARS Validation Report," by S. Cho, C.K. Huyck, S. Ghosh and R.T. Eguchi, 8/8/06 (PB2007-106983).

MCEER-06-0008   "Review of Current NDE Technologies for Post-Earthquake Assessment of Retrofitted Bridge Columns," by J.W. Song, Z. Liang and G.C. Lee, 8/21/06 (PB2007-106984).

MCEER-06-0009   "Liquefaction Remediation in Silty Soils Using Dynamic Compaction and Stone Columns," by S. Thevanayagam, G.R. Martin, R. Nashed, T. Shenthan, T. Kanagalingam and N. Ecemis, 8/28/06 (PB2007-106985).

MCEER-06-0010   "Conceptual Design and Experimental Investigation of Polymer Matrix Composite Infill Panels for Seismic Retrofitting," by W. Jung, M. Chiewanichakorn and A.J. Aref, 9/21/06 (PB2007-106986).

MCEER-06-0011   "A Study of the Coupled Horizontal-Vertical Behavior of Elastomeric and Lead-Rubber Seismic Isolation Bearings," by G.P. Warn and A.S. Whittaker, 9/22/06 (PB2007-108679).

MCEER-06-0012   "Proceedings of the Fourth PRC-US Workshop on Seismic Analysis and Design of Special Bridges: Advancing Bridge Technologies in Research, Design, Construction and Preservation," Edited by L.C. Fan, G.C. Lee and L. Ziang, 10/12/06 (PB2007-109042).

MCEER-06-0013   "Cyclic Response and Low Cycle Fatigue Characteristics of Plate Steels," by P. Dusicka, A.M. Itani and I.G. Buckle, 11/1/06 06 (PB2007-106987).

MCEER-06-0014   "Proceedings of the Second US-Taiwan Bridge Engineering Workshop," edited by W.P. Yen, J. Shen, J-Y. Chen and M. Wang, 11/15/06 (PB2008-500041).

MCEER-06-0015   "User Manual and Technical Documentation for the REDARS™ Import Wizard," by S. Cho, S. Ghosh, C.K. Huyck and S.D. Werner, 11/30/06 (PB2007-114766).

MCEER-06-0016   "Hazard Mitigation Strategy and Monitoring Technologies for Urban and Infrastructure Public Buildings: Proceedings of the China-US Workshops," edited by X.Y. Zhou, A.L. Zhang, G.C. Lee and M. Tong, 12/12/06 (PB2008-500018).

MCEER-07-0001   "Static and Kinetic Coefficients of Friction for Rigid Blocks," by C. Kafali, S. Fathali, M. Grigoriu and A.S. Whittaker, 3/20/07 (PB2007-114767).

MCEER-07-0002   "Hazard Mitigation Investment Decision Making: Organizational Response to Legislative Mandate," by L.A. Arendt, D.J. Alesch and W.J. Petak, 4/9/07 (PB2007-114768).

MCEER-07-0003   "Seismic Behavior of Bidirectional-Resistant Ductile End Diaphragms with Unbonded Braces in Straight or Skewed Steel Bridges," by O. Celik and M. Bruneau, 4/11/07 (PB2008-105141).

MCEER-07-0004 "Modeling Pile Behavior in Large Pile Groups Under Lateral Loading," by A.M. Dodds and G.R. Martin, 4/16/07(PB2008-105142).

MCEER-07-0005 "Experimental Investigation of Blast Performance of Seismically Resistant Concrete-Filled Steel Tube Bridge Piers," by S. Fujikura, M. Bruneau and D. Lopez-Garcia, 4/20/07 (PB2008-105143).

MCEER-07-0006 "Seismic Analysis of Conventional and Isolated Liquefied Natural Gas Tanks Using Mechanical Analogs," by I.P. Christovasilis and A.S. Whittaker, 5/1/07.

MCEER-07-0007 "Experimental Seismic Performance Evaluation of Isolation/Restraint Systems for Mechanical Equipment – Part 1: Heavy Equipment Study," by S. Fathali and A. Filiatrault, 6/6/07 (PB2008-105144).

MCEER-07-0008 "Seismic Vulnerability of Timber Bridges and Timber Substructures," by A.A. Sharma, J.B. Mander, I.M. Friedland and D.R. Allicock, 6/7/07 (PB2008-105145).

MCEER-07-0009 "Experimental and Analytical Study of the XY-Friction Pendulum (XY-FP) Bearing for Bridge Applications," by C.C. Marin-Artieda, A.S. Whittaker and M.C. Constantinou, 6/7/07 (PB2008-105191).

MCEER-07-0010 "Proceedings of the PRC-US Earthquake Engineering Forum for Young Researchers," Edited by G.C. Lee and X.Z. Qi, 6/8/07.

MCEER-07-0011 "Design Recommendations for Perforated Steel Plate Shear Walls," by R. Purba and M. Bruneau, 6/18/07, (PB2008-105192).

MCEER-07-0012 "Performance of Seismic Isolation Hardware Under Service and Seismic Loading," by M.C. Constantinou, A.S. Whittaker, Y. Kalpakidis, D.M. Fenz and G.P. Warn, 8/27/07, (PB2008-105193).

MCEER-07-0013 "Experimental Evaluation of the Seismic Performance of Hospital Piping Subassemblies," by E.R. Goodwin, E. Maragakis and A.M. Itani, 9/4/07, (PB2008-105194).

MCEER-07-0014 "A Simulation Model of Urban Disaster Recovery and Resilience: Implementation for the 1994 Northridge Earthquake," by S. Miles and S.E. Chang, 9/7/07, (PB2008-106426).

MCEER-07-0015 "Statistical and Mechanistic Fragility Analysis of Concrete Bridges," by M. Shinozuka, S. Banerjee and S-H. Kim, 9/10/07, (PB2008-106427).

MCEER-07-0016 "Three-Dimensional Modeling of Inelastic Buckling in Frame Structures," by M. Schachter and AM. Reinhorn, 9/13/07, (PB2008-108125).

MCEER-07-0017 "Modeling of Seismic Wave Scattering on Pile Groups and Caissons," by I. Po Lam, H. Law and C.T. Yang, 9/17/07 (PB2008-108150).

MCEER-07-0018 "Bridge Foundations: Modeling Large Pile Groups and Caissons for Seismic Design," by I. Po Lam, H. Law and G.R. Martin (Coordinating Author), 12/1/07 (PB2008-111190).

MCEER-07-0019 "Principles and Performance of Roller Seismic Isolation Bearings for Highway Bridges," by G.C. Lee, Y.C. Ou, Z. Liang, T.C. Niu and J. Song, 12/10/07.

MCEER-07-0020 "Centrifuge Modeling of Permeability and Pinning Reinforcement Effects on Pile Response to Lateral Spreading," by L.L Gonzalez-Lagos, T. Abdoun and R. Dobry, 12/10/07 (PB2008-111191).

MCEER-07-0021 "Damage to the Highway System from the Pisco, Perú Earthquake of August 15, 2007," by J.S. O'Connor, L. Mesa and M. Nykamp, 12/10/07, (PB2008-108126).

MCEER-07-0022 "Experimental Seismic Performance Evaluation of Isolation/Restraint Systems for Mechanical Equipment – Part 2: Light Equipment Study," by S. Fathali and A. Filiatrault, 12/13/07 (PB2008-111192).

MCEER-07-0023 "Fragility Considerations in Highway Bridge Design," by M. Shinozuka, S. Banerjee and S.H. Kim, 12/14/07 (PB2008-111193).

MCEER-07-0024   "Performance Estimates for Seismically Isolated Bridges," by G.P. Warn and A.S. Whittaker, 12/30/07 (PB2008-112230).

MCEER-08-0001   "Seismic Performance of Steel Girder Bridge Superstructures with Conventional Cross Frames," by L.P. Carden, A.M. Itani and I.G. Buckle, 1/7/08, (PB2008-112231).

MCEER-08-0002   "Seismic Performance of Steel Girder Bridge Superstructures with Ductile End Cross Frames with Seismic Isolators," by L.P. Carden, A.M. Itani and I.G. Buckle, 1/7/08 (PB2008-112232).

MCEER-08-0003   "Analytical and Experimental Investigation of a Controlled Rocking Approach for Seismic Protection of Bridge Steel Truss Piers," by M. Pollino and M. Bruneau, 1/21/08 (PB2008-112233).

MCEER-08-0004   "Linking Lifeline Infrastructure Performance and Community Disaster Resilience: Models and Multi-Stakeholder Processes," by S.E. Chang, C. Pasion, K. Tatebe and R. Ahmad, 3/3/08 (PB2008-112234).

MCEER-08-0005   "Modal Analysis of Generally Damped Linear Structures Subjected to Seismic Excitations," by J. Song, Y-L. Chu, Z. Liang and G.C. Lee, 3/4/08 (PB2009-102311).

MCEER-08-0006   "System Performance Under Multi-Hazard Environments," by C. Kafali and M. Grigoriu, 3/4/08 (PB2008-112235).

MCEER-08-0007   "Mechanical Behavior of Multi-Spherical Sliding Bearings," by D.M. Fenz and M.C. Constantinou, 3/6/08 (PB2008-112236).

MCEER-08-0008   "Post-Earthquake Restoration of the Los Angeles Water Supply System," by T.H.P. Tabucchi and R.A. Davidson, 3/7/08 (PB2008-112237).

MCEER-08-0009   "Fragility Analysis of Water Supply Systems," by A. Jacobson and M. Grigoriu, 3/10/08.

MCEER-08-0010   "Experimental Investigation of Full-Scale Two-Story Steel Plate Shear Walls with Reduced Beam Section Connections," by B. Qu, M. Bruneau, C-H. Lin and K-C. Tsai, 3/17/08.

MCEER-08-0011   "Seismic Evaluation and Rehabilitation of Critical Components of Electrical Power Systems," S. Ersoy, B. Feizi, A. Ashrafi and M. Ala Saadeghvaziri, 3/17/08.

MCEER-08-0012   "Seismic Behavior and Design of Boundary Frame Members of Steel Plate Shear Walls," by B. Qu and M. Bruneau, 4/26/08.

MCEER-08-0013   "Development and Appraisal of a Numerical Cyclic Loading Protocol for Quantifying Building System Performance," by A. Filiatrault, A. Wanitkorkul and M. Constantinou, 4/27/08.

MCEER-08-0014   "Structural and Nonstructural Earthquake Design: The Challenge of Integrating Specialty Areas in Designing Complex, Critical Facilities," by W.J. Petak and D.J. Alesch, 4/30/08.

MCEER-08-0015   "Seismic Performance Evaluation of Water Systems," by Y. Wang and T.D. O'Rourke, 5/5/08.